JOURNAL OF THE

Electrochemical Society

111, No. 7 July 1964

PRODUCTS GRAPHITE PRODUCTS GLC DIVISION YOU CAN TRUST

GREAT LAKES CARBON CORPORATION

18 EAST 48th STREET, NEW YORK, N. Y. 10017 — OFFICES IN PRINCIPAL CITIES

Stackpole Anodes last longer... COST LESS

Stackpole GraphAnodes® have "long life" built-in. Controlled manufacturing insures structural uniformity. Careful inspection of anode surfaces assures perfect cell alignment. Such care produces anodes that wear evenly, last longer and produce less cell contamination. Special Stackpole impregnants lengthen diaphragm life and reduce cell maintenance.

GraphAnodes are supplied with holes, slots, threads, bevels, and other features to meet individual needs. For those doing their own finishing, unmachined anodes within commercial tolerances can be supplied.

Whether you have diaphragm cells or mercury cells, Stackpole offers the shapes you require in a wide range of strength, porosity and resistance characteristics. For more information on how long-lasting, economical Stackpole GraphAnodes can cut costs for you, write: Stackpole Carbon Company, Carbon Division, St. Marys, Pa. Phone: 814-834-1521 TWX: 814-826-4808.

STACKPOLE
CARBON DIVISION

JOURNAL OF THE

JULY 1964

EDITORIAL

A. J. Salkind . . . 144C — Electrochemical Education and Training

TECHNICAL PAPERS

J. Burbank . . . 765 — Morphology of PbO_2 in the Positive Plates of Lead Acid Cells

J. L. Weininger . . . 769 — Thermogalvanic Cells with Silver Iodide as a Solid Electrolyte

R. J. Adams, H. L. Weisbecker, and W. J. McDonald . . . 774 — The Effect of Abrasion on the Specifc Surface Area of Metals and Glass

J. S. L. Leach and A. Y. Nehru . . . 781 — The Corrosion of Uranium, Zirconium, and Some Alloys in Alkaline Solutions

D. L. Douglass and H. A. Fisch . . . 787 — The Effect of Heat-Treatment on the Corrosion and Hydrogen Pickup Behavior of a Zr-Sn-Nb Alloy in High Temperature Water and Steam

M. E. Straumanis and K. A. Poush . . . 795 — The Trivalency of Gallium Ions Formed during the Dissolution of the Metal in Acids

J. Vergnolle . . . 799 — Distributed Network Analysis of Porous Electrodes Capacitors

L. B. Griffiths and A. I. Mlavsky . . . 805 — Growth of α-SiC Single Crystals from Chromium Solution

T. G. R. Rawlins . . . 810 — Measurement of the Resistivity of Epitaxial Vapor Grown Films of Silicon by an Infrared Technique

W. F. Finch and E. W. Mehal . . . 814 — Preparation of $GaAs_xP_{1-x}$ by Vapor Phase Reaction

T. Gabor . . . 817 — Epitaxial Growth of Gallium Arsenide on Germanium Substrates, I. The Relationship Between Fault Formation in Gallium Arsenide Films and the Surface of Their Germanium Substrate

T. Gabor . . . 821 — Epitaxial Growth of Gallium Arsenide on Germanium Substrates, II. Deteroriation of the 111 Surface of Germanium at 570°-850°C

T. Gabor . . . 825 — Epitaxial Growth of Gallium Arsenide on Germanium Substrates, III. Deposition on High Index Planes and on Curved Surfaces

A. K. Kuriakose and J. L. Margrave . . . 827 — The Oxidation Kinetics of Zirconium Diboride and Zirconium Carbide at High Temperatures

G. M. Schmid and R. N. O'Brien . . . 832 — "Oxygen" Adsorption and Double Layer Capacities; Gold in Perchloric Acid

W. G. B. Mandersloot . . . 838 — Electrodialytic Demineralization Using Permselective Membranes, I. Energy Consumption and Production Rate

ELECTROCHEMICAL SOCIETY

VOL. 111 • NO. 7

J. O'M. Bockris and S. Srinivasan . . . 844 — Theoretical Calculation of the Separation Factors in the Hydrogen Evolution Reaction for the Slow Discharge Mechanism

J. O'M. Bockris and S. Srinivasan . . . 853 — Theoretical Calculations of the Separation Factors in The Hydrogen Evolution Reaction for the Slow Electrochemical Desorption Mechanism

J. O'M. Bockris and S. Srinivasan . . . 858 — Theoretical Calculations of the Separation Factors in the Hydrogen Evolution Reaction for the Slow Recombination Mechanism

J. W. Johnson, H. Wroblowa, and J. O'M. Bockris . . . 863 — The Mechanism of the Electro-Oxidation of Acetylene on Platinum

TECHNICAL NOTES

F. Ogburn . . . 870 — Growth Twins and Branching of Electrodeposited Copper Dendrites

W. A. Pliskin and R. P. Gnall . . . 872 — Evidence for Oxidation Growth at the Oxide-Silicon Interface from Controlled Etch Studies

L. H. Brixner, P. A. Flournoy, and K. Babcock . . . 873 — Note on Calcium-Orthovanadate

G. R. Cronin and R. W. Haisty . . . 874 — The Preparation of Semi-Insulating Gallium Arsenide by Chromium Doping

W. J. McAleer, M. A. Kozlowski, and P. I. Pollak . . . 877 — Polycrystalline Silicone Films on Foreign Substrates

R. R. Monchamp, W. J. McAleer, and P. I. Pollak . . . 879 — A Kinetic Study of the System Si-$SiCl_4$

R. W. Brander . . . 881 — Epitaxial Growth of Silicon Carbide

D. A. Vermilyea . . . 883 — Ta_2O_5 Films Formed with Nonsteady Potentials

BRIEF COMMUNICATIONS

W. K. Liebmann . . . 885 — Orientation of Stacking Faults and Dislocation Etch Pits in β-SiC

F. V. Williams . . . 886 — The Effect of Orientation on the Electrical Properties of Epitaxial Gallium Arsenide

J. H. Westbrook, A. U. Seybolt, and A. J. Peat . . . 888 — A Thermal Probe for Segregation Detection

FEATURE SECTION

W. J. Hamer . . . 145C — Scientific Communication—Presidential Address

CURRENT AFFAIRS

. . . 141C-160C

Manuscripts submitted to the Journal should be sent, in triplicate, to the Editorial Office at 30 East 42 St., New York, N. Y., 10017. They should conform to the revised Instructions to Authors published on pp. 159C-160C of this issue. Manuscripts so submitted become the property of The Electrochemical Society and may not be published elsewhere, in whole or in part, unless permission is requested of and granted by the Editor.

The Electrochemical Society does not maintain a supply of reprints of papers appearing in its Journal. A photoprint copy of any particular paper, however, may be obtained by corresponding direct with the Engineering Societies Library, 345 E. 47 St., New York, N. Y., 10017.

Inquiries re positive microfilm copies of volumes should be addressed to University Microfilms, Inc., 313 N. First St., Ann Arbor, Mich.

Walter J. Johnson, Inc., 111 Fifth Ave., New York, N. Y., 10003, have reprint rights to out-of-print volumes of the Journal, and also have available for sale back volumes and single issues, with the exception of the current calendar year. Anyone interested in securing back copies should correspond direct with them.

Published monthly by The Electrochemical Society, Inc., at 215 Canal St., Manchester, N. H.; **Executive Offices, Editorial Office** and **Circulation Dept.**, and **Advertising Office** at 30 East 42 St., New York, N. Y., 10017, combining the JOURNAL and TRANSACTIONS OF THE ELECTROCHEMICAL SOCIETY. Statements and opinions given in articles and papers in the JOURNAL OF THE ELECTROCHEMICAL SOCIETY are those of the contributors, and The Electrochemical Society assumes no responsibility for them.

Claims for missing numbers will not be allowed if received more than 60 days from date of mailing plus time normally required for postal delivery of JOURNAL and claim. No claims allowed because of failure to notify the Circulation Dept., The Electrochemical Society, 30 East 42 St., New York, N. Y., 10017, of a change of address, or because copy is "missing from files." Subscription to members as part of membership service; subscription to nonmembers $24.00 plus $1.50 for postage outside U.S. and Canada. Single copies $1.70 to members, $2.25 to nonmembers.

Entered as second-class matter at the Post Office at Manchester N. H., under the act of August 24, 1912. Postage paid at Manchester, N. H.

Editorial

Electrochemical Education and Training

THE changes and advances in educational background and training of applicants for membership in The Electrochemical Society were discussed by Mr. Frank LaQue in his Presidential address, which was published in the July 1963 issue of *This Journal*. Among the points uncovered by Mr. LaQue's survey of educational institutions, was the fact that there is only very limited opportunity for students to get direct training in Electrochemistry or Electrochemical Engineering at either the graduate or the undergraduate level. Rather, most institutions provide the opportunity to study at least some aspects of these subjects as parts of other courses, but in a much limited way.

At first glance this may appear to be a sufficient and proper, even a desirable method of providing education and training in the various branches of electrochemistry, assuming that the material presented is not too meager. The practical consequence, however, is that much of the important subject matter of our field is overlooked. There is generally little attempt to correlate the facts presented in the other courses, particularly with respect to their application to electrochemical engineering. The failure to coordinate then often leads to complete neglect of the newer aspects of our discipline; and the lack of emphasis on electrochemistry as such is coupled with a complete lack of recognition of The Electrochemical Society as a Scientific Institution.

The neglect of Electrochemistry as an important subject in its own right gets carried over into nonacademic fields. For instance in the new edition of the "Chemical Engineering Handbook," the Electrochemistry discussion section was eliminated; the Battery discussion was completely rewritten and included as part of the Electrical Engineering Section. So far as I can ascertain these matters were not checked with The Electrochemical Society. This treatment seems particularly unfortunate in view of the dynamic interest in electrochemical engineering currently being shown in various Chemical Engineering departments; and one deplores the misspelled words as well as the unsophisticated discussion of batteries which resulted.

I believe that the lack of interest in our field of science displayed by some colleges is a consequence of their lack of even *one* faculty member whose research and teaching interests are in this discipline. Many of us are active in the various Alumni Associations of American Universities, and perhaps we should try to help stimulate this interest through those organizations where possible. In some cases it should be possible for qualified members of the Society to serve as classroom lecturers on a one-afternoon or a one-night a week basis in order to provide institutions with a staff member oriented toward electrochemistry and electrochemical engineering; this might provide the necessary initial stimulus.

—A. J. Salkind[1]

[1] Physical Chemistry Division, Research Center, The Electric Storage Battery Co.; Adjunct Professor of Chemical Engineering, Polytechnic Institute of Brooklyn.

Morphology of PbO_2 in the Positive Plates of Lead Acid Cells

Jeanne Burbank

U. S. Naval Research Laboratory, Washington, D. C.

ABSTRACT

Several preparations of PbO_2 including positive active material from lead antimony and lead calcium cells were examined by electron microscopy. The morphology of the particles is believed to have a bearing on positive paste retention and plate performance in the lead acid cell. The anodic coating of PbO_2 formed on pure lead sheet in H_2SO_4 was found to be prismatic when first formed, but lost its prismatic character on prolonged anodization and on cycling.

The primary component of the positive plate in the fully charged lead acid cell is PbO_2. This material exists in two polymorphic forms, the low-temperature α form is orthorhombic, and the high-temperature β form is tetragonal (1-3). Both phases have been observed in the positive plate active material of the battery and in anodic corrosion products on lead (4-7). The corrosion products, the surfaces of battery plates, and electrodeposits of PbO_2 have been examined by electron microscopy (7-11).

Mineral deposits of PbO_2, plattnerite, do not commonly exhibit well-developed crystals, but occur in nodular masses (12). Synthetic β PbO_2 crystallized by hydrothermal treatment exhibits a morphology characteristic of its rutile structure type (13); however, most synthetic PbO_2 preparations do not give crystals large enough to be described by optical methods.

The lead calcium storage battery was developed for float service in the telephone system (14, 15) and has proved satisfactory in such installations. In recent years the lead calcium cell has been used on submarines in float service, but many failures were experienced in the early installations. As part of an investigation of this problem, the positive plates were examined by electron microscopy. The major difference between failing and successful cells was found to be a startling contrast in morphology of the particles of PbO_2 in the positives (16). It is generally agreed that the strength of particulate conglomerates is imparted by the morphology of the several species present. For example, Sliepcevich, Gildart, and Katz (17) discussing Portland Cement concrete state that ". . .the strength of the concrete is attributable to an abundance of crystals in the form of splines, needles and films matted together and bonded together by the amorphous mass." In agreement with this picturization, positive battery plates that contain mostly nondescript pebble-like nodular PbO_2 particles were found to soften and fail. On the other hand, plates made up of PbO_2 particles that were prismatic needles with many branches, possibly twinned, maintained capacity and retained a firm texture.

Astakhov, Kiseleva, and Kabanov (11) examined electrolytic deposits of the two polymorphs of PbO_2 by electron microscopy and indicated that there was a relation between mechanical strength and morphology of the crystals in the electrode; they further suggested that the same considerations would apply to the stability of battery plates.

For this investigation commercial battery plates from several manufacturers in both lead antimony and lead calcium cells were examined by electron microscopy. Considerable variation was found in the particle morphology.

Experimental

Carbon replicas (18) were prepared of the specimens of PbO_2, and, after removal of the PbO_2 by solution in dilute HNO_3 containing H_2O_2, the replicas were examined in an RCA EMU-2B electron microscope.

Particulate specimens of PbO_2 were dispersed by floating on water in a crystallizing dish and picked up on parlodion films supported on specimen screens of the electron microscope. The carbon replicas were deposited by vacuum evaporation. After replication, the parlodion supporting film was dissolved in acetone by flooding the sample resting on a folded piece of filter paper from which the screens were then gently lifted with fine tweezers. The carbon replica would tend to be cemented to the screen mesh by any residual softened parlodion. The specimen was then touched to clean blotting paper and dropped onto the surface of the acid H_2O_2 solution. Following solution of the PbO_2, a matter of a minute or two, the specimen was transferred to a surface of distilled water. After rinsing, it was transferred to blotting paper or onto a peg for air drying.

The active material from the battery plates and a cycled specimen of lead sheet were extracted with saturated ammonium acetate solution in order to obtain dispersion of the PbO_2 into discrete particles. Acid extraction of Pb_3O_4 also gave a residue of PbO_2 that was examined. The extracted material was dispersed by placing a drop of the run on slurry on the surface of distilled water in a crystallizing dish where the particles would float out across the surface, and these were then mounted for replication as described above.

Anodized lead sheet was replicated directly after blotting dry. The surface was scored into small squares, and the sample was gently lowered into dilute acetic acid containing H_2O_2. Carbon films floated free on the surface and were transferred to

distilled water for rinsing. The films were then picked up on specimen screens of the electron microscope and air dried.

Results and Discussion

Anodic corrosion product on pure lead.—Earlier studies by electron diffraction (19) showed that the initial deposition of PbO_2 on pure lead by anodization in H_2SO_4 was preferentially oriented, and that on further anodization the deposit had random orientation. The initial deposit, Fig. 1, appears to be entirely prismatic, and clusters of crystallites of similar orientation are clearly discernible. This is the kind of deposit that is too thin to give x-ray diffraction patterns, but strong electron diffraction patterns are registered. The areas of similarly oriented crystallites confirm the electron diffraction observations of preferred orientation reported in the earlier studies. When the deposit was thickened by prolonged anodization, the coating began to spall from the surface. The electron micrograph, Fig. 2, of the anodic sample at this stage suggests that there is a total loss in prismatic character, and also shows the flaky nature of the coating. A coating of this type gives a polycrystalline diffraction pattern. As the specimen was cycled, the coating continued to shed, and it has been shown by Feitknecht and Gaumann (7-8) that the surface becomes covered with nodular concretions of PbO_2. The individual particles are

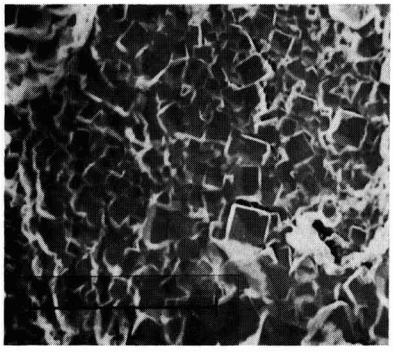

Fig. 1. Pure lead sheet anodized in H_2SO_4 for 68 hr. This thin coating of PbO_2 is prismatic and appears to exhibit definite areas of preferred orientation of the crystallites.

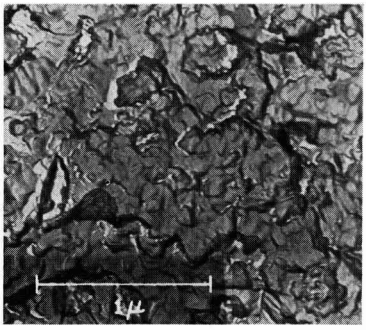

Fig. 2. Pure lead sheet anodized in H_2SO_4 for 1464 hr. The individual crystallites of thinner films (Fig. 1) have disappeared, and the coating is flaking away from the surface.

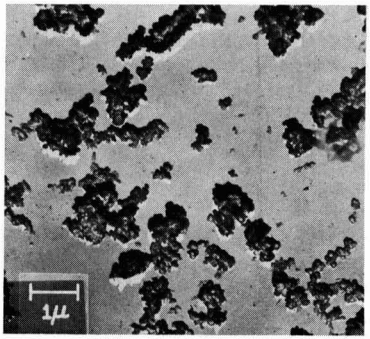

Fig. 3. Particles of PbO_2 isolated from a sheet of pure lead cycled 8 times in H_2SO_4. The individual particles are difficult to disperse and tend to clump together; however, they appear to be approximately 0.1μ in diameter, and to be spheroidal. These particles are believed to be obtained by conversion from $PbSO_4$ and, unless bound by mechanical or chemical forces, readily detach themselves from the electrode surface.

submicron size and appear to be spheroidal. Figure 3 shows a carbon replica of such particles isolated from the surface of the cycled specimen. These particles are rather uniform in size and appear to be approximately 0.1μ in diameter. This is in the same range observed by Feitknecht and Gaumann and Burbank (8, 20); however, on the basis of x-ray line broadening, Feitknecht (7) estimated the particles to be about 100Å. It is difficult to obtain good dispersion of such fine material by the techniques used in this work; however, these certainly lie within the colloidal range. It is these particles that form a reddish cloud in the electrolyte near the electrode surface if gas evolution is vigorous enough, and in turn give rise to lead trees as they circulate in the cell and come into contact with the negative electrode. As the anodic coating builds up, it tends to lose electrical contact with the lead surface and continuity between individual particles. In Planté plate formation it is necessary to retain the PbO_2 particles in a mass on the surface in order to get adequate capacity from the plates. Feitknecht's electron micrographs taken during self-discharge show that prismatic sulfate crystals grow during open-circuit stand. In a study of lead calcium cells (16) it was shown that even in pasted plates when the active material is composed of nondescript nodular PbO_2 particles, the plates would not give satisfactory capacity until sufficient prismatic $PbSO_4$ had been formed to bind the mass together. Planté in 1887 (21) described similar behavior thus: "A singular phenomenon frequently observed with secondary lead cells: it is found that immediately after charging, the battery will not pass enough current to heat a platinum wire, but after standing on open-circuit for about 24 hours it will heat the same wire to incandescence." He attributed this to a film of gas, but it appears from the electron microscopic investigations that during the 24 hr stand sufficient sulfate crystallized to cement the particles into a conducting mass.

Battery plates.—The positive active material from commercial battery plates shows a wide vari-

ety of particle morphology varying from complex prismatic crystals to nodular forms. Some commercial plates appear to be entirely prismatic in nature while others are entirely nondescript nodular formations. Still others contain clusters of well-developed prismatic crystals in a matrix of nondescript material. These formations are illustrated in the electron micrographs shown in Fig. 4-8. It

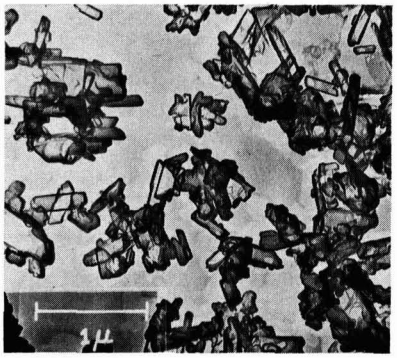

Fig. 4. Positive active material from lead calcium cells showing almost entirely prismatic crystallization. Plates composed of these particles remained firm and retained capacity in shallow cycling tests.

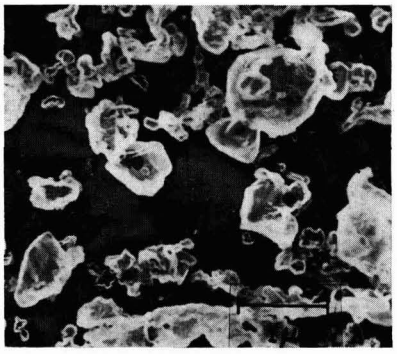

Fig. 5. Positive active material from lead calcium cells showing predominantly nodular crystallization. Plates composed of these particles softened and failed after a few weeks of shallow cycle testing.

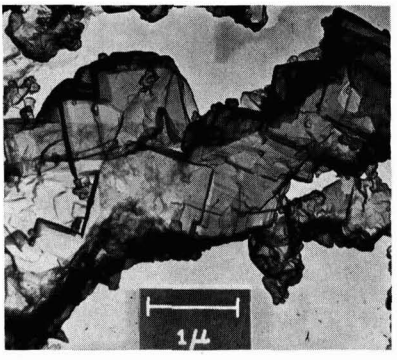

Fig. 6. Positive active material from a lead antimony cell. Massive prismatic conglomerates were characteristic of the active material in this sample.

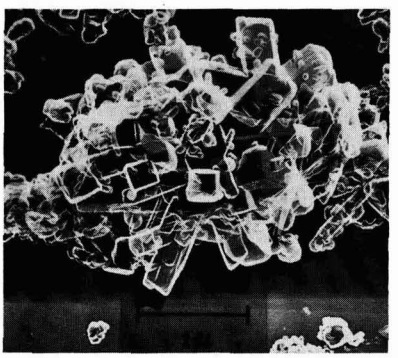

Fig. 7. A large cluster of prismatic crystals showing many side arms illustrating the interlocking believed to be associated with morphology of this type which is believed to impart mechanical strength to the positive paste.

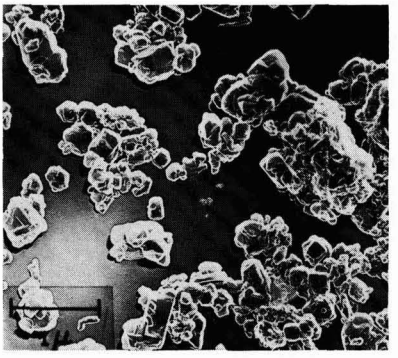

Fig. 8. Particles of positive active material showing an intermediate development of prismatic character. These particles retain some prismatic form, but are not characterized by intricate branching and would not be expected to impart mechanical strength to the active mass.

has been shown in an earlier study (16) that plates containing large amounts of prismatic material maintained capacity whereas plates comprised mainly of nondescript particles suffered drastic capacity loss and failed because of softening of the active mass. If the plates containing nondescript particles were operated in such a way as to retain prismatic sulfate crystals in the active material, satisfactory performance could be obtained from them. It is apparent that morphology of the particles plays a significant role in the retention of the positive active material in the lead acid cell.

Miscellaneous preparations.—Reagent grade PbO_2 was also examined as a matter of curiosity, and the sample available at this Laboratory showed a mixture of prismatic and nondescript particles Fig. 9. The growth habit of the prismatic crystals was different from that exhibited by the prismatic battery samples.

If Pb_3O_4 is extracted with acids that react with the divalent lead, PbO_2 is deposited. The lattice of Pb_3O_4 contains both di- and tetravalent lead, and the residue of PbO_2 is formed by deposition from solution. This material is not contained as such in

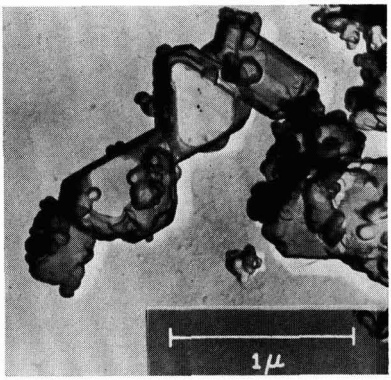

Fig. 9a. Particles of reagent grade PbO_2. Prismatic crystals showing a growth habit different from those contained in the active material of the cells illustrated in Fig. 4, 6, and 7.

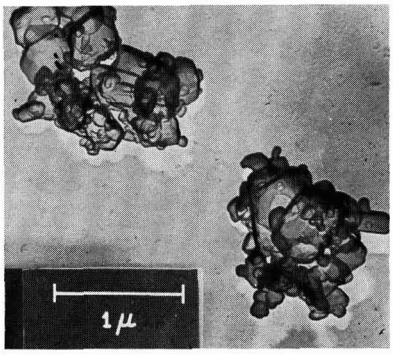

Fig. 9b. Particles of reagent grade PbO_2. Mixture of nodular and prismatic forms. This type of material formed the bulk of the sample.

Fig. 10. PbO_2 obtained by extraction of Pb_3O_4. The smallest individuals appear to be spheroidal, and the large particles may be conglomerates of these small units. There appears to be no tendency toward prismatic development.

the Pb_3O_4 lattice. Figure 10 is an electron micrograph of the PbO_2 residue obtained from extracting Pb_3O_4 and shows a lack of well developed crystals. The individual particles are very small, and no prismatic forms were observed.

It is concluded that the morphology of battery active materials may be correlated with the performance of the plates at least under certain conditions. Optical microscopic examination of the active materials (22) has also shown variations in structure of a different order of magnitude. These studies suggest that improvements in battery performance may be expected to result from such examinations of structures and physical mechanisms of operation. It is hoped that this study will serve to stimulate further investigations of paste morphology and its relation to electrochemical and mechanical properties of battery active materials.

Manuscript received Jan. 28, 1964.

Any discussion of this paper will appear in a Discussion Section to be published in the June 1965 JOURNAL.

REFERENCES

1. A. I. Zaslavskii, Yu. D. Kondrashov, and S. S. Tolkachev, *Doklady Akad. Nauk. S.S.S.R.*, **75**, 559 (1950).
2. A. I. Zaslavskii and S. S. Talkachev, *J. Phys. Chem. USSR*, **26**, 743 (1952).
3. W. B. White, F. Dachille, and R. Roy, *Am. Ceram. Soc. J.*, **44**, 170 (1961).
4. H. Bode and E. Voss, *Z. Elektrochem.*, **60**, 1053 (1956).
5. P. Ruetschi and B. D. Cahan, *This Journal*, **104**, 406 (1957).
6. J. Burbank, *ibid.*, **106**, 369 (1959).
7. W. Feitknecht, *Z. Elektrochem.*, **62**, 795 (1958).
8. W. Feitknecht and A. Gaumann, *J. Chim. Phys.*, **49**, 135 (1952).
9. J. E. Buskirk, P. D. Boyd, and V. V. Smith, Paper presented at the Electrochemical Society Meeting, Houston, Texas, October 1960 (Extended Abstract 19).
10. D. Spahrbier, Thesis: Zum elektrochemischen Verhalten der Bleidioxydelektroden Technischen Hochschule, Stuttgart, 1960.
11. I. I. Astakhov, I. G. Kiseleva, and B. N. Kabanov, *Doklady Akad. Nauk. S.S.S.R.*, **126**, 1041 (1959).
12. C. Palache, H. Berman, and C. Frondel, "Dana's System of Mineralogy," Vol. 1, p. 581, John Wiley & Sons, Inc., New York (1944).
13. H. R. Davidson, *Am. Min.*, **26**, 18 (1941).
14. H. E. Haring and U. B. Thomas, *Trans. Electrochem. Soc.*, **68**, 293 (1935).
15. U. B. Thomas, F. T. Forster, and H. E. Haring, *ibid.*, **92**, 313 (1947).
16. J. Burbank, Batteries, Proceedings of the 3rd International Symposium, Bournemouth, England, October 1962, p. 43.
17. C. M. Sliepcevich, L. Gildart, and D. L. Katz, *Ind. Eng. Chem., Ind. Ed.*, **35**, 1178 (1943).
18. D. E. Bradley, *Brit. J. Appl. Phys.*, **5**, 65, 96 (1954).
19. J. Burbank, *This Journal*, **103**, 87 (1956).
20. J. Burbank, *ibid.*, **104**, 693 (1957).
21. G. Planté, Récherches sur L'Electricité, Librarie de A. Fourneau, Paris 1879, p. 72 ff.
22. A. C. Simon and E. L. Jones, *This Journal*, **109**, 760 (1962).

Thermogalvanic Cells with Silver Iodide as a Solid Electrolyte

J. L. Weininger

Research Laboratory, General Electric Company, Schenectady, New York

ABSTRACT

Experiments with the thermocells Ag/α-AgI/Ag and I_2/α-AgI/I_2 are described and compared with theory. The combination of the solid electrolyte, α-AgI, with iodine gas diffusion electrodes gives the iodine cell a figure of merit of 1×10^{-3} deg^{-1} and a theoretical efficiency of 5.1%. In operation of this cell, iodine gas is evolved at the cold electrode and consumed at the hot electrode. These electrode reactions are reversible. In the silver cell, complications are introduced by the formation of silver dendrites at the cathode.

Thermogalvanic cells, "thermocells" for short, are nonisothermal cells usually with identical electrodes in contact with an electrolyte. A difference in temperature of the two electrodes produces an emf (thermopotential) which causes a galvanic current to flow. The temperature coefficient of the thermopotential is the "thermoelectric power" of the electrolytic cell analogous to the thermoelectric power of electronic thermal converters.

Thermocells with solid electrolytes were first studied by Reinhold (1, 2) who was primarily interested in their thermodynamic aspects. Wagner (3) elaborated on the theory and studied the interrelation of the thermogalvanic effect with other heat effects. More recent investigations are due to Holtan (4, 5). A very recent and comprehensive review is due to Agar (6).

Among solid electrolytes silver halides have the largest ionic conductivities. Over the past years they have been studied in this Laboratory as electrolytes for galvanic cells (7, 8) as well as for thermocells. Alpha-silver iodide, a stable form of AgI in the temperature range 146°-552°, is particularly suitable for use in thermocells. This report, therefore, deals with thermocells containing α-AgI as the electrolyte. Two types of thermocells are considered. In the "silver cell" the electrodes are silver (Ag/α-AgI/Ag); in the "iodine cell" iodine gas diffusion electrodes are used (I_2/α-AgI/I_2). Both cells are discussed, but more emphasis is placed on the iodine cell which is thought to have more promise of practical application.

Mechanism.—The mechanisms of the present thermocells are shown in Table I. For the silver cell, the mechanism was proved by Reinhold; the present work experimentally verifies the mechanism of the iodine cell. The latter is also the subject of a recent patent (9). The thermoelectric power of the iodine cell and the dependence of this important parameter on the iodine vapor pressure were first reported by Wagener (10).

Silver Thermocell—Ag/α-AgI/Ag

Cell construction.—Three cell types shown in Fig. 1 were used.

Cell I consists of two silver electrodes, 2 mm thick, which sandwich the AgI electrolyte. The lower electrode (anode) is heated. The electrolyte is a disk 4 mm thick and 5.07 cm^2 in area), contained in a Pyrex spacer to prevent deformation.

In Cell II the cathode (colder electrode) is a silver cup which is maintained above the transformation temperature of α-AgI (146°). AgI is melted and solidified in the cathode under an inert atmosphere to establish the electrolyte. The anode (hotter electrode) is a block of silver at the end of the tip of a soldering iron.

Cell III has the same electrodes and heating arrangement but the electrolyte is a porous ceramic disk (alumina) impregnated with AgI. The porous

Table I. Mechanism of thermocells

	Silver thermocell	Iodine thermocell
	$\oplus$ Ag/α-AgI/Ag $\ominus$ cold hot at T at $T + \Delta T$	$\oplus$ I_2 (Me) α-AgI/I_2 (Me) $\ominus$ hot cold at $T + \Delta T$ at T where Me = inert electrode
Anode:	Temperature: $T + \Delta T$ Reaction: $Ag \rightarrow Ag^+ + e^-$	T $I^- \rightarrow \frac{1}{2}I_2 + e^-$ (or, $AgI \rightarrow \frac{1}{2}I_2 + Ag^+ + e^-$) P_{I_2} increases
Electrolyte:	Ag^+ moves from hot to cold electrode.	Ag^+ moves from cold to hot electrode.
Cathode:	Temperature: T Reaction: $Ag^+ + e^- \rightarrow Ag$	$T + \Delta T$ $\frac{1}{2}I_2 + e^- \rightarrow I^-$ (or, $Ag^+ + \frac{1}{2}I_2 + e^- \rightarrow AgI$).
Net change per Faraday electricity:	transport of 1 mole of silver from hot to cold electrode.	P_{I_2} decreases transport of ½ mole of iodine from cold to hot electrode.

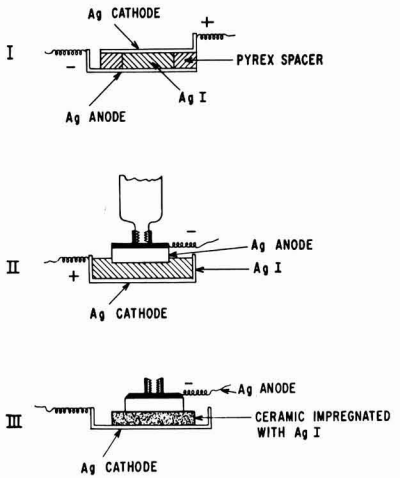

Fig 1. Silver thermocells

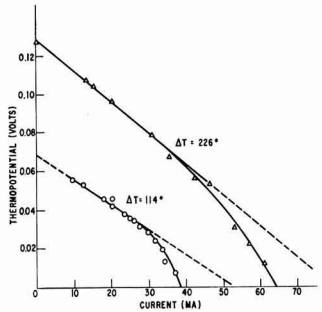

Fig. 2. Thermopotential-current curves for silver thermocell I

matrix was used in an attempt to overcome dendrite formation.

Results.—The experiments confirmed the known mechanism, *i.e.*, that transport of silver takes place from the hot to the cold electrode, with the former as the negative pole.

The thermopotential-current curves obtained with Cell I are shown in Fig. 2. The pertinent data of the two plots are:

$\Delta T = 114°C$, $T_{hot} = 397°$, $T_{cold} = 283°$, $\Delta E/\Delta T = 0.60$ mv/deg, slope = 1.33 ohms

$\Delta T = 226°C$, $T_h = 382°$, $T_c = 156°$, $\Delta E/\Delta T = 0.56$ mv/deg, slope = 1.57 ohms.

With the given geometry the internal resistance should have been 0.056 ohm. Thus, the measured values indicated only about 4% effective contact. In another experiment at $\Delta T = 85°$, an open cell voltage of 46 mv was measured. On passing a total of 290 coulombs in the external circuit, the anode had lost an amount of Ag equivalent to 373 coulombs, which was not deposited on the cathode. Thus, a 22% loss of Ag from the anode and almost constant cathode weight were evidence of an irreversible change. This was explained by the appearance of cell I at the end of the experiment, which is illustrated schematically in Fig. 3. The anode was

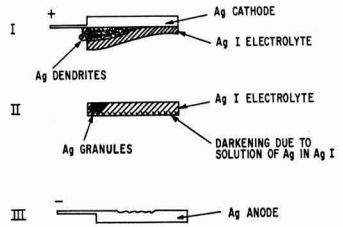

Fig. 3. Dendrite formation in operation of silver thermocell

etched in spots (III), indicating irregular dissolution of silver ions. These formed dendrites at the cathode (I) instead of depositing on the electrode. Silver grains extended also from the cathode into the electrolyte (II).

Better short-term performance was obtained with cell II because of its tighter construction and closer electrode spacing, but dendrite formation became an even more serious problem. At $\Delta T = 414° - 150 = 264°C$, by shorting the cell through the 0.011 ohm range of an ammeter a current of 500 ma was obtained. Dendrites were first seen 8 min after the start of the experiment and after 53 min the cell became internally shorted. As the current slowly decreased, a total passage of about 1000 coulombs was estimated.

With the construction of cell III, dendrite formation was slowed down, but some polarization occurred so that the lifetime of the cell was increased by a factor of 20 whereas the resistance of the cell increased by a factor of 5.

These experiments indicate that dendrite formation and the lack of deposition of silver at the cathode are formidable obstacles to the proper functioning of the silver thermocell. To obtain larger current production, commensurate with the large conductivity of the electrolyte, would require homogeneous deposition and migration of the carrier-ion (Ag^+). In the iodine thermocell, a different set of experimental difficulties are encountered.

Iodine Thermocell—I_2/α-AgI/I_2

Both the iodine and silver thermocells have the same electrolyte with its highly desirable ionic conductivity (ρ = 0.38 ohm-cm at 500°, 0.47 ohm-cm at 350°) (11, 12). They differ, however, in that the carrier-ion (Ag^+) moves in opposite directions with respect to the temperature gradient. Hence, the net transport of material, iodine and silver, respectively, is in opposite directions. This is illustrated in Table I, which also shows that in the iodine cell the iodine pressure is increased at the cold electrode (anode) and decreased at the hot electrode (cathode).

Cell construction.—Two main problems in the design of the iodine cell are the use of gas diffusion electrodes, and the contraction of the room temperature form of AgI on heating and at the transition point β-AgI $\rightarrow$ α-AgI.

Most metals react with iodine at elevated temperatures. However, for preliminary experiments platinum and tantalum were chosen as electrodes because they had proved to be satisfactory for the

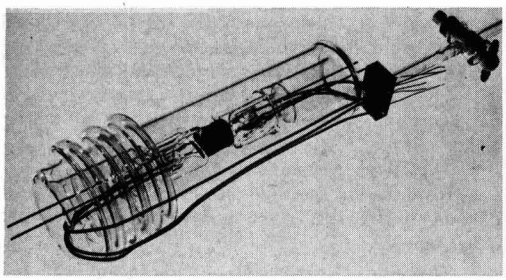

Fig. 4. Iodine thermocell

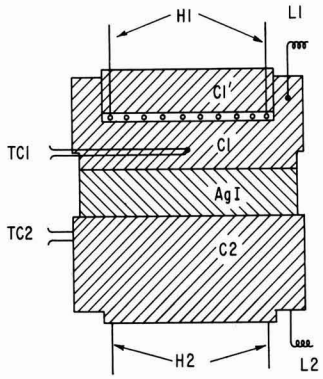

Fig. 5. Detail of iodine thermocell

iodine electrode in the galvanic cell I_2/α-AgI/Ag (8). Later on, porous carbon was found to be a preferable electrode material. Hence the electrodes were prepared from "Ultra-purity" graphite rods, supplied by the United Carbon Products Company. These electrodes had a porosity of 27% and a resistivity of 8×10^{-4} ohm-cm.

Below the temperature of transformation of β-AgI to α-AgI at 145.80°C (12) and during this transformation the electrolyte contracts on heating. Thus, the cell must accommodate contraction and expansion of the electrolyte, on heating and cooling, without either losing contact between electrode and electrolyte, or putting undue strain on the electrodes and their supports. This presents a problem of cell design that was solved by mounting the cell on glass supports within the Pyrex housing which contained glass bellows. The cell is shown in the photograph of Fig. 4. Details of the cell are sketched in Fig. 5. The electrolyte is a disk of AgI, 14 mm in diameter and 3 mm thick. The electrodes, with the same diameter and a thickness of 6 mm, contain small doubly wound spiral heaters (H_1 and H_2) made of 0.010 in. platinum wires, which were insulated with a thin layer of Al_2O_3. These heaters were covered with graphite plugs (*e.g.*, Cl'). The thermocouple leads (TC1 and TC2) were also insulated and the electric leads (L_1 and L_2) were pressure-fitted into the graphite blocks. The two electrodes were identical except that on one there was a shoulder to provide a temporary wall (not shown) for melting the AgI under an inert atmosphere. For operation, iodine crystals were placed in the housing and the cell was evacuated and

Table II. Performance of the iodine cell

Experiment No.	T_h °C	T_c °C	ΔT °C	ΔE, mv	$\Delta E/\Delta T$, mv/deg	Internal resistance, ohms
1	342	262	80	95	1.19	79
2	340	184	156	208	1.33	67*
3	498	218	280	347	1.24	91**
4	335	165	170	232	1.36	61

* At current <0.6 ma.
** At current >1 ma.

closed. At room temperature an iodine vapor pressure of approximately 0.3 mm Hg was then established.

Results.—Table II summarizes the thermopotention-current curves shown in Fig. 6. Within the experimental error the temperature coefficient of the thermopotential, the "thermoelectric power" of the cell, is in agreement with values calculated from thermodynamics. This is discussed below. The internal resistance of the cell, 70 ± 10 ohms, depends on the effective contact area of the interfaces between the inert electrode, the electrolyte, and the gas.

An important characteristic of the iodine thermocell is the advance of the solid electrolyte into the pores of the hot electrode. The coulombic (current-delivering) capacity of the cell, therefore, will be limited by the geometry of the electrodes, but reversing the temperature gradient will renew the capacity of the cell. A test of this capacity is shown in Fig. 7. The cell was discharged through an ex-

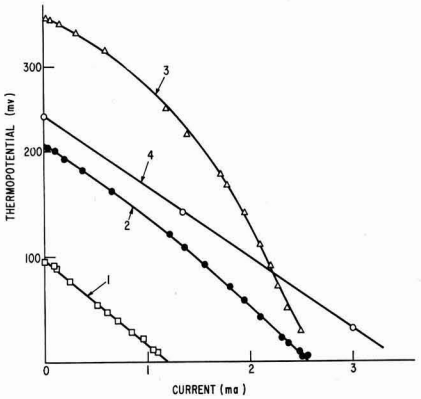

Fig. 6. Thermopotential-current curves for iodine cell

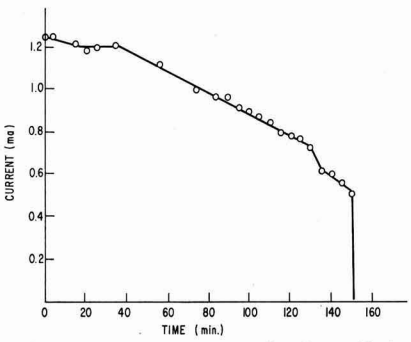

Fig. 7. Coulombic capacity of iodine cell; cell on 100 ohm load; capacity 8.5 coulombs.

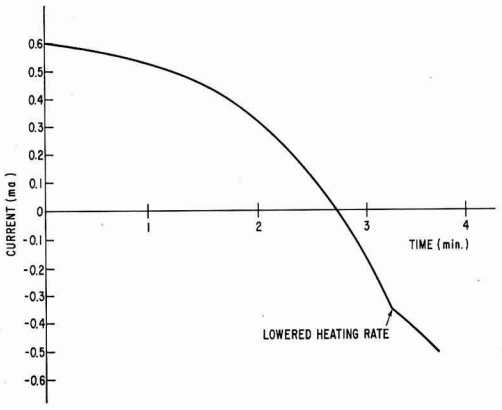

Fig. 8. Current output of iodine thermocell on reversal of temperature gradient.

ternal resistance of 100 ohms ($\Delta T = 150°$, $T_h = 361°$, $T_c = 211°$, open cell potential = 204 mv, $\Delta E/\Delta T = 1.36$ mv/deg). The test was terminated when the current dropped to 0.5 ma, slightly more than one-half its original value. A total of 8.5 coulombs was obtained.

Response to a change in the temperature gradient seemed to be instantaneous. An illustration of this is the reversal of current on reversing the temperature gradient of the cell at the end of the above life test. This is shown in Fig. 8. At time zero the heating of the hot electrode was discontinued and the temperature of the other electrode was increased. The change from positive to negative current proceeded smoothly, and the indicated change of the slope of the curve was due to lowering the heating current of the newly "hot" electrode. This change in cell output was instantaneous.

The motion of the electrolyte was observed as a regularly advancing front of AgI at the outside of the hot carbon electrode. Likewise, it receded on reversing the thermal gradient. In fact, the data of Fig. 6 were obtained on current reversal after exhausting the cell in the reverse direction. The few steps in the current-time curve of Fig. 7 are believed to be real and due to blockage of some of the electrode's pores.

Increasing the iodine pressure by raising the temperature of the whole assembly did not improve the cell performance. This improvement would be expected if the diffusion of iodine in the electrodes were enhanced by reducing the pressure at the anode where iodine is formed, and by increasing the pressure at the cathode, where iodine is consumed. In the present cell, however, the anode and cathode were in one gaseous environment in which the iodine pressure was equalized by convection.

When the cell in one of its discharge cycles was nearly exhausted, an interesting current oscillation was observed. The current showed irregular but periodic fluctuations. This phenomenon is not yet understood, but it might be traced to the breakdown of the electrode/electrolyte/vapor interface. For example, the complete coverage of the inert electrode by the electrolyte, or the inability of the diffusing gas to reach the site of the electrode reaction could account for these oscillations.

Summarizing the experimental results:

1. The thermoelectric power of 1.2 to 1.4 mv/deg has been experimentally established for the iodine cell.

2. The electrode reactions are very fast.

3. Reversal of the sign of the potential (hence current) on reversing the temperature gradient is instantaneous.

4. The internal resistance of the present cell, approximately 70 ohms, is large. A perfect three-phase interface with the present design would give a cell resistance of 0.11 ohm. Such a 700-fold improvement in cell performance may not be realized due to the specific nature of a gas diffusion electrode. However, this experimental fact points up the area in which further work should be pursued.

Discussion

Recently, Euler (13) has discussed the present iodine thermocell and has considered it as one of several promising unconventional thermal converters. In comparing it with other converters, the advantages of the thermocell are its basically simple construction and its reasonably large power output. These advantages are due to the combination of the solid electrolyte with iodine gas as the electrokinetically active species. As with other thermal converters the disadvantage of the thermocell is its inherently low efficiency of converting thermal into electrical energy. In the following discussion, before dealing with the thermal efficiency of the cell, the experimentally obtained thermoelectric power of the iodine cell is compared with that calculated from thermodynamic considerations. The efficiency of the thermocell and its applications are then considered (including the heat input into the thermocell in relation to solar energy conversion).

Evaluation of the thermoelectric power of the iodine cell.[1]—The thermodynamic evaluation of the thermoelectric potential is complicated by the irreversibility of the nonisothermal system. In terms of entropy changes homogeneous transport processes and heterogeneous effects at the phase boundaries (electrodes) must be considered. From a modern viewpoint of ionic conductance, the homogeneous potential difference, which is due to the temperature gradient, is given in terms of heats of transport for interstitial ions (14). The heterogeneous effects include contact potential differences at the electrodes as well as the heterogeneous cell reactions. Fortunately, in the cell containing α-AgI as the electrolyte, the cell reaction overshadows all the other contributions to the over-all entropy of the process so that for a first approximation the Gibbs-Helmholtz equation may be applied. Presumably this is due to small magnitude of the transport entropies in the already disordered cationic lattice and due to the small magnitude of the contact potentials.

[1] An excellent comprehensive review of thermogalvanic cells, particularly of their theoretical aspects, has been published recently (6). The author states that the figure of merit for solid electrolytes is less than 0.5×10^{-3} deg $^{-1}$. However, for AgI the figure of merit is about 1×10^{-3}.

Table III. Variation of thermoelectric power of iodine cell with temperature

Temperature °C	°K	C_p	$S_T - S_{298°}$ cal/deg mole	½S I_2	dE/dT, mv/deg
550	823	9.06	9.15	35.5	+1.54*
500	773	9.05	8.60	34.7	1.50
400	673	9.03	7.32	34.6	1.49
300	573	9.01	5.85	33.8	1.46
200	473	9.00	4.14	33.0	1.43
150	423	8.99	3.15	32.5	1.41

* By convention a plus sign of the thermoelectric power corresponds to a positive current, at the cold interface, flowing in a direction from the electrode to the electrolyte.

Table IV. Comparison of experimental and calculated thermoelectric power

Experiment No.	Mean temperature, °K	Thermoelectric power Experimental	Calculated
4	523	1.36	1.45
2	535	1.33	1.45
1	574	1.19	1.46
3	631	1.24	1.48

Following Holtan (4) for the cell reaction

$$I^- = 1/2I_2 + e^-$$

we can calculate the thermopotential

$$\Delta E/\Delta T = -\Delta S/nF = -(1/2)\, S_{I_2}$$

For small temperature gradients this has been shown to give good agreement for the cells $Cl_2/PbCl_2/Cl_2$, $Cl_2/AgCl/Cl_2$, and $Br_2/AgBr/Br_2$ (5). For the iodine cell $I_2/AgI/I_2$ the range of applicability of the equation should be even larger because of the greater ease of transport in the solid electrolyte.

The entropy of iodine gas at 25°C is given by Eastman, (15) $S_{I_2\,(298°K)} = 61.8$ e.u., and the heat capacity is given by Kelley (16)

$$C_p = 8.94 + 0.14 \times 10^{-3}T - 0.17 \times 10^{-5}\, T^{-2}$$

from which we obtain the thermoelectric power for the iodine cell as shown in Table III.

In Table IV the experimental and calculated values of the thermoelectric power are compared at the mean temperatures at which the cell was operated. Although there is considerable experimental error in determining the thermoelectric power it is seen that the deviation of the experimental from the theoretical value becomes larger at higher temperatures. This may reflect the extent to which the above simplifying assumption in the calculation of $\Delta E/\Delta T$ were valid.

Efficiency of iodine thermocell.—Analogous to electronic thermoelectric converters the efficiency of electrolytic thermocells depends on the thermoelectric power of the cell, α, in volts/degree (above denoted by $\Delta E/\Delta T$), the electrical resistivity, ρ, in ohm-cm, and the thermal conductivity, k, in watts/centimeter-degree. These quantities are accurately known for the iodine cell except for the thermal conductivity of α-AgI, which is estimated to be k = 0.004 w/cm deg. At 500° and 350°C, ρ = 0.38 and 0.47 ohm-cm, respectively. With α = 1.3 mv/deg a figure of merit, $Z = \alpha^2/\rho k$ of 1.1 x 10^{-3} at 500° and 0.9 x 10^{-3} at 350° is obtained.[2] This compares favorably with the best semiconducting elements. A change of the cell geometry would affect absolute values of power output and heat losses, but would not change the efficiency. This is illustrated by a relation due to Telkes (17)

$$\text{Efficiency} = \frac{1}{\dfrac{2T_h}{T_h - T_c} + \dfrac{4k\rho}{10^{-6}\,\alpha^2\,(T_h - T_c)}} \times 100\,(\%)$$

where k, ρ, and α have the same meaning as before, but α is expressed in millivolt/degree, and T_h and T_c are the temperatures of the hot and cold side of the cell, respectively, in degrees K. The efficiency defined by this equation is the percentage of the maximum power output relative to the heat input at the hot electrode or junction. The first term in the denominator is a Carnot heat term; the second term resembles the above figure of merit. For the iodine cell, at a mean temperature of 350°C, and a temperature gradient of 300° this efficiency is 5.1%.

Applications of thermocells.—The efficiency of 5.1 represents the theoretical limit of the heat which can be converted into electrical energy by the iodine cell at a reasonable mean temperature and temperature gradient. It assumes that heat is conducted only from the hot to the cold electrode through the solid electrolyte without any heat losses except those due to the cell reaction. In practice the operating temperatures of the cells containing the AgI electrolyte are sufficiently low so that radiation effects can be neglected. Losses by conduction in the mechanical supports of the electrodes, and by convection of the iodine gas, must be minimized. At best an actual efficiency of a few per cent will be achieved. Thus, the application of thermocells is limited to the conversion of waste heat, and possibly to solar energy conversion.

In connection with solar energy conversion, the solar intensity must be increased by a factor of 10 in order to increase the heat input into the thermocell. For maximum cell output this can be shown to be necessary by matching the value of solar intensity with the geometrical requirements and thermal properties of the AgI electrolyte. It follows that for conversion of solar energy, in addition to the solution of design problems of the thermocell, provision must be made for a focusing device. Furthermore, for continuous operation of the iodine cell, means of reversing the temperature gradient must also be found.

Acknowledgments

The design of the iodine cell is largely due to W. R. Grams and W. L. Mowrey. Their assistance is greatly appreciated. The author is also indebted to R. E. Hoffman and T. O. Rouse for critical comments on the manuscript.

Manuscript received Aug. 27, 1963; revised manuscript received Feb. 15, 1964.

[2] An experimental determination of the thermal conductivity of α-AgI is now being made. The estimates of the figure of merit may have to be changed accordingly.

Any discussion of this paper will appear in a Discussion Section to be published in the June 1965 JOURNAL.

REFERENCES

1. H. Reinhold, *Z. anorg. u. allgem. Chem.*, **171**, 181 (1928).
2. H. Reinhold and A. Blachny, *Z. Elektrochem.*, **39**, 290 (1933).
3. C. Wagner, *Ann. Phys.*, **3** [5], 629 (1929).
4. H. Holtan, *J. Chem. Phys.*, **19**, 519 (1951); **20**, 539 (1952).
5. H. Holtan, *Koningl. Nederland Akad. Wetenschap. Proc.*, **B56**, 498 (1953).
6. J. N. Agar, "Advances in Electrochemistry and Electrochemical Engineering," P. Delahay, Editor, Vol. 3, II, Interscience Publishers, New York (1963).
7. J. L. Weininger, *This Journal*, **105**, 439 (1958).
8. J. L. Weininger, *ibid.*, **106**, 475 (1959).
9. J. L. Weininger, (to General Electric Company) U. S. Pat. 2,890,259, June 1959.
10. K. Wagener, *Z. physik. Chem.* (*n.F.*) **21**, 74 (1959).
11. K. H. Lieser, *ibid.*, **9**, 302 (1956).
12. C. Tubandt and W. Lorenz, *Z. physik. Chem.*, **87**, 513 (1914).
13. J. Euler, *Chemie-Ing.-Techn.*, **34**, 567 (1962).
14. R. E. Howard and A. B. Lidiard, *Phil. Mag.*, (8) **2**, 1462 (1957).
15. E. D. Eastman, *J. Amer. Chem. Soc.*, **45**, 81 (1923).
16. K. K. Kelley, U. S. Bur. Mines Bull. 584 (1960).
17. M. Telkes, *J. Appl. Phys.*, **25**, 765 (1954).

The Effect of Abrasion on the Specific Surface Area of Metals and Glass

R. J. Adams, H. L. Weisbecker, and W. J. McDonald

Minnesota Mining & Manufacturing Company, St. Paul, Minnesota

ABSTRACT

The surface areas of polished and abraded surfaces have been investigated using adsorption from solution of carbon-14 tagged acetic acid, stearic acid, and N-ethyl-N-perfluoroöctanesulfonylglycine. Adsorption rates, isotherms, heats of adsorption, and desorption characteristics are given for the unique acetic acid system. The effects of abrasion conditions on the surface area of steel have been investigated in detail. Specific surface areas ranging from two up to ten were obtained for various abrasive speeds, loads, and mineral types, and comparable surface areas were obtained for abraded surfaces of glass. Measured areas decreased with increased adsorbate chain length and with increased abrasion temperature. Accordingly, a possible mechanism for abrasion of steel is suggested which involves formation of microcracks. At the higher localized temperatures, more of these surface fissures may become sealed due to surface flow or reaction with oxygen.

Detailed studies of the processes of abrasion and polishing of metals are important for several reasons. Aside from surface finish and lubrication considerations, the new surfaces generated may have unique chemical properties and may influence bulk tensile and fatigue characteristics. Information has been contributed by many investigators [a partial listing is given (1-6)]; however, many questions remain unanswered. Samuels (7) has outlined the most pertinent of these.

Prominent among these problems is the question of the detailed microstructure of the so-called "deformed layer" formed by the abrasive action (1) and the effect of various abrasion parameters on this structure. One purpose of this work was to investigate the nature of abraded metal surfaces with respect to their specific surface area[1] and study the effect of abrasion conditions on this area. It was hoped that this study would afford an insight into the mechanism of abrasion and structure of the deformed layer.

Work has appeared concerning the effect of surface area on the chemical reactivity of metal surfaces as regards the phenomena of oxidation, corrosion, and adhesion. Some of these studies have concerned abraded surfaces (8, 9). However, difficulty in measuring and interpreting measurements of surface area has been a factor in the common neglect of this quantity in studies concerning surface reactivity. Another purpose of this study was to provide detailed reference data concerning surfaces generated by abrasion.

Adsorption from solution of carbon-14 tagged organic acids was used to estimate the surface area. This method was chosen because of its experimental simplicity, excellent sensitivity, and because adsorption phenomena at liquid-abraded metal interfaces are of interest *per se*. Several investigators have evaluated the merits of solution adsorption of tagged acids and other adsorbates for the measurement of surface area (9-12). In general, results for powders and planar metal surfaces using solution adsorption techniques have shown good agreement

[1] "Specific surface area" for planar solids is defined as the ratio of the true surface area (as approximated by the adsorption measurement) to the gross geometric area (planar area of the sample). Some authors have referred to this quantity as the "roughness factor" to avoid confusion with the specific surface area of powders (reported in square meters per gram); however we regard this term as misleading. In this work, the symbol R_s has been adopted to represent the specific surface area.

with values found by gas adsorption and other independent methods (13-16).

Three adsorbates were used in this work; acetic acid, N-ethyl-N-perfluoroöctanesulfonylglycine[2] and stearic acid, each tagged with carbon-14 in the carboxyl group. This permits an evaluation of the effect of adsorbate chain length on the measured surface area, since the chain lengths are in the ratio 1:6:9. The adsorption of stearic acid on powders and planar metal surfaces has been well characterized (12, 14). Results for acetic acid adsorbed on planar metal surfaces are of interest since, to our knowledge, this system has not been previously investigated. Acetic acid might be expected to give a better fit to micro-irregularities than the long chain acids which are commonly used. The glycine derivative was also chosen to permit comparison of these results with those of Ryan *et al.* (11) and to evaluate the effect of molecular cross-sectional area. Cyclohexane was chosen as the solvent based on low oxygen solubility and the results of Smith *et al.* (10) who found uniform monolayer coverage using this solvent.

It should be pointed out that surface areas measured by adsorption from solution should be considered as relative values due to resolution and the assumptions involving adsorbate molecular area and surface coverage which are needed to calculate the surface area. For an excellent discussion of the problems involved in surface area measurements, the reader is referred to a book by Adamson (17).

This study of surface area includes a detailed description of the effect of such variables as speed, load, and abrasive particle size. These quantities have usually been neglected in earlier work.

Experimental

Materials.—Acetic acid and stearic acid tagged with carbon-14 in the carboxyl position were obtained from New England Nuclear Corporation. Carbon-14 tagged N-ethyl-N-perfluoroöctanesulfonylglycine was obtained from Ryan *et al.* (11) who have described its preparation in a previous paper. Eastman Kodak white-label grade stearic acid and fractionally distilled Merck reagent grade glacial acetic acid (b.p. 116.5° ± 0.2°C) were used to dilute the tagged acetic and stearic acids. The specific activity of the adsorbates was determined by counting infinitely thin samples in a windowless Q-gas counter coupled with a Nuclear Chicago Model 186 scaler.

Stock solutions of the acids were prepared using cyclohexane exclusively as the solvent. These solutions (0.2*N* acetic acid, 0.02*N* stearic acid, and saturated glycine derivative) were diluted to obtain the working solutions used in this study.

Matheson technical grade cyclohexane was distilled, run through a column of activated alumina and silica gel, and finally redistilled in a fractionating column. The product did not spread when placed on clean acidic, basic, and neutral water surfaces.

[2] This compound is the fluorocarbon acid, $C_8F_{17}SO_2N(C_2H_5)CH_2C^*OOH$. In all subsequent references, the compound is referred to as the "glycine derivative."

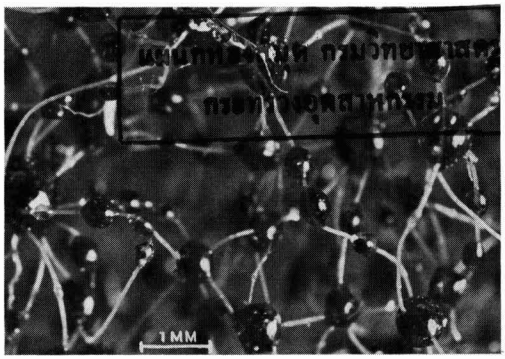

Fig. 1. Photomicrograph of "Scotch-Brite" brand abrasive material showing mineral particles embedded in binder globules which are dispersed throughout a nonwoven nylon web.

The solvent was stored in air-tight bottles containing sodium chunks until used in adsorption runs.

Disks of mechanically polished platinum and fire polished Corning No. 7740 Pyrex glass were used in this study. The steel samples used were cut from low carbon cold-rolled 1020 steel rod obtained from Bethlehem Steel Company. Circular samples, 1 in. in diameter by ⅛ in. thick, were carefully machined from these bars so as to obtain relatively smooth surfaces. The samples were degreased in benzene and rinsed with acetone prior to the abrasive treatments. Analysis by emission spectroscopy yielded the following minor constituent concentrations in the steel: Mn, 1.0%; Cr, 0.1%; Ni, 0.3%;Si, 0.2%; C, 0.25%; P, 0.01%; and S, 0.02%.

Two distinctly different abrasive materials were used; resinbond coated abrasive disks and a low density abrasive product consisting of a nonwoven web of nylon fibers bonded with a relatively hard rigid binder containing mineral particles. A photomicrograph of this material is shown in Fig. 1. This latter material is sold under the name, "Scotch-Brite" Low Density Abrasive product.[3] In the remainder of the paper this product will be referred to as "low density abrasive."

Procedure.—Three surface treatments were used; heat pretreatment at 500°C in a He atmosphere, abrasion in air, and abrasion under solvent. The first method, the heat pretreatment procedure, was the same as that used by Ryan *et al.* (11) of this laboratory. The second method involved holding the sample against the abrading tool in air for 2 min, followed by immersion in adsorbate solution. A delay of less than 1 sec occurred during the transfer from the abrading tool to the adsorbate solution. The third method consisted of abrading up to four samples under solvent for 2 min with constant load conditions followed by rapid transfer to the adsorbate solution so that the surfaces did not dry. Several experiments were carried out with tagged adsorbate in the abrading solution. No detectable differences in measured surface area were observed between these experiments and the ones involving transfer to adsorbate solution.

[3] Registered trade mark of the Minnesota Mining & Manufacturing Company, St. Paul, Minnesota. (See U.S. Patent 2,958,593 assigned to Minnesota Mining & Manufacturing Company, which describes in detail this type of low-density abrasive product.)

A typical experiment involved pretreatment of the sample by one of these techniques and immersion in the adsorbate solution for a predetermined time. The solutions were kept at 29.0° ± 0.1°C and were stirred from time to time during the adsorption. Adsorbate concentrations were checked by radiochemical assay and fresh solutions were prepared when these concentrations deviated more than 3% from the desired value. The samples were removed and quickly blotted dry with absorbent tissues leaving only adsorbed acid on the surface. The reliability of this procedure was checked for several samples by immersion in the adsorbate solution, blotting, and counting followed by reimmersion, blotting, and counting. The two count rates agreed to within 0.5% for all samples. Smith and McGill (10) also observed this excellent reproducibility and both their results and this work agree with Ryan *et al.* (11) who used olephobic surfaces.

The samples were mounted in brass holders which masked all but a 2.45 cm^2 circular area of the surface and were counted in a windowless Q-gas counter long enough to obtain less than 1% standard deviation in the count rate.

Specific surface areas were calculated from the isotherm plateau count rate using the adsorbate cross-sectional area, specific activity of adsorbate, counter efficiency, and the gross sample area (2.45 cm^2). The adsorbate molecular areas have been determined by others from film balance data on liquid substrates. The values used were 20.5$Å^2$ (18, 19) for acetic and stearic acids and 63$Å^2$ for the glycine derivative (11). The accuracy of these values was verified by area measurements on known smooth surfaces. All three adsorbates gave specific surface areas of near unity on polished glass surfaces when these molecular areas were used. The counter geometry factor was 50% as determined by using a standard carbon-14 source. The backscatter factors were checked with a standard source and agreed with values in the literature (20). Autoradiographs for all three adsorbates at various adsorption times were prepared by mounting samples containing activity on Eastman Kodak "No Screen" autoradiograph plates. These were stored in boxes containing drying agent to minimize loss of adsorbed acetic acid due to exchange with atmospheric moisture.

Results

Adsorption rates.—The rates of adsorption as a function of adsorbate concentration for acetic acid on steel abraded with CA-A-180 [4] are shown in Fig. 2. Similar rates were observed for 0.001*N* stearic acid and 3.0 x $10^{-6}N$ glycine derivative. Adsorption rates for Pyrex glass were slightly higher than those for steel and nearly twice this rate was observed for heat pretreated platinum.

[4] This notation designates the type of abrasive tool used. The first two letters indicate the type of tool; CA means coated abrasive disks, SB means "Scotch-Brite" Brand Low Density abrasive (described in experimental section). The second letter designates the type of abrasive mineral; A means Al_2O_3 and S means SiC. The last symbol refers to the abrasive mineral particle size; VF, Med., and C referring to Very Fine (avg. size 40μ), Medium (avg. size 134μ) and Coarse (avg. size 240μ) grades, respectively; this notation is used for "Scotch-Brite" Brand abrasives only. In the case of coated abrasives, the number refers to the particle size; grade 80 is 244μ, grade 180 is 94μ and grade 320 is 33μ.

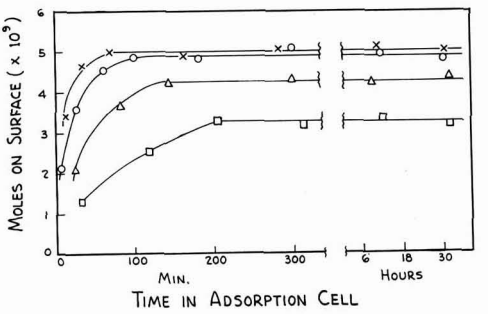

Fig. 2. Adsorption-time curves for acetic acid on abraded cold rolled steel. Samples abraded in air at 59 fps with CA-A-180 tool. Cyclohexane was the solvent, geometric sample area was 2.45 cm^2 and the temperature was 29.0°C. X, 0.004*N*; ○, 0.002*N*; △, 0.001*N*; □, 0.00025*N*.

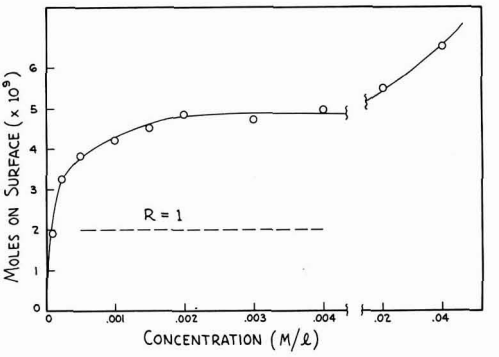

Fig. 3. Adsorption isotherm for acetic acid on abraded cold-rolled steel. Data in Fig. 2, together with additional data, were used to construct this isotherm; temperature 29.0°C.

Isotherm type.—Isotherms were constructed from the rate data by plotting the equilibrium value of adsorption as a function of adsorbate concentration. The isotherms obtained, one of which appears in Fig. 3, are of the variety classified as "Type I" by Brunauer (21) and can be interpreted as indicating formation of a monolayer with no further adsorption until higher adsorbate concentrations are reached. Isotherms of this type were obtained for all three adsorbates on cold rolled steel, platinum, and glass. The increase in adsorption at higher concentrations is probably due to multilayer formation and occurs at lower concentrations (relative to a saturated solution) for acetic acid than for stearic acid or the glycine derivative. This may reflect the fact that acetic acid forms a much thinner monolayer film compared with the long chain stearic acid and glycine derivative molecules, so that long range surface forces (*i.e.*, electrostatic dipole forces, etc.) induce formation of multilayers more easily than would be expected for the long chain adsorbates. The concentration ranges in which plateau adsorption occurred for stearic acid and the glycine derivative were 10^{-4}-10^{-2}M and 2-4 x 10^{-6}M, respectively.

The isotherms were found to fit the Langmuir adsorption equation (22) rather nicely. A typical result appears in Fig. 4. In general, good agreement

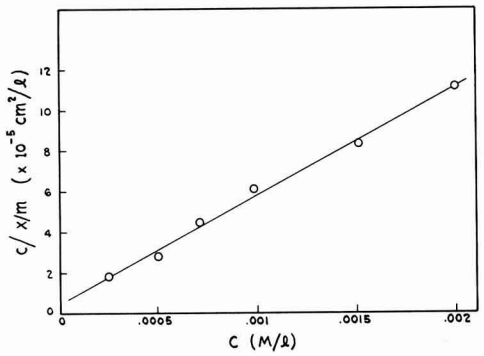

Fig. 4. A typical fit of the isotherm data of Fig. 3 to the Langmuir equation $C/(x/m) = 1/ab + C/a$, where C is adsorbate concentration, x/m is the number of moles of adsorbed acid per unit geometric surface area, a and b are constants. $R_{slope} = 2.3$; $R_{plateau\ of\ isotherm} = 2.4$.

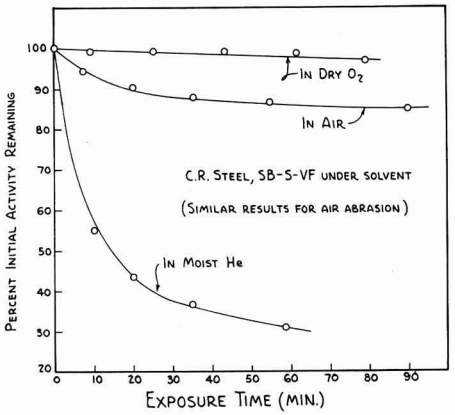

Fig. 5. Graph illustrating the "decay effect" for acetic acid adsorbed on cold-rolled steel. Abraded samples containing adsorbed radioactive acetic acid were counted at various intervals during exposure to three different atmospheres; dry O_2, ambient air, and moist He.

in true surface area calculated from the slope of the Langmuir plot and from the isotherm plateau value was obtained.

Heat of adsorption.—Heats of adsorption were calculated from the temperature dependence of the parameter "b" in the Langmuir equation (23). The results (Table I) reveal excellent agreement between acetic and stearic acids independent of the measured surface roughness. This strongly suggests similar adsorption mechanisms independent of the abrasive treatment for these two acids. The glycine derivative yielded higher values for the heat of adsorption (4 kcal/mole higher). This quite probably reflects the fact that there are two possible adsorption sites for this molecule, the carboxyl group and the tertiary nitrogen atom. All of the values are definitely in the vicinity of that expected for chemisorption.

Reversibility of adsorption.—Data were taken on desorption of acetic acid, stearic acid, and the glycine derivative from steel by pure cyclohexane. Adsorption reversibility was exhibited by all three adsorbates; 60% of the adsorbed acetic acid was removed at infinitely long desorption time, 52% for stearic acid, and 29% for the glycine derivative. Since the heats of adsorption indicated chemisorption for these adsorbates, apparently the chemisorption products have sufficient solubility in cyclohexane to explain the desorption. Bordeaux and Hackerman (12) found partially reversible and partially irreversible adsorption for stearic acid on iron. Further work including solution analysis for metal content is needed to clarify the adsorption mechanism. We were unsuccessful in attempts to obtain I. R. spectra of the adsorbed film by using the "Attenuated Total Reflectance" technique (24), due to the minute quantity of adsorbate on the samples.

Table I. Heats of adsorption for abraded steel

Adsorbate	SB-A-Med. in air 59 fps, kcal/mole	SB-S-VF under solvent 2.2 fps, kcal/mole
Acetic acid	14.0 (4.1)[a]	14.3 (7.5)
Glycine derivative	17.6 (2.5)	18.0 (4.4)
Stearic acid	14.1 (2.0)	

[a] Measured specific surface areas are given in parentheses. Duplicate runs indicated an error of ±1 kcal/mole.

Decay effect for acetic acid.—The amount of adsorbed acetic acid (presumably as a metal acetate) on a surface was found to decrease on exposure to the atmosphere (Fig. 5), no such loss being observed for stearic acid or the glycine derivative. This decay effect was not observed when the samples were kept in dry helium or in dry O_2 but storage in moist helium accentuated the effect. One likely explanation is that atmospheric moisture hydrolyzes the chemisorption product to yield free acetic acid. The rate of loss in air was slow enough to easily permit sample handling with negligible loss.

Surface area measurements.—Experimental results on surface areas are tabulated in terms of specific surface area (R_s) in Tables II-V. All single values represent the average of two or more runs and reproducibility of ±10% or better. Surface areas of polished platinum and glass surfaces, previously shown to be smooth (11), were measured with acetic acid. Specific surface areas close to unity (0.8-1.1) resulted, supporting the validity of the monolayer assumption and the value used for the acetic acid molecular area.

Table II presents the data on glass. Note that polished glass gives values of R_s near unity for all three adsorbates but that abraded samples give larger values, the increase being accentuated by the use of shorter chain length adsorbates.

Table III presents data on the effect of abrasion in air on the surface area of cold rolled steel. The effect of speed, mineral, abrasive type, and adsorbate are investigated. The following generalizations may be drawn from the data:

1. Decreases in abrasive speed always result in increases in specific surface area (R_s).

Table II. Specific surface areas for polished and abraded Pyrex glass

Pretreatment	Adsorbate: Acetic acid	Glycine der.	Stearic acid
Polished, heated in purified He	0.7-1.1[b]	0.8-1.1	0.9
Abraded[a] under cyclohexane	8.1	4.8	2.3
Abraded[a] in air	7.5	4.6	2.2

[a] Abraded samples treated with CA-A-180 2.2 fps for 10 min @ 2 psi load.
[b] The range reported represents the results of twelve samples. Single values are averages of two or more runs with a ±10% reproducibility.

Table III. Specific surface area (R_s) on abrasion in air

Tool	Adsorbate: Acetic acid	Glycine derivative	Stearic acid
Tool speed: 59 fps			
CA-A-80	2.2	2.0	1.7
CA-A-180	2.4	2.6	2.0
CA-A-320	2.3	2.0	1.5
SB-A-VF	3.8	3.1	1.9
SB-S-VF	5.9	4.5	2.0
Tool speed: 2.2 fps			
CA-A-180	3.5	2.9	2.2
CA-S-180	3.7	3.0	2.0
SB-A-VF	4.7	3.3	1.9
SB-S-VF	6.5	4.9	2.0

Cold rolled steel samples, 1 psi load. Values shown are averages of at least two runs with a ±10% reproducibility.

2. SiC mineral produces larger values of R_s than Al_2O_3.

3. Low density abrasives produce larger values of R_s than coated abrasives under identical conditions.

4. Increases in measured surface area are accentuated by the use of short chain length adsorbates.

Table IV considers the effect of abrasion in solvent. Generalizations 2-4, noted above, are seen to hold without exception, and another may be added:

5. Abrasion in solvent yields larger values of R_s than abrasion in air.

Table V considers a more detailed investigation of the effect of speed utilizing acetic acid. Generalizations 1-3, noted above, are seen to hold, again without exception.

Experiments on the effect of load showed the results to be insensitive to the effect of load over the range 0.25-4.0 psi. Grit size exerted negligible influence on R_s with coated abrasives, but coarser grits gave larger values with low density abrasives.

Discussion

Topographical model of abraded surfaces.—Profilometer contour traces and optical microscopic examination (resolution near wavelength of visible light) were carried out for all abrasion treatments studied. Specific surface areas estimated from these observations did not exceed 1.7, even for rather

Table IV. Specific surface area (R_s) on abrasion in solvent

Tool	Adsorbate: Acetic acid	Glycine derivative	Stearic acid
CA-A-80	4.7	3.4	2.2
CA-S-80	6.2	4.4	2.8
CA-A-180	5.2	3.2	1.8
CA-S-180	5.9	4.6	2.6
CA-A-320	5.2	3.3	1.9
CA-S-320	5.8	4.4	2.7
SB-A-VF	5.4	3.3	2.2
SB-S-VF	7.5	4.4	3.3

Speed: 2.2 fps, load: 1 psi, cold rolled steel samples. Observed error was ±10% or better for two or more runs.

Table V. Effect of speed on specific surface area (R_s)

Tool	Speed: 0.39 fps	0.88 fps	2.2 fps	59 fps
Abrasion in air				
CA-A-180	4.1	3.8	3.5	2.4
CA-S-180	4.3	3.9	3.7	2.7
SB-A-VF	6.0	5.3	4.7	3.8
Abrasion under cyclohexane				
CA-A-180	5.5	5.4	5.2	
CA-S-180	6.8	6.3	5.9	
SB-S-VF	10.1	9.4	7.5	
SB-A-VF	7.7	6.5	5.4	

Adsorbate, acetic acid; load, 1 psi; cold rolled steel samples. Observed error was ±10% or better for two or more runs.

coarse grained abrasives. Other investigators have also found low values for abraded and sandblasted metal surfaces (25, 26). In view of the data found in this study (R_s=2-10) and other work (9, 12) the surfaces must contain numerous micro-irregularities which are unresolved by optical microscopy. It is difficult to observe micro-irregularity relief on the surface of abraded metals by standard electron microscopy techniques, however work is presently underway toward that end.

Plumb (27) has pointed out that large surface areas can be achieved conceptually by superimposing small asperities on large ones ad-infinitum. The authors noticed, however, that the present data suggests an interesting alternate possibility, namely that a significant portion of the surface area of abraded steel is contributed by the presence of microcracks which may be generated during abrasion.

This conclusion is corroborated by the following observations. First, abraded glass, which is known to contain Griffith microcracks (28), yielded high roughness factors (~8 for acetic acid) and successively lower values as the adsorbate chain length increased (Table II). The chain length effect can obviously be rationalized in terms of steric hindrance and/or increased tendency for "bridging" small surface fissures with increasing chain length. Griffith cracks on glass have been shown, by indirect means, to be as deep as the deepest grinding pits, yet very narrow at the surface (less than 50Å) and could well yield true areas several times larger

than the geometric area. They are far too small for observation by optical microscopy and, as yet, have defied observation by electron microscopy. When steel was abraded under certain conditions, the measured surface areas and chain length effect were strikingly similar to abraded glass (Table III and IV).

Second, the effect of abrasion conditions on the surface area of steel (and the chain length effect) are nicely explained by the microcrack hypothesis.

These effects may be stated as follows: The specific surface area is increased by lowering the speed of abrasion, by abrading in cyclohexane rather than air, by using low density abrasives rather than coated abrasives or by using SiC rather than Al_2O_3.

Each of these conditions have the effect of lowering the abrasion temperature. Reduction in abrasive speed at constant load results in lower power consumption and reduced temperature. The presence of a solvent atmosphere will certainly result in reduced temperature. Stock removal and heat generated by coated abrasives is several times greater than for the unique, flexible low density abrasive. The latter product exhibits an abrasive action not unlike sandblasting since the flexible web construction allows freedom of motion of the abrasive grains, resulting in lower stock removal and a more shallow cut.

Retention of a microcrack type of surface topography would be especially sensitive to the surface temperature. These fissures would propagate under the influence of tensile stresses at the immediate side and rear areas of the abrasive grain as it traverses the surface. However, at higher abrasion temperatures, the cracks would be expected to reseal [localized abrasion temperatures may well equal the melting point of steel (29)] either by plastic flow or by augmented oxidation. Thus, there would be more retention of microcracks under conditions of low abrasion temperature, resulting in higher surface area and a more dramatic adsorbate chain length effect.

Abrasion in solvent has the effect of excluding air as well as lowering the temperature and both effects would tend to increase the surface area. An experiment designed to separate these effects is depicted in Fig. 6. Samples were prepared by abrasion in both air and solvent, and subsequently exposed to laboratory air prior to immersion in the adsorbate solution. A rapid decrease in the amount adsorbed was observed during the first 2 min of exposure to air, reaching a constant value which remained stable for at least 24 hr. However, this value is still significantly higher for samples abraded in solvent than for those abraded in air, indicating a permanent increase in surface area for abrasion in solvent. The initial drop is probably due to oxidation since the initial rate is very rapid; this conclusion is confirmed by solvent abrasion and exposure to helium.

The surprising but unmistakable difference between SiC and Al_2O_3 may also be explicable in terms of temperature. Silicon carbide is a much better thermal conductor than aluminum oxide and this

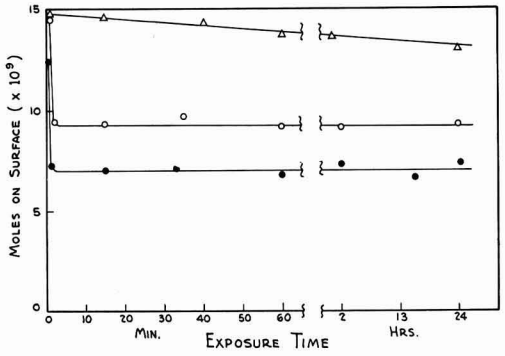

Fig. 6. Effect of exposure of abraded steel surfaces to various atmospheres. Samples abraded with SB-S-VF at 2.2 fps and 1 psi load were exposed to the media labeled on the curves. After various times they were placed in 0.004*N* tagged acetic acid solutions. When adsorption equilibrium had been attained, they were withdrawn, quickly dried, and counted. △, Solvent abraded—exposed in cyclohexane; ○, solvent abraded—exposed in air; ●, air abraded—exposed in air.

would result in higher interface temperatures with Al_2O_3. The rate of wear of SiC on ferrous metals has been reported to be higher than that obtained with Al_2O_3 (30). This may indicate that a stronger metal-abrasive interaction occurs for SiC than for Al_2O_3, thus producing more severe tears.

One might not expect formation of such fissures on the surface of materials as ductile as metals. However, the structure and exact physical nature of the "deformed layer" (1) immediately underlying the oxide film on abraded surfaces are not well known. Interestingly enough, Atkinson (2) recently observed tears caused by polishing steel surfaces. The over-all dimensions of these tears are not far from the estimated dimensions of the proposed microcracks.

In order to rationalize the data at varying adsorbate chain length and the specific surface areas obtained, these cracks would have to be of the order of 50-150Å wide and approximately one to several microns in length and/or depth depending on the number of cracks per unit apparent area. If the fissures were, say, 5μ deep and 5μ long, there would have to be about 10^7 cracks/cm^2 to obtain R_s values in the vicinity of 5. This estimation assumes that the walls of the cracks are smooth and that the surface area contributed by the cracks is superimposed on a surface of specific surface area equal to two. Ernsberger (28) observed approximately 10^5 microcracks/cm^2 on the surface of unabraded glazing quality plate glass.

Adsorption method.—It should be noted that the surface area measurement used in this work is predicated on the monolayer assumption. For this reason, the authors would like to close by re-examining the evidence which supports this assumption and contradicts other assumptions which might be advanced.

Alternate possibilities might include: (*a*) multimolecular layer formation; (*b*) retention of adsorbate solution in micro-irregularities on the surface; (*c*) amount of adsorption influenced more by

chemical reactivity of abraded surface (*e.g.*, continuous reaction between adsorbate and metal oxide) than by true surface area.

As mentioned previously, the observed isotherms fit the Langmuir equation and exhibit discrete plateaus with the typical rise at higher concentrations. This would seem to rule out multilayer formation, particularly in view of the measured specific surface areas of unity on surfaces expected to be smooth. The excellent reproducibility of the blotting procedure has been mentioned, and one can also consider how unlikely it would be that such consistent abrasion effects could be measured if retention of liquid on the surface was a factor, the chain length effect would be particularly inexplicable from such a point of view.

Table I shows that the heat of adsorption is similar for all three adsorbates independent of the measured surface area. This discourages arguments based on assumed difference in chemistry of the surface as described in (c) above.

It appears at present that the most consistent argument is that saturated monolayers are formed and that the equilibrium amount adsorbed at "plateau" concentrations is an approximation of the true surface area. Furthermore, the results indeed show that higher resolution is achieved with acetic acid than with commonly used long chain adsorbates.

Autoradiographs prepared for steel samples abraded in air (for which lower R_s values were found) showed uniform adsorbate coverage, independent of adsorption time, within the relatively gross limits of resolution of this method. Samples for which higher surface areas were obtained, revealed concentration of adsorbate along the abrasive scratch pattern. This is consistent with the microcrack postulation since these fissures would be concentrated near the gross abrasive scratches.

The tentative hypothesis of the production of microcracks in grinding metals is sufficient to explain our results to date. This investigation is being extended to attempt direct observation of the postulated microcracks by electron microscopy. Double layer capacity measurements are also planned in an attempt to obtain independent correlation with the present surface area data.

Acknowledgments

The authors are grateful to Dr. John P. Ryan, of the Nuclear Research Group, for helpful discussions and for the use of some of his equipment in this work. They are also indebted to the staff of the Coated Abrasives and Low Density Abrasives Laboratories for their support and many helpful discussions.

Manuscript received Oct. 3, 1963.

Any discussion of this paper will appear in a Discussion Section to be published in the June 1965 JOURNAL.

REFERENCES

1. L. E. Samuels, "The Nature of Mechanically Polished Surfaces," pp. 122-127, American Electroplaters Society, 1959 Technical Proceedings.
2. R. H. Atkinson, *Plating*, **49**, 485 (1962).
3. T. M. Buck and F. S. McKim, *This Journal*, **103**, 593 (1956).
4. J. G. Poor, H. Chessin, and C. L. Alderuccio, *Plating*, **47**, 811 (1960).
5. J. Goddard, H. J. Marker, and H. Wilman, *Proc. Phys. Soc.*, **80**, 771 (1962).
6. R. P. Argawala and H. Wilman, *J. Iron Steel Inst.*, **179**, 124 (1955).
7. L. E. Samuels, *Plating*, **48**, 46 (1961).
8. P. M. Aziz and H. P. Godard, *This Journal*, **104**, 738 (1957).
9. R. C. Plumb and J. E. Lewis, *Int. J. Appl. Rad. and Isot.*, **1**, 33 (1956).
10. H. A. Smith and R. M. McGill, *J. Phys. Chem.*, **61**, 1025 (1957).
11. J. P. Ryan, R. J. Kunz, and J. W. Shepard, *ibid.*, **64**, 525 (1960).
12. J. J. Bordeaux and N. Hackerman, *ibid.*, **61**, 1323 (1957).
13. T. L. O'Connor and H. H. Uhlig, *ibid.*, **61**, 402 (1956).
14. M. C. Kordecki and M. B. Gandy, *Int. J. Appl. Rad. and Isot.*, **12**, 27 (1961).
15. S. H. Maron, E. G. Bobalek, and S. M. Fok, *J. Colloid Sci.*, **11**, 21 (1956).
16. J. W. Swaine, Jr., and R. C. Plumb, *J. Appl. Phys.*, **33**, 2378 (1962).
17. A. W. Adamson, "Physical Chemistry of Surfaces," pp. 425-454, 573-597, Interscience Publishers, Inc., New York (1960).
18. N. K. Adam, "The Physics and Chemistry of Surfaces," p. 24, Oxford University Press, Oxford (1938).
19. M. J. Vold, *J. Colloid Sci.*, **7**, 196 (1952).
20. H. Sobotka and S. Rosenberg, "Monomolecular Layers," pp. 175, 192, American Association for Advancement of Science (1951).
21. S. Brunauer, "The Adsorption of Gases and Vapors," vol. I, p. 166, Princeton University Press, Princeton, N. J. (1945).
22. I. Langmuir, *J. Am. Chem. Soc.*, **40**, 1361 (1918).
23. A. W. Adamson, "Physical Chemistry of Surfaces," p. 574, Interscience Publishers, Inc., New York (1960).
24. J. Fahrenfort, *Spectrochim. Acta*, **17**, 698 (1961).
25. A. G. Eubanks, W. A. Pennington, and D. G. Moore, *This Journal*, **109**, 382 (1962).
26. "The Finishing of Aluminum," G. H. Kissin, Editor, p. 195, Reinhold Publishing Corp., New York (1963).
27. R. C. Plumb, *This Journal*, **105**, 367 (1958).
28. F. M. Ernsberger "Advances in Glass Technology," pp. 511-523, Plenium Press, New York (1962).
29. E. P. Bowden and D. Tabor, "The Friction and Lubrication of Solids," p. 38, Clarendon Press, Oxford (1950).
30. E. J. Duwell and W. J. McDonald, *Wear*, **4**, 372 (1961).

The Corrosion of Uranium, Zirconium, and Some Alloys in Alkaline Solutions

J. S. Llewelyn Leach and A. Y. Nehru

Department of Metallurgy, Imperial College of Science and Technology, London, England

ABSTRACT

The corrosion of uranium, zirconium, and an uranium-zirconium alloy was studied as a function of potential in some alkaline solutions. The behavior of zirconium was found to be in qualitative agreement with results previously obtained in more acid solutions. The interpretation of the data for uranium and the alloy involved assumptions concerning changes in the nature of the protective oxide layer associated with changes in the formation potential. Such differences are not shown on the *p*H-potential diagram generally accepted for the uranium-water system and a new diagram has been derived. Electron diffraction measurements were employed in an attempt to verify the present interpretation.

The high-temperature aqueous corrosion of uranium and zirconium has been the object of several detailed studies (1-5). The early work ascribed increases in the corrosion rate as well as the physical damage to the accumulation in the metal of the corrosion-product hydrogen formed during the reaction which, in the absence of oxygen, has the general form

$$xM + yH_2O = M_xO_y + yH_2$$

Although it appears to be clearly established that hydrogen is active in the corrosion attack, there is some disagreement as to the precise nature of its role.

It was shown recently (1) that the corrosion rate of uranium, uranium-5 weight per cent (w/o) zirconium, and zirconium, cathodically polarized in a slightly acidic solution at temperatures below 100°C, was simply related to the hydrogen activity at the oxide-electrolyte interface over a wide range of potential. The corrosion rate was found to increase with increasing cathodic polarization indicating that the effect of the potential on the kinetics was greater than its effect in decreasing the thermodynamic driving force. This behavior was interpreted as resulting from the dissolution of hydrogen in the oxide leading to changes, within the film, of an electrical nature (causing increased ionic diffusion rates) rather than mechanical failure.

The present paper describes the results of corrosion rate measurements on uranium, uranium-10 w/o zirconium, and zirconium in alkaline solutions, with particular reference to the effect of cathodic polarization. It is shown that, although the behavior at high values of *p*H may be explained in the same general terms as the corrosion in acidic solution, the relationships with potential (*i.e.*, hydrogen activity) are much more complex for uranium and the alloy.

Experimental

The experimental method which has been described previously (1, 6, 7) permits measurement without removal of the specimen from the test environment. The technique involves the continuous measurement of the intensity of light reflected from the surface of the corroding specimen. Monochromatic light can be used giving interference effects superimposed on an absorption curve while white light gives absorption effects only.

To derive absolute values of oxide thickness requires a knowledge of either the refractive index or the absorption coefficient of the oxide depending on the method used. Over the range of thickness where both methods can be applied, the ratio of the refractive index to the absorption coefficient appears to be constant (1). As these two parameters depend on different physical properties it seems likely that they are independently constant. However, the exact magnitude of either is open to doubt, and in consequence the amount of oxidation is given in terms of relative oxide thickness rather than in absolute units.

In the present instance the white light method has been used which permits measurements of thicker oxide films due to the greater intensity available.

The test solutions were prepared by dissolving ANALAR reagents in distilled water and were constituted as follows:

*p*H 9.7 solution	0.2*N* Na_2CO_3 + 0.2*N*	$NaHCO_3$
*p*H 11.6 solution	0.1*N* Na_2CO_3	
*p*H 13 solution	0.1*N* NaOH	or 0.1*N* KOH

Oxygen-free nitrogen was continuously bubbled through the solutions before and during use to remove dissolved oxygen.

The marked corrosion resistance of zirconium necessitated making the measurements at higher temperatures (90°C). Additional features were incorporated in the test cell to provide a temperature control accurate to within ± 1°C.

Of the materials examined, the high purity zirconium was supplied by A.E.R.E.[1] (impurity analysis: O, 125 ppm; C, 50 ppm; N, 170 ppm; H, 24 ppm). No heat treatment was given before examin-

[1] Atomic Energy Research Establishment, Harwell, England.

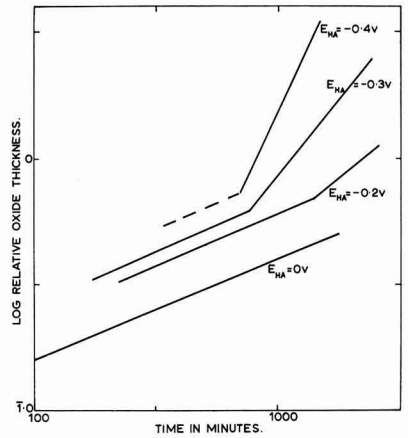

Fig. 1. Corrosion of zirconium, O_2-reduced 0.1*N* KOH solution, 90°C.

ation. The uranium was supplied by A.E.R.E. and certified as 99.95% pure (impurity analysis: O, 40 ppm; N, 10 ppm; C, 30 ppm; Si, 8 ppm; Fe, variable 10-90 ppm; Al, 3 ppm). It was not subjected to a preliminary heat treatment. The alloy, prepared from 99.95% pure uranium and low hafnium 99.9% pure zirconium (Van Arkel), was supplied in the arc-cast condition. Before testing, it was homogenized (by annealing in vacuo) at 1000°C for seven days and then water-quenched. The methods used for mounting the specimen and preparation of the surface have been described previously (1, 6).

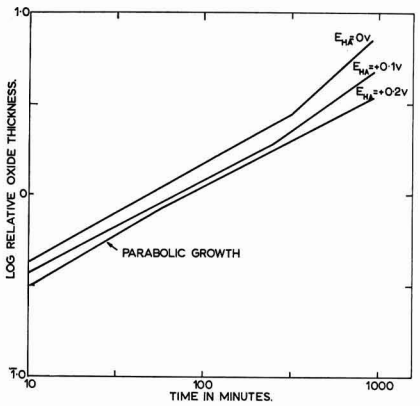

Fig. 2a. Corrosion of uranium, O_2-reduced 0.2*N* Na_2CO_3 + 0.2*N* $NaHCO_3$ solution, room temperature.

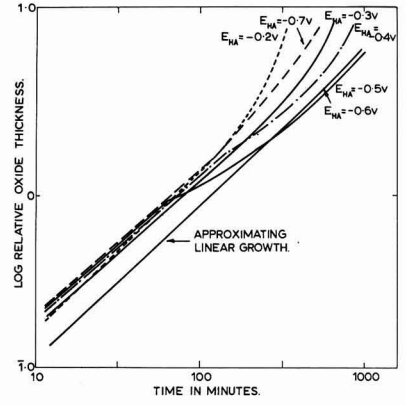

Fig. 2b. Corrosion of uranium, O_2-reduced 0.2*N* Na_2CO_3 + 0.2*N* $NaHCO_3$ solution, room temperature.

Results

Figure 1 illustrates the corrosion of zirconium in *p*H 9.7 solution at 90°C. The method of plotting enables calculation of the kinetics of film growth from the slope of the curves. The chief points of interest are given below:

(I). The corrosion rate increases with increasing cathodic polarization.

(II). A transition from less rapid to more rapid kinetics is easily distinguishable for two values of potential (E_{HA} = −0.2v, −0.3v),[2] and appears to take place at an approximately constant film thickness.

(III). The growth law governing the early stages of corrosion may be expressed by $y^{2.5} = kt$ where, y is the oxide thickness, k is a constant, and t is time.

Figures 2a and 2b show the corrosion behavior of pure uranium in *p*H 9.7 solution. The following observations are of interest:

(I). At and above E_{HA} = 0v (Fig. 2a), the corrosion rate is either parabolic or parabolic changing to an approximately linear law. The corrosion rate increases with increasing cathodic polarization.

(II). Between −0.2v and −0.5v E_{HA} (Fig. 2b), the corrosion rate initially approximates to a linear law and changes in time to a complex law (accelerating rate). In this potential range, the rate decreases with increasing cathodic polarization.

(III). Below −0.5v E_{HA} (Fig. 2b), there is a tendency for the initial corrosion to approximate more closely to the linear law. The rate increases with increasing cathodic polarization.

The corrosion of uranium-10 w/o zirconium in *p*H 9.7 solution is illustrated in Fig. 3a and 3b. It can be seen that the results indicate a continuation of the trends established for the pure metal with, however, two significant differences:

(I). The over-all corrosion rate of the alloy is lower.

(II). The changes in the corrosion process of the alloy occur at more negative potentials, *i.e.*, first, between −0.2v and −0.3v E_{HA} (instead of between 0v and −0.2v E_{HA}) and, second (apparently) below −0.7v E_{HA} (instead of between −0.5v and −0.6v E_{HA}).

The corrosion behavior of pure uranium in *p*H 11.6 solution bears a marked resemblance to the behavior in *p*H 9.7 solution. Figures 4a and 4b show that the changes in corrosion process occur at approximately the same hydrogen activity potentials (E_{HA}), although the over-all corrosion rate is higher in the more alkaline solution.

The corrosion of uranium and the alloy in *p*H 13 solution has not been investigated in detail. How-

[2] $E_{HA} = E_H + 0.0591$ pH where E_H is the potential with respect to the normal hydrogen scale.

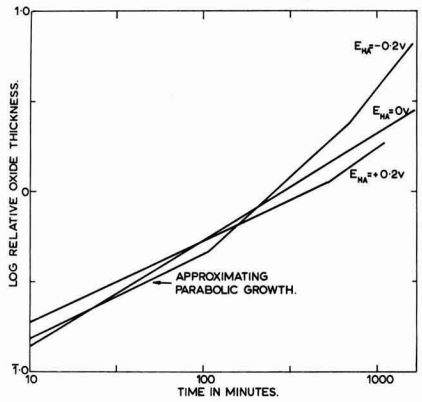

Fig. 3a. Corrosion of uranium-10 w/o zirconium, O_2-reduced 0.2*N* Na_2CO_3 + 0.2*N* $NaHCO_3$ solution, room temperature.

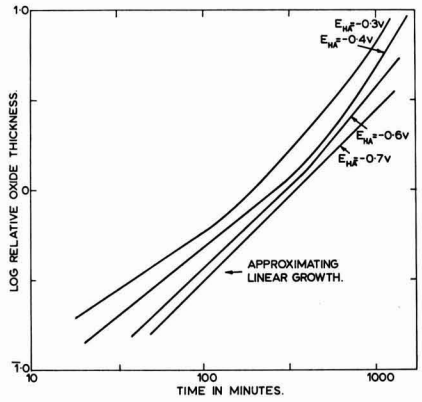

Fig. 3b. Corrosion of uranium-10 w/o zirconium, O_2-reduced 0.2*N* Na_2CO_3 + 0.2*N* $NaHCO_3$ solution, room temperature.

ever, the measurements which were made (Fig. 5) show the same type of complex behavior observed in other alkaline solutions. Again, it is clear that the over-all corrosion rate at any given potential is increased by greater alkalinity and decreased by alloying.

Discussion

A comparison of the present results with our earlier observations in pH 5.4 solutions shows that while the characteristics of the corrosion of zirconium remain virtually unaffected by the change in environment those of uranium and its alloys are significantly altered. The results obtained for the two metal systems will be discussed separately for the sake of simplicity.

Zirconium.—The low corrosion rate of zirconium in the temperature range to which this experimental technique is restricted makes it difficult to cause a change from protective to nonprotective kinetics within a reasonable length of time. Nevertheless, by cathodically polarizing the specimens it has been possible to show at 90°C (at least, in two instances) a kinetic sequence which is normally associated with very much higher temperatures. The increase in corrosion rates which accompanies cathodic polarization may be related to an increase in electronic conductivity of the corrosion-product oxide after the model previously proposed (1) to account for similar results obtained with uranium. If, as is thought to be the case (8), the oxide formed on zirconium is an anion-deficient n-type semiconductor, then the addition of a positively charged ion such as H^+ is likely to cause the type of effect we have observed.

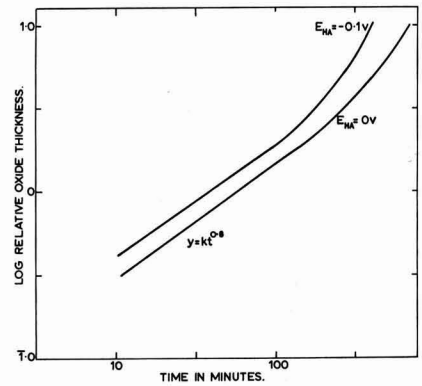

Fig. 4a. Corrosion of uranium, O_2-reduced 0.1*N* Na_2CO_3 solution, room temperature.

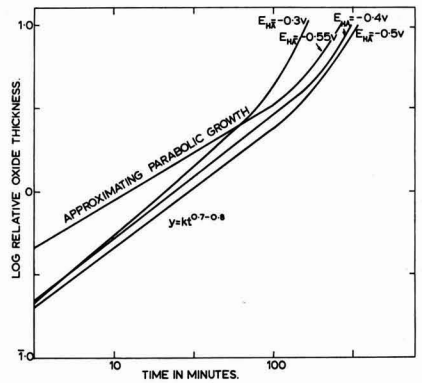

Fig. 4b. Corrosion of uranium, O_2-reduced 0.1*N* Na_2CO_3 solution, room temperature.

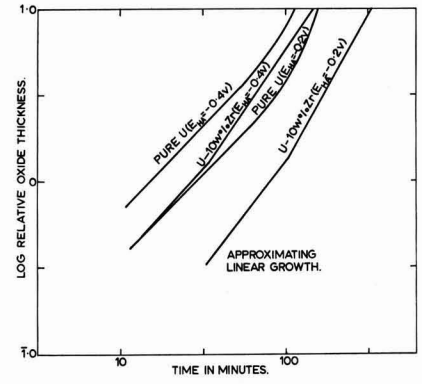

Fig. 5. Corrosion of uranium and uranium-10 w/o zirconium, O_2-reduced 0.1*N* NaOH solution, room temperature.

It should be pointed out, however, that in the initial stages of corrosion (up to 200 or 300 min), when the oxide film is still very thin, the sensitivity of the equipment was not always sufficient to allow accurate measurement, and in some cases the experimental scatter was considerable. In the series of measurements illustrated in Fig. 1, this scatter was particularly marked for the test carried out at $E_{HA} = -0.4$v, and it was difficult to obtain a reasonable straight-line fit for the period of protective growth. It is interesting, however, that in the cases where two well-defined growth laws can be seen, the transition from one to the other appears to take place at approximately the same film thickness. This observation may be compared with similar observations made by us on uranium in acidic solution from which it was concluded that cathodically induced hydrogen appears to change the corrosion rate without altering the protective thickness of the oxide (1, 9).

The kinetics of oxide growth bear a marked resemblance both in alkaline and acid solutions, although tests in the latter were not carried out for long enough to obtain a transition. The power of 2.5 for the protective growth law in *p*H 13 solution agrees reasonably with the exponent 2.66 found by us in acid solution, and both values compare favorably with the observations of other workers at higher temperatures (8, 10). The somewhat higher over-all rates in alkaline solution are difficult to explain from the present results. Coriou and coauthors (11) have pointed out from work on Zircaloy that such increases may be only in part due to the effect of *p*H, and that the oxides formed in alkaline solutions require further study.

Uranium and uranium-10 w/o zirconium.—The difference between the corrosion behavior of uranium in alkaline solutions and in *p*H 5.4 solution has been clearly established. Briefly, the present results show (i) that oxide growth in alkaline solutions is, in many cases, governed by complex laws, and (ii) that the direct relationship between corrosion rate and applied potential found in acidic environments is no longer apparent. In addition, visual observations of specimens tested in alkaline solutions have shown that the corrosion films are generally duller and less compact than their counterparts in acidic (*p*H 5.4) solution.

While it seems likely that such differences in behavior and appearance should correspond to a difference, either in structure or in composition, between the corrosion films formed in the two environments, the existence of two distinct species is not indicated by the data presented by Pourbaix and co-workers (2). Figure 6 shows the *p*H-potential diagram derived by these investigators, from thermodynamic data, for the uranium-water system. This figure has been recalculated from the original on the basis of hydrogen activity potentials to conform to the method adopted in this paper for the plotting of results. Here, the sole species considered stable in the *p*H-potential range of interest (*p*H 5.4 to *p*H 13 and +0.2v to −0.7v E_{HA}) is given as UO_2. Nevertheless, since the diagram has been

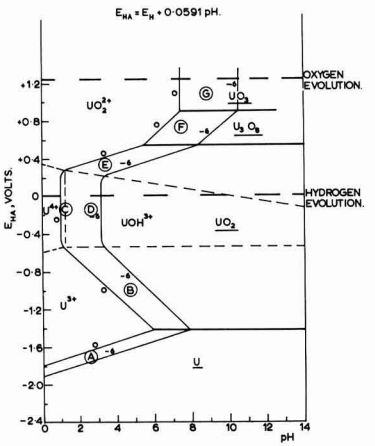

Fig. 6. *p*H-potential diagram for U-H_2O system (after Pourbaix)

derived for equilibrium conditions, it is possible that during processes of high irreversibility such as are encountered during the corrosion of uranium, the configuration may be significantly altered. As one example of this type of effect, it is worth noting that, although FeO is thermodynamically unstable with respect to Fe and Fe_3O_4, below 570°C, a layer of FeO has been found during the oxidation of iron at temperatures as low as 400°C (12). Of more specific interest to the present work is an observation made in the early stages of this investigation that rapid film growth occurs on uranium in very acid solutions (0.1*N* HCl, *p*H 1) where according to the thermodynamic data no solid phase should be stable.

There is, moreover, some evidence which suggests that the data from which the Pourbaix diagram for uranium-water is derived are incomplete and might not permit a comprehensive representation of the system. First, both Waber (13) and Katz and Rabinowitch (14) have observed and commented on the possible formation of the hydroxide $U(OH)_4$ instead of UO_2 in aqueous corrosion films on uranium. Pourbaix, himself, is not emphatic in denying the occurrence of this phase but prefers the alternative choice for his diagram. Second, some values for the free energy of formation used in calculating the Pourbaix diagram are 3-4% lower than values reported by Latimer (15). This is a noticeable disagreement in view of the fact that a relatively small difference in free energy can have considerable effect on the potential at which a given species is stable. Finally, Willardson, Moody, and Goering (16) have shown that the oxidation of UO_2 to higher oxides is accompanied by changes in type of semiconductivity caused by deviations from stoichiometry, and have identified two stable oxide phases U_4O_9 and U_3O_7 of O/U ratio intermediate to UO_2 and U_3O_8. Capacity measurements on uranium electrodes in aqueous solutions have also been interpreted (17, 18) as showing the formation of higher oxides during corrosion, although it was difficult from the results to ascertain changes in semiconductivity. From the present point of view, the omission

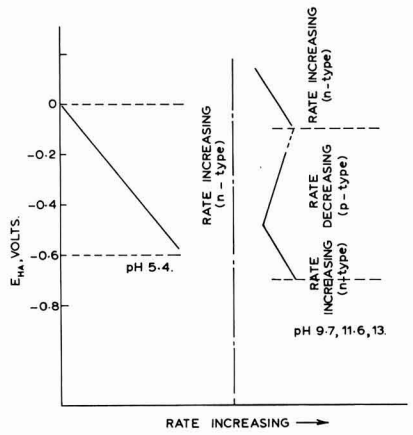

Fig. 7. Over-all corrosion rate of uranium as a function of pH and potential.

of the intermediate oxides from the diagram is serious since measurements in this investigation have been conducted within the potential range in which these species are most likely to be stable.

In view of these shortcomings and others which may arise when the conventional pH-potential diagram is applied to nonequilibrium conditions, it is not unreasonable to reconstruct relevant portions to fit the present results. It should be stressed, however, that the resulting diagram may be more in the nature of a metastable equilibrium diagram rather than a substitute for that proposed by Pourbaix (2) and his colleagues.

Figure 7 illustrates the differences between the corrosion trends of uranium in pH 5.4 solution and in alkaline solutions. A hypothetical demarcation has been shown at pH 7. The rate in pH 5.4 solution increases continuously with decreasing potential, whereas two transitions are found in alkaline solutions.

As pointed out earlier in the discussion, an increase in corrosion rate with increasing cathodic polarization suggests that the oxide forming is an n-type semiconductor. Conversely, a decrease in rate under similar circumstances would indicate the formation of a p-type oxide. Hence, the corrosion behavior of uranium in alkaline solutions may be ascribed to changes in the semiconductivity of the corrosion-product from n- to p- to n-type as the potential is decreased. It should be stressed, however, that the absence of parabolic growth at certain potentials in high pH solutions does not necessarily imply the absence of a diffusion process. Instead, as the over-all corrosion rate in these solutions is considerably higher than in pH 5.4 solution, it is believed that the period during which the diffusion-controlling film is growing is too short to allow detection by the measuring instrument. The over-all corrosion rate is defined as the amount of corrosion occurring in a given length of time and the use of this parameter becomes necessary in instances where it is difficult to define the corrosion rate in terms of the constants of the growth laws.

Changes in conductivity mechanism of the type described above could arise from the formation of nonstoichiometric phases during corrosion in alkaline solutions. Within the domain of stabilty of a given species, the oxygen-rich region (positive, in terms of potential) will tend to be p-type while oxygen deficiency will result in n-type semiconductivity (*e.g.*, UO_{2+x} ~ p-type, U_4O_{9-x} ~ n-type, U_3O_{8+x} ~ p-type). Note, that since the exact potentials at which the changes in mechanism occur are not known from the results, a divison has been made in Fig. 7 at the arbitrarily chosen values −0.1v E_{HA} and −0.7v E_{HA}. These two potentials, hence, bound the domain of stability of one species while immediately below lies the oxygen-rich region of a stable compound of lesser O/U ratio and immediately above is the oxygen-deficient region of the next phase. The fact that the transitions in the corrosion process of uranium-10 w/o zirconium occur at more negative potentials can be ascribed to the difference between the free energies of formation of pure oxides and those of the mixed oxides which result from the corrosion of the alloy.

Figure 8 shows the pH potential diagram constructed to fit the present results. The major differences between this figure and the diagram due to Pourbaix and co-workers are listed below:

1. The intermediate oxide phases U_4O_9 and U_3O_7 have been shown as occurring within the potential boundaries −0.1v E_{HA} and −0.7v E_{HA} and +0.45v E_{HA} and −0.1v E_{HA}, respectively, and the hydroxide $U(OH)_4$ has been chosen in preference to UO_2 as the lowest oxidized phase of uranium. The complete sequence of solid phases is, therefore, U-$U(OH)_4$-U_4O_9-U_3O_7-U_3O_8-UO_3. A consideration of the free energies of formation showed that the values determined theoretically from this particular sequence gave the best approximations to the available data, and differed by only 3-4% from those quoted by Pourbaix and co-workers. Values used by Pourbaix are compared with the recalculated values in Table I.

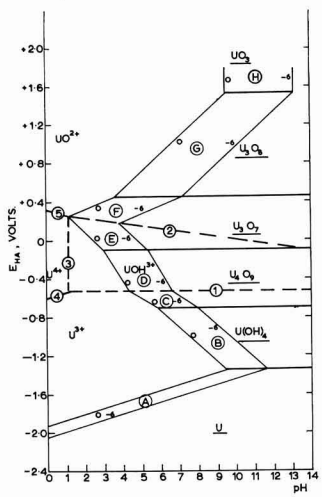

Fig. 8. pH-potential diagram for U-H_2O system (modified version)

Table I. Free energy of formation of solid species

	Pourbaix values, kcal/g mole	Calculated values, kcal/g mole
$U(OH)_4$	−351.6	−351.6
U_4O_9		−1041.9
U_3O_7		−796.7
U_3O_8	−804	−833
UO_3	−273	−273

Table II. Free energy of formation of ionic species

	Pourbaix values, kcal/g mole	Calculated values, kcal/g mole
U^{3+}	−124.4	−131.1
U^{4+}	−138.4	−145.1
UOH^{3+}	−193.5	−200.2
UO^{2+}	−236.4	−243.1

2. The ionic activity lines of the Pourbaix diagram (marked A to G in Fig. 6) have been shifted 2 *p*H units to the right. This permits the differences between the corrosion behavior of uranium in acid and alkaline solutions to be ascribed to the existence of different species in the two environments. The free energies of formation for the ionic species recalculated after the shift are again found to differ only slightly from the values given by Pourbaix. Table II shows the values adopted by Pourbaix compared with the new ones used in Fig. 8.

Electron diffraction.—An attempt was made to verify the theoretical *p*H-potential diagram by electron diffraction measurements. Specimens of uranium were corroded at several values of potential between +0.8v E_{HA} and −1v E_{HA} in both *p*H 5.4 solution and in alkaline solutions, washed in ether and benzene, and transferred to a Hitachi HU 11 electron microscope which incorporated a special attachment for glancing angle diffraction. The diffraction chamber was provided with a vacuum seal which isolated it from the rest of the microscope and enabled the specimens to be under high vacuum within about 5 min of removal from the corrosion cell. This prevented serious atmospheric oxidation of the specimen before it could be photographed. Best results were obtained with a 50 kv electron beam.

The diffraction patterns were calibrated against a graphite d_{110} ring obtained by transmission using identical microscope settings. The results are summarized in Fig. 9 (the reference numbers indicate the sources where the lattice parameters of the relevant oxides were found).

The patterns obtained from specimens corroded in *p*H 5.4 solution were simple to identify, and showed that the corrosion product formed at all values of potential was UO_2. Corrosion in alkaline solutions gave some diffuse patterns with wide rings and these were, consequently, difficult to measure and interpret. The pattern for U_3O_7, however, was clearly identifiable as were several U_3O_8 lines in the oxide formed at +0.5v E_{HA} and +0.8v E_{HA}. The pattern obtained from the test at

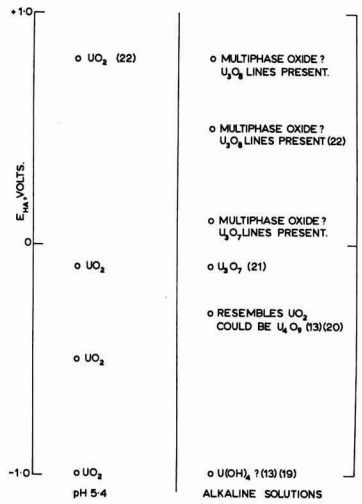

Fig. 9. Identification of uranium oxides by electron diffraction

−1v E_{HA} closely resembled that of UO_2, but the rings were very diffuse. On the basis of x-ray work, this is believed by some workers (13, 19) to indicate the presence of the hydroxide $U(OH)_4$.

Conclusions

It is established from the results that the corrosion of uranium and the uranium-zirconium alloy in alkaline solutions differs significantly from the corrosion in *p*H 5.4 solution, and this difference in behavior is ascribed to the formation of oxides other than UO_2 in solutions of high *p*H. The corrosion rate of zirconium in alkaline solutions is somewhat higher than in *p*H 5.4 but the mechanism appears to remain virtually unaltered. Zirconium ions are known to display a unique valency and oxides higher than ZrO_2 do not normally exist.

Electron diffraction measurements while failing to establish accurately the stability ranges of the various oxide phases shown in the newly constructed *p*H-potential diagram for uranium gave supporting evidence for their existence. The electron diffraction results agreed with the corrosion rate results to the extent of indicating clearly the marked difference between the corrosion products in the two types of environment.

Although the reversals in the corrosion rate of uranium and the alloy associated with cathodic polarization in alkaline solutions require a different and more complex explanation than does the simple behavior found in acidic solutions, the proposed mechanism of oxide growth remains the same. These results lend further support to the suggestion that a relationship exists between the electronic conductivity of the oxide, its hydrogen content, and the corrosion rate.

Acknowledgments

The authors wish to acknowledge the financial support of the United Kingdom Atomic Energy Authority during the investigation, and their indebt-

edness to Professor J. G. Ball for encouragement and for the provision of laboratory accommodation.

Manuscript received Dec. 3, 1963.

Any discussion of this paper will appear in a Discussion Section to be published in the June 1965 JOURNAL.

REFERENCES

1. J. S. Llewelyn Leach and A. Y. Nehru, "Corrosion of Reactor Materials," Vol. I, p. 58, I.A.E.A., Vienna (1962).
2. E. Deltombe, N. de Zoubov, and M. Pourbaix, Cebelcor Rapport Technique No. 31 (1956).
3. M. W. Burkart, U.S.A.E.C. Rept., Westinghouse Electric Corp., WAPD-127, Part III (1956).
4. J. E. Draley and W. E. Ruther, *This Journal,* **104**, 329 (1957).
5. D. E. Thomas and S. Kass, *ibid.*, **104**, 261 (1957).
6. A. Y. Nehru, Ph.D. Thesis, London University, 1963.
7. A. E. Stebbens and L. L. Shrier, *This Journal,* **108**, 30 (1961).
8. H. A. Porte, J. G. Schnizlein, R. C. Vogel, and D. F. Fischer, U.S.A.E.C. Rept. Argonne National Laboratory, ANL-6046 (1959).
9. J. S. Llewelyn Leach, "Properties of Reactor Materials and the Effects of Radiation Damage," p. 383, Butterworths, London (1962).
10. B. Lustman and F. Kerze, "Metallurgy of Zirconium," McGraw-Hill Book Co., New York (1955).
11. H. Coriou, L. Grall, J. Meunier, M. Perlas, and H. Willermoz, "Corrosion of Reactor Materials," Vol. II, p. 193, I.A.E.A., Vienna (1962).
12. E. A. Gulbransen and R. Ruka, *J. Metals,* Am. Inst. Mining & Met. Engr., **188**, 1500 (1950).
13. J. T. Waber, "Aqueous Corrosion of Uranium and its Alloys," Conf. on Aqueous Corrosion of Reactor Materials, Brussels (1959).
14. J. J. Katz and E. Rabinowitch, "The Chemistry of Uranium," Nat. Nucl. Eng. Series, Div. VIII-5, McGraw-Hill Book Co., New York (1951).
15. W. M. Latimer, "Oxidation Potentials," Prentice-Hall Inc., New York (1952).
16. R. K. Willardson, J. W. Moody, and H. L. Goering, U.S.A.E.C. Rept., Battelle Memorial Institute, BMI-1135 (1956).
17. J. S. Llewelyn Leach, *J. Inst. Met.,* **88**, 24 (1959).
18. H. S. Isaacs and J. S. Llewelyn Leach, *This Journal,* **110**, 680 (1963).
19. J. B. Schroeder, D. A. Vaughan, and C. M. Schwartz, *ibid.*, **106**, 486 (1959).
20. A. F. Wells, "Structural Inorganic Chemistry," Third ed., p. 966, Clarendon Press, Oxford (1962).
21. H. R. Hoekstra, A. Santoro, and S. Siegel, *J. Inorganic and Nuclear Chem.,* **18**, 166 (1961).
22. R. K. Hart, *Trans. Faraday Soc.,* **49**, 299 (1953).

The Effect of Heat-Treatment on the Corrosion and Hydrogen Pickup Behavior of a Zr-Sn-Nb Alloy in High Temperature Water and Steam

D. L. Douglass

Vallecitos Atomic Laboratory, General Electric Company, Pleasanton, California

and H. A. Fisch

Lamp Metals and Components Department, General Electric Company, Cleveland, Ohio

ABSTRACT

Heat-treatment was shown to increase the rate of corrosion of Zr-2Sn-2Nb over that of the annealed condition, but the rate of hydrogen pickup as a function of total corrosion was found to be relatively insensitive to heat treatment. The effects of heat treatment have been analyzed in terms of changes in: (i) alloy constitution, (ii) composition of microconstituents, and (iii) the metal texture and oxide orientation. Stereoscopic examination of oxide-film surfaces by electron microscopy revealed cracking both at grain boundaries and at interfaces between phases. Extensive and abrupt changes in film topography, which also were sites of film cracking, were observed.

A 2 atomic per cent (a/o) tin-2 a/o niobium alloy of zirconium in the annealed condition has been shown (1) to have mechanical properties superior to those of Zircaloy-2 and a corrosion resistance only slightly inferior to that of Zircaloy-2. Additional corrosion studies were warranted by this excellent combination of properties. The alloy is susceptible to heat-treatment with further improvement of its mechanical properties. This paper presents the results of a program to evaluate the corrosion behavior and hydrogen absorption of the annealed alloy and to determine the effects of heat-treatment on corrosion resistance.

Experimental Procedure

Sample preparation.—Two, 10-lb ingots were prepared by consumable arc melting in vacuum in a copper-cooled crucible. Ingots were remelted three times to obtain homogeneity. Ingot A (see Table I) was used to provide specimens for the investigation of the annealed alloy. Ingot B provided specimens for the heat-treatment studies.

Ingot A was jacketed with copper and Ingot B with mild steel before being extruded at 800°C. The extrusion reduced the ingots from the original 3-in. diameter to ¾-in. rod. These extruded rods were cold-rolled into 65-mil strips (3 passes with inter-

Table I. Chemical analysis of Zr-2Sn-2Nb ingots

	Ingot A Weight per cent (w/o)	Ingot A a/o	Ingot B w/o	Ingot B a/o
Tin	2.58	1.97	2.53	1.94
Niobium	1.97	1.93	1.94	1.90
Hydrogen	0.0022	0.20	0.0040	0.36
Nitrogen	0.0049	0.032	0.0110	0.072
Oxygen	0.1560	0.89	0.1000	0.57
Carbon	—	—	0.030	0.23
Zirconium	Balance		Balance	

mediate anneals) and cut into blanks which were vacuum-annealed at 775°C for ½ hr and fast-cooled (80°C/min). Corrosion coupons approximately 1x½-in. were machined from these blanks so that each specimen had four machined edges and two as-rolled surfaces.

Corrosion testing.—The coupons were degreased, pickled in HNO_3-HF-H_2O, and corrosion tested in water at 316° and 360°C and in steam at 400°, 440°, and 482°C, in static autoclaves of 347 stainless operated at 1500 psi. Deionized deoxygenated water was used in all tests. Twenty coupons were placed in an autoclave for each temperature condition. At the end of each incremental exposure, one coupon was removed and cut into six pieces. Hydrogen analysis by vacuum fusion and metallographic and x-ray examinations for hydride precipitation were performed on separate pieces of the coupon. The remaining coupons were left in the autoclave for longer exposures.

Heat treatment.—The blanks from Ingot B were heat-treated by sealing them, along with zirconium turnings, in quartz capsules under 1/3 atm of argon. Gettering of the atmosphere was performed before heat treatment by heating the turnings at one end of the capsule for several minutes. Quenching was performed by breaking the capsule under water after the desired time at temperature. Coupons were machined from these blanks and corrosion tested in 360°C water and 400°C steam.

X-ray diffraction.—The oxide films on the coupons from Ingot B were examined in a high-angle diffractometer with filtered copper radiation. A sample spinner was employed to rotate the sample about an axis perpendicular to the rolled surface of the strip.

Electron microscopy.—Oxide film surfaces were examined by electron microscopy using two-stage replication. Replicas were prepared by pressing replicating tape firmly against the surface, stripping off the tape, shadowing the tape with chromium at an oblique angle and finally shadowing with carbon normal to the surface of the tape. The carbon surface was coated with molten wax to prevent breakup of the replica, and the replicating tape was dissolved in acetone. The wax was dissolved subsequently, and the replicas were washed thoroughly. Stereo pairs were taken of all micrographs and subsequently studied with the aid of a stereoscope to determine the exact topographical nature of the oxide surfaces.

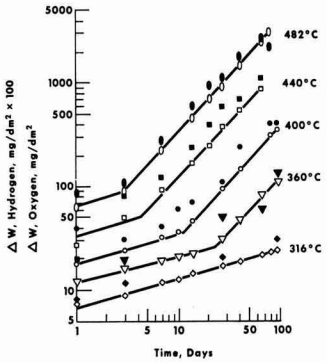

Fig. 1. Corrosion and hydrogen pickup kinetics of annealed samples. Open symbols, oxygen; closed symbols, hydrogen.

Results

Corrosion and Hydrogen Absorption of Annealed Samples

The effect of temperature on corrosion weight gain and associated hydrogen absorption for annealed samples is shown in Table II and in Fig. 1. As is characteristic for many zirconium-base alloys, the corrosion weight gain behavior follows a quasi-cubic rate law in the initial pretransition region, and a roughly linear rate in the post-transition region. On a log-log graph the transition point is arbitrarily taken to be the intersection of the lines representing the two rate law periods. The actual transition is gradual rather than abrupt. The slopes of the pretransition curves varied between 0.26 and 0.30 with no apparent relationship to exposure temperature. Posttransition slopes ranged between 1.01 and 1.08 and increased with increasing exposure temperature. These slopes are the exponents, n, in

Table II. Effect of temperature on corrosion and hydrogen pickup behavior on annealed alloy

(70-Day exposure data)

Temp, °C	Medium	Oxygen weight gain, mg/dm²	ppm, H_2	Hydrogen pickup Per cent of theoretical	Weight gain, mg/dm²	H:O weight gain ratio
316	Water	21.5	0	0	0	0
360	Water	81.0	16	6.3	0.6	0.0074
400*	Steam	(302) *	(94) *	(10.3) *	(4.0) *	(0.013) *
440	Steam	879	260	9.7	11	0.011
482	Steam	2585	601	27	8.4	0.010

* 84-Day data.

Table III. Summary of rate law exponents

Sample history	Exposure temp, °C	Exponent from: $\Delta W = kt^n$ Pretransition	Posttransition
Annealed 775°C ¼ hr	316	0.26	—
Annealed 775°C ¼ hr	360	0.28	1.01
Annealed 775°C ¼ hr	400	0.30	1.02
Annealed 775°C ¼ hr	442	0.29	1.08
Annealed 775°C ¼ hr	482	0.29	1.08
Annealed 800°C 24 hr	360	0.25	1.00
Annealed 800°C 24 hr	400	—	1.06
Annealed 950°C 24 hr, furnace-cooled	360	—	0.73
Annealed 950°C 24 hr, furnace-cooled	400	—	0.74
Annealed 950°C 24 hr, water-quenched	360	—	0.78
Annealed 950°C 24 hr, water-quenched	400	—	0.83
Annealed 950°C 24 hr, water-quenched, tempered 24 hr at 600°C	360	—	0.84
Annealed 950°C 24 hr, water-quenched, tempered 24 hr at 600°C	400	—	1.09
Hot-rolled then cold-rolled 30%	360	0.26	0.94
Hot-rolled then cold-rolled 30%	400	—	0.89

the equation $\Delta W = kt^n$, in which ΔW is the weight gain in mg/dm² and t is the exposure time in days. Individual values for these slopes are given in Table III.

During the corrosion reaction, hydrogen is liberated according to the following reaction

$$Zr + 2H_2O \rightarrow ZrO_2 + 2H_2$$

A portion of this hydrogen is taken up by the metal, the remainder is released to the environment. The hydrogen pickup of the annealed alloy is shown in Table II and Fig. 1, 2, and 3. Figure 1 shows that hydrogen absorption kinetics closely follow the weight change kinetics. The absorbed hydrogen values in parts per million given in Table II are the differences between initial and final values. Since the hydrogen analyses were only accurate to ± 5 ppm, specimens with hydrogen absorption values below 5 ppm may be considered as having absorbed no hydrogen.

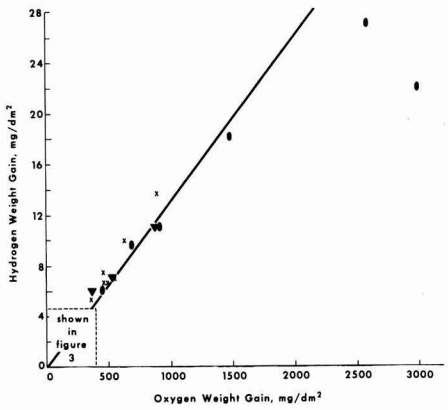

Fig. 2. Relationship between absorbed hydrogen and oxygen weight gains.

	Test temperature, °C				
	316	360	400	440	482
Annealed alloys posttransition	●	▲	■	▼	solid oblong
Heat-treated alloys		+	×		

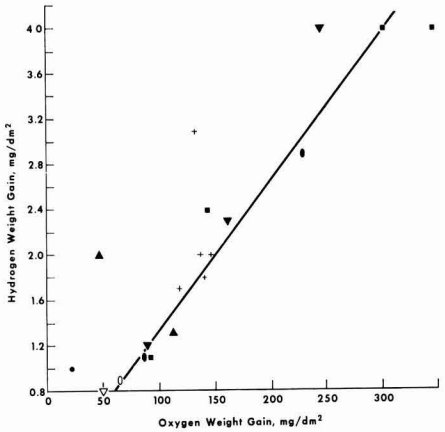

Fig. 3 Relationship between absorbed hydrogen and oxygen weight gains.

	Test temperature, °C				
	316	360	400	440	482
Annealed alloys					
Pretransition				▽	open oblong
Posttransition	●	▲	■	▼	solid oblong
Heat-treated alloys		+			

Figures 2 and 3 show that the ratio of hydrogen weight gain to oxygen weight gain of 0.013 is nearly constant over the temperature range investigated and that there is no difference between pickup in the pretransition and posttransition regions of the weight gain curve. This is in contrast to the observations of Cox (2) who found, for Zircaloy-2 and other zirconium alloys, that the curve for hydrogen absorption could be divided into three regions each having different ratios.

Effect of Heat-Treatment on Corrosion Resistance and Hydrogen Absorption

Total weight gain curves for heat-treated coupons exposed in 360°C water and 400°C steam are given in Fig. 4 and 5. All heat-treated coupons, with one exception, produced comparable corrosion weight gains after 100 days in 360°C water. A specimen which had been water-quenched from 950°C exhibited weight gains two or three times greater than the others. Tempering of the quenched structure for 100 hr at 500°, 600°, or 700°C resulted in weight gains comparable to those of both the fully annealed and cold-worked samples. The same general behavior was observed in 400°C steam. The as-quenched sample again showed greater weight gains than the others.

The increase in weight gain with time of the quenched samples did not follow the quasi-cubic to linear transition behavior observed with the an-

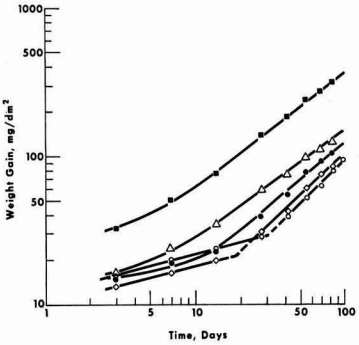

Fig. 4. Effect of heat treatment on 360°C water corrosion. ■, 950°C 24 hr, water quenched; △, 950°C 24 hr, furnace-cooled; ◇, hot rolled and cold rolled (~30%); •, 950°C 24 hr, water-quenched, tempered at 600°C 100 hr; ○, annealed at 800°C 24 hr, furnace cooled.

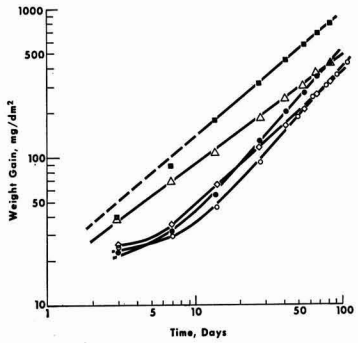

Fig. 5. Effect of heat treatment on 400°C steam corrosion. ■, 950°C 24 hr, water-quenched; △, 950°C 24 hr, furnace-cooled; ◇, hot rolled and cold rolled (~30%); •, 950°C 24 hr, water-quenched, tempered at 600°C 100 hr; ○, annealed at 800°C 24 hr, furnace-cooled.

nealed specimens. In 360°C water, the specimen quenched from 950°C showed a continuously increasing slope which reached a limiting value of 0.78. This value, while not corresponding to any of the exponents for known rate laws, may be taken as the equivalent of the posttransition linear rate observed for the annealed specimens. Both the cold-rolled and 800°C-annealed samples showed an initial quartic, rather than cubic, time relationship followed by a transition to a linear time relationship.

The same general behavior was observed in 400°C steam, but the initial slopes could not be determined. For the cold-rolled and 800°C-annealed specimens the slopes reached limiting values of 0.89 and 1.06, respectively. The samples which were furnace-cooled from 950°C showed a corrosion rate slope of 0.74 and the samples water-quenched from 950°C showed a corrosion rate slope of 0.83. These data are summarized in Table III.

The coupons were analyzed for hydrogen pickup after corrosion tests were completed. These results are given in Table IV. The per cent of theoretically available hydrogen which was absorbed by the heat-treated samples and the ratio of absorbed hydrogen to oxygen were generally higher than those for the fully annealed alloy. The median ratio for the heat-treated alloys, 0.015, was higher by a statistically significant amount than the value 0.013 observed for the annealed alloys.

Oxide Film Orientation

Monoclinic ZrO_2 films were observed on all samples investigated in this work. Although the film structures were identical on all alloys, differences in relative intensities of various ZrO_2 reflections are evidence of different film textures. Diffraction patterns of several samples are given in Table V, for both films and substrates.

According to Chirigos and Thomas (3) the monoclinic oxide on Zircaloy-2 is oriented with the (111) planes parallel with the (0001) planes of the metal; because of the similarity of Zircaloy-2 and Zr-2Sn-2Nb, a similar relationship of oxide-to-metal is to be expected for the latter alloy. The (111) oxide reflections on the annealed and cold-rolled samples were the strongest as shown in Table V. The strongest reflection from the substrate was for the (0002) planes (second order basal plane reflection). Evidently the oxide and metal both have the orientations observed by Chirigos and Thomas. However, the water-quenched samples showed weak basal

Table IV. Effect of heat treatment on corrosion and hydrogen pickup behavior

(98 Day exposure data)

Heat-treatment	Corrosion results: Corrosion conditions	Corrosion results: Oxygen weight gain, mg/dm²	ppm H_2	Hydrogen pickup: Weight gain, mg/dm²	Hydrogen pickup: Per cent of theoretical	H:O Ratio
Annealed 800°C, F.C.[a]	360°C water	112	33	1.3	9.6	0.012
Annealed 800°C F.C.	400°C steam	346	103	4.0	9.8	0.011
Betatized 950°C, F.C.	360°C water	139	40	1.8	10.2	0.013
Betatized 950°C, F.C.	400°C steam	495	150	6.7	10.9	0.014
Betatized 950°C, A.C.[b]	360°C water	136	45	2.0	11.8	0.015
Betatized 950°C, A.C.	400°C steam	471	150	6.7	11.5	0.014
Betatized 950°C, W.Q.[c]	400°C steam	900	310	13.6	12.2	0.015
Betatized 950°C, W.Q. + 100 hr 500°C	360°C water	132	71	3.1	18.9	0.023
Betatized 950°C, W.Q. + 100 hr 500°C	400°C steam	634	232	10.0	12.7	0.016
Betatized 950°C, W.Q. + 100 hr 700°C	360°C water	146	46	2.0	11.1	0.014
Betatized 950°C, W.Q. + 100 hr 700°C	400°C steam	551	155	7.0	10.1	0.013
Hot-rolled + 30% cold-work	360°C water	117	40	1.7	11.9	0.015
Hot-rolled + 30% cold-work	400°C steam	357	122	5.4	12.2	0.015

[a] F.C., furnace-cooled; [b] A.C., air-cooled; [c] W.Q., water-quenched.

Table V. Relative intensities of x-ray patterns of uncorroded metal and of corrosion films

Phase	(hkl)	Base metal		Corrosion tests							
				360°C Water				400°C Steam			
		Annealed 800°C	Water-quenched from 950°C	Annealed 800°C	Annealed and cold-rolled	Water-quenched from 950°C	Water-quenched & 600°C tempering	Annealed 800°C	Annealed and cold-rolled	Water-quenched from 950°C	Water-quenched & 600°C tempering
ZrO_2	(111)	—	—	100	100	8	14	100	100	12	36
αZr	(100)	0	30	0	0	0	0	0	0	0	0
ZrO_2	(002)	—	—	75	100	100	100	86	100	100	100
αZr	(002)	100	10	0	0	0	0	0	0	0	0
ZrO_2	(200)	—	—	50	60	0	0	0	0	0	0
ZrO_2	(102)	—	—	40	65	55	38	55	50	55	50
αZr	(101)	15	15	0	0	0	0	0	0	0	0
ZrO_2	(211)	—	—	20	18	0	0	18	20	2	10
ZrO_2	$(21\bar{1})$	—	—	20	20	25	20	32	20	23	15
αZr	(102)	45	15	0	0	0	5	0	0	0	0
ZrO_2	(220)	—	—	10	0	8	0	13	5	6	0
ZrO_2	(013)	—	—	55	50	20	20	75	70	23	36
αZr	(110)	8	100	0	0	0	50	0	0	0	0
ZrO_2	$(13\bar{1})$	—	—	10	18	8	10	23	20	10	18
ZrO_2	$(11\bar{3})$	—	—	25	25	2	5	32	30	4	12
αZr	(103)	100	60	45	25	0	15	0	0	0	0
αZr	(200)	0	5	0	0	0	0	0	0	0	0
αZr	(112)	15	5	0	0	0	5	0	0	0	0
αZr	(201)	0	0	0	0	0	0	0	0	0	0
ZrO_2	$2\theta_{Cu} = 71.2$	—	—	25	40	50	28	45	50	40	43
αZr	(004)	30	0	15	0	0	0	0	0	0	0
αZr	(202)	0	0	0	0	0	0	0	0	0	0
αZr	(104)	30	5	15	0	0	0	0	0	0	0
αZr	(203)	0	0	0	0	0	0	0	0	0	0
ZrO_2	$2\theta_{Cu} = 92.6$	—	—	12	0	0	0	0	0	0	0
αZr	(210)	0	10	0	0	0	0	0	0	0	0
αZr	(211)	0	10	0	0	0	0	0	0	0	0
αZr	(114)	30	50	0	10	0	15	0	10	0	12
αZr	(212)	0	0	0	0	0	0	0	0	0	0
ZrO_2	$2\theta_{Cu} = 106$	0	0	25	10	0	0	0	0	0	0

plane reflections, the strongest x-ray peak being the $(11\bar{2}0)$ reflection. The oxide on the quenched sample was oriented with the (001) planes parallel to the $(11\bar{2}0)$ planes of the quenched metal. The (200), (211), (013), and $(11\bar{3})$ oxide reflections on the annealed samples were strong but were non-existent or weak on quenched samples.

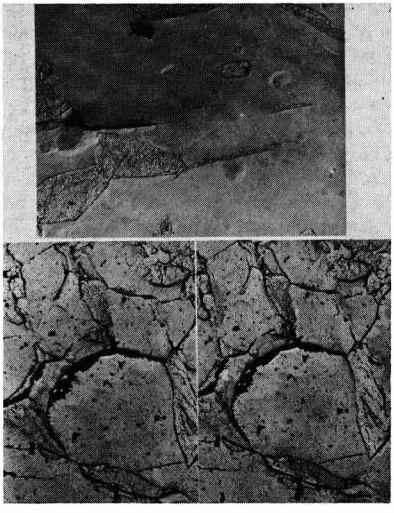

Fig. 6. Structure of annealed alloy, 24 hr at 800°C and furnace-cooled. Corroded 112 days in 360°C water. a (upper), Alloy substrate; b (lower), Stereo pair of oxide film surface (negative replica). Magnification approximately 3000X.

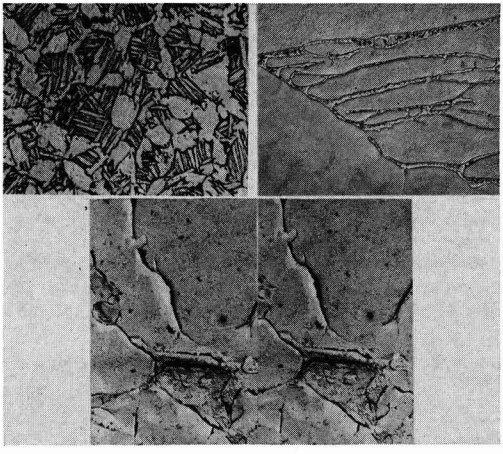

Fig. 7. Structure of 950°C annealed, furnace-cooled alloy. Corroded 100 days in 360°C water. a (upper), Alloy substrate; left, magnification approximately 250X; right, approximately 3000X. b (lower), stereo pair of oxide film surface (negative replicas); Magnification approximately 3000X.

Topography and Morphology of Oxide Films

The topographical features of the oxide films and the relationship of the film structure to the metal substrate structure were easily discernible in stereo pairs of electron micrographs. Four stereo pairs which were particularly informative are shown in Fig. 6, 7, 8, and 9, and may be viewed by the reader with a stereoscope.

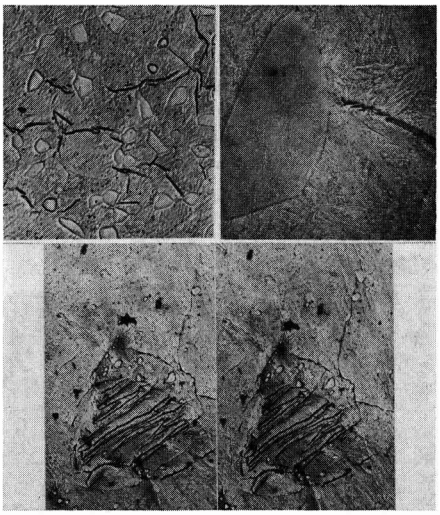

Fig. 8. Structure of quenched and tempered alloys. a (upper), Alloy substrate, quenched from 950°C and tempered 100 hr at 500°C, corroded 100 days in 360°C water; magnification, left, 250X; right, 3000X. b (lower), Stereo pair of oxide film surface (negative replicas). History same as a. 3000X.

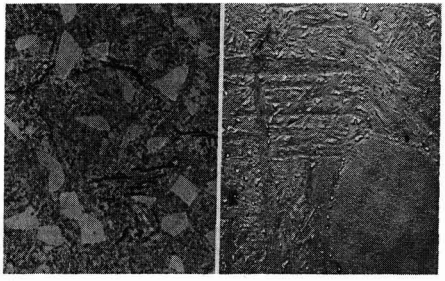

Fig. 8c. Alloy substrate, quenched from 950°C and tempered 100 hr at 600°C, corroded 100 days in 360°C water. Notice larger precipitate size and more advanced stages of martensite break down compared to a; left, 375X; right, 3000X.

Fig. 9. Structure of hot-rolled plus cold-rolled alloy, corroded 100 days in 360°C water. a (upper), Alloy substrate, 6000X. b (lower), stereo pair of oxide film surface (negative replicas). Magnification approximately 3000X.

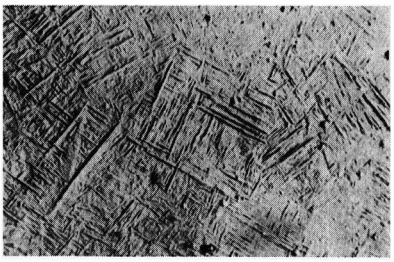

Fig. 10. Martensitic substrate structure, water-quenched from 1000°C. No primary alpha present, solution temperature was above $\beta/\beta + \alpha$ transus. Magnification approximately 250X.

Although macroscopic examination of the films indicated that they were crack-free and protective, the electron micrographs definitely established that many cracks were present. The cracks generally appeared at interfaces such as grain boundaries or the interfaces between two phases. An example of a grain boundary crack may be seen in Fig. 6, and an example of cracks between two phases may be seen in Fig. 7. Figure 7 also shows a crack which formed entirely within a primary alpha grain. Numerous interfacial cracks formed in the cold-rolled sample, Fig. 9. The quenched alloys were martensitic, consisting of a surface-roughened, acicular structure shown in Fig. 10. Much of the martensitic structure did not appear in the oxide films (such as in Fig. 8) indicating the oxide film masks out the structure of the substrate readily.

It should be emphasized that there are differences in the topography of the films which cannot be seen readily without a stereoscope. For example, the cracked patch in Fig. 8 is a raised mound in the replica (surface depression on the oxide surface) which probably resulted from a higher corrosion rate in this region. Another example of surface depressions in the oxide may be found in the negative stereo pair in Fig. 7 (the mottled region just below the center of the micrograph). This mottled region on the oxide is surrounded by a protruding ridge, at the bottom of which exists a crack (the black, fan-like structure). In most instances, the oxide films were cracked where the topography changed abruptly.

All stereo pairs revealed a significant amount of surface porosity as evidenced by small protruding whiskers in the replicas. The depth of these pores could be estimated from the height of the whiskers. It is not known whether the plastic replicating tape completely filled the pores or whether all of the tape was extracted from the pores during removal of the tape. The importance and nature of these features warrants further work.

Discussion

Rate Laws

Various heat-treatments effected appreciable differences in the corrosion behavior of the alloys, but it is difficult to analyze these differences in terms of the usual rate laws. It appears that many of the samples initially corroded in accordance with some frac-

tional-power-exponent rate law, which is indicative of some type of diffusion-controlled process. Eventually all of the samples exhibited a transition to corrosion in accordance with a more rapid rate law having higher values of the exponent. The higher values of the exponent are characteristic of a linear rate law in cases where $n \sim 1$, but the intermediate values, between 0.5 for a parabolic rate law and unity for a linear rate law, are puzzling. It is possible that a combination of rate laws is applicable because only a portion of the film area is protective (in which region a diffusion-controlled process takes place), while the remaining area of the sample is corroding according to a linear rate law. The fact that cracks in the film were observed rather extensively gives support to this idea. Further, the presence of porosity over certain areas, see Fig. 9, may allow those areas to corrode linearly, although it is not known if the porosity is deep enough to allow the reactants direct access to each other.

It is still doubtful that values of the exponent, n, obtained from log-log plots of weight gain *vs.* time are meaningful in view of Wanklyn's work (4) on individual grains of zirconium. Wanklyn has studied the formation of interference films by noticing color changes on numerous individual zirconium grains and has found a wide variety of rate laws for the grains. In addition to differences in over-all thickness, Wanklyn observed the formation of large "pustules" on grains which had the thinnest oxide films. Grains which oxidized rapidly appeared to form uniform thick films, whereas the more resistant grains eventually exhibited the highly localized attack in the form of pustules. Rate laws cannot be assigned with certainty to the oxidation of polycrystalline metals when the single grains exhibit such a wide variation in behavior.

Alloy Constitution

The difference in corrosion behavior as affected by heat-treatment can be analyzed in terms of the relative corrosion rates of the different phases. Let us consider how the constitution of the alloys can be changed by heat treatment.

The constitution of the alloy at the quenching temperature, 950°C, was $\alpha + \beta$ even though the isothermal sections of high-purity alloys indicate that the alloy should be entirely within the beta region (5). The primary alpha was stabilized by the presence of 1000 ppm oxygen, thus resulting in partitioning of the niobium to the beta phase and of the tin and oxygen to the alpha phase. Quenching resulted in supersaturation of the primary alpha and the transformation of the beta martensitically to a distorted alpha having a solute content in excess of that shown in the equilibrium diagram (5). The structure, therefore, consisted of two alpha-phases of different composition: primary alpha with $\sim$ 1 a/o Nb and $\sim$ 7 a/o Sn, and alpha prime with $\sim$ 1-2 a/o Nb and $\sim$ 1-2 a/o Sn.[1] The corrosion rate of the primary alpha would be higher than that of the alpha prime due to the higher tin content of the former.

Tempering of the quenched structure improved the corrosion resistance considerably. This effect is related to the rejection of a precipitate from the martensitic alpha (see Fig. 8a and c). Tempering at 500°C produced a very fine precipitate; tempering at 600°C produced a much coarser precipitate. The primary alpha phase was void of precipitate whether tempering was performed at 500° or 600°C. This is rather surprising in view of the high tin content of the primary alpha which was considerably higher than the solubility limits at either tempering temperature. It was expected that rejection of Zr_4Sn would occur in the primary alpha, but electron microscopy failed to reveal any precipitation. Optical micrographs of the corroded samples, Fig. 8a and c, show the hydrides observed in the martensitic matrix of quenched alloys as well as tempered alloys. The hydrides did not form in the primary alpha phase, and when growing in the martensitic phase apparently were stopped on reaching the primary alpha particles.

Annealing at 800°C also was performed within the $\alpha + \beta$ region, but the composition of the two phases was markedly different from that of the alloy quenched from 950°C. The tin content of the primary alpha was lower, and the niobium content of the beta-phase was higher than the sample quenched from 950°C. If the niobium content of the beta-phase is high, transformation may be expected during cooling (6). According to the only isothermal sections available for high purity alloys (5), beta should decompose into three phases, $\alpha + \beta_f + Zr_4Sn$; the final beta, β_f, having a composition presently unknown but different from the original beta. The decomposition products of the high-temperature beta are seen in Fig. 6a as small polyphase regions. The fact that the samples annealed at 800°C were polyphase and also showed the most resistance to corrosion gives strong support to the supposition that the corrosion resistance of all the phases is nearly identical.

The good corrosion resistance of the cold-worked sample may be attributed to its similarity in structure to that of the sample annealed at 800°C. The cold-worked structure is elongated slightly by the rolling, but otherwise is very similar with respect to microconstituents.

Heat-treatment has been observed to have a strong influence on corrosion resistance in Zr-Nb binary alloys (7, 8), primarily due to gross changes in the composition of microconstituents. Klepfer (7) and Richter and Tverberg (8) showed that heat treatment in the $\alpha + \beta$ region for binary Zr-Nb alloys resulted in corrosion rates much higher than the corrosion rates for material annealed in the region below the monotectoid temperature. In the latter material an alpha-zirconium phase containing about 1% Nb is in equilibrium with a body-centered cubic phase of about 90% Nb-10% Zr; both phases have excellent corrosion resistance. Heating in the $\alpha + \beta$ region produces an alpha phase which is very similar to that formed below the monotec-

[1] These compositions were estimated from available ternary isotherms and unpublished research on the effect of oxygen on the constitution of Zr-Sn-Nb alloys.

toid temperature, but the body-centered cubic phase in equilibrium with the alpha contains between zero and ~ 20% Nb, depending on the temperature. Klepfer showed that as the annealing temperature within the $\alpha + \beta$ region increased, the niobium content of the beta-phase decreased. Richter and Tverberg showed a similar behavior for ternary Zr-Nb-Sn alloys for tin contents of up to 1%. It has been shown (1, 5, 7, 8) that the corrosion resistance of β-zirconium decreases with increasing niobium, and thus the over-all corrosion resistance of the two-phase alloy decreases as the amount of the beta-phase increases and/or as its niobium content increases.

Changes in Oxide and Metal Orientations

Another factor which may be partly responsible for the different corrosion behaviors after heat treatment could be the changes noted in orientations of both oxide and metal. The anisotropy of corrosion (9) would manifest itself in different corrosion kinetics as the texture of the substrate changed. Likewise, a change in oxide orientation might be expected to alter both the rate of oxygen diffusion through the oxide and the rate of growth of the oxide. Although no evidence exists for anisotropy of oxygen diffusion in zirconia (10), it is reasonable to expect diffusion anisotropy in low-symmetry structures as exemplified by self-diffusion in bismuth (11).

In this study, the strong $(11\bar{2}0)$ texture of the quenched samples and the strong (0001) texture of the annealed samples are the principal texture differences. Bibb and Fascia (9) have shown that metal orientation significantly affects the corrosion rate of single crystals of zirconium, some of their data are summarized in Table VI. Although Bibb and Fascia found that the weight gains in a given time of (0001) and $(11\bar{2}0)$ faces were similar, a shift in orientation from the $(11\bar{2}0)$ face of less than 16° gives an orientation of $(21\bar{3}1)$, the crystal face which they found to have the poorest corrosion resistance.

Pole figures were not run on the Zr-Sn-Nb samples, but the fact that medium intensities of the $(10\bar{1}3)$ and $(11\bar{2}4)$ reflections were observed in the quenched sample indicates that this sample did not have a perfect $(11\bar{2}0)$ texture and probably was close to the $(21\bar{3}1)$ texture. The $(21\bar{3}1)$ reflection for the quenched samples had a relative intensity of 10, but this reflection was not detected in the annealed samples. Additional evidence supporting a $(21\bar{3}1)$ texture of the quenched samples may be obtained by considering the relative intensities of the low-multiplicity planes of zirconium powder, *e.g.*, $(21\bar{3}1)$—6 for powder *vs.* 10 for the quenched sample; $(11\bar{2}4)$—3 for powder *vs.* 50 for the quenched sample.

The quenched samples showed a weight gain at a rate about two times that of the annealed samples, which is quantitatively similar to the ratio observed by Bibb and Fascia for the $(21\bar{3}1)$ and (0001) crystal face textures.

Table VI. Anisotropy of zirconium single crystal corrosion in 360°C water (9)

Crystal face	Weight gain, mg/dm² after 100 days	Time to transition, days
(0001)	22	170
$(10\bar{1}4)$	23	115
$(10\bar{1}1)$	26	130
$(21\bar{3}1)$	41	130
$(21\bar{3}0)$	16.5	300
$(11\bar{2}0)$	25	155

Hydrogen Pickup

The relative insensitivity of hydrogen pickup rate with respect to heat treatment and composition has been noted in binary Zr-Nb alloys by Klepfer (7). Richter and Tverberg (8) also studied binary Zr-Nb alloys and observed slight differences in hydrogen pickup rates, but no clear correlation between pickup and heat treatment or between pickup and composition could be established. Richter and Tverberg investigated several ternary Zr-Nb-Sn alloys and found that various alloys subjected to different heat treatments picked up hydrogen at about the same rate as that which Klepfer observed in the binary Zr-Nb alloys and as that observed in this study on Zr-2Sn-2Nb.

The location of hydrides (see Fig. 8) is somewhat puzzling. There appears to be no hydride in the primary alpha phase. The beta phase[2] is an equilibrium phase at 360°C, the corrosion test temperature, and if beta were present, one would expect that the hydrogen would locate preferentially in this phase due to a higher solubility than in alpha. However, the high temperature beta transformed to martensite during the quench, and no evidence of beta was found by x-ray diffraction after exposure at 360°C for 100 days. It would thus appear that tin restricts the solubility of hydrogen in alpha zirconium, whereas niobium increases the solubility. If it is assumed that the hydrogen was soluble at the test temperature, then precipitation should occur during cooling to room temperature.

No clear explanation of hydrogen pickup in zirconium alloys containing niobium has thus far been given. Fortunately, the rate of pickup is low in these alloys, and thus, if good corrosion resistance can be achieved, the amount of hydrogen absorbed will be low and integrity of mechanical properties can be maintained.

Manuscript received Aug. 30, 1963. This paper was presented at the New York Meeting, Sept. 29-Oct. 3, 1963.

Any discussion of this paper will appear in a Discussion Section to be published in the June 1965 JOURNAL.

REFERENCES

1. D. L. Douglass, "Nuclear Metallurgy," AIME, VII, 31 (1960).

[2] There are two beta phases present in the Zr-Nb system which exhibits a monotectoid reaction. The low temperature beta has the composition 10Zr-90Nb, whereas the high temperature form for the Zr-2Sn-2Nb alloy has a composition of less than 20% Nb, depending on the temperature. The high temperature form may transform to α' and/or ω upon quenching.

2. B. Cox, *This Journal*, **109**, 1 (1962).
3. J. N. Chirigos and D. E. Thomas, *Proc. A.E.C. Metallurgy Conf.*, March 1952. Report TID-5084.
4. J. N. Wanklyn, C. F. Britton, D. R. Silvester, and N. J. M. Wilkins, "The Corrosion of Zirconium and Its Alloys in High Temperature Steam. Part III. The Influence of the Environment on Oxidation," AERE-R 4130 (1962).
5. O. S. Ivanov and V. K. Grigorovich, "Structure and Properties of Zirconium Alloys," Peaceful Uses of Atomic Energy, Second Geneva Conference, Properties of Reactor Materials, **5**, 34 (1958).
6. R. F. Hehemann, *U.S.A.E.C. Symposium on Zirconium Alloy Development*, GEAP-4089, **1**, Paper 10 (1962).
7. H. H. Klepfer, *J. Nuc. Mat.*, In press.
8. H. Richter and J. C. Tverberg, *U.S.A.E.C. Symposium on Zirconium Alloy Development*, GEAP-4089, **I**, Paper 4 (1962).
9. A. E. Bibb and J. R. Fascia, Abstract in *J. of Metals*, **15**, 82 (1963), and personal communication.
10. D. L. Douglass, *Proc.* International Conference on the Corrosion of Nuclear Materials, IAEA, Salzburg, Austria, **2**, 223 (1962).
11. W. Seith and A. Keil, *Z. Elektrochem.*, **39**, 540 (1933).

The Trivalency of Gallium Ions Formed during the Dissolution of the Metal in Acids

M. E. Straumanis and K. A. Poush

Department of Metallurgical Engineering,
University of Missouri School of Mines and Metallurgy, Rolla, Missouri

ABSTRACT

Gallium dissolves very slowly in dilute acids such as HCl, H_2SO_4, and $HClO_4$. The rate can be substantially accelerated if the metal is connected with a Pt electrode in the same solution. From the volume of the hydrogen developed the valency of 3 is calculated for the Ga ions going into solution. The same ionic charge is obtained from coulometric measurements using a Ga amalgam as an anode. This is in contradiction with the valency of one recently reported in the literature. However, microscopic observations revealed that the valency of one is only apparent, because Ga° disintegrates partially while going into solution anodically. The diameter of the smallest observable Ga particles is less than 7×10^{-5} mm. If the solution is not cooled the formation of large metallic spheres is observed. Disintegration explains the deviation from Faraday's law, and the presence of the small particles—the reducing ability of the electrolyte. The postulation of Ga ions of lower valency is therefore, not necessary.

One of the basic problems in corrosion and anodic dissolution of metals is the valency or charge of ions with which the latter go into solution. There are investigations which seem to prove that, for instance, Be, Mg, and Zn, under certain conditions, may go into solution in the form of monovalent ions and then immediately react with the electrolyte or an oxidizer if present. Thus, the existence of lower valency ions cannot be proved directly, but the deviation from Faraday's law in the sense that more metal went into solution than calculated, points indirectly toward the anodic formation of lower valency ions.

Such observations were also made on gallium anodes (1): more Ga went into solution than required by Faraday's law and the anolyte showed some reducing ability. It was concluded that in the initial stage of dissolution monovalent gallium ions were ejected by the anode. The existence of such ions was derived (2) from experiments in which Ga was dissolved in concentrated $HClO_4$, whereby this was assumed to be (partially) reduced to Cl^-

$$4Ga^+ + 8H^+ + ClO_4^- \rightarrow 4Ga^{3+} + Cl^- + 4H_2O \quad [1]$$

A second possibility that the active hydrogen, developed during the dissolution reaction, might act as a reducing agent was not considered

$$ClO_4^- + 8H \rightarrow Cl^- + 4H_2O \quad [2]$$

The aim of the present contribution is to prove that Ga^o does go into solution in the form of Ga^{3+}, and that the deviation from Faraday's law and the reducing ability of the anolyte are due to partial disintegration of the Ga anode into very fine particles which may act as a reducing agent. The experimental procedure is as follows: (i) collecting and measuring the volume of hydrogen evolved from the metal dissolving in acids provides confirmation of

$$Ga + 3H^+ \rightarrow Ga^{3+} + 1.5H_2 \quad [3]$$

(ii) determining the valency of Ga-ions going into solution from a Ga-amalgam electrode by measuring the number of coulombs, and (iii) examining the solvent for very fine metallic particles which may be expelled from the Ga anode while the current is flowing.

The Trivalency from the H_2-Volume Developed

Unfortunately, pure Ga metal dissolves so slowly in acids such as HCl, H_2SO_4, and $HClO_4$, even when they are hot and concentrated, that it was impossible to collect sufficient amounts of hydrogen to establish the stoichiometry of reaction [3]. The dissolution rates of Ga amalgams were even lower. Therefore, it was necessary to accelerate the veloc-

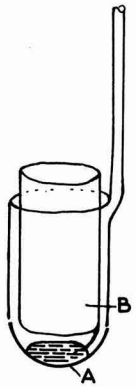

Fig. 1. Device for dissolving the Ga of the amalgam A by immersion into HCl, H_2SO_4, or $HClO_4$. B, Pt cylinder and connection with A.

ity of the reaction. This was achieved by connecting the Ga amalgam with a cylindrical platinized platinum electrode as a cathode (Fig. 1). Since this cathode has a low hydrogen overpotential, the gas can readily develop on it, while Ga is going into solution anodically.

About 0.13g of gallium (99.9% pure) were weighed precisely and dropped into some Hg; Ga amalgam was formed (3). Then this amalgam was connected with the hollow platinum cylinder and the couple was immersed in the acid, held in a flask. The contents were preheated to a temperature of 37°-38°C in a constant temperature water bath and saturated with hydrogen (4). Reaction [3] started at once. The gas was collected above water in a burette, using a leveling bulb.

Volume-time curves were drawn to determine the end of the dissolution reaction, which required 3-6 hr. The valency of Ga ions was calculated from the weight of Ga dissolved and the volume of hydrogen developed. The results are summarized in Table I.

Table I. Valency of Ga ions going into solution anodically (from a Ga-amalgam anode)

Acid	Normality	Valency	Average
H_2SO_4	4.2	3.02	
	4.0	2.98	
	7.2	2.98	
	7.2	2.93	
	8.6	2.97	2.976
HCl	6.1	3.01	
	6.1	2.88	
	6.1	2.96	
	6.1	2.94	
	6.1	3.01	
	6.1	2.90	2.950
$HClO_4$	9.2	2.79	
	9.2	2.77	
	4.6	2.90	
	8.3	2.96	
	8.3	2.98	
	8.3	2.91	2.884

Considering that there is still some hydrogen loss during the 3-6 hr of collection of the gas, it becomes clear from the valency numbers of Table I that Ga goes into solution as a trivalent ion, Ga^{3+}. Besides, no Cl^- could be detected in the solutions of $HClO_4$ after the dissolution of Ga was completed, which indicates again that Ga^+ was not formed during the experiments and that there were no reduction reactions according to [2].

Nevertheless, the objection can be raised that reaction [3] may proceed in two steps, according to Davidson and Jirik (1)

$$Ga + H^+ \rightarrow Ga^+ + 0.5H_2 \qquad [4]$$

and

$$Ga^+ + 2H^+ \rightarrow + Ga^{3+} + H_2 \qquad [5]$$

As the sum of reactions [4] and [5] is equal to reaction [3], Table I is no proof for the initial monovalency of Ga ions; it shows only that the stable valency of Ga-ions is 3.

However, there are the following objections against Eq. [4] and, as a consequence, against [5]: (i) The presence of Ga^+ could not be proved in the solution, and therefore, it was previously assumed that Ga^+ ions have only a very short lifetime (1); (ii) in the experiments as shown by Fig. 1, there was no reduction of ClO_4^-, (hence there were no Ga^+ ions (2), although a reaction similar to [5] could also proceed), and (iii) it was shown by James and Stoner (5) that in the case of Zn-amalgam only Zn^{2+} ions were formed during anodic dissolution. This might be also true with gallium (no expulsion of lower valency Ga ions).

The Trivalency of Ga Ions from Coulometric Measurements

As Ga electrodes are difficult to handle and may easily melt (melting point 29.8°C), another arrangement than described previously (5) was used for the coulometric proof of trivalency of Ga ions expelled by gallium amalgam. Figure 2 explains the method. A precisely weighed piece of Ga (about 0.015-0.028g) was dropped into mercury held in the beaker and covered with an acidic solution as

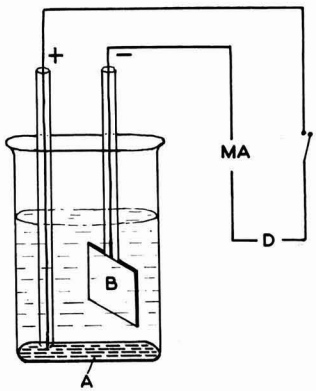

Fig. 2. Number of coulombs delivered by a certain amount of Ga: A, Ga-amalgam; B, platinized Pt electrode; MA, precise milliammeter; D, variable resistance.

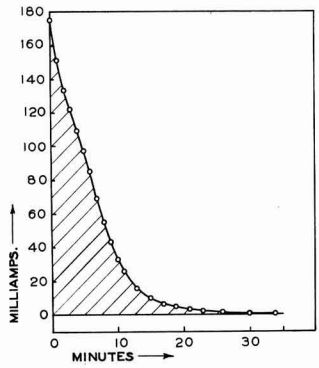

Fig. 3. Current delivered by the cell, Fig. 2, *vs.* time. Acid 0.5*N* $HClO_4$; shaded area: 69.5 amp sec (coulombs) = 0.0167g Ga.

shown in Fig. 2. Then a connection was made with the platinum electrode through a milliammeter. Immediately Ga went into solution and hydrogen was developed on the Pt cathode. The amount of current was plotted against the time as shown in Fig. 3. The experiment was continued until the current dropped to zero on the milliammeter. The milliampere minutes were determined from the shaded area of Fig. 3 by three methods: by weighing the paper of the shaded area, by direct counting of the square millimeters of that area, and by a planimeter. All three methods gave results in good agreement with each other. Then the milliampere-minutes were converted into coulombs and the amount of Ga present in the mercury was calculated assuming trivalency of Ga-ions (Eq. [3]). The results are summarized in Table II. This table shows clearly that Ga is going into solution solely as a trivalent ion. If the output values are slightly lower than the amount of Ga weighed in, then the difference is easily explained: slight formation of H_2-bubbles

Table II. Check of trivalency of Ga ions going anodically into solution from Ga amalgam

Acid	Input of Ga, g	Coulombs drawn	Output of Ga, g	Diff. Δ in %
1.8*N* H_2SO_4	0.0082	33.8	0.0081	−1.2
1.8*N* H_2SO_4	0.0170	69.4	0.0167	−1.7
1.8*N* H_2SO_4	0.0296	119.0	0.0287	−3.4
1.8*N* H_2SO_4	0.0156	63.7	0.0153	−1.9
1.8*N* H_2SO_4	0.0194	80.8	0.0194	0
				Δ = −1.6
0.9*N* H_2SO_4	0.0169	70.5	0.0169	0
0.9*N* H_2SO_4	0.0284	115.0	0.0278	−2.1
0.9*N* H_2SO_4	0.0093	37.6	0.0091	−2.1
				Δ = −1.4
0.45*N* H_2SO_4	0.0154	62.1	0.0149	−3.2
0.45*N* H_2SO_4	0.0176	70.4	0.0169	−4.0
0.45*N* H_2SO_4	0.0131	53.0	0.0128	−2.3
				Δ = −3.2
0.5*N* $HClO_4$	0.0137	57.6	0.0138	+0.7
0.5*N* $HClO_4$	0.0091	36.0	0.0087	−2.2
0.5*N* $HClO_4$	0.0207	86.5	0.0208	+0.5
0.5*N* $HClO_4$	0.0166	69.5	0.0167	+0.6
0.5*N* $HClO_4$	0.0206	84.0	0.0203	−1.4
				Δ = −0.3

was observed on the surface of the amalgam, except in perchloric acid, and some oxidation might also have occurred, as the work was done in presence of air. Thus, very slight amounts of Ga went into solution outside the circuit shown in Fig. 2. Besides, the differences obtained are nearly always within the limits of error.

Finally there is no reason to assume that Ga from a compact piece would go differently into solution, *e.g.*, with a lower than 3 valency, as compared with the amalgam.

In order to check the correctness of the quantitative determination of active metals dissolved in mercury by the coulometric method (Fig. 2 and Table II), experiments with zinc were made: the differences between the input and output values were even smaller, they rarely exceeded 0.5%.

Disintegration of Gallium

If gallium goes into solution in acids solely as a trivalent ion, then why, using compact Ga as an anode, is more Ga dissolved than calculated from Faraday's law (1, 2)? The answer is a simple one: partial disintegration of the anode into very fine particles (6-10). Weight loss is caused not only because of faradaic current, but also because of the dropout of single Ga particles (11). If all the weight loss is attributed to the faradaic current, a lower calculated valency than 3 for the Ga ions going into solution follows automatically.

The partial disintegration of Ga anodes while the current was flowing was proved as follows: a Ga anode was made by pressing metallic Ga into a hole drilled in Plexiglass and having a Pt lead (Fig. 4). The anode was cooled down and immersed in cooled H_2SO_4. As soon as the circuit was closed a stream of grayish particles (sometimes interrupted by grayish flakes) started to drop from the anode to the bottom of the beaker. The particles were decanted with distilled water, dried, and observed under the microscope. Under high magnification (oil immersion) aggregates of very small particles could be seen. They were metallic because of their metallic luster (see Fig. 5). The particles were not held together by a surface oxide film as in the

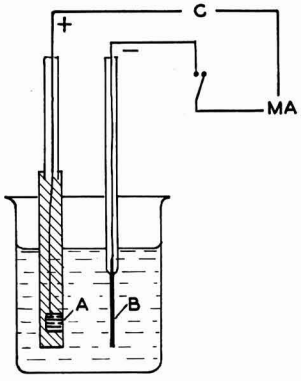

Fig. 4. Arrangement for observation of disintegration of a Ga anode A; B, cathode of Pt; electrolyte-0.5*N* H_2SO_4; current density 850 ma cm^{-2}; C, battery; MA, milliammeter.

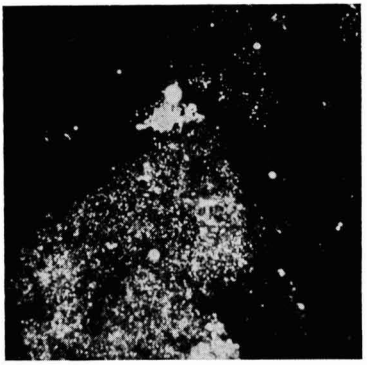

Fig. 5. Metallic Ga particles formed because of the partial disintegration of the Ga anode. Conditions: see Fig. 4. Magnification 1430X.

case of Mg (9, 10); they appeared separately, but easily stuck together to form particle aggregates. The diameter of the smallest visible particles was below 7×10^{-5} mm in diameter. If the anodic dissolution was performed without cooling, Ga spheres could frequently be observed. They were recognized by their larger size, spherical shape, and high metallic luster. X-ray pictures of the particles were not taken, because there was no doubt as to their metallic nature.

Discussion and Conclusions

Tables I and II show that 3-valent Ga-ions are produced in acidic solutions and that Ga-ions from Ga-amalgam go into solution as trivalent ions. Furthermore, there is no reason to assume that Ga-ions from a compact piece of the metal will be expelled with a charge lower than 3. While the metal is dissolving, it undergoes a partial disintegration into fine and very fine particles. This, of course, causes a deviation from Faraday's law, if the metal is dissolved anodically. The metallic particles, having a large specific surface, and an active potential (12) may act in the presence of oxidizers as reducers directly or through the active hydrogen developed on their surface. Thus, the ClO_4^- ion may be partially reduced to Cl^- (Eq. [2]). In the experiments of Fig. 1 (also Table I) no Cl^- ions could be found after the completion of the dissolution process, because the hydrogen was developed on the platinized Pt electrode which has a low hydrogen overpotential, inefficient in reduction processes, as molecular hydrogen is produced.

Disintegration of Ga anodes was observed at high current densities. There still may be a question as to whether disintegration also occurs at low current densities. This should happen because of the following reasons: an anode is rarely attacked evenly throughout, especially at low current densities; it will go into solution, as frequently observed, at preferential places (formation of etch pits) and, therefore, at high local current densities. Thus, if disintegration occurs, it will occur at these places. So it may be assumed that disintegration is to a certain degree proportional to the current density.

There is still a possibility that the 3 electrons of each Ga atom going into solution might not be released simultaneously but successively on the surface of the metal or of the amalgam. However, at present we have no experimental means to investigate this possibility. The question as to whether a Ga^+ is formed first and then immediately the Ga^{3+} by further release of two electrons, is therefore, useless.

Acknowledgment

We are grateful to the Office of Naval Research for financial support, to Dr. W. J. James, Professor of Physical Chemistry at the School of Mines and Metallurgy, for discussion, and to Mr. R. L. Martin for making the coulometric measurements.

Manuscript received Oct. 24, 1963. Revised manuscript received Dec. 16, 1963. This paper was presented at the New York Meeting, Sept. 29-Oct. 3, 1963.

Any discussion of this paper will appear in a Discussion Section to be published in the June 1965 JOURNAL.

REFERENCES

1. A. W. Davidson and F. Jirik, *J. Am. Chem. Soc.*, **72**, 1700 (1950).
2. K. Schug and A. Sadowski, *ibid.*, **83**, 3538 (1961).
3. E. S. Gilfillan, Jr. and H. E. Bent, *ibid.*, **56**, 1663 (1934). See also J. H. Hildebrand, "Regular Solutions," Prentice Hall, New York (1962).
4. G. Geffcken, *Z. physik. Chem.*, **49**, 257 (1904).
5. W. J. James and G. E. Stoner, *J. Am. Chem. Soc.*, **85**, 1354 (1963).
6. B. Roald and M. A. Streicher, *This Journal*, **97**, 283, 287, 288 (1950).
7. M. E. Straumanis and D. L. Mathis, *J. Less-Comm. Met.*, **4**, 213 (1962).
8. M. E. Straumanis and D. L. Mathis, *This Journal*, **109**, 434 (1962).
9. M. E. Straumanis and B. K. Bhatia, *Metall.*, **16**, 535 (1962).
10. M. E. Straumanis and B. K. Bhatia, *This Journal*, **110**, 357 (1963).
11. G. A. Marsh and E. Schaschl, *ibid.*, **107**, 960 (1960).
12. O. Stelling, *Z. Elektrochem.*, **41**, 712 (1935).

Distributed Network Analysis of Porous Electrode Capacitors

Jean Vergnolle

Centre de Recherches Techniques de la C.S.F., Paris, France

ABSTRACT

Assuming parameters distributed in a homogeneous anode of planar or cylindrical type, equations are given from which, with the aid of an analog computer, expressions are derived for equivalent series capacitance C, resistance (ESR) R, and for loss factor. Results are presented as families of curves, with the loss angle of the dielectric as a parameter, showing the decrease of C and R with frequency. The cathode has also a determinant influence on the characteristics.

In most capacitors with localized constants and relatively simple geometry, the equivalent impedance is easily determined. Electrolytic capacitors are a class apart, especially those in which the anode is a porous sintered mass with a useful area of a few tenths square meter per cubic centimeter. Such capacitors have a capacitance distributed inside the porous mass; the useful area has been coated with a very thin skin of dielectric, and the over-all capacitance results from the integration of the extremely small capacitances of the elementary areas facing the conducting material which impregnates the anode. A characteristic common to all capacitors of this type is the decrease of the apparent capacitance with frequency as well as the increase of the loss angle that may reach and even exceed $\pi/4$. Before attempting any calculation, it will be realized that the current, which passes between the porous metal and the conducting material filling its pores, by capacity effect, generates an energy in the dielectric skin by dielectric losses, as well as in the conducting material by the Joule effect; these phenomena determine the loss factor. At the higher frequencies, the resistance in the pores is shunted by the surrounding capacitance of the elementary capacitors; the effect of this low-pass filter is to prevent the current from entering the anode, resulting in a drop of the over-all capacitance, which tends to become localized near the external surface of the anode (*cf.* Fig. 1 and 2).

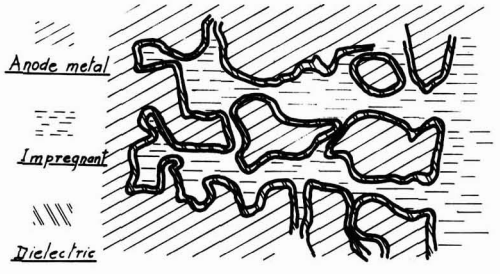

Fig. 1. Artist's conception of a cross section through a porous anode (current lines contained in the figure plane).

Fig. 2. Equivalent electrical network

Calculations will be made of the apparent capacitance and ESR, as well as the loss factor of the capacitors, taking into consideration characteristic parameters whose nature and number have been suggested by experimental data and by reasoning.

After examination of the complex anode impedance, the cathode (1) will be considered briefly, permitting an evaluation of the over-all impedance of a porous electrode capacitor.

Setting up the Anode Equations (2, 3)

We shall consider a porous anode as a homogeneous medium at the scale of the apparent dimensions with distributed capacitance, which will henceforth be referred to as nominal or specific capacitance, expressed in farads per cubic centimeter. The anode core is the porous metal mass relatively infinitely conducting: the cathode system is the impregnant, characterized by its finite conductivity χ that appears in the pores, multiplied by a factor p related to the state of division of the medium. The nominal capacitance per unit volume will be designated by K. Assuming an apparent intrinsic loss factor δ of the dielectric due, as will be seen later, partially to its nature and partially to an ESR distributed between the impregnant and the insulating skin itself, K will be a complex quantity given by

$$K = K_0(1-j\delta)\,(1+\delta^2)^{-1} \simeq K_0(1-j\delta) \qquad [1]$$

if δ is small enough; K_0 decreases slowly with angular frequency following an approximate law

$$K_0 = K_1\,\omega^{-2\delta/\pi} \qquad [2]$$

that is not the author's subject, and thus will not be discussed (4, 5).

Let us consider (*cf.* Fig. 3) a certain "current tube" whose shape is related to the macroscopic anode geometry, and in this tube an elementary volume dV between two equipotential surfaces, marked off by their abscissae x and $x+dx$ taken along a current line. The nominal capacitance of dV is

$$dC_1 = (\partial C_1/\partial x)\,dx = K\,dV = K(\partial V/\partial x)\,dx \qquad [3]$$

and the resistance between the two surfaces (in the impregnant)

$$dR_1 = (\partial R_1/\partial x)\,dx = (dx/p\chi)\,(\partial V/\partial x)^{-1} \qquad [4]$$

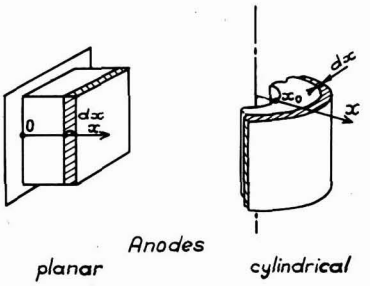

Fig. 3. Principal anodes structures investigated by using the corresponding dependence of $\partial V/\partial x$ on x.

Let $Z(x) = R(x) - j/\omega C(x)$ be the impedance between the anode and the plane $x > x_o$ in the case that no current would flow beyond this plane in the anode core, i.e., considering x as the outer surface of the porous anode. When increasing the thickness by dx, the impedance of the new structure becomes $Z + dZ$, where

$$(Z + dZ)^{-1} = (Z + dR_1)^{-1} + j\omega dC_1$$

from which

$$dZ = dR_1 - jZ^2\omega dC_1 \qquad [5]$$

$$\left\{ \begin{array}{l} dR = dR_1 - 2(R/C)dC_1 \qquad [6] \\ d(1/C\omega) = \omega(R^2 - 1/C^2\omega^2)dC_1 \qquad [7] \end{array} \right.$$

This is where the macroscopic geometry of the anode comes in; it decides the shape of the current tubes and the expression for $\partial V/\partial x$. Two main structures are met with in practice: the so-called "planar" one in which the current lines are normal to a reference equipotential plane, and the so-called "cylindrical" one in which these lines are normal to a reference equipotential cylinder; the latter is by far the most common type. For planar anodes and a tube of unit section; $\partial V/\partial x = 1$; for cylindrical anodes and a "tube" contained between two cross-sectional planes one unit apart, $\partial V/\partial x = 2\pi x$. Taking into consideration the basic equations [3] and [4], the system [6] and [7] becomes, for planar types

$$\left\{ \begin{array}{l} dR/dx = 1/p\chi - 2KR/C \qquad [8] \\ dC/dx = (1 - R^2C^2\omega^2)K \qquad [9] \end{array} \right.$$

$$x_o = 0$$

and for cylindrical types

$$\left\{ \begin{array}{l} dR/dx = (2\pi p\chi x)^{-1} - 4\pi KxR/C \qquad [10] \\ dC/dx = (1 - R^2C^2\omega^2)2\pi Kx \qquad [11] \end{array} \right.$$

$$x_o \geqslant 0$$

When $x \to x_o$, *i.e.*, when the porous material layer tends to be infinitely thin, ESR tends to zero, like capacitance, the over-all loss factor of the anode remaining. The variable will be normed using

$$\mathcal{X} = K\omega x^2/2p\chi \qquad [12]$$

Combined with an appropriate norm for R and C, a set of differential equations is obtained from [8] and [9] (or [10] and [11]) which contains only one independent variable $\mathcal{X}$ including both size dependence, x, and frequency dependence, ω. An appropriate norm for R and C is obtained when dividing by the limiting values for $\mathcal{X} \to 0$, *i.e.*, by the "initial values" C_i and R_i. One has, for planar types

$$C_i = Kx, \quad R_i = x/3p\chi \qquad [13]\ [14]$$

for cylindrical types

$$C_i = \pi Kx^2\mathcal{G}, \quad R_i = \mathcal{R}/4\pi p\chi \qquad [15]\ [16]$$

with the auxiliary functions of the ratio ρ (cf. Fig. 4 and 5)

$$\mathcal{G} = 1 - 1/\rho^2 \qquad [17]$$

$$\mathcal{R} = \tfrac{1}{2} - (\rho^2 - 1)^{-1} + 2\,\mathrm{Ln}\,\rho(\rho^2 - 1)^{-2} \qquad [18]$$

The normed values of C and R are

$$\mathcal{Y}_C = C/Kx, \quad \mathcal{Y}_R = 3p\chi R/x \qquad [19]\ [20]$$

for planar types and

$$\mathcal{Y}_C = C/\pi Kx^2\mathcal{G}, \quad \mathcal{Y}_R = 4\pi p\chi R/\mathcal{R} \qquad [21]\ [22]$$

for cylindrical types. It is remarkable that ESR of the cylindrical anodes remains constant, whatever be $\mathcal{X}$ (low), either the radius x or the frequency ω be low; on the other hand, x remaining constant, when $\rho \to 1$, capacitance and ESR of the thin layer are given by the simplified formulas

$$C_i = 2\pi Kx^2(\rho - 1) \qquad [23]$$

$$R_i = (\rho - 1)/6\pi p\chi \qquad [24]$$

and when $\rho = \infty$ (no solid central core)

$$C_i = \pi Kx^2 \qquad [25]$$

$$R_i = 1/8\pi p\chi \qquad [26]$$

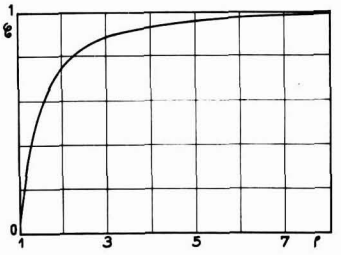

Fig. 4. Auxiliary function $\mathcal{G}(\rho)$

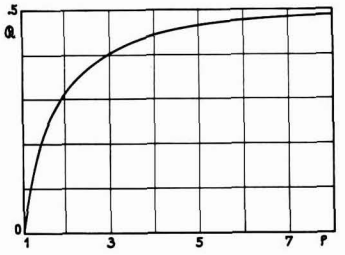

Fig. 5. Auxiliary function $\mathcal{R}(\rho)$

Invariant Curves for Anodes

Although mathematical solutions may be derived for the above differential systems, the author pre-

ferred using an ANALAC analog computer which gave invariant curves ($\mathcal{Y}$, $\mathcal{X}$) and whose interest becomes evident in the case of cylindrical anodes for which mathematics yield very complicated functions of Bessel's functions. Logarithmic coordinates are extensively and advantageously employed for these kinds of problems, and we shall now examine asymptotic solutions for $\mathcal{X} \to 0$ and $\mathcal{X} \to \infty$.

For planar types, like $Z = R - j/C\omega$

$$F = 6p_\chi Z/x = 2\mathcal{Y}_R - 3j/\mathcal{X}\mathcal{Y}_C \qquad [27]$$

with

$$\mathcal{X} = K_o\omega x^2(1 - j\delta)/2p_\chi(1 + \delta^2) = \mathcal{X}'(1 - j\delta)/(1 + \delta^2) \qquad [28]$$

For small values of $\mathcal{X}$ ("initial range"), $\mathcal{Y}_C = \mathcal{Y}_R = 1$.

$$F = 2 - 3j/\mathcal{X} = 2\mathcal{Y}_R' - 3j/\mathcal{X}\mathcal{Y}_C' = 2 + 3\delta/\mathcal{X}' - 3j/\mathcal{X}'$$

ESR is represented by

$$\mathcal{Y}_R' = 1 + 3\delta/2\mathcal{X}' \qquad [29]$$

and capacitance by

$$\mathcal{Y}_C' = 1 \qquad [30]$$

$$\tan\Delta = RC\omega = (2/3)\mathcal{X}'\mathcal{Y}_R'\mathcal{Y}_C' = 2\mathcal{X}'/3 + \delta \qquad [31]$$

In this range, capacitance is constant, ESR decreases like $\mathcal{X}'^{-1}$, while loss factor increases linearly with $\mathcal{X}'$ from its initial value δ.

For high values of $\mathcal{X}'$ ("extreme range")

$$\mathcal{Y}_R = 3/2\sqrt{\mathcal{X}}, \qquad \mathcal{Y}_C = 1/\sqrt{\mathcal{X}} \qquad [32]\ [33]$$

$$F = 3(1 - j)[(1 + \delta^2)(1 - j\delta)\mathcal{X}']^{-1/2} \qquad [34]$$

Putting

$$T_\delta = [(1 + \delta^2)^{1/2} + \delta]^{1/2} \qquad [35]$$

then

$$F = 3(T_\delta - j/T_\delta)/\sqrt{\mathcal{X}'} \qquad [36]$$

Whence

$$\mathcal{Y}_R' = 3T_\delta/2\sqrt{\mathcal{X}'}, \quad \mathcal{Y}_C' = T_\delta/\sqrt{\mathcal{X}'} \qquad [37]\ [38]$$

$$\tan\Delta = T_\delta^2 \qquad [39]$$

Those formulas become, when δ is very small

$$T_\delta \simeq 1 + \delta/2 \qquad [40]$$

$$\mathcal{Y}_R' = 3(1 + \delta/2)/2\sqrt{\mathcal{X}'}, \quad \mathcal{Y}_C' = (1 + \delta/2)/\sqrt{\mathcal{X}'} \qquad [41]\ [42]$$

$$\tan\Delta = 1 + \delta \qquad [43]$$

The "capacitance critical point" is important in practice, and defined, equating $\mathcal{Y}_C'$ values derived from Eq. [30] and [38]

$$\mathcal{X}_C' = T_\delta^2 \qquad [44]$$

Similarly, "ESR critical point" might be defined equating $\mathcal{Y}_R'$ values derived from Eq. [29] and [37]. It is significant only when δ is negligible, then

$$\mathcal{X}_R' = 9T_\delta^2/4 \simeq 9(1 + \delta)/4 \qquad [45]$$

For cylindrical types, like $Z = R - j/C\omega$

$$F = 4\pi p_\chi Z = \mathcal{R}\mathcal{Y}_R - 2j/\mathcal{G}\mathcal{X}\mathcal{Y}_C = \mathcal{R}\mathcal{Y}_R' - 2j/\mathcal{G}\mathcal{X}'\mathcal{Y}_C' \qquad [46]$$

For low values of $\mathcal{X}$, following the same computation process,

$$\mathcal{Y}_R' = 1 + 2\delta/\mathcal{G}\mathcal{R}\mathcal{X}', \quad \mathcal{Y}_C' = 1 \qquad [47]\ [48]$$

$$\tan\Delta = (1/2)(\mathcal{R}\mathcal{G}\mathcal{X}'\mathcal{Y}_R'\mathcal{Y}_C') = \mathcal{R}\mathcal{G}\mathcal{X}'/2 + \delta \qquad [49]$$

For high values of $\mathcal{X}$, where

$$\mathcal{Y}_R = 1/\mathcal{R}\sqrt{\mathcal{X}}, \qquad \mathcal{Y}_C = 2/\mathcal{G}\sqrt{\mathcal{X}} \qquad [50]\ [51]$$

$$\mathcal{Y}_R' = T_\delta/\mathcal{R}\sqrt{\mathcal{X}'}, \qquad \mathcal{Y}_C' = 2T_\delta/\mathcal{G}\sqrt{\mathcal{X}'} \qquad [52]\ [53]$$

$$\tan\Delta = T_\delta^2 \qquad [54]$$

The capacitance critical point is defined by

$$\mathcal{X}' = 4T_\delta^2/\mathcal{G}^2 \qquad [55]$$

Figures 6, 7, and 8 show the three invariant families of curves, depending on the parameter δ. for planar anodes. Figures 9, 10, and 11 are drawn as regards cylindrical types with $\rho = 8$ (as an example).

These curves represent variation of R, C, and tan Δ with frequency ω, this variable being directly proportional to $\mathcal{X}'$, following Eq. [28]. The critical point is characterized by the "critical frequency" ω_C, which is an upper practical limit for utilization of the anode; above a frequency approximately 5 ω_C, capacitance and ESR decrease like $\omega^{-1/2}$. For planar types, $\mathcal{X}'$ is simply the ratio $\omega/(\omega_C)_o$, and for cylin-

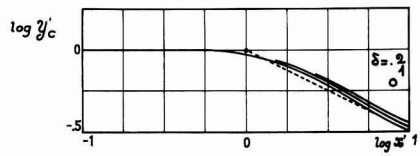

Fig. 6. Invariant family of curves (log $\mathcal{Y}_C'$, log $\mathcal{X}'$) for planar anodes (δ as the parameter) (extreme asymptote in dotted line).

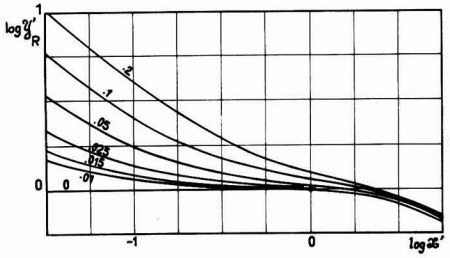

Fig. 7. Invariant family of curves (log $\mathcal{Y}_R'$, log $\mathcal{X}'$) for planar anodes (δ as the parameter).

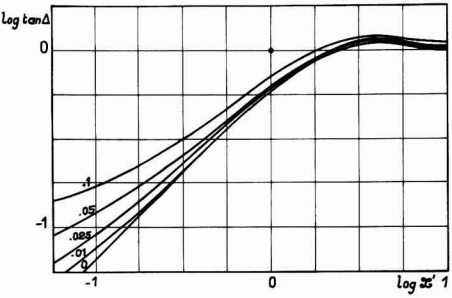

Fig. 8. Invariant family of curves (log tan Δ, log $\mathcal{X}'$) for planar anodes (δ as the parameter).

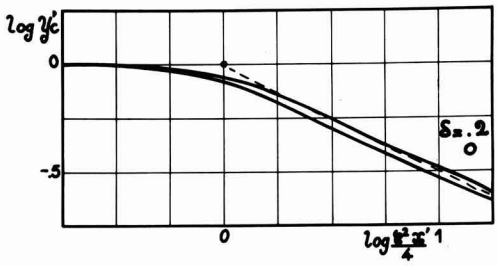

Fig. 9. Invariant family of curves (log $Y_{C'}$, log X') for cylindrical anodes (δ as the parameter) ($\rho = 8$) (extreme asymptote in dotted line).

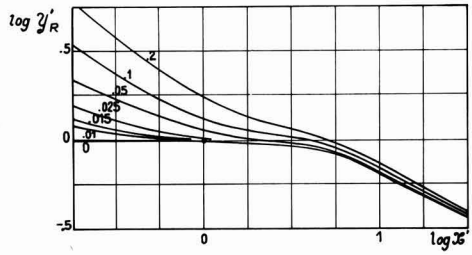

Fig. 10. Invariant family of curves (log $Y_{R'}$, log X') for cylindrical anodes (δ as the parameter) ($\rho = 8$).

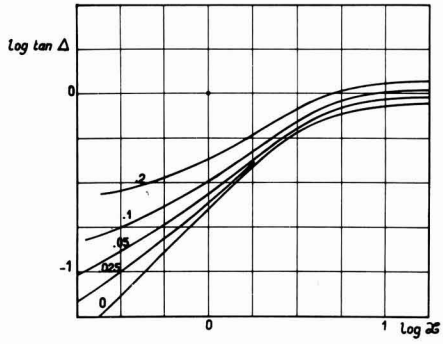

Fig. 11. Invariant family of curves (log tan Δ, log X') for cylindrical anodes (δ as the parameter) ($\rho = 8$).

drical ones, it is similarly $(4/\mathcal{G}^2)[\omega/(\omega_C)_o]$, $(\omega_C)_o$ being the critical frequency for a nil δ. Experimentally one may observe a slope of the curve (LnC, Lnω) different from zero in the initial range, and higher than 0.5 in the extreme one, depending on Eq. [2], or possibly, another physical law.

Theoretical Comparison of Planar and Cylindrical Anodes

Before making any further assumptions it seems worthwhile comparing planar and cylindrical anodes with results already obtained; this comparison will make sense when made in respect to two anodes with the same useful volume and the same limit capacitance. Having first used anodes of unit cross section or unit length, it will now be necessary to take into consideration the area of cross section a or length l of the cylinder; the initial capacitances are then respectively Kax_p and $\pi Kx_c^2 l\mathcal{G}$, the indices p and c being applied to the values of x to distinguish the thickness x_p from the external radius x_c, *i.e.*

$$\pi x_c^2 l\mathcal{G} = ax_p \qquad [56]$$

Further on these indices will designate the magnitudes relative to the anodes of each of the two types. A new assumption will be added, *i.e.*, the equality of the loss factors δ.

Under these conditions, the series resistances in the initial range, essentially laid down by δ, are necessarily the same. If δ is small, there is an intermediate range where $R \simeq (R_i)_o$, and where

$$R_p/R_c \simeq (\mathcal{G}/3\mathcal{R})(2\pi x_c l/a)^2 = 4x_p^2/3\mathcal{G}\mathcal{R}x_c^2 \qquad [57]$$

(throughout this range, the capacitances are still equal and constant). The ratio

$$(\omega_{cp})_o/(\omega_{cc})_o = (\mathcal{G}x_c/2x_p)^2 = \mathcal{G}a/4\pi x_p l = (a/2\pi x_c l)^2 \qquad [58]$$

compares practical upper utilization limits.

In the "extreme range," where only the apparent external areas come are considered, the following equation is valid for all values of δ.

$$R_p/R_c = C_c/C_p = 2\pi x_c l/a = 2x_p/\mathcal{G}x_c = 2(\pi l x_p/\mathcal{G}a)^{1/2} \qquad [59]$$

Applications with Supplementary Hypothesis

The expressions derived for the equivalent series resistance and capacitance contain the parameter δ, which may be a function of frequency; it consists of an inherent, quasi frequency independent value δ_1 of the dielectric (and of the interface dielectric-impregnant) and of a frequency dependent loss arising from the series resistance of the impregnant in pores extending essentially perpendicular to the direction x; thus

$$\delta = \delta_1 + \omega K_o/\alpha\chi = \delta_1 + 2p\mathcal{X}'/\alpha^2 = \delta_1 + 2p\mathcal{X}'/q \qquad [60]$$

q (or α) is a new auxiliary parameter; q is dimensionless like p. A more thorough analysis of the effects would take into account the fact that, strictly, the new series resistance is depth dependent and thus frequency dependent; but we shall assume the critical frequencies of the narrowest pores are pushed back beyond the usual frequencies.

We shall now show how to utilize the computations and families of curves given in the previous section, taking due account of the introduction of new parameters. Instead of being constant, δ is linearly increasing with X', according to Eq. [60]. And so, the invariant plots already made are still usable as charts for obtaining the new invariant curves ($Y_{C'}$, X'), ($Y_{R'}$, X'), and (tan Δ, X') arising from our additional assumptions. We shall suppose the new parameter q is always high enough to assure $\delta <<< 1$, whatever X' in a usual range, since values of δ_1 are lower than 1% for Ta_2O_5.

Simple calculations lead to the following results.
Plane anodes—Initial range

$$Y_{C'} = 1, Y_{R'} = 1 + 3p/q + 3\delta_1/2X' \qquad [61]\ [62]$$

$$\tan\Delta = \delta_1 + 2(1/3 + p/q)X' \qquad [63]$$

Extreme range

$$Y_{C'} = (1 + \delta_1/2)/\sqrt{X'} + p\sqrt{X}/q\,,$$

$$\mathcal{Y}_R' = 3/2[(1 + \delta_1/2)/\sqrt{\mathcal{X}'} + p\sqrt{\mathcal{X}'}/q] \quad [64]\ [65]$$

$$\tan \Delta = 1 + \delta_1 + 2p\mathcal{X}'/q \quad [66]$$

Cylindrical anodes—Initial range

$$\mathcal{Y}_C' = 1, \quad \mathcal{Y}_R' = 1 + 4p/G\mathcal{R}q + 2\delta_1/G\mathcal{R}\mathcal{X}' \quad [67]\ [68]$$

$$\tan \Delta = \delta_1 + (\mathcal{R}G/2 + 2p/q)\mathcal{X}' \quad [69]$$

Extreme range

$$\mathcal{Y}_C' = (1/G)[(2 + \delta_1)/\sqrt{\mathcal{X}'} + 2p\sqrt{\mathcal{X}'}/q,$$

$$\mathcal{Y}_R' = (1/\mathcal{R})[(1 + \delta_1/2)/\sqrt{\mathcal{X}'} + p\sqrt{\mathcal{X}'}/q] \quad [70]\ [71]$$

$$\tan \Delta = 1 + \delta_1 + 2p\mathcal{X}'/q \quad [72]$$

As a general rule, in the initial range, capacitance is not affected by δ variations, but tan Δ increases just a little more rapidly; in the extreme range, decreasing of capacitance is counter-balanced by an increasing term $(\sqrt{\mathcal{X}'})$, whereas tan Δ follows a linear growth. Loss factor depends mainly on the dielectric quality δ_1 at low frequencies, and on the anode porosity (p/q) at high frequencies (6).

Role of the Cathode

All the computations made so far have only introduced the impedance between an origin equipotential at the apparent external surface of the anode, but a conducting mass is necessarily inserted between the anode and the cathode: it is a layer of graphite, as in tantalum or niobium capacitors of the so-called "solid type," or a layer of electrolyte, as in those of the so-called "liquid" type. This layer, mainly in the latter case, introduces an additional resistance, r, which can be taken as fixed at all frequencies. The cathode is an electrode which is relatively comparable to the anode, with its own capacitance, resistance, and loss factor; these parameters vary in a highly complex manner with frequency if, in a liquid electrolyte, the cathode is porous, in order to increase its surface area and to lower its impedance. In all cases a porous cathode can be considered as a thin layer of a material with electrical parameters distributed throughout its mass and deposited on a support which constitutes the last equipotential surface to be considered. Physically, capacitance is shunted by a very low resistance, what is equivalent to a very high capacitance with an ESR, both varying with frequency. The equivalent electrical diagram of a complete capacitor is therefore as follows (Fig. 12).

We might try to extend to the electrolytic cathode the conclusions of our previous calculations. Roughly, the capacitance per unit smooth area Γ increases with the electrolyte concentration, and, at the high concentrations used in porous electrodes capacitors, it goes through a maximum when the voltage between the electrode and the solution is zero; it decreases with frequency at a negative power with an absolute value decreasing with higher concentration (about -0.1 to -0.3). For a-c voltages, the only ones we are concerned with, a polarization series resistance Π appears, as inversely proportional to frequency. Unfortunately, a comparative examination of the curves (Π,ω) and (Γ,ω)

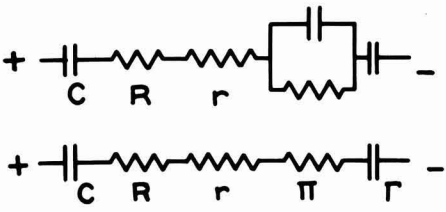

Fig. 12. Equivalent electrical diagrams of a complete capacitor

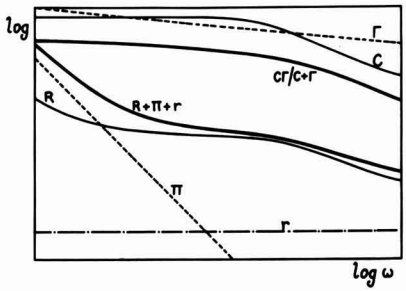

Fig. 13. Typical variations with ω of the different elements of the impedance of a liquid electrolyte capacitor with a smooth cathode.

relative to smooth cathodes with localized constants and to porous cathodes with distributed constants has so far failed to yield an explanation in terms of the criteria already adopted. In fact, for porous electrodes, Π and Γ decrease approximately like $\omega^{-1/3}$; coating a smooth silver cathode with a porous silver layer dipped in 40° Be sulfuric acid may divide Π by a factor of about 100 and multiply Γ by the same factor.

It is then easy to see the deteriorating effect of a smooth cathode with a capacitance of the same order of magnitude as C in the initial range: the resultant capacitance of the capacitor is halved. The cathode capacitance decreases whereas the anode capacitance hardly varies, so that the net capacitance decreases. These effects are illustrated in Fig. 13, drawn somewhat arbitrarily: in the extreme range it shows the over-all capacitance decreases more slowly than C; the over-all ESR is considerable regarding R in the initial range; the two resistances then tend to come together, but at very high frequencies the resistance r causes the curves to diverge. With the same assumptions, substituting a porous cathode for a smooth one brings about a gain of Γ such that the resultant capacitance is practically equal to C. The over-all ESR, shown in Fig. 14, is hardly higher than R in the initial range, but in the extreme range both curves are necessarily again divergent; whatever be the upper validity range of our hypothesis, at the higher frequencies, r then dominates and the over-all ESR is not dependent on the nature of the cathode.

Conclusion

Returning to an idea that arose during the first physical and technological investigations on porous anode tantalum capacitors, we have attempted, with the collaboration of the ANALAC Analog Computing Center, to explain the dynamic behavior of electro-

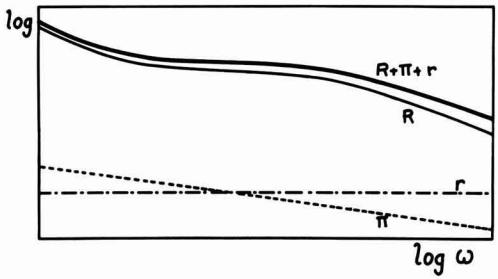

Fig. 14. Typical variations with ω of the different real elements of the impedance of a liquid electrolyte capacitor with a porous layer cathode.

lytic capacitors with liquid or solid semiconductor impregnant. We have tried to find the cause of observed variations of capacitance and loss factor with frequency and various characteristic parameters, more with regard to the "geometric" phenomena due to the low-pass filter action of porous anodes, than the deeper physical phenomena which affect the parameters themselves. We have shown how relatively simple families of curves allow the treatment of planar and cylindrical capacitors. These computations should assist in the interpretations of the experimental results. Using this tool and under light so projected, the author contemplates soon publishing as a whole experimental results as well on liquid electrolyte capacitors as on semiconductor ones; he preferred not to make heavy the present paper and to set aside the reported publication so as to show how study of an electric wave propagation through a porous anode permits to find again the theoretical preceding results.

Acknowledgment

For this work, done under contract MWDP F 61 MWP A 59, concerning general investigations on capacitors prepared by anodic oxidation and preferentially with a solid impregnant, we have enjoyed the aid of Dr. Kleefstra, who made experimental studies of the properties of electrolytic capacitors in the very low frequency range, and of Dr. Apter, who adapted the problem to the machine after the preliminary work of the late Dr. Ricou. Our sincere thanks are due to these engineers for the fundamental role they have played.

Manuscript received Dec. 4, 1962; revised manuscript received Nov. 1, 1963.

Any discussion of this paper will appear in a Discussion Section to be published in the June 1965 JOURNAL.

REFERENCES

1. N. Thien-chi and J. Vergnolle, *Onde Electrique*, **35**, 318 (1955).
2. P. Bourgault, A. C. Capacitance measurements of a porous electrode, Report for the Canadian Government.
3. J. S. Newman and C. W. Tobias, *This Journal*, **109**, 1183 (1962).
4. L. Young, "Anodic Oxide Films," Academic Press, London (1961).
5. J. Vergnolle and M. Kleefstra, C. R. (forthcoming paper).
6. D. A. McLean, *This Journal*, **108**, 48 (1961).

SYMBOLS

a	Cross-sectional area of a planar anode
l	Length of a cylindrical anode
x	Space coordinate (radial coordinate for cylindrical anode); also denoting space coordinate of outer position of porous anode
x_o	Space coordinate for solid anode core
ρ	x/x_o
$\mathcal{G}, \mathcal{R}$	Form factors for cylindrical anodes defined by Eq. [17] and [18] and represented in Fig. 4 and 5
$V(x)$	Volume within the surface, $x = \text{const.}$
$\partial C_1/\partial x$	Series equivalent capacitance per unit length of the porous anode
K	Complex equivalent series capacitance of the anode per unit volume
K_o	Real part of K
χ	Specific conductivity in the pores (impregnant conductivity)
$\partial R_1/\partial x$	Effective resistance per unit length of the pores
$p = \left(\frac{\partial R_1}{\partial x} \chi \frac{\partial V}{\partial x}\right)^{-1}$	A form factor characterizing porosity
δ	Effective loss factor of the dielectric
q	Another form factor characterizing porosity
T_δ	Function defined by Eq. [33]
δ_1	An intrinsic loss factor of the dielectric for the pore free case
$Z = R - j/C\omega$	Impedance between anode core x_o and external surface x
ω	Angular frequency
$\tan\Delta = RC\omega$	Apparent loss factor of an anode or of a whole capacitor
$\mathcal{X}$	A dimensionless coordinate combining position, frequency, specific capacitance, and conductivity defined by Eq. [12]
$\mathcal{X}'$	Real part of $\mathcal{X}$.[1]
R_i, C_i	Asymptotic values for R, C, for $\mathcal{X}' \to 0$ ("initial range")
R_∞, C_∞	Asymptotic values for R, C, for $\mathcal{X}' \to \infty$ ("extreme range")
$(R_i)_o$	Asymptotic value for R in the initial range for $\delta = 0$
$\mathcal{Y}_R = R/R_i$	A dimensionless coordinate, essentially representing R, and being a function of $\mathcal{X}$
$\mathcal{Y}_{R'}$	The same one, function of $\mathcal{X}'$, (real)[1]
$\mathcal{Y}_c = C/C_i$	A dimensionless coordinate, essentially representing C, and being a function of $\mathcal{X}$
$\mathcal{Y}_c'$	The same one, function of $\mathcal{X}'$, (real)[1]
$\mathcal{F}$	A dimensionless coordinate, essentially representing Z
$\mathcal{X}_{R'}, \mathcal{X}_{c'}$	Dimensionless abscissae at which $R_\infty = R_i$ and $C_\infty = C_i$, respectively (critical points)
ω_R, ω_c	Corresponding values of angular frequency (critical frequency)
r	Resistance of the structure outside of x (cathode-anode interval)
Γ	Cathode polarization equivalent series capacitance
Π	Cathode polarization equivalent series resistance

[1] *Note*: When considering capacitance as complex, or imperfect, we use $\mathcal{X}$ and $\mathcal{Y}$ coordinates; when considering it as perfect and incorporating its imaginary part in ESR, we use $\mathcal{X}'$ and $\mathcal{Y}'$ coordinates.

Growth of α-SiC Single Crystals from Chromium Solution

L. B. Griffiths and A. I. Mlavsky

Tyco Laboratories, Inc., Waltham, Massachusetts

ABSTRACT

The travelling solvent method of crystal growth has been successfully adapted to the growth of α-SiC single crystals, using pure chromium as the solvent. Since molten chromium does not wet chemically cleaned SiC in a uniform and reproducible manner, a prewetting procedure was developed which involves a heat treatment of the SiC at 1200°-1300°C *in vacua* at 10^{-9}-10^{-10} Torr, followed immediately by the evaporation of a thin (10^4Å) film of pure chromium onto the clean surfaces. The chromium solvent zones were passed under the influence of a temperature gradient in a simple r. f. furnace; the average specimen temperature was 1750°C. Subsequent metallographic and x-ray examination revealed that good crystal growth had occurred. Growth rates of the order of 0.75 mm hr^{-1} were obtained under the above conditions. p-n junctions prepared by deposition, from chromium solution, of one conductivity type onto the opposite type were assembled into diode structures. Junction capacitance varies with bias in accordance with a $V \propto 1/C^2$ law, indicating an abrupt (step) junction. The forward I-V characteristics are unique for SiC devices in that the forward voltage drop is 1.2-1.5v compared to 2-5v reported for previous diodes at comparable current densities. The slope of the forward biased characteristics was found to be $e/2.4kT$. Considerable leakage is observed (under reverse bias); the peak inverse voltage, which ranges from 6-15v, is much lower than expected from the resistivity of the bulk material. This low voltage breakdown is tentatively discussed in terms of a peculiar dislocation structure in the region of the p-n junction. The over-all rectifying properties of the devices prepared by TSM persist up to at least 540°C.

Silicon carbide, a highly refractory semiconductor, occurs in two major crystallographic modifications. The so-called high-temperature, α-modification has a hexagonal structure which is most conveniently described as a distorted wurtzite structure. Depending on the polytype, of which a great number exist, the energy gap (1-3) is 2.7-3.2 ev. The β (cubic) modification, which is usually formed below 2000°C, has an energy gap of 2.3 ev (3).

The combination of high energy gap and refractoriness [decomposition (4) occurs at *ca.* 2800°C] makes α-SiC potentially very useful for high-temperature semiconductor devices. However, device development has been hampered by the difficulties encountered in the preparation of high-quality single crystals and p-n junctions.

α-SiC p-n junctions have been prepared by growth from the vapor phase (5-7), by the standard semiconductor techniques of alloying and diffusion (8, 9), and during growth from solution (10). This paper describes an improved version of the latter technique, the travelling solvent method of crystal growth (TSM) (11, 12).

TSM is based both on the temperature gradient zone melting technique of Pfann (13) and also a variant thereof (14) in which an aluminum-rich zone is passed through silicon under the influence of a temperature gradient to yield a large area p-n junction. Hergenrother (10) applied a similar technique to the growth of α-SiC p-n junctions, using a chromium-rich solvent. Modifications and improvements of these techniques have been made in this laboratory for the crystal growth of compound semiconductors. In the particular case of SiC, stringent surface preparation of α-SiC insures uniform and ready wetting by the solvent and effects a considerable improvement in the basic technique.

Experimental

Principle of the method.—In the application of TSM, a temperature gradient is impressed across a thin solvent zone sandwiched between two pieces of the solid to be grown. Initially dissolution occurs at both solvent-solid interfaces. However, since the equilibrium solubility is greater at the hotter interface, a concentration gradient is established and solute diffuses across the liquid zone and precipitates onto the cooler seed crystal. The process may therefore be divided into several stages, *i.e.,* wetting of the solid by the solvent; dissolution at both interfaces; establishment of the concentration gradient; and finally precipitation of the solute on the seed crystal. Irrespective of which stage is rate determining, there is theoretically no dependence of the growth rate on the zone thickness. The driving force for passage of the solvent zone is provided solely by the concentration gradient which is a function of both the temperature gradient and also the slope of the liquidus at the particular temperature (average zone temperature) of growth.

Selection of a suitable solvent is based on the criteria that it should readily wet the solid in question, and exhibit increasing equilibrium solute content with increasing temperature, *i.e.,* the slope of the liquidus in the particular system should be positive. The solvent should preferably have a lower melting point than that of the solute, exhibit low vapor pressure at the temperature of growth, and

possess negligible solid solubility. The final feature is desirable from the viewpoint of the physical properties of the final crystal and is particularly significant for semiconductors.

Practical considerations.—TSM depends on a difference in solubility at the hot and cool solid-liquid interfaces. In principle, therefore, any alloy system exhibiting a liquidus of positive slope should favor zone movement. The liquidus slope ds/dT is given by:

$$\frac{ds}{dT} = \frac{F}{D \cdot \frac{dT}{dx}}$$

where F is the flux through the solvent zone, D the diffusion coefficient, and dT/dx the temperature gradient. If we consider an acceptable growth rate of 0.125 mm/hr, a liquid metal diffusion coefficient of 10^{-4} cm^2/sec, and a temperature gradient across the solvent zone of 10°C/mm, which is a reasonable estimate, then:

$$\frac{ds}{dT} = \frac{1.25 \times 3.2 \times 10^{-2}}{10^{-4} \times 3.6 \times 10^{3} \times 10^{2}} = 10^{-3}$$

i.e., expressing S as a percentage solubility, it is required that $ds/dT > 0.1$ at growth temperature.

The solvent zone must be sufficiently thick to provide stable interfaces with the solid over the entire contacting surfaces, while its maximum thickness is chosen to enable some solid material to be present always. The particular experimental arrangement used in the present work precluded the use of solvent zones thicker than 0.35 mm since both convection currents and r.f. stirring tended to destroy the temperature gradient in thicker zones.

The crystal growth experiments discussed in this paper were performed with chromium as the solvent. We have established a tentative constitutional diagram of the Cr-SiC alloy system in the region of interest (Fig. 1). The eutectic which occurs at about 1600°C is advantageous since it permits crystal growth well below the melting point of chromium. At the melting point, the vapor pressure of chromium is high and would cause serious experimental difficulties.

Silicon and platinum were initially used as solvents, but were discarded since the liquidus slopes in both systems are apparently too steep to provide growth rates of practical significance.

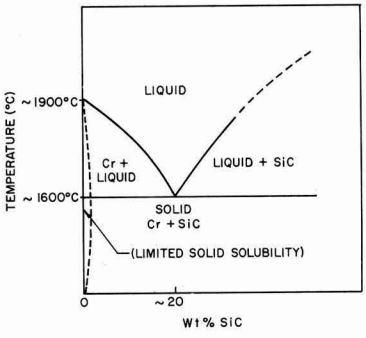

Fig. 1. Tentative constitutional diagram of chromium-rich end of Cr-SiC system.

Specimen preparation.—Initial efforts of crystal growth were hindered by difficulties encountered in the wetting of SiC surfaces with chromium. This resulted in erratic zone movement. Good wetting was achieved when the silicon carbide surfaces were cleaned by the following procedure. After the specimens were machined to a suitable size and shape, they were heated by electron bombardment to about 1300°C in a vacuum of 10^{-9} to 10^{-10} mm Hg. The immediate visual result of the vacuum heat treatment was a greatly enhanced reflectivity. A thin film of chromium was then evaporated from a heated tungsten filament onto the specimens in the same apparatus. All experiments were performed utilizing (0001) crystallographic surfaces. Good adhesion between the evaporated films and the silicon carbide surfaces was obtained, as indicated by the lack of blistering or peeling of the films when they were heated to 1300°C. The apparatus used in this phase of the work is shown in Fig. 2.

Crystal growth and p-n junction fabrication.—Pairs of chromium-coated specimens were assembled in "sandwiches," with chromium slices of 0.1-0.3 mm thick between the coated surfaces. This assembly was heated in an argon atmosphere, inside the apparatus shown in Fig. 3. The upper surface of the sandwich was cooled by natural radiation; the maximum specimen temperature observed with an optical pyrometer was about 1750°C. SiC specimens

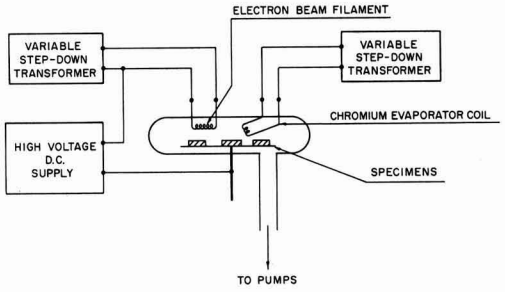

Fig. 2. Schematic of vacuum system with electron beam heating and chromium evaporation facilities.

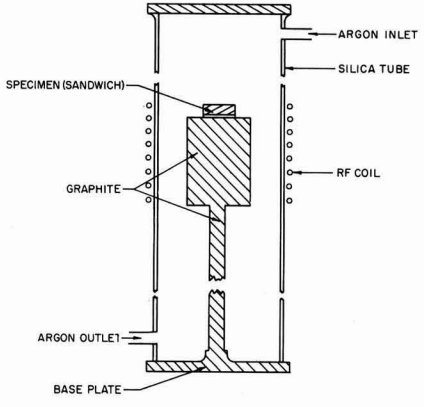

Fig. 3. Assembly for TSM crystal growth of SiC

Table I. Physical properties

Conductivity type	Hall coefficient, cm^3/coul	Resistivity, ohm-cm	Mobility, cm^2/volt-sec
p	57	9.0	6.3
n	2-35	0.4-4.0	83-107

of different thicknesses were used, and the time required for complete traverse of the chromium zone was recorded. The direction of growth was always in the "c" direction.

p-n junctions may be fabricated readily by TSM. The introduction of dopants into the solvent during crystal growth makes possible the deposition of either conductivity type. As a test of feasibility we took advantage of the fact that nitrogen is a strong n-type dopant in SiC and added a small quantity of N_2 to the argon atmosphere during growth of a p-type SiC crystal. The resultant crystal was subsequently examined metallographically.

Table I lists some physical properties of both p- and n-type SiC crystals obtained from Norton Company. The n-type material is green and transparent, while p-type is dark blue and also transparent. Using the procedures outlined above, p-type SiC has been deposited onto n-type seeds and *vice versa*. p-n junctions were thus fabricated using this partially characterized material without additional doping during crystal growth.

Contacting procedures.—Contacts of pure platinum were evaluated for use as ohmic contacts to p-n junctions. While exhibiting an excellent linear current-voltage relationship, they possessed very high resistances. Accordingly the use of platinum was discontinued.

An alloy of 99:1 Au-Ta doped with either aluminum or antimony was subsequently evaluated for contacting to p- and n-type material, respectively. Gold-tantalum alloys have been used both by Westinghouse Company (15) and also by Philips Research Laboratories (16). Tantalum additions aid in the wetting of gold to SiC. Quite excellent ohmic contacts were obtained when the alloy was heated in contact with the SiC in an r.f. furnace to 1150°C for a few minutes.

Results and Discussion

Figure 4a is a photomicrograph of a ground and polished crosssection through a typical SiC specimen after zone passing. The arrows indicate the initial position of the chromium layer; excellent regrowth is observed. Figures 4b and 4c, which show x-ray back reflection photographs of the seed and regrown material, respectively, demonstrate that true crystalline propagation of the seed has occurred. These results clearly demonstrate that the surface cleaning procedure is adequate to allow wetting of the SiC by the chromium. (There was no difficulty in wetting at Cr-Cr interfaces.) The high vacuum heat treatment was initially undertaken on the basis that a film of SiO_2 existed on the SiC and prevented wetting. Under high vacuum heating such a film would be removed by dissociation to SiO, which is volatile. Since the α-SiC structure consists of alternate layers of silicon and carbon atoms tetrahedrally bound to their neighbors, only one surface of a SiC crystal is likely to be coated with a continuous SiO_2 film; the opposite surface terminates in a layer of carbon atoms. This surface "polarity" may be observed readily by etching SiC platelets; distinct differences in surface structure become clearly apparent.

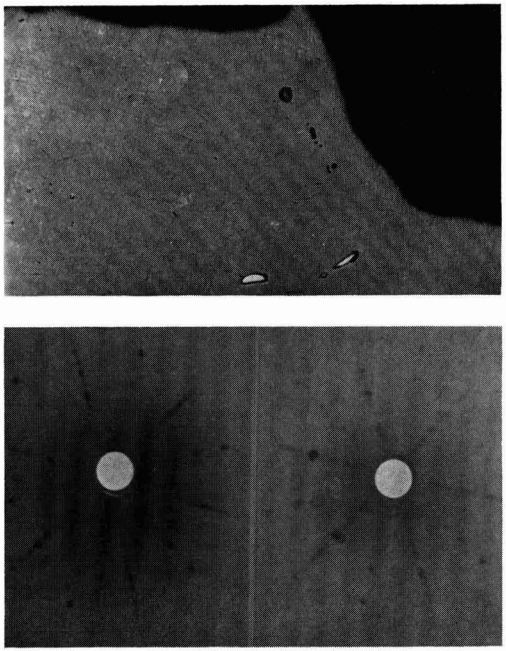

Fig. 4. Photomicrograph of cross section with corresponding x-ray patterns of TSM grown SiC crystal.

A second possibility is that adsorbed gas on the SiC prevents wetting. However, unless the particular species is strongly chemisorbed, it appears unlikely that it would prevent wetting by chromium. The exact nature of the interface between chromium and "untreated" SiC is therefore still unresolved.

Of considerable interest is the fact that α-SiC (hexagonal) may be grown from chromium-rich solution at temperatures well below the β/α "transition" temperature of about 2000°C. This so-called transition in SiC is not a true allotropic, solid-state transition. In general, experimental evidence has demonstrated that preparation of SiC at temperatures below about 2000°C produces the cubic modification while the hexagonal form results, usually from vapor phase growth, above 2000°C. The transition is not sharp, and a wide range of hexagonal polytypes may be produced. Thermal cycling through 2000°C does not cause a crystallographic-type change. It appears that in the presence of an α-SiC seed and the particular experimental conditions of TSM the hexagonal modification may be grown below 2000°C. From the measurements of the time taken for passage of chromium-rich solvent through various thicknesses of SiC a growth rate of ~ 0.75 mm/hr was deduced. Figure 5 summarizes the data

which refer to a specimen temperature of 1750°C.

Figure 6 shows a photomicrograph of a cross section through the crystal doped with nitrogen during growth. It is clear that the quite flat, uniform junctions may be prepared by TSM, although at present we must resort to over-compensation to influence conductivity type. The junction shown in Fig. 6 was delineated by electrolytic etching in hydrofluoric acid at room temperature for 30 sec.

Using material of the type referred to in Table I, several crystals of 10 mm diameter, 2-3 mm thick, and containing a single p-n junction have been prepared. A die cut from one such crystal is shown in Fig. 7. This specimen measures 3 x 3 x 2 mm. The darker colored p-type material remained transparent after the chromium solvent zone had passed through it.

Several dice were cut from the junction-bearing crystal and provided with Au-Ta ohmic contacts in the manner previously described. The junction areas of the finished experimental diode structures were about 5 mm². A typical oscilloscope trace of the room temperature voltage-current characteristics of silicon carbide diodes is shown in Fig. 8. Of particular interest is the forward characteristic in which turnover occurs at about 1.3v. This value is considerably lower than that previously observed in silicon carbide (17), but of the order expected for this material. Figure 9 illustrates the results obtained from point-by-point measurements in the forward direction. The forward characteristics may be represented by the empirical relationship

$$I = A \exp \frac{eV}{nkT} \qquad (1)$$

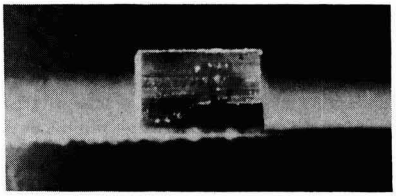

Fig. 7. View of die cut from typical TSM crystal. Magnification 8X.

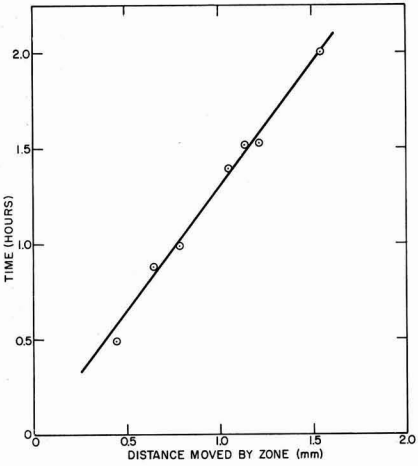

Fig. 5. Time-distance relationship for SiC crystal growth for chromium solution; temperature about 1750°C.

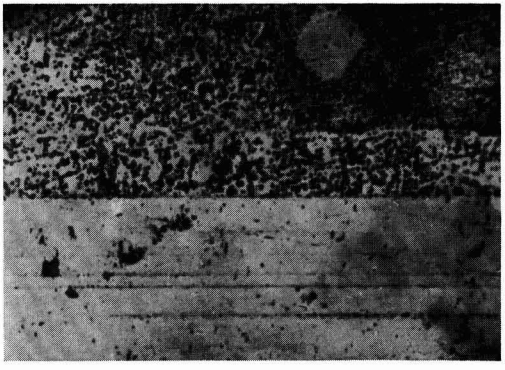

Fig. 6. Photomicrograph of cross section through SiC crystal showing junction produced by nitrogen doping during growth; electrolytically etched in HF solution. Magnification 250X.

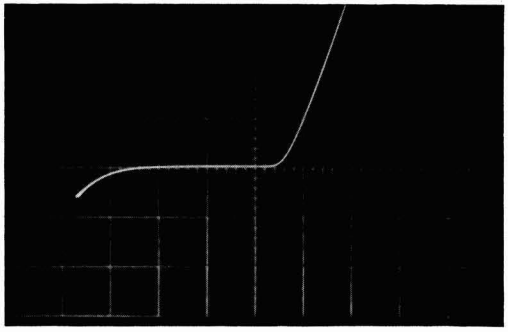

Fig. 8. Oscilloscope trace of room temperature characteristic of SiC p-n junction diode; vertical axis 5 ma/cm; horizontal axis 2 v/cm.

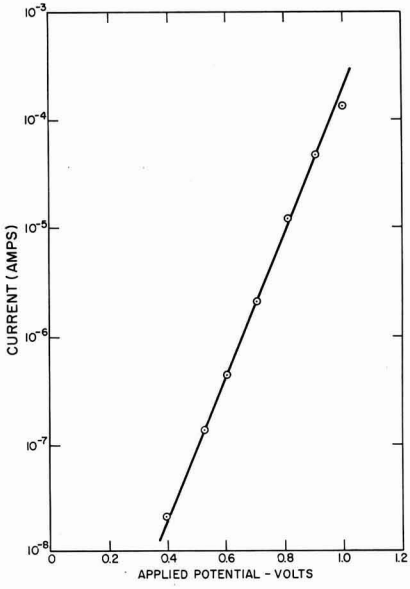

Fig. 9. Forward characteristic of SiC p-n junction diode

where V is the applied voltage, and A is the diffusion current. The quantity n is determined from the slope of the curve in Fig. 9 to be 2.4. Values of n of this order have been observed in silicon carbide diodes made from vapor grown junctions (2). Such high values may result from the relatively high impurity content of presently available material. To some extent, however, a high value of n reflects the nature of the junction, which in the case of SiC, frequently contains a thin semi-insulating region between the p and n sides. The physical extent of such a layer will be strongly influenced by the temperature of growth. In addition to affecting the value of n, the presence of a semi-insulating region will be reflected in the forward voltage drop. In fact, a contributory factor to the relatively low F.V.D. observed on many of our diodes (c.f., 1.3v) would appear to result from the temperature of crystal growth being several hundred degrees lower than that for vapor grown junctions.

Considerable information regarding the nature of p-n junctions is obtainable from the variation of junction capacitance with applied voltage. The theoretical dependence is given by the relation

$$C_v = \frac{C_o}{\left(1 - \frac{V}{\phi}\right)^x} \qquad [2]$$

where C_v is the junction capacitance at a bias voltage V. C_o is the junction capacitance at zero basis, ϕ is the "built-in" junction potential, and x is 1/2 for an abrupt junction and 1/3 for a diffuse junction. Very careful measurements on TSM-grown silicon carbide junctions, Fig. 10, have yielded the relationship:

$$V \propto \frac{1}{C^2} \qquad [3]$$

Extrapolation to infinite capacitance yields the value of ϕ which, in an ideal p-n junction, can be identified as that voltage which produces a flat band condition across the junction. The value of 2.1v shown in Fig. 10 is reasonable for α-SiC. For a simple p-n junction, ϕ cannot exceed the fundamental energy gap of the particular semiconductor, but, with the presence of a semi-insulating region between the p and n sides, Eq. [2] is inapplicable and ϕ has no real significance; extrapolation of $1/C^x$ *vs.* V plots yields voltages, corresponding to infinite capacitance which are very large and certainly greater than the band gap. This is understandable, since, in a true p-n junction structure, the capacitance is provided by the space charge region which varies with bias, whereas the capacitance of the semi-insulating region will be essentially independent of bias. Several diodes have exhibited large apparent values of ϕ. A detailed discussion of junction structure and properties in relation to growth parameters will be published elsewhere.

The temperature dependence of the diode characteristics is illustrated in Fig. 11, 12, and 13, which show oscilloscope traces for a typical junction at 30°, 320°, and 540°C, respectively. The forward

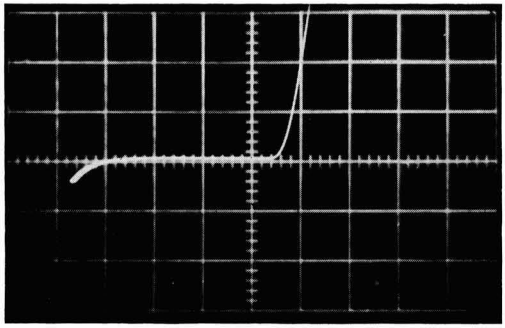

Fig. 11. Variation of SiC rectifier characteristics with temperature; vertical axis 5 ma/cm; horizontal axis 2 v/cm.

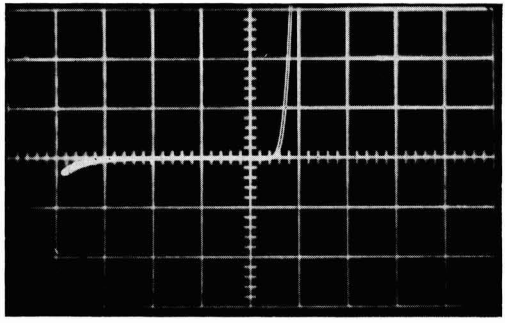

Fig. 12. (same as above)

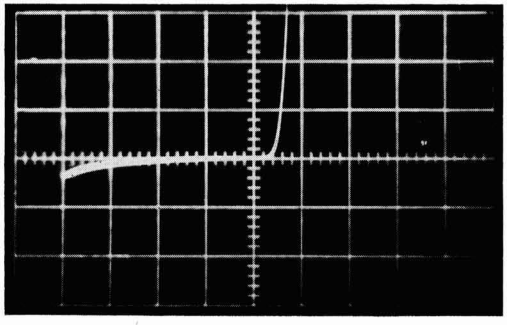

Fig. 13. (same as above)

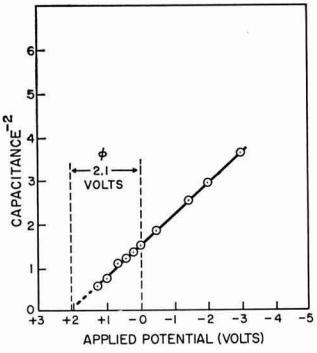

Fig. 10. Variation of SiC diode junction capacitance with applied voltage.

characteristic improves continuously as the temperature increases. The reverse characteristic begins to "soften" only at temperatures above 500°C. Even at room temperature, the reverse characteristic of these devices is smaller than expected; typical values of peak inverse voltage range from 6v to about 15v. The low peak inverse voltages of TSM-prepared diodes may be the result of inadequate surface treatment of the assembled structure, *i.e.*, high surface leakage. However, repeated etching and washing treatments produced little or no improvement.

Metallographic examination of diode structures indicated that if, during alloying of contacts, the gold alloy flowed down the sides of a specimen and thus came into contact with the edges of the junction region, deep penetration of the junction by a thin film of gold occurred in times of the order of minutes only. It is recalled that in these structures the junction region coincides with the initial plane of crystallization. This plane is believed to contain a network of screw dislocations which allows the remarkably rapid penetration of gold. TSM grown crystals of other solids have revealed interesting and unique dislocation configurations (18) in the same general region. The presence of such a dislocation network in the vicinity of the junction could explain the rather high reverse leakage observed.

Summary

It has been shown that TSM is a simple technique for growing relatively large crystals of silicon carbide and of forming p-n junctions during crystal growth. Successful application of the method requires that SiC surfaces be rigorously clean. Uniform wetting by chromium is a prerequisite for successful zone passage and occurs only on ultra-clean SiC. The regrown material is α-SiC, even though the growth process is performed well below the β/α "transition" temperature of about 2000°C.

Acknowledgments

The authors wish to thank Mr. T. Fuller for valuable experimental assistance and Dr. A. J. Rosenberg for many helpful discussions during this work, which was performed under U.S. Air Force Contract No. AF 19(604) 8803.

Manuscript received July 26, 1963; revised manuscript received Oct. 17, 1963. This paper was presented at the Pittsburgh Meeting, April 15-18, 1963.

Any discussion of this paper will appear in a Discussion Section to be published in the June 1965 JOURNAL.

REFERENCES

1. L. Patrick, *J. Appl. Phys.*, **28**, 765 (1957).
2. W. J. Choyke and L. Patrick, "Silicon Carbide," p. 306, J. R. O'Connor and J. Smiltens, Editors, Pergamon Press Inc., New York (1960).
3. A. Addamiano, R. M. Potter, and V. Ozarow, *This Journal*, **110**, 517 (1963).
4. R. I. Scace and G. A. Slack, "Silicon Carbide," p. 24, Pergamon Press Inc., New York (1960).
5. A. H. Smith, "Silicon Carbide," p. 53, Pergamon Press Inc., New York (1960).
6. J. A. Lely, *Ber. deut. keram. Ges.*, **32**, 229 (1959).
7. D. R. Hamilton, *This Journal*, **105**, 735 (1958).
8. Hung-Chi Chang *et al.*, "Silicon Carbide," p. 496, Pergamon Press Inc., New York (1960).
9. R. N. Hall, *J. Appl. Phys.*, **29**, 914 (1958).
10. K. Hergenrother, U. S. Pat. 2,996,456 (1961).
11. A. I. Mlavsky and M. Weinstein, *J. Appl. Phys.*, **34**, 2885 (1963).
12. L. B. Griffiths and A. I. Mlavsky, Paper presented at the Pittsburgh Meting, Electrochemical Society, April 1963.
13. W. G. Pfann, *Trans. AIME*, **203**, 961 (1955).
14. W. G. Pfann, "Zone Melting," p. 201, John Wiley & Sons, Inc. (1958).
15. Westinghouse Research Laboratories, Scientific Reports under Air Force Contract AF 19(604)-8499.
16. H. J. van Daal *et al., Physics and Chemistry Solids*, **24**, 1 (1963).
17. H. J. van Daal *et al., J. Appl. Phys.*, Suppl. to **32**, 2225 (1961).
18. M. Weinstein, H. LaBelle, Jr., and A. I. Mlavsky, Paper presented at Electrochemical Society Meeting, New York, 1963.

Measurement of the Resistivity of Epitaxial Vapor Grown Films of Silicon by an Infrared Technique

T. G. R. Rawlins

Northern Electric Research and Development Laboratories, Ottawa, Ontario, Canada

ABSTRACT

An infrared reflectivity technique is outlined whereby the reflectivity may be correlated with d-c resistivity of thin vapor deposited epitaxial silicon layers. The theory underlying the method is outlined and calculated curves for different planes of polarization are given. Experimental results are described for a range of resistivities between 0.03-60 ohm-cm. Limitations of the equipment used are discussed and the validity of the method examined.

It is well known that diffused transistors fabricated from epitaxial silicon (silicon having a thin lightly doped layer grown on top of a heavily doped single crystal substrate) have vastly improved characteristics over transistors fabricated from conventional material (1). In order to produce transistors of controlled properties, it is necessary to measure the thickness and the resistivity of the layers. A nondestructive infrared interference method for the measurement of thickness has been proposed by Spitzer and Tannenbaum (2) and enlarged upon by Albert and Combs (3).

A variety of methods have been tried for measurement of resistivity, most of these have been electrical methods either direct or indirect. One method, that has been used extensively, has been to fabricate shallow junction diodes on the surface and calculate resistivity from the capacitance-voltage characteristics [see for example (4)]. This method is, however, destructive and comparatively time-consuming. Other methods in the case of silicon, which are nondestructive, rely on the properties of various types of contacts (5). These contacts do not usually have reproducible properties. In many instances these methods are not very practical and are limited in resistivity range.

It was with these many short-comings in mind that an infrared method was sought. The infrared method is also convenient in that thickness and resistivity may be measured on the same instrument.

In principle, high frequency resistivity (assumed proportional to d-c resistivity) may be found from the optical constants n and k. Thus any method of measurement which leads to values for n and k may be used, since the complex refractive index is given by

$$N = n - ik$$

and from Maxwell's equations

$$N^2 = \epsilon\mu - i4\pi\mu\sigma/\omega$$

where ϵ is the permittivity, μ permeability, σ conductivity (high frequency), and $\omega = 2\pi$ x frequency.

Conventionally, reflectivity may be used to find n and k (6, 7). However, the case of epitaxial silicon reflectivity is different in that interference fringes are obtained, which somewhat complicate the situation, and a different expression for the reflectivity from a layer is obtained (8). In any case it becomes impracticable to measure resistivity in this way for, apart from the above factors, it is found that for the range of resistivities, which are usually of interest for epitaxial layers (0.1 ohm-cm – 100 ohm-cm), n is essentially constant and k is extremely small (9). In the case of conventional reflectivity measurements for reasonably accurate results, it is necessary that $k \geqq 0.2$, *i.e.*, significant absorption (6, 7). It therefore becomes necessary to "magnify" the very small values of k ($10^{-4} - 10^{-1}$) in order to be able to use reflection spectra for differentiating between layers of different resistivities. In addition, such a method must only allow penetration of the incident radiation into the topmost region of the deposited layer. In fact these requirements are met in the method of attenuated total reflection due to Fahrenfort (10) and Fahrenfort and Visser (11). The essentials of this method are such that radiation is allowed to travel in a dense medium towards a boundary between this medium and one which is less dense. The latter medium is the sample of immediate interest, having a finite (but usually small) value of k. The angle of incidence of the radiation on the boundary is arranged such that it is slightly greater than the critical angle. The reflectivity is then no longer 100% but depends quite markedly on the value of k for the sample [see (10, 11)]. This implies a transfer of energy into the second medium. Some of this energy is absorbed, according to the value of k and the particular wavelength.

Theory

An outline of the theory, which is appropriate to the use of the method for resistivity measurement, will be given below.

The Fresnel coefficients may be obtained by applying the boundary conditions for radiation incident on an interface between dense and less dense media [c.f. (12)].

These expressions give the ratios of the amplitudes of the reflected or transmitted electric vectors for both planes of polarization of the incident electric vector. Analogous expressions may be obtained for the magnetic vectors.

Also

$$N_0 \sin \phi_0 = N_1 \sin \phi_1 \quad \text{(Snell's law)} \qquad [1]$$
$$N_0 = n_0$$
$$N_1 = n_1 - ik_1$$

(Since N_1 is complex, it is apparent from [1] that ϕ_1 must be complex.)

Using the Fresnel equations, Snell's law and the definition of the Poynting vector, we may obtain equations for the reflectivity for the two planes of polarization, *i.e.*, for polarization perpendicular to the plane of incidence

$$R_s = [(n_0 \cos \phi_0 - x)^2 + y^2]/[(n_0 \cos \phi_0 + x)^2 + y^2]$$

where x and y are parameters given by

$$x - iy = [(n - ik)^2 - n_0^2 \sin^2 \phi_0]^{1/2}$$

A similar expression may be obtained for the other plane of polarization. When various appropriate values of n_0, n_1, k_1, and ϕ_0 are substituted in the reflectivity equations, results such as those shown in Fig. 1 and 2 are obtained. From these graphs it may be seen that, when the second medium has a finite non-zero value of extinction coefficient for angles of incidence greater than the critical angle, defined

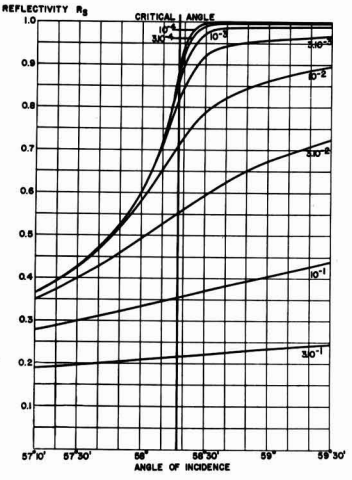

Fig. 1. Calculated reflectivity *vs.* angle of incidence curves for polarization perpendicular to the plane of incidence and various values of k: $n_0 = 4.02$ (germanium), $n_1 = 3.42$ (silicon).

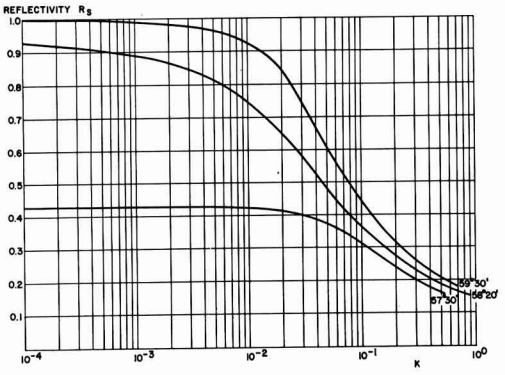

Fig. 2. Re-plotted version of Fig. 1, showing reflectivity *vs.* k for different angles of incidence.

as $\sin^{-1}(n_1/n_0)$, the reflectivity varies according to the value of k. This is also true for angles of incidence less than the critical angle. However, in this case, the difference in reflectivity for a given change in k very rapidly becomes much less (see Fig. 2). It is evident from the graphs that the difference is greatest at, or slightly above the critical angle.

Now according to electromagnetic theory

$$(n - ik)^2 = \epsilon\mu - \mathrm{i}\, 4\pi\mu\sigma/\omega$$

or

$$n^2 - k^2 = \epsilon\mu = \epsilon \text{ (assume } \mu = 1)$$
$$nk = 2\pi\mu\sigma/\omega = \sigma/\nu$$

Hence n and k are dependent on σ. Also experimentally (9) it is found that at a given wavelength the absorption coefficient increases with increasing carrier concentration, *i.e.*, since absorption coefficient $\alpha = 4\pi k/\lambda$, reflectivity must vary with carrier concentration. [For a more complete theoretical treatment, see ref. 13.]

Experimental

As the refractive index of silicon is (nominally) $3.42 - ik$ (14) it is necessary to pick another semiconductor, namely germanium, $n = 4.02$, as the optically denser medium (14). Since both incident beam and reflected beam should be attenuated as little as possible, it is preferable that the germanium should have small absorption, *i.e.*, intrinsic germanium so that little or no impurity absorption occurs and only that due to lattice vibrations is significant.

Further, it is apparent from the analysis (13) that the two media must be in intimate contact in order to give the best results, *i.e.*, there should be no intermediate air space. In practice this is difficult to achieve. However, various microwave experiments (15) show that the effect will still occur even when there is substantial separation. However, it is evident that the relative difference may be expected to be considerably reduced. Due to this fact, and to the fact that the surface of vapor-grown material is not perfectly flat, it is more convenient to be able to investigate a relatively small portion of the total area, since the variation in flatness may be expected to be less over the more restricted area. Hence, better contact should be achieved. This requirement, therefore, suggests that a condensing system be used. A further factor, suggesting the necessity for a condensing system, is that it is convenient to have the same amount of energy incident on every sample. This means that the beam should be condensed sufficiently so that the whole of the beam will fall on the smallest and most irregular samples, without any portion of it being lost, *i.e.*, sampling area is maintained constant.

In order to ensure that the angular accuracy and reproducibility are maintained, a parallel beam should fall on the sample.

Most of these requirements are satisfied by a commercially available micro-attenuated total reflectance unit.[1]

A schematic of the optical system of this unit is shown in Fig. 3 and 4. A condensing system is used to bring the beam to a focus just before the germanium hemicylinder. The cylindrical surface refracts the radiation such that a parallel beam falls on the sample [c.f., Fahrenfort (10)]. The size of the sample is approximately 1 x 6 mm, *i.e.*, the beam is condensed to this approximate size. The main drawback is that the angular accuracy is not as adequate as desirable [see (11)]. It is also necessary for the germanium hemicylinder to be very accurate and free from surface defects on the polished surfaces in order to prevent aberrations and scattering.

Results and Conclusions

Some typical reflectance curves, using random polarization, for a variety of epitaxial vapor-de-

[1] Connecticut Instrument Corp., Wilton, Conn.

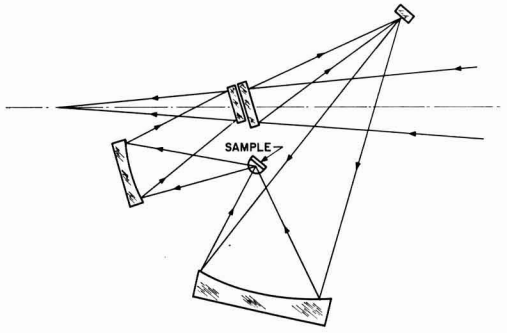

Fig. 3. Optical system of the micro-attenuated total reflectance unit.

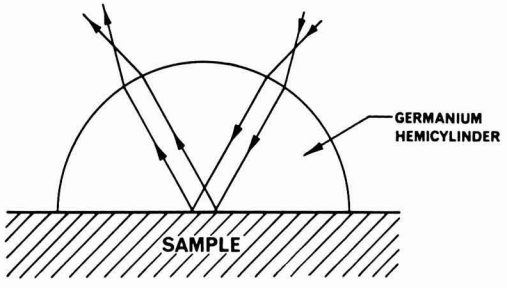

Fig. 4. Enlarged portion of Fig. 2 showing the sample and germanium hemicylinder.

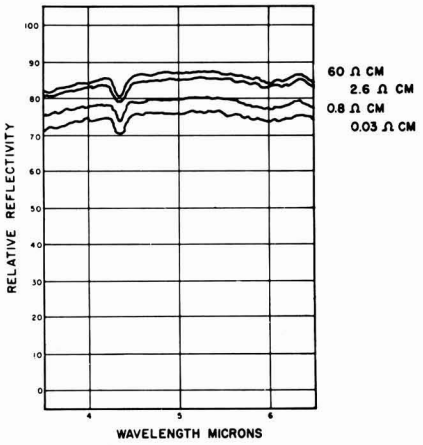

Fig. 5. Relative reflectivity vs. wavelength for epitaxial silicon slices of different resistivity.

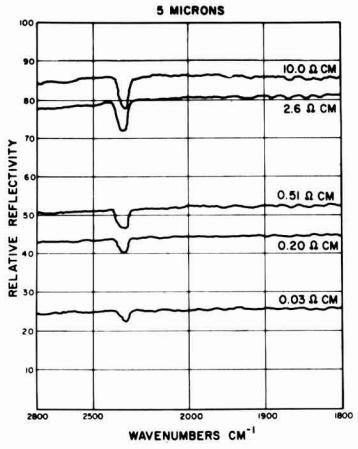

Fig. 6. Relative reflectivity vs. wavelength for further epitaxial silicon slices.

posited slices are shown in Fig. 5 and 6. In Fig. 5, which is a tracing of a number of curves, the reflection unit was placed in the sample beam of a Beckman I.R. 5A Rock Salt Spectrophotometer. A beam attenuator was used in the reference beam in order to increase the relative transmission. Usually the actual transmission in the sample beam was approximately 15-30%, which compares reasonably well with the 50-55% observed with an aluminized mirror substituted for hemicylinder prism and sample, *i.e.*, the sample etc. must cause some scattering, absorption, and reflection losses. Also evident in the spectra are atmospheric absorption bands, due to the longer sample beam path length. The layer resistivities were measured by means of the diode capacitance technique [c.f. (4)].

Figure 6 shows further tracings, in this case the curves were run on a Perkin-Elmer Model 21 Spectrophotometer under exactly the same conditions, except that scale expansion as well as beam attenuation was used. As before the sample resistivities were measured by means of the diode capacitance-voltage technique. Figures 5 and 6 are unfortunately not directly comparable due to the scale expansion and beam attenuation used; it should be emphasized that the ordinate is relative reflectivity.

It is, therefore, apparent that the method is sound, although the difference in reflectivity is not as great as that which might be predicted from absorption measurements and the above calculated curves.

Further experimental work is required, both to improve and refine the technique, and to give a better idea of reproducibility and accuracy. First, as noted above, the reflectivity observed does not agree with that predicted from the theory. It is felt that the explanation for this lies first in the lack of angular accuracy inherent in the unit. Indeed, from this respect as well as others, such as convenience of loading the sample, it may be best to design an instrument for the specific purpose, probably with a fixed angle, as it has been found quite difficult to maintain the angle constant when samples are changed. Second it is felt that the germanium hemicylinder may not be sufficiently adequate for the purpose of the measurement. It is quite likely that the germanium is insufficiently pure (the resistivity was only close to intrinsic resistivity) and is, therefore, absorbing. Any absorption will cause a loss in reflected energy. It is also likely that the geometrical shape is inaccurate. Any variation in curvature will change the refracting power of the surface, so that the beam will not be parallel when it is incident on the sample. This in turn will cause further loss in energy. After the blank has been machined, it is necessary to polish it. This may introduce further sources of energy loss due to scattering, as well as change in dimensions or flatness. In addition, if the sample itself is not flat, or has a poor surface, or is not in contact with the germanium, additional energy will be lost.

Thus, it seems likely that the above-noted mechanisms account for any discrepancies. It should be noted that, in any case, limits should be set on the range of resistivities which may be measured; the limitation being the actual value of k. From the theoretical curves it may be expected that $k = 10^{-4}$ is the lowest practical value under most circumstances. This corresponds to approximately 10 ohm-cm at 10μ for n-type material (9). The high limit of k may be set by the ability to distinguish materials of different values of k. In practice the lower limit enables one to cover the whole conventional range of resistivities, from approximately 0.001 ohm-cm upwards, consistent only with being able to resolve sufficiently small changes in relative reflectivity.

It is difficult at this stage to give any exact idea of precision due to difficulties already noted, however it may be stated that, provided great care is taken to maintain a constant angle, a sample may be removed and replaced to give relative reflectivities constant to within a few per cent. As discussed above the accuracy is primarily limited by the unit

itself, although the roughness of the sample also contributes as does the sample area.

A further point should be made clear with reference to the practicality of the method for measuring resistivities in thin layers. It is obvious that for the epitaxial silicon to affect the reflectivity, there must be penetration into it. As epitaxial layers are usually only about 10μ thick, it is valid to question whether the substrate will have any effect on the measurement. It will become clear from the theory (13) that the penetration is less than a wavelength. Thus, a suitable wavelength may be chosen between the energy gap absorption region and the region of high lattice absorption (in germanium) such that penetration is no problem. In practice no difficulty is encountered, for interference fringes would be observed on scanning the whole spectrum if the penetration were substantial.

Finally it should be emphasized that the method gives only the resistivity of the surface layer.

Acknowledgments

I would like to thank R. R. Senechal and W. D. Westwood for useful discussions and M. Naqi for programming the reflectivity equations. This work was sponsored in part by the Defence Research Board of Canada.

Manuscript received Nov. 26, 1963. This paper was presented at the New York Meeting, Sept. 29-Oct. 3, 1963.

Any discussion of this paper will appear in a Discussion Section to be published in the June 1965 JOURNAL.

REFERENCES

1. H. C. Theuerer, J. J. Kleimack, H. H. Loar, and H. Christensen, *Proc. I.R.E.*, **48**, 1642 (1960).
2. W. G. Spitzer and M. Tannenbaum, *J. App. Phys.*, **32**, 744 (1961).
3. M. P. Albert and J. F. Combs, *This Journal*, **109**, 709 (1962).
4. C. O. Thomas, D. Kahng, and R. C. Manz, *ibid.*, **109**, 1055 (1962).
5. E. E. Gardner, J. F. Hallenback, Jr., and P. A. Schumann, Jr., *Solid State Electronics*, **6**, 311 (1963).
6. I. Simon, *J. Optical Soc. Am.*, **41**, 336 (1951).
7. D. G. Avery, *Proc. Phys. Soc. (London)*, **65B**, 425 (1952).
8. T. G. R. Rawlins, 9th Ottawa Symposium on Applied Spectroscopy, 1962.
9. W. G. Spitzer and H. Y. Fan, *Phys. Rev.*, **108**, 268 (1957).
10. J. Fahrenfort, *Spectrochimica. Acta.*, **17**, 698 (1961).
11. J. Fahrenfort and W. M. Visser, *ibid.*, **18**, 1103 (1962).
12. M. Born and E. Wolf, "Principles of Optics," p. 38, Pergamon Press (1959).
13. T. G. R. Rawlins, To be published.
14. C. A. Salzberg and J. J. Villa, *J. Opt. Soc. Am.*, **47**, 244 (1957).
15. W. Culshaw and D. S. Jones, *Proc. Phys. Soc.*, **66B**, 859 (1954).

Preparation of $GaAs_xP_{1-x}$ by Vapor Phase Reaction

W. F. Finch[1] and E. W. Mehal

Texas Instruments Incorporated, Dallas, Texas

ABSTRACT

A method for producing epitaxial $GaAs_xP_{1-x}$ utilizing an open tube flowing atmosphere system is presented. The various alloy compositions are synthesized and deposited by using $AsCl_3$, PCl_3, H_2, and Ga as the initial reactants. The complete range of $GaAs_xP_{1-x}$ compositions has been prepared by varying the mole ratio PCl_3 and $AsCl_3$ introduced into the reactor gas stream. Experimental conditions required for achieving good epitaxial growth of these materials on <111> oriented GaAs substrates are discussed.

Preparation of III-V semiconductors by vapor phase reaction was first reported by Antell and Effer (1). Later Lyons and Silvestri (2) demonstrated epitaxial GaAs growth from a vapor. Others have continued this work in open and closed systems using volatile halides and oxides as transport media.

Gershenzon and Mikulyak (3) prepared GaP by reaction of gallium suboxide with phosphorus in the vapor phase. A variety of oxygen compounds were also formed, and the GaP was thought to be doped with oxygen. Oxygen was later shown to cause a deep donor level (4) (0.4 ev) in GaP.

Pizzarello (5) prepared solid solutions of GaP in GaAs by transporting a mixture of GaAs and GaP with iodine in a closed system. The deposits were not epitaxial, but the entire composition range was synthesized and identified from x-ray powder diffraction patterns. Variation in band gap as a function of composition was measured. Also, lattice parameter variation was found to obey Vegard's law.

Halogen doping experiments by Antell (6) have shown that chlorine and iodine do not behave as donors or acceptors in InAs, GaP, and presumably other III-V semiconductors. For this reason halogen vapor transport systems seem better than oxygen systems for III-V semiconductor vapor growth. A variety of halide sources has been used in closed system experiments (7), but open tube experiments have used primarily HCl. Open systems offer considerable flexibility compared to closed systems, but HCl is difficult to obtain in high purity and is easily contaminated through reaction with metal valves and flow meters.

This paper describes the vapor phase reaction of Ga and GaAs with $AsCl_3$ and PCl_3 in an open system to form epitaxial $GaAs_xP_{1-x}$ deposits on GaAs substrates. This technique has several advantages over earlier open tube systems. High-purity $AsCl_3$

[1] IBM. Components Division, Poughkeepsie, New York.

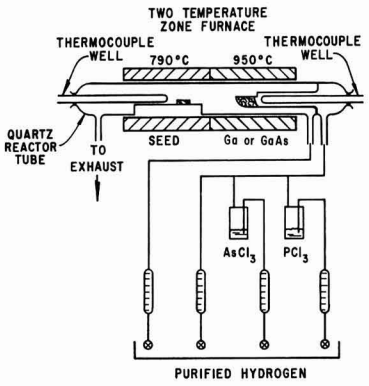

Fig. 1. $GaAs_xP_{1-x}$ epitaxial deposition system

and PCl_3 can be prepared by laboratory distillation and can serve as a pure arsenic and phosphorus source as well as a halogen source. The vapor pressures of $AsCl_3$ and PCl_3 are high enough so that they can be transported as gases by displacement from a bubbler, thus avoiding contact with the usual metal parts necessary in HCl systems. Also, the ratio of arsenic to phosphorus introduced into the system can be varied during growth allowing graded composition structures to be grown in a single operation.

Experimental

Figure 1 shows the experimental apparatus. Hydrogen, purified by Pd diffusion, is metered into the system through four flow meters. Two are connected to $AsCl_3$ and PCl_3 bubblers while a third controls further dilution of the displaced $AsCl_3$ and PCl_3 vapors. The diluted vapors then pass over Ga or GaAs feed material[2] at an elevated temperature, and the reaction products are further diluted with hydrogen from the fourth flow meter. These gaseous products are swept through a decreasing temperature gradient to the cooler end of the reaction tube where they combine to deposit $GaAs_xP_{1-x}$ on a GaAs seed. Both mechanically and chemically polished (111) oriented seeds have been used with equal success.

Typical operating conditions are: feed material temperature, 900°-950°C; seed temperature, 775°-820°C; $AsCl_3$ bubbler flow rate, 10-100 cm^3/min; PCl_3 bubbler flow rate, 1-10 cm^3/min; dilution hydrogen flow rates, 20-200 cm^3/min.

The chemical compositions of the $GaAs_xP_{1-x}$ deposits were identified primarily by x-ray diffraction. Since no composition difference was seen in $GaAs_xP_{1-x}$ deposited on a seed and on adjacent walls of the reaction tube, most of the x-ray measurements were done from powder patterns of material adjacent to the seed. A few wet chemical measurements were made and were found to be within 4% of the x-ray values.

Junction electroluminescence was used as an indirect measurement of composition. Zinc was diffused into several n-type deposits of different compositions to form p-n junctions. The light emitted on forward bias had a wavelength which corresponded to an energy transition approximately equal to the energy gap of the composition involved.

Transport properties were measured for two compositions of $GaAs_xP_{1-x}$. A 100μ thick deposit of $GaAs_{0.9}P_{0.1}$ was grown using $n \sim 10^{15}$ cm^{-3} [3] GaAs as feed material. The seed was lapped away and the deposit was cut into a 1.0 x 0.2 cm rectangular bar. Direct current Hall effect and resistivity measurements showed $n = 1.4 \times 10^{17}$ cm^{-3} and $\mu_H = 1.2 \times 10^3$ cm^2/volt-sec at room temperature. This mobility is below what might be expected for this composition and doping level. It was later discovered that the PCl_3 used in this preparation was contaminated with $POCl_3$.

A deposit of $GaAs_{0.6}P_{0.4}$ was grown on a high resistivity ($\rho \geqq 10^6$ ohm-cm) seed using $n \sim 10^{16}$ cm^{-3} [3] GaAs as feed material. Hall effect and resistivity measurements showed $n = 3.0 \times 10^{16}$ cm^{-3} and $\mu_H = 1.8 \times 10^3$ cm^2/volt-sec. These values seem reasonable for this composition.

Crystalline characteristics of the $GaAs_xP_{1-x}$ have been examined by staining techniques and microscopic observation. X-ray techniques were used to measure the orientation of the deposit. Deposit thickness was optically measured on a cleaved or angle lapped edge. No staining was necessary here because the deposit is a different color from the seed. Compositions having phosphorus greater than $GaAs_{0.35}P_{0.65}$ are transparent varying from dark red to greenish-yellow.

Results and Discussion

The complete composition range of $GaAs_xP_{1-x}$ has been grown epitaxially on GaAs. The two important variables that control the product composition are the composition of the feed material and the ratio of $AsCl_3$ to PCl_3 introduced into the system. The composition of the deposit was not dependent on the temperature of the feed material for the temperature range investigated (900°-950°C). Figure 2 shows the effect of the mole ratio of $AsCl_3$ to PCl_3 introduced into the system on the deposit composition for both Ga and GaAs feed material.

[3] The carrier concentration of the feed materials is presented as an order of magnitude number estimated from resistivity and emission spectrographic data.

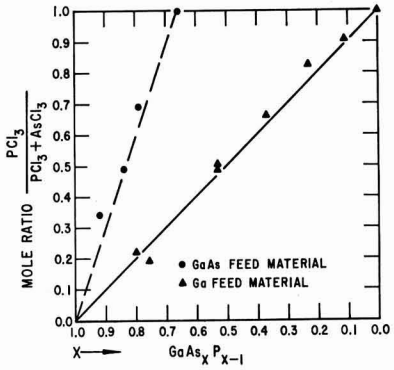

Fig. 2. $GaAs_xP_{1-x}$ deposit composition as a function of $AsCl_3$ and PCl_3 gas phase compositions.

[2] The Ga was six nines grade purity and the GaAs was prepared initially from five nines grade purity Ga and As. The $AsCl_3$ and PCl_3 were distilled reagent grade materials.

The complete composition range has been synthesized using Ga feed material; however, $GaAs_{0.67}P_{0.33}$ was the highest phosphorus composition produced using GaAs as a feed material. This information can be used to give some insight into the nature of the chemistry involved. The literature generally agrees that a reaction between Ga and a halide source will form mono-, di-, and tri-halides. The di-halide is thought to be a loosely associated $Ga(GaCl_4)$ complex and does not exist in the gaseous state. The gallium feed data in Fig. 2 have shown that the composition of $GaAs_xP_{1-x}$ formed is roughly proportional to the mole ratio of arsenic to phosphorus present in the system. The GaAs feed data in Fig. 2 have shown that the reaction between PCl_3 and GaAs produces $GaAs_{0.67}P_{0.33}$. This indicates that the ratio of arsenic to phosphorus present in the deposition zone must be 2 to 1. Equation [1]

$$4GaAs + 2PCl_3 \rightarrow 3GaCl + GaCl_3 + As_4 + \tfrac{1}{2}P_4 \quad [1]$$

gives such a ratio. Knowing that under these temperature conditions 3 moles of GaCl are formed for every mole of $GaCl_3$ we can propose the following over-all series of reactions.

$$4GaAs + 2[nAsCl_3 + (1-n)PCl_3] \rightarrow 3GaCl + GaCl_3 + As_4 + 2\left[\frac{n}{4}As_4 + \frac{1-n}{4}P_4\right] \quad [2]$$

$$3GaCl \rightarrow 2Ga + GaCl_3 \quad [3]$$

$$6Ga + As_4 + 2\left[\frac{n}{4}As_4 + \frac{1-n}{4}P_4\right] \rightarrow 6GaAs_xP_{1-x} \quad [4]$$

where $x = (2 + n)/3$. First the GaAs reacts with the $AsCl_3$ and PCl_3 (Eq. [2]). In the decreasing temperature gradient the GaCl disproportionates (Eq. [3]) forming gallium which is then able to react (Eq. [4]) with the arsenic and phosphorus which are available in the gas phase.

The reaction shown in Eq. [2] is complicated by the fact that $AsCl_3$ and PCl_3 are reduced by hydrogen at elevated temperatures. This means that while the over-all reaction proposed in Eq. [2] is correct the mechanism may involve HCl as an intermediate.

The reactions with gallium feed material are similar to the gallium arsenide feed material reactions except that, in the former, $AsCl_3$ is the only arsenic source.

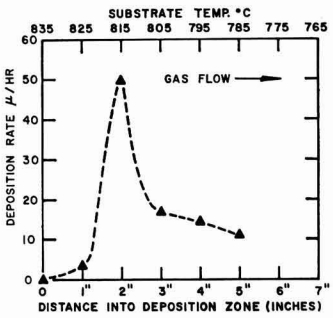

Fig. 3. Deposition rate as a function of position of substrate in deposition zone and temperature.

The deposit growth rate has not been extensively investigated as such, but the following trends have been established. The two primary growth rate variables are the $AsCl_3$ and PCl_3 flow rates and the position of the seed in the temperature gradient.

The normal ranges of flow rates of H_2 saturated with $AsCl_3$ and PCl_3 vapor from the bubblers are 10-100 cm^3/min and 1-10 cm^3/min, respectively. (Vapor pressure of PCl_3 is approximately ten times higher than that of $AsCl_3$.) In general, increased flow rates give increased growth rate. Very high flow rates, however, tend to etch the seed, and no deposition occurs. This is because the H_2 saturated with $AsCl_3$ and PCl_3 flow past the feed material too rapidly to react completely and are subsequently reduced to produce HCl as a by-product. The HCl then etches the GaAs seed at a rate higher than the growth can occur.

Figure 3 shows the deposition rates during a 4.5 hr growth with PCl_3 and $AsCl_3$ vapor flow rates of 4 and 20 cm^3/min, respectively. The gallium feed material temperature was 950°C. Six GaAs seeds were placed at 1-in. intervals in the cooler end of the reactor and the temperature gradient was adjusted to 10°C/in. No deposit grew on the hottest seed. On the second seed the deposition rate was 3.3 μ/hr, and no deposit occurred on the adjacent supporting quartz shelf. This indicates that the growth process is surface catalyzed at this point in the reactor. On the next seed a growth rate of 50 μ/hr was obtained, and a very thick deposit was formed on the surrounding quartz. The process here is probably a combination of surface catalysis and condensation of a supersaturated vapor species. On the next three seeds the deposition rate varied from 17 to 11 μ/hr with a moderate deposit on the quartz. This is a combination of surface catalysis and normal condensation from the vapor.

Values presented in Fig. 3 show a typical deposition rate gradient. The curve can be shifted to the left by raising the feed material temperature, but this tends to eliminate the region in which growth is by surface catalysis only.

Epitaxial growth is easily achieved in the surface catalyzed region, but the rate is too slow for practical use. Epitaxial growth in the region of rapid deposition is possible but unpredictable. The most reproducible, practical growth is achieved in the

Table I. Physical characteristics of deposits produced at various substrate temperatures

Run No.	Seed temperature, °C	Result
7	650	"Powdery" deposit
8	675	Very fine grain polycrystalline
9	725	Large grain polycrystalline
11	775	Single-epitaxial, rough surface
29	790	Single-epitaxial, smooth surface
38	830	Single-epitaxial, slow growth rate
37	850	Seed etched, no deposit
63	790 → 600	Single-epitaxial, slightly rough surface

region immediately beyond the rapid deposition zone. Initially, only about 30% of the deposits grown in this region were epitaxial. Later, by beginning the growth at 840°C and slowly lowering the seed temperature to 790°C, about 80% of the deposits were epitaxial.

The series of runs shown in Table I was made to establish the temperature conditions for epitaxially depositing $GaAs_{0.67}P_{0.33}$ on a GaAs substrate. In each run GaAs was used as a feed material at 915°C, and the substrates were placed in the deposition zone about 1.5 in. past the region of rapid deposition. Epitaxial growth was achieved when the substrate temperature was between 775° and 830°C. With the gas concentration and flow conditions used, vapor etching was noticed at the higher temperature, and nonepitaxial deposits were observed for lower temperatures.

The evidence that our epitaxial yield was increased from 30 to 80% by starting growth at 840°C and slowly lowering the seed temperature to 790°C suggested that initial nucleation was a critical phase of growth. Several runs, similar to run 63 in Table I, were made in which the temperature was substantially lowered in several steps after an initial period of 790°C growth. It was established that the deposit can remain epitaxial and single crystalline as low as 600°C. Below this temperature arsenic begins to condense in the deposition zone making further growth difficult.

Acknowledgments

The authors wish to thank Dr. D. Miller for x-ray analyses, Dr. R. Biard for the information about the performance of the electroluminescent diodes he made from our samples, and Mr. T. Robertson for his assistance in the experimental work.

This work was supported by the Electronic Technology Division, Air Force Systems Command at Wright-Patterson Air Force Base, under Air Force Contract No. AF 33(657)-9196.

Manuscript received Sept. 5, 1963.

Any discussion of this paper will appear in a Discussion Section to be published in the June 1965 JOURNAL.

REFERENCES

1. G. R. Antell and D. Effer, *This Journal*, **106**, 509 (1958).
2. V. J. Lyons and V. J. Silvestri, *ibid.*, **108**, 177C (1961).
3. M. Gershenzon and R. M. Mikulyak, *ibid.*, **108**, 548 (1961).
4. M. Gershenzon and R. M. Mikulyak, *Solid State Electronics*, **5**, 313 (1962).
5. F. A. Pizzarello, *This Journal*, **109**, 226 (1962).
6. G. R. Antell, *J. Appl. Phys.*, **31**, 1686 (1960).
7. N. Holonyak, D. C. Jillson, and S. F. Bevacqua in "Metallurgy of Semiconductor Materials," **15**, pp. 49-59, Interscience Publishers, New York (1962).

Epitaxial Growth of Gallium Arsenide on Germanium Substrates

1. The Relationship between Fault Formation in Gallium Arsenide Films and the Surface of Their Germanium Substrate

T. Gabor*

Research Laboratories, Westinghouse Electric Corporation, Pittsburgh, Pennsylvania

ABSTRACT

Morphological and etching studies on films of gallium arsenide deposited on germanium substrates have revealed twin planes, grains, and stacking faults. The evidence suggests that these defects are related to the faceting of the substrate and to the presence of oxide films.

The deposition of gallium arsenide films on low index planes of germanium substrates has been described (1-4), and recently films altogether free of stacking faults have been grown (5). We have found it much more difficult to avoid the formation of faults in films grown on {111} surfaces of germanium than in films grown on gallium arsenide substrates. The aim of the work described in this communication was to examine the causes of fault formation when germanium was used as substrate.

Experimental

Flow system.—A stream of hydrogen containing arsenic trichloride was passed over gallium arsenide in an open tube. The resulting gas mixture then flowed over germanium substrates in a lower temperature region. The substrates were lying horizontally on semicylindrical holders so that some growth took place even on the sides that were facing downwards. The experimental conditions, the chemical equilibria, and transport taking place in this system have previously been described (6).

Substrates and outgassing.—{111} wafers cut from Czochralski-grown crystals and germanium webs were used as substrates. The latter are grown by pulling two dendrites from the melt, the material connecting the dendrites being pulled up by surface tension (7, 8). Various procedures were used for the cleaning of the crystals. The Czochralski-crystals were etched in CP4 while the webs were sometimes etched in CP4 at other times in aqueous HF. In most cases after etching the crystals were rinsed in water then in redistilled methanol. The second distillation of the methanol was performed in a quartz apparatus. The solvent was blown off the crystals with a stream of ultrapure hydrogen. A similar technique

* Present address: Battelle Memorial Institute, Columbus, Ohio.

was also used with double-distilled water. On a few occasions, especially when no CP4 etching was performed, the substrates were washed with a nonionic surface active agent, "SteroxAJ"[1] (2.5 cc/liter), in an ultrasonic bath followed by three washes with distilled water. In still other cases trichloroethylene was used for cleaning.

Before deposition, the substrates were heated at high temperatures ($\leqq$ 650°C) for periods up to 20 min in a stream of hydrogen. In some experiments the furnace was heated to the deposition temperature, and the arsenic trichloride was added to the stream of hydrogen before the substrates were brought into the deposition region.

Contamination of substrates with antimony.—A stream of hydrogen was passed over antimony (55 mg) at 400°C and then over the substrates at 250°C for 10 min. The direction of the flow of gas was then reversed, and the deposition zone was heated in a stream of hydrogen to 610°C and kept there for 5 min before starting the growth experiment. This treatment was shown (9) to deposit $10^{14} - 10^{15}$ at. Sb/cm^2 Ge.

Results

Etching of cross sections of gallium arsenide films.—On etching {211} cross sections of gallium arsenide films with a solution of $K_3Fe(CN)_6$ (2) : H_2O (25) : KOH (3), two different types of areas were delineated. One etched rapidly and gave a rough dark brown looking surface after only 30 sec. The other etched more slowly and took longer (2-3 min) before it appeared dark at magnifications up to 200X and showed etch pits at 500X.

The etching studies revealed the following defects:

1. Twin planes in the germanium substrate extended into the gallium arsenide film with unchanged spacing. Figure 1 shows a typical differentially etched {211} section of the growth on the edge of a germanium crystal. The latter contained twin planes lying in {111} planes perpendicular to the plane of the picture. (The picture was taken with the gallium arsenide deposit in focus; the germanium substrate has etched more slowly and was slightly out of focus so that only two of its three twin planes can be seen.) The <110> traces of the twins in the gallium arsenide deposit separate dark and light etched areas. Similar lines separating dark from light areas also originate at edges where macroscopic faces of the germanium substrate meet. Other etched {211} cross sections showed the same phenomenon.

2. Etched cross sections of the growth on the {111} planes showed grains. Figure 2 shows a cross section after a 10-sec etch (with long etching the roughness of the interface could not be seen because of the rapid dissolution of the gallium arsenide deposit and the attack of the etchant on the side of the exposed germanium). On longer etching and for cross sections cut in a {110} plane, the grains remained the same color as the surrounding growth, whereas in {211} cross sections they were of the opposite type to the growth surrounding them: they etched rapidly and became dark whereas the surrounding growth etched slowly and vice versa. In growth occurring at the edge of {111} germanium wafers (Fig. 1) and also in growth on {111} planes when the system was badly contaminated[2] grains were found not only at the interface but also throughout the deposit.

3. Lines propagating in the inclined {111} planes away from the substrate were seen. These were never found to delineate dark and light areas.

Morphological studies.—Information about the early stages of growth was derived from the examination of growth islands that were found in some cases where growth was slow. Most of these islands were trigonal. In very few cases, probably due to

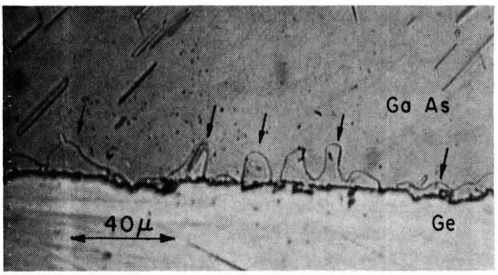

Fig. 2. Etched cross section of GaAs film grown on {111} Ge substrate. Arrows indicate misoriented areas.

[1] The author thanks Monsanto Chemical Company for the supply of the surface active agent.

[2] For example when a large amount of zinc chloride was used as the transporting agent in a sealed tube.

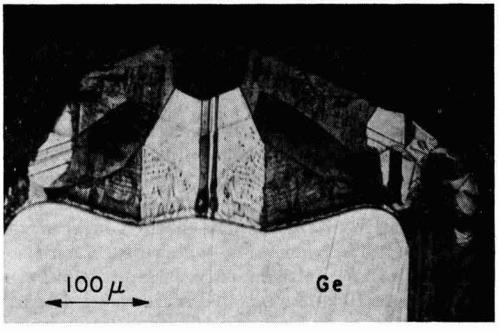

Fig. 1. {211} section of GaAs grown on Ge. Twins contained in the latter propagate through the epitaxial film. Changes in polarity across the twins are shown by the differential etch.

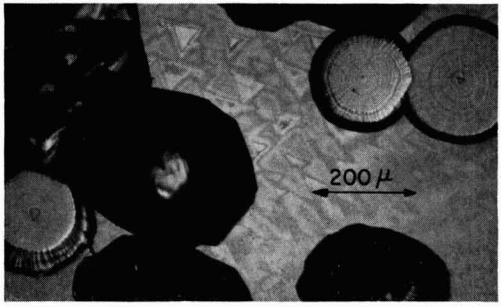

Fig. 3. Circular and triangular growth islands of GaAs observed on the downward facing plane of a {111} Ge crystal.

Fig. 4. Interference micrograph showing growth steps on the {111} plane where faults propagating in the three inclined {111} planes reach the surface.

some impurity preventing epitaxial growth, they were circular. Figure 3 shows a rare case where both were present. The triangles showed interference colors suggesting growth of only a few thousand angstroms thickness. The apices of some of these triangles point in the $[2\bar{1}\bar{1}]$ whereas others in the $[\bar{2}11]$ direction.

Stacking faults were formed on both the Czochralski crystals and on the webs, and none of the cleaning procedures (see Experimental section) resulted in their elimination. The intersection of the faults with the {111} surface of the films was visible without etching because growth is faster along one side of the fault than along the other. Figure 4 shows an interference micrograph of the surface of a thick film in which the faults have interacted with each other as has been described for the case of stacking faults in silicon films by Booker and Stickler (10).

Films grown on substrates that had not been outgassed also showed faults. Growth islands obtained on such substrates had a feathered structure (Fig. 5), and films grown on them did not show the well-defined lines of the stacking faults that were obtained on outgassed samples but instead showed a diffuse structure (Fig. 6).

Deliberately contaminated substrates yielded unusual growth structures. For example, when the substrate was contaminated with antimony, a large number of whiskers and round hills like the one in Fig. 7 were found on the substrate that was nearest to the source region (highest temperature). This

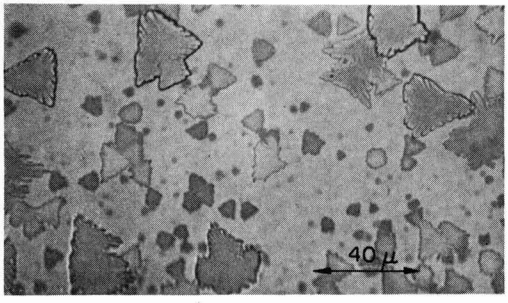

Fig. 5. Growth islands of GaAs showing feathered structure obtained on the downwards facing plane of an oxide-contaminated {111} Ge crystal.

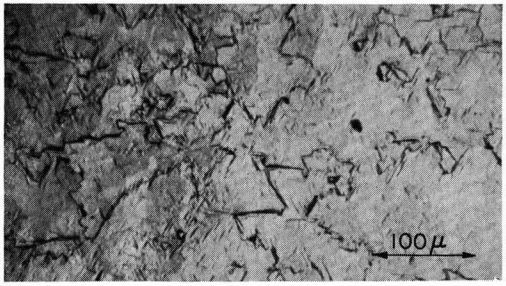

Fig. 6. Faults on surface of GaAs film grown on oxide-contaminated {111} Ge substrate.

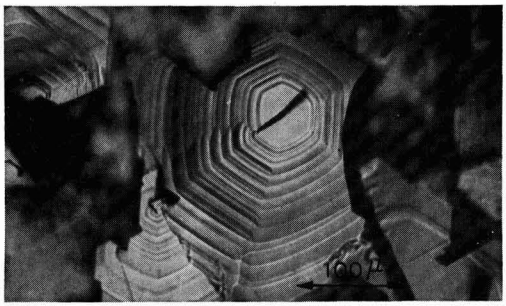

Fig. 7. GaAs growth structure obtained on Sb-contaminated {111} surface of Ge crystal.

hill showed the interaction of growth steps from a dominant dislocation with those from small imperfect dislocations. In the same experiment, individual trigonal growth islands reached a height of 18μ on the crystal furthest away from the source region, whereas in the absence of antimony they did not grow higher than 3-4μ.

Discussion

In gallium arsenide, on one side of a twin plane it is the gallium atoms, on the other side the arsenic atoms that in a {211} cross section have two broken bonds, the other type of atom having only one. The observation that the twin planes in the substrate propagate through the growing film and are revealed after etching as lines separating dark from light areas (Fig. 1) suggests that the etch distinguishes between the two possible types of polarity.

The two vertical lines in Fig. 1 that separate dark from light areas and originate where macroscopic faces on the edge of the crystal meet must similarly be intersections of twin planes with the {211} cross section. A possible explanation for their formation may be the deposition of the same type of atom on both faces. For example, if the first layer that deposits on a macroscopic {111} plane of germanium consists of arsenic atoms, then, on a {111} facet that forms an angle of 70° with it, the first layer must consist of gallium atoms, or vice versa, otherwise mismatch will occur at the edge.[3] Due to the difference in reactivity between the gallium and arsenic atoms (11), the first layer on all facets will consist of entirely gallium or arsenic atoms. Thus, depend-

[3] This was first pointed out by A. I. Bennett.

ing on the orientations of adjacent facets, there is a probability that, if nucleation starts independently on both facets, the film will not be able to grow together without the formation of a fault. If the two grains join along a {111} plane, the boundary between them will be a twin plane.

Facets of atomic dimensions must be present on any substrate. However, these facets may not be large enough to allow independent nucleations to take place. Faceting on a macroscopic scale may however occur during the outgassing of the substrates (12).[4]

An additional cause of faceting may be the deposition of gallium and the absence of sufficient amounts of arsenic to form gallium arsenide at the beginning of the experiment. When outgassing is performed at high temperatures for prolonged periods, the source gallium arsenide must lose considerable amounts of arsenic, resulting in a gallium rich mixture when the carrier gas is introduced. The formation of a thin film, or of microscopic islands of gallium, on the surface of the substrates at 600°-700°C will result in melts containing 25-35% Ge (13). The dissolution of germanium should cause the formation of faceted pits (14).

The degree of misorientation in the growing film appeared to be related to the roughness of the substrate, and it decreased with the distance from the interface. This means that growth with one type of polarity was favored. On etching the surface of a film ($> 100\mu$ thick) as described by Gatos and Lavine (11), well-developed triangular pits, all having an apex pointing in the $[\bar{2}11]$ direction, were obtained. This suggests that under the experimental conditions that were used in this work, the outermost layer consisted of gallium atoms.

The faults propagating in the three {111} planes inclined to the interface were similar to the stacking faults that have been described in films of germanium (15, 16) and silicon (17, 18). A possible explanation for the varying growth rates on the two sides of each fault may be the following: The growth may take place by the propagation of two-dimensional nuclei parallel to the surface. When such a layer reaches the intersection of a fault with the surface, its propagation may be prevented due to the stacking order being different on the two sides of the fault. The number of layers reaching the fault may be different on the two sides because it must depend on the probability of nucleations occurring on different sides. These nucleation probabilities will themselves depend on the distribution of other faults.

The growth on a {111} substrate of triangles with an apex pointing in the $[\bar{2}11]$ direction (Fig. 3) must have involved the formation of a fault. We do not know whether this was caused by mismatched growth on facets or by impurities. In the case of Fig. 5, it was evidently the oxide contamination that caused the growth islands to have the feathered structure and some of them to be misoriented. Growth islands pointing in opposite directions cannot grow into an unfaulted layer and must result either in the formation of stacking faults or of grains that are misoriented relative to each other (Fig. 2).

[4] Note added in proof: a method of preparing smooth, etched germanium substrates has recently been described [J. A. Amick, *RCA Rev.*, **24**, 555 (1963)].

Acknowledgments

The author thanks H. D. Larson for the cross sectioning and polishing work, K. Liang for his assistance in growing the films, and H. C. Chang and D. R. Hamilton for helpful discussions.

Manuscript received Dec. 6, 1963; revised manuscript received Feb. 10, 1964.

Any discussion of this paper will appear in a Discussion Section to be published in the June 1965 JOURNAL.

REFERENCES

1. N. Holonyak, Jr., D. C. Jillson, and S. F. Bevacqua, *Met. Soc. Conf.*, **15**, 49, (1961).
2. R. R. Moest and B. R. Shupp, *This Journal*, **109**, 1061 (1962).
3. T. Okada, T. Kano, and Y. Sasaki, *J. Phys. Soc. Japan*, **16**, 2591 (1961).
4. A. E. Blakeslee, Paper presented at Electrochemical Society Pittsburgh Meeting, May 1963.
5. A. E. Blakeslee, Private communication.
6. R. R. Fergusson and T. Gabor, *This Journal*, **111**, 585 (1964).
7. S. O'Hara and A. I. Bennett, *J. Appl. Phys.*, **35**, 686 (1964).
8. S. Dermatis and J. W. Faust, Jr., *Communication and Electronics (IEEE)*, **1**, (March 1963).
9. J. E. McNamara, *This Journal*, **108**, 199 (1961).
10. G. R. Booker and R. Stickler, *J. Appl. Phys.*, **33**, 3281 (1962).
11. H. C. Gatos and M. C. Lavine, *This Journal*, **107**, 427 (1960).
12. T. Gabor, *ibid.*, **111**, 821 (1964).
13. E. M. Savitskii, V. V. Baron, and M. A. Tylkina, *Zhur. Neorg. Khim.*, **3**, 763 (1958).
14. J. W. Faust, Jr., A. Sagar, and H. F. John, *This Journal*, **109**, 824 (1962)
15. T. B. Light, Metallurgy of Semicond. Materials, Proc. AIME Conf., Los Angeles (1961).
16. O. Haase, *ibid.*
17. H. J. Queisser, R. H. Finch, and J. Washburn, *J. Appl. Phys.*, **33**, 1536 (1962).
18. G. H. Schwuttke, *ibid.*, **33**, 1538 (1962).

Epitaxial Growth of Gallium Arsenide on Germanium Substrates

II. Deterioration of the {111} Surface of Germanium at 570°-850°C

T. Gabor†

Research Laboratories, Westinghouse Electric Corporation, Pittsburgh, Pennsylvania

ABSTRACT

It has been shown that on heating germanium crystals in hydrogen or in vacuum at temperatures 570°-850°C, deterioration of the 111 planes takes place. Temperature gradients and adsorbed impurities are the probable causes of the deterioration. Impurities cause the formation of etch- and growth-structures which in their absence would be unstable.

When preparing devices from germanium, one often has to heat the crystals to high temperatures. For example, in the epitaxial deposition of germanium or gallium arsenide on germanium substrates, the latter are exposed to high temperatures during outgassing, when impurities, especially oxides, are removed from the surface. This work was undertaken to examine whether the smoothness of the germanium surface can be preserved under such conditions. The effect of any deterioration on the crystallographic quality of gallium arsenide films is described in Part I (1) of this series.

Experimental

The crystals and the purification procedures have been described in Part I. Details of the heat treatments are given below. Numbers within the same bracket mean that these figures represent different areas of the same sample. The crystals were heated:

A. With continuous pumping, Fig. [4, 7, 9].
B. In sealed quartz tubes
   a. In vacuum, Fig. [1, 2, 3], [10], [11].
   b. In hydrogen, Fig. [8].
C. In open flow systems in hydrogen, Fig. [5, 6].

Specific details are given in Table I.

The quartz used for the sealed tube experiments was cleaned in aqua regia. The tubes had an approximate volume of 20 cc. The weight changes in nearly all of the experiments were within the experimental error of ±0.2 mg. The two {111} faces of the wafers had a total area of about 1 cm^2, compared to which figure the area of the edges may be neglected.

† Present address: Battelle Memorial Institute, Columbus, Ohio.

Table I. Details

Fig.	Evacuation of tube: Temp, °C	Hr	Pressure, mm Hg	Heat treatment: Temp, °C	Hr	Pressure, mm Hg
4, 7, 9				820	15	2×10^{-7}
1, 2, 3,* a	500	2	3×10^{-6}	570	8	
10	500	3	1×10^{-6}	720	20	
11	500	3.5	2×10^{-6}	680	16	
8,* b	500	2	3×10^{-6}	570	8	150 (H_2)
5, 6,* c				680	17	760 (H_2)

* Heated in a temperature gradient: a, the sample at the highest temperature was at 780°C; b, the sample at the highest temperature was at 780°C, and that sample lost 1.0 mg weight; c, the sample at the highest temperature was at 700°C ("upstream").

Observations

Some faceting was observed on nearly all samples that were heat-treated. The smoothness of the surface was best preserved when the last wash before heat-treatment was performed with double distilled water, and the latter was blown off the surface by a stream of hydrogen. The degree of deterioration increased with increasing temperature and with increasing temperature gradient. In case of experiments that were performed in an atmosphere of hydrogen, the roughening of the surface was the least prevalent when the hydrogen was purified by diffusion through a palladium alloy tube.

On nearly all samples, either some tetrahedral pits or growth triangles were observed. In addition to these many unexpected structures were found. Some of these are described below:

1. Simultaneous formation of pits and hillocks.—Figure 1 shows hillocks on a germanium crystal. The black dots are whiskers. They most likely consist of either germanium or of silicon dioxide, the latter originating from the quartz tube, although the composition of the whiskers could not be established from an electron diffraction pattern. Figure 2 shows a replica of the crystal, shadowed at an angle of 30° to the specimen plane. A cross section of the structure shown at the top of Fig. 2 is drawn in Fig. 3. The

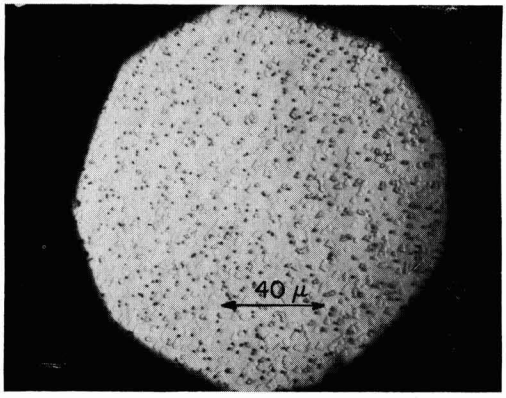

Fig. 1. Growth triangle and whiskers

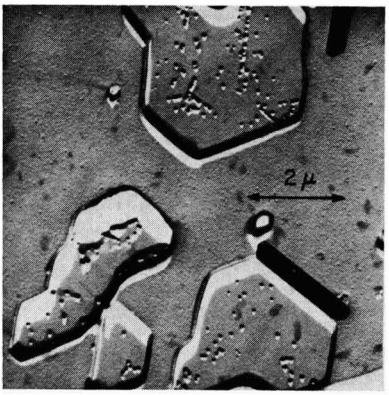

Fig. 2. Shadowed replica of part of Fig. 1

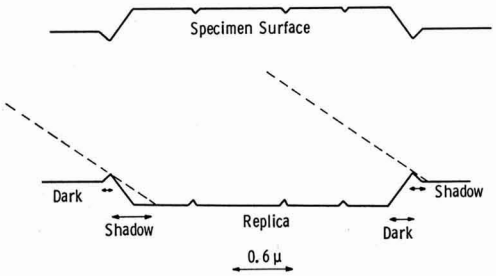

Fig. 3. Cross section of growth structure shown on top of Fig. 2

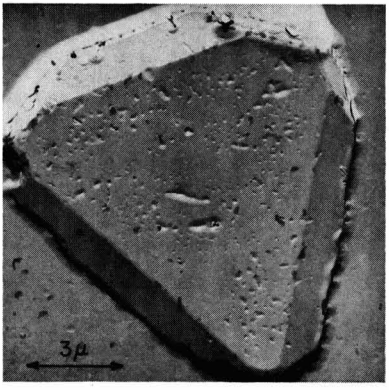

Fig. 4. Etch pit

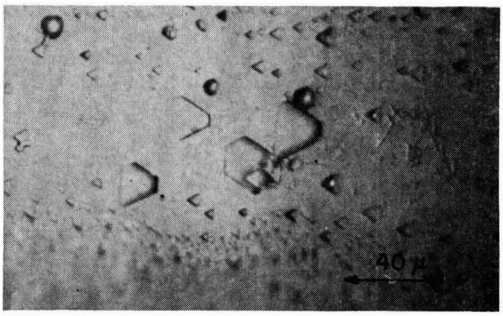

Fig. 5. Simultaneous formation of pits and hillocks

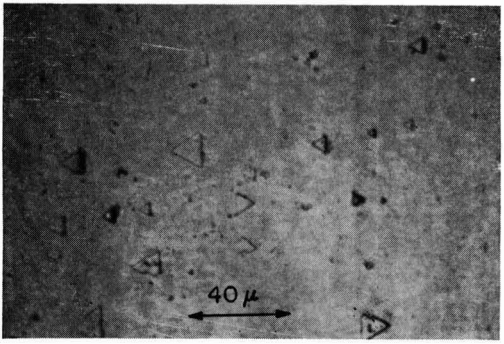

Fig. 6. Growth triangles pointing in opposite directions

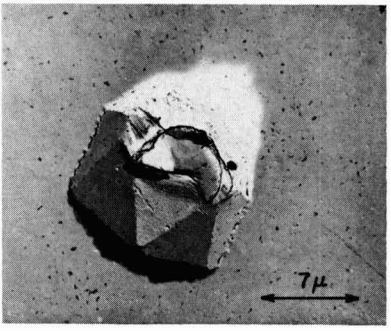

Fig. 7. Etch pit

vertical dimensions given in this figure are approximate. They were estimated from the width of the dark and light lines at the edge of the structure. The light lines represent areas that were in the shadow of protrusions on the replica. Figure 2 shows that the hillocks are surrounded by channels and that there are small pits on top of the hillocks.

On another crystal, the electron micrograph of the shadowed replica showed that small hillocks were formed at the bottom of the pits. This is illustrated in Fig. 4. A further example of simultaneous pit and hillock formation is shown in Fig. 5. The large truncated triangles are growth areas. Five or six circular growth structures can also be seen.

2. Growth triangles pointing in different directions.—Figure 6 shows another area of the same crystal used in Fig. 5. This picture was again taken using side illumination in order to show that all the triangles are growth structures.

3. Facets with orientations other than {111}.—In these experiments, facets other than {111} were found both in pits and in hillocks. Figure 7 shows the replica of an etch pit, and Fig. 8 shows {100} faces on some of the growth pyramids.

4. Other structures.—Examples of other unexpected structures are given here. Figure 9 shows the

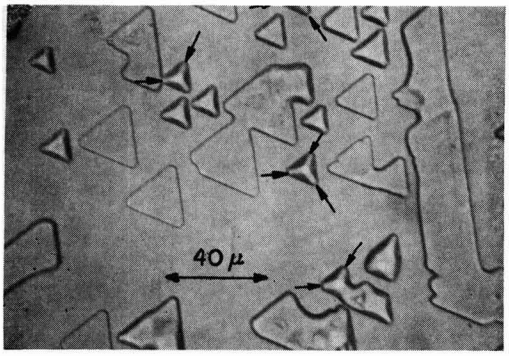

Fig. 8. Growth structures; some of the {100} faces are shown by arrows.

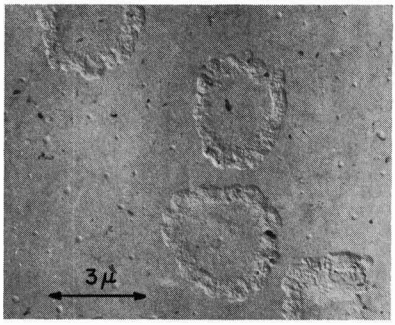

Fig. 9. Circular pattern

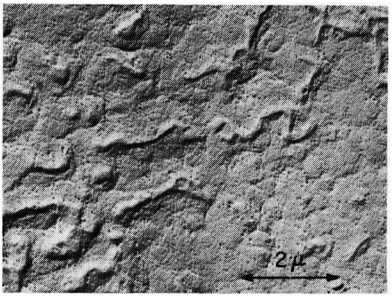

Fig. 10. Rough surface

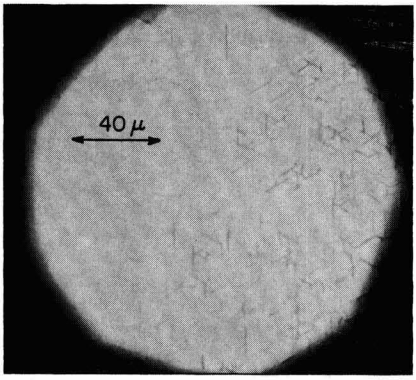

Fig. 11. Lines in <110> directions

replica of a circular pattern, while Fig. 10 shows the replica of a rough structure that was obtained even though the temperature during the heat treatment was nearly uniform. Figure 11 shows a structure that was often encountered. This consists of lines running in <110> directions. Due to the small difference in height of the lines it could not be proved unequivocally, but it is thought that they are depressions. They have an appearance similar to the "Y-etch figures" found in evaporated epitaxial films of germanium by Courvoisier *et al.* (2).

Heat treatment at temperatures close to 850°C often resulted in the formation of wormlike structures (3).

Discussion

While this work was in progress, Gatos and Lavine (3) described the deterioration of germanium surfaces on heat treatment. They examined one crystal at a time, thereby eliminating the complicating phenomenon of transport of material from one crystal to the other. Our work was directed towards the examination of deterioration encountered during device fabrication in general, with special emphasis on deterioration taking place in epitaxial growth experiments. Therefore, (*a*) in most cases several samples were used, and these were spread out along the tube; (*b*) the effect of temperature gradients was also examined; (*c*) when working under vacuum, the pressures in most cases were above 10^{-6} mm Hg.

In order to make the deterioration of the surfaces easier to observe, the period of heat treatment given to samples in this work was longer than that to which they would have been exposed during device preparation. However, deterioration to a lesser degree must occur over shorter periods. Similarly, the temperature gradients were larger than those usually encountered (see next paragraph).

When several crystals are used in the same experiment, it is difficult to assure that no temperature gradient occurs either during the heating up of the furnace or during the actual device preparation. Also, in experiments designed to examine the effect of deposition temperature on epitaxial growth, one may be tempted to place a series of substrates along a temperature gradient. Even when a gradient is not established on purpose, the gases, mostly flowing from the direction of a hotter source region, will establish a gradient along the cooler deposition region. Under such conditions, material may be transported from one sample to another through the vapor phase and also along the individual samples, both by surface diffusion and by transport in the gas phase.[1] In addition to the removal and deposition of complete epitaxial layers, the formation of tetrahedral pits with faces consisting of inclined {111} planes and having an apex pointing in the $[\bar{2}11]$ direction, and the deposition of growth triangles with an apex pointing in the $[2\bar{1}\bar{1}]$ direction is to be expected (4).

The formation of misoriented growth islands like the triangles having an apex pointing in the $[\bar{2}11]$ di-

[1] The observation that, when hydrogen was used, the deterioration of the surface was a function of the purity of the gas suggested that traces of oxygen may play a major role in the transport of germanium.

rection (Fig. 6) was probably caused by the presence of adsorbed impurities (4). Similarly, it is probably impurities that caused the formation of the other unexpected structures. Even though a crystal plane may break up into a hill and valley structure if the total surface free energy of the resultant structure is lower than that of the original plane (5, 6), in case of clean germanium surfaces, the {111} plane is the closest packed and should therefore have the lowest specific surface free energy, γ_s.

A certain amount of impurities must be present on any semiconductor surface that was in contact with solvents. Reversible and irreversible electrochemical deposition is to be expected (7). In addition, the complete removal of the solvent is unlikely, even when the solvent is blown off the surface of the crystal; during drying, the nonvolatile impurities[2] dissolved in the solvent will deposit on the surface. The effect of impurities on γ_s has been shown for some other systems (9-11). Even though the concentration of impurities may be less than what can be detected by studies of adsorption of oxygen on germanium (12), they may sufficiently change γ_s to cause deterioration of the surface. In the present work the effect of impurities is most evident in the appearance of planes other than {111} and also in the circular structures[3] shown in Fig. 9. The latter were probably caused by impurities deposited by the solvent.

Due to the relatively small weight changes, in most cases it was not possible to differentiate between the effect of flow to or from the vapor phase and that of surface diffusion. Thus three different explanations may be given for the formation of the structures shown in Fig. 1-3. The grooves around the hillocks may have been caused by deposition of an epitaxial film, this film not being able to grow around and link up with the faster growing areas. Or, if germanium was lost to the gas phase, the top of the hillocks may correspond to the original surface, perhaps the loss of germanium there being retarded by the presence of adsorbed impurities [a similar phenomenon was described by Rhead and Mykura (14); they found that when a silver crystal was heated, pyramids with shallow grooves around them were formed due to the loss of metal). Finally, the structures may have been formed by surface diffusion. The latter explanation may also hold in case of Fig. 4. Alternatively, in this case the growth at the bottom of the pits may have taken place by deposition during the cooling of the furnace.

Gatos and Lavine did not find any deterioration below 690°C. In this work, deterioration occurred even at 570°C. This discrepancy was probably caused by transport due to a thermal gradient, and also by the presence of impurities that were liberated from the quartz during sealing off when the experiments were performed in closed tubes.

[2] In case of organic solvents, such as methanol, oxidation and polymerization reactions can lead to the formation of nonvolatile residues (8).

[3] A similar phenomenon was found by Hale (13) on thermal etching of silicon.

Acknowledgments

The author thanks R. J. Engle for the electron micrographs, K. Liang for help with the experiments, and H. C. Chang, H. F. John, R. Stickler, and W. A. Tiller for helpful criticism of the manuscript.

Manuscript received Oct. 21, 1963. This paper was presented at the New York Meeting, Sept. 29-Oct. 3, 1964.

Any discussion of this paper will appear in a Discussion Section to be published in the June 1965 JOURNAL.

REFERENCES

1. T. Gabor, *This Journal*, **111**, 817 (1964).
2. J. C. Courvoisier, L. Jansen, and W. Haidinger, Transactions 9th Nat. Vacuum Symp., Amer. Vacuum Soc., 14 (1962).
3. H. C. Gatos and M. C. Lavine, *Ann. N. Y. Acad. Sci.*, **101**, 983 (1963).
4. G. R. Booker and R. Stickler, *J. Appl. Phys.*, **33**, 3281 (1962).
5. C. Herring, *Phys. Rev.*, **82**, 87 (1951).
6. W. W. Mullins, *Phil. Mag.*, **6**, 1313 (1961).
7. G. B. Larrabee, *This Journal*, **108**, 1130 (1961).
8. H. F. John, Symp. Cleaning Electronic Device Components and Materials, Tech. Pub. No. 246, Amer. Soc. Test. Materials (1958).
9. J. L. Walter and C. G. Dunn, *Acta Met.*, **8**, 497 (1960).
10. G. R. Hennig, Proc. 1st and 2nd Conf. Carbon, 103 (1956).
11. J. M. Blakely and H. Mykura, *Acta Met.*, **9**, 595 (1960).
12. M. Green and A. Liberman, *Phys. Chem. Solids*, **23**, 1407 (1962).
13. A. P. Hale, *Vacuum*, **13**, 93 (1963).
14. G. E. Rhead and H. Mykura, *Acta Met.*, **10**, 843 (1962).

Epitaxial Growth of Gallium Arsenide on Germanium Substrates

III. Deposition on High Index Planes and on Curved Surfaces

T. Gabor[1]

Research Laboratories, Westinghouse Electric Corporation, Pittsburgh, Pennsylvania

ABSTRACT

When depositing gallium arsenide on low index planes of germanium from the vapor phase by halogen transport, stacking faults are readily formed. Films free of these faults were obtained when planes that were at an angle of a few degrees with a {111} face or curved surfaces were used as substrates. It is suggested that fast propagation of steps along the surface caused the formation of new stacking faults parallel to the existing ones, thereby completing loops and preventing the propagation of the faults. The rate of growth was much faster on curved surfaces than over the {111} planes.

The formation of stacking faults in epitaxial films of gallium arsenide grown on low index planes of germanium substrates has been described in Part I of this series (1). Even though it is desirable to prevent the formation of faults, a method that would prevent the propagation of those faults that are formed may also be of interest. Such a method was found in the use of high index planes and of curved surfaces of germanium as substrates.

Experimental

The substrates were high index planes prepared from Czochralski-grown crystals, as-grown germanium webs (1) (the areas connecting the flat central part of these crystals with the dendrites, the so-called "fillet regions" are curved), and both {111} Czochralski crystals and webs with a curvature established over part of the surface.

Wafers were cut from a Czochralski ingot at 10° to a {111} plane in a <211> direction, and were then lapped, polished, and etched. Substrates 5° and 1° off the {111} plane were obtained by angle-lapping, polishing, and etching.

Several methods were used for the preparation of concave surfaces. For example a "Kodak Photo Resist" pattern, consisting of a series of channels separating square areas was etched into a {111} Czochralski crystal. The etching solution consisted of HF[1] : H_2O_2[1] : H_2O[4]. Depressions were also prepared by a jet etching technique (2). Alternatively, a Czochralski wafer was pressed against a rotating steel rod, and slurries of lapping and polishing powders were applied. In a few cases, convex surfaces were also prepared. Webs were touched with needles that were previously immersed into a solution of wax, or small, 7 mil diameter metal spheres coated with wax were made to adhere by short heating. After etching, a protrusion remained where the surface was covered with wax or with the sphere.

Details of the deposition experiments involving arsenic trichloride as the transporting agent in an open flow system have been described (1, 3). In one experiment with a web substrate, zinc chloride was used as the transporting agent in a sealed tube.

[1] Present address: Battelle Memorial Institute, Columbus, Ohio.

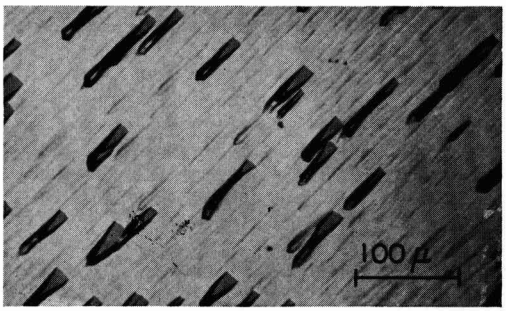

Fig. 1. Growth on substrate 10° off {111} plane. The long axis of triangles are in <211> direction.

Results

Gallium arsenide films free of stacking faults could easily be grown on high index planes and on curved surfaces of germanium, even under conditions such that deposition on {111} planes gave extremely poor films.

When using planar substrates, even though stacking faults were absent, triangular pits formed. Growth on a substrate that was cut at 10° to a {111} plane in a <211> direction is shown in Fig. 1. The pits point in a <211> direction, and their short side is at the same level as the surrounding growth while the apex is lower. Deposition on a plane 5° off the

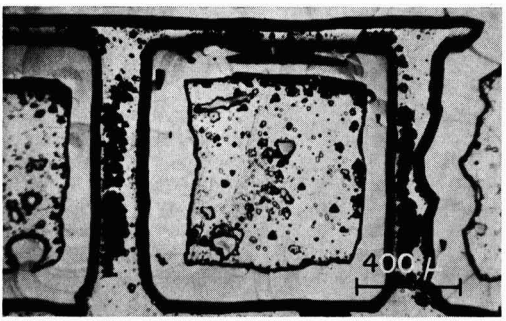

Fig. 2. Squares show {111} planes of a Czochralski crystal. Smooth growth of GaAs on the edges of squares took place over sloping sides of channels that were etched into the crystal.

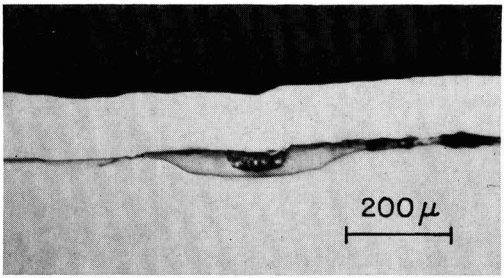

Fig. 3. Cross section through a channel and the surrounding areas of the sample shown in Fig. 2. Practically no growth took place over the {111} planes. Light colored band is cross section of nickel coating. Dark area inside channel is probably due to deposition of polycrystalline nickel.

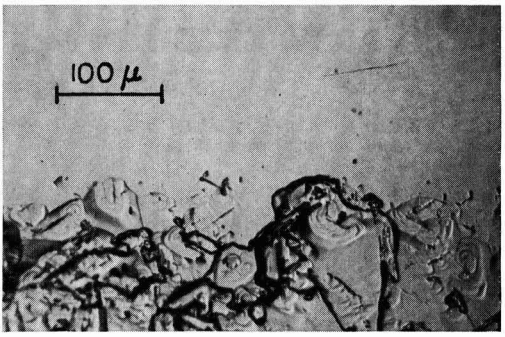

Fig. 4. Smooth area shows growth over curved fillet region of web. Poor growth shown in lower half of picture occurred over the {111} plane.

{111} gave similar results, while stacking faults were present when a substrate 1° off the {111} plane was used.

Only a few examples can be given of growth on curved substrates. When channels were etched into a crystal, smooth growth was obtained on the sloping sides, while there was practically no growth over the square {111} areas (Fig. 2). A cross section over a channel and over the surrounding square areas is shown in Fig. 3.

Figure 4 shows growth over the transition area between the {111} plane of a web and the curved fillet region. The extremely poor growth over the former was caused by a large amount of zinc chloride having been used for transport in a sealed tube. The polished and etched ($K_3Fe(CN)_6$[2] : H_2O[25] : KOH[3]; 40 sec) cross section in a {211} plane is shown in Fig. 5. The area below the curved line is the fillet region. The striations in the gallium arsenide may have been caused by impurity segregation. The few stacking faults that could be revealed did not originate as usual at the Ge-GaAs interface, but in an area where the growing film has already established a crystallographic plane. The same etch revealed a highly misoriented growth [presence of grains (1) throughout the whole film] over the {111} areas. The thickness of the film over the {111} areas was less than half of that over the curved region.

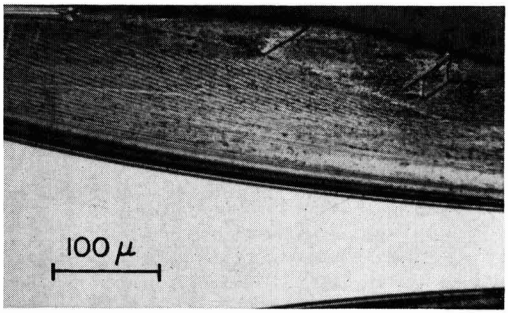

Fig. 5. Cross section in {211} plane of sample shown in Fig. 4. Light area shows the fillet region of web, darker area with the striations the GaAs film.

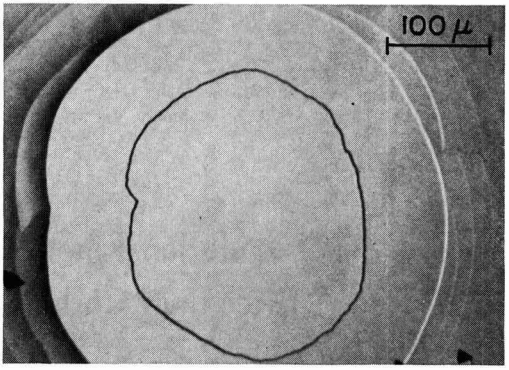

Fig. 6. Growth over protrusion on substrate

Growth obtained over a convex area is shown in Fig. 6.

Discussion

It has previously been shown (4) that the crystallographic perfection of epitaxial germanium films grown on germanium substrates was improved when the substrates were cut at an angle of a few degrees with the {111} plane. High index planes and curved substrates both have surfaces which are composed of an infinitesimal number of atomic steps. One would expect deposition at these steps to be energetically favored, causing these steps to "flow" along the surface.

It has been suggested (1) that independent nucleations may be required for growth on the two sides of a fault; thus the propagation of a step parallel to the surface may be prevented along the intersections of stacking faults with the surface. If the rate of growth parallel to the surface is increased, as must be the case when the surface consists of an infinitesimal number of steps, there might not be sufficient time for independent nucleations to take place, so that the areas having the wrong stacking order may be overgrown by the film without the latter changing its stacking order. This corresponds to the formation of intrinsic faults parallel to extrinsic faults that may be present and vice versa. Figure 7 shows that a loop is thus created and the propagation of the fault is prevented.

The formation of pits in films grown on high index planes may be caused by the inability of the ad-

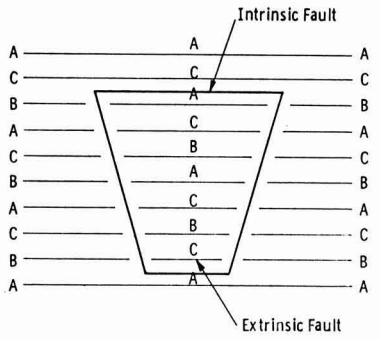

Fig. 7. Intrinsic fault generated due to fast sidewise growth of C-layer (2nd from top). Propagation of fault is prevented by loop formation.

vancing steps to overgrow all areas where there is an obstacle to growth. Once a difference in level is established between the film and the area containing the fault, the overgrowth by successive steps should be always less likely. The bottom of the pit then establishes the energetically favorable {111} surface.

We can only speculate on the reason for the presence of pits when high index planes were used as substrates and for their absence in films grown on curved surfaces. The formation of pits may be related to the relative positions of the favored growth direction and the direction of the steps.

Acknowledgment

The author thanks K. Liang for his help with this work, H. D. Larson for performing the cross sectioning and polishing operations, and H. C. Chang and W. A. Tiller for helpful discussions.

Manuscript received Oct. 23, 1963. This paper was presented at the Pittsburgh Meeting, April 15-18, 1963.

Any discussion of this paper will appear in a Discussion Section to be published in the June 1965 JOURNAL.

REFERENCES

1. T. Gabor, *This Journal*, **111**, 817 (1964).
2. G. R. Booker and R. Stickler, *Brit. J. Appl. Phys.*, **13**, 446 (1962).
3. R. R. Fergusson, T. Gabor, *This Journal*, **111**, 585 (1964).
4. H. S. Ingham, P. J. McDade, and D. M. J. Compton, *Met. Soc. Conf.*, **12**, 285 (1960).

The Oxidation Kinetics of Zirconium Diboride and Zirconium Carbide at High Temperatures

A. K. Kuriakose[1] and J. L. Margrave[1]

Department of Chemistry, University of Wisconsin, Madison, Wisconsin

ABSTRACT

Kinetic studies have been made of the oxidation of zirconium diboride at 945°-1256°C, and of zirconium carbide at 554°-652°C. The ZrB_2-O_2 reaction is parabolic throughout the temperature range studied, whereas the ZrC-O_2 reaction is linear. In the former case ZrO_2, together with a molten layer of boron oxide, is formed which protects against further direct attack of oxygen on the ZrB_2, while in the latter, a rather porous film of zirconium oxide is formed which is not protective. The rate of oxidation of ZrB_2 is directly proportional to the oxygen partial pressure between 102 and 744 mm.

Because of the very refractory nature, hardness, and high tensile strengths, in general, of the borides, carbides, and nitrides of the transition metals, they are promising materials in many high-temperature applications. A knowledge of the oxidation kinetics of these materials is essential for such uses, and hence the present investigation of the high-temperature oxidation kinetics for zirconium diboride and zirconium carbide was undertaken.

The oxidation of ZrB_2 has been studied by Brown (1), Berkowitz (2), and Meerson *et al.* (3). Brown, working at atmospheric pressure in the temperature range 649°-1315°C, observed a minimum rate of oxidation around 1000°C, an accelerated rate in pure oxygen compared to dry air, and a much higher rate in moist air than in dry air. Berkowitz found a parabolic rate law to be followed after the first 40 min of oxidation at an oxygen partial pressure around 10 Torr, between 1200° and 1530°C. Brown used porous compacts of the diboride, and there were uncertainties in the surface areas, whereas Berkowitz used electron-beam melted samples of high purity. Meerson *et al.*, from metallographic examination of the scales formed on ZrB_2 on oxidation in air at 1000°C, suggested the presence of ZrO covered by molten B_2O_3 during the initial stages of the reaction. According to them, as oxidation proceeds, B_2O_3 slowly evaporates and oxygen, while diffusing through ZrO, reacts with it to form ZrO_2 in about 10-20 hr. Berkowitz, however, found only ZrO_2 and no evidence for the presence of ZrO in the oxidation product. The resistance of ZrB_2 to scale formation was investigated also by Markevich and Markovskii (4).

Very recently, Bartlett, Wadsworth, and Cutler (5) reported an investigation of the kinetics of oxidation of ZrC powder in the temperature region 450°-580°C, and Berkowitz (2, 6) the oxidation kinetics of a zone-refined ZrC at 853°-1892°C. Watt,

[1] Present address: Department of Chemistry, Rice University, Houston, Texas.

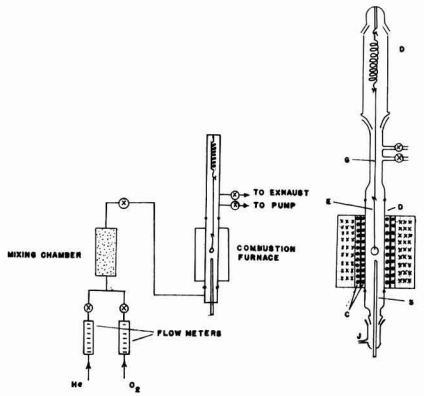

Fig. 1. Schematic diagram of the apparatus used for studying high temperature oxidation kinetics. a (left) Diagram of gas-flow system. b (right) Combustion furnace and accessories.

Crockett, and Hall (7), Thielke (8), and Hinnüber and Rüdiger (9) have also made some measurements on the oxidation of ZrC.

This investigation covers the temperature ranges 554°-652°C for ZrC and 945°-1256°C for ZrB_2, at oxygen pressures up to 744 mm Hg. The progress of reaction was derived by observing directly the weight gained by the samples with time. Electron-beam melted samples of both ZrB_2 and ZrC were used. Only specimens which did not have any apparent cracks were utilized.

Apparatus and Experimental Procedure

A schematic diagram of the gas-flow system and the apparatus is given in Fig. 1a. Figure 1b presents a detailed view of the combustion furnace and accessories. The mullite combustion tube, A, (15 in. long and 1½ in. diam) is mounted vertically and heated by two concentric furnace windings, C, of Kanthal wire. The inner winding is on the mullite itself. Pyrex tubes with standard ground-glass joints are sealed on to the mullite tube at both ends. An inlet tube, J, for the reacting gas, and a chromel-alumel thermocouple, F, are attached from the bottom, and two outlets are provided at the top, one for evacuating the system and the other for venting the gases to the hood. A helical quartz spring, D, calibrated for load *vs.* extension is suspended vertically as shown in the figure and the sample to be examined is attached to the lower hook of the spring by means of 0.007 in. nickel wire and a piece of quartz fiber, E, so that the sample, S, is only about 1 cm above the thermocouple bead. The proximity of the sample to the thermocouple insures accurate temperature measurement of the sample. The temperature of the heating furnace is regulated to ±2°C. When the extension of the spring is measured by means of a cathetometer, a change in weight of 0.2 mg can be determined, and with the relatively low sensitivity of the spring no vibrations were caused by the gas-flow through the system.

All the experiments were done at a total pressure of 740 ± 5 mm, and various partial pressures of O_2 were obtained by mixing it with purified helium gas. The sample was initially heated in an atmosphere of helium to the desired temperature and the zero reading on the cathetometer taken against a fixed point (end) on the suspension wire. The system was then evacuated, O_2 gas was suddenly admitted, and the flow rate slowly adjusted. The time when oxygen was introduced was taken as zero. The readings of the cathetometer at suitable intervals of time were recorded and each run was continued until a sufficient number of points was obtained to establish the kinetics of the process.

The zirconium diboride used had a composition $ZrB_{1.95}$ with 1.7% of Hf and a carbon content of about 200 ppm. Circular pieces of the material weighing about 0.5-0.8g were cut from zone-melted cylindrical bar and polished by grinding with fine abrasive powder. Any small cracks on the sample were visible and the cracked portions, if any, were removed by breaking them off. The specimens were then thoroughly washed with water and dried in air. The areas of the samples were calculated from the measured dimensions to the nearest 1 mm^2. A similar procedure was used for the zirconium carbide samples. The electron-beam melted ZrC was 99.5+% pure with trace impurities.

The oxide films on the oxidized samples of ZrB_2 were removed by microsand blasting. The same piece could be repolished by grinding again and, thus, could be used several times. This method, apparently, did not affect the nature of the substrate material, and identical rates of oxidation within experimental error were observed (*cf.* section on prerun treatment). In the case of ZrC, separate pieces were used for each run.

Results and Discussion

Oxidation of Zirconium Diboride

From the extension of the spring at various intervals of time, the weight gains of the sample in milligrams per square centimeter at the respective time intervals were evaluated. The straight lines which were obtained by plotting (weight gain/square centimeter)^2 *vs.* time (Fig. 2) show that the oxidation of ZrB_2 follows a parabolic rate law. Rate

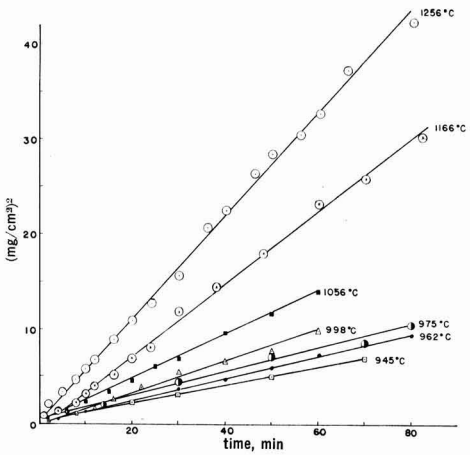

Fig. 2. Parabolic plot for the oxidation of ZrB_2 in pure oxygen at 945°-1256°C. Oxygen pressure, 1 atm.

Table I. Parabolic rate constants for the oxidation of ZrB_2 at 1056°C after various prerun treatments

Prerun treatment	Parabolic rate constant, $(mg/cm^2)^2/min$
Preheated for ½ hr at the temperature of the experiment	0.2368
Oxidized sample repolished and no preheating	0.2459
Fresh sample with no preheating	0.3000

Table II. Parabolic rate constants with various flow rates of O_2 in the oxidation of ZrB_2 at 1056°C

Flow rate, ml/min	Rate constant, k_p, $(mg/cm^2)^2/min$
20	0.2206
50	0.2612
100	0.2459

constants were obtained from the slopes of the straight lines.

Prerun treatment.—The prerun treatment was varied in a few runs and the parabolic rate constants obtained in each case are recorded in Table I. These data indicate that there is no significant change in the rate of oxidation of ZrB_2 when the sample is preheated or when the oxidized material is repolished and used without preheating, although when a fresh piece is used without preheating, the rate constant is higher. Hence, in all the other runs the fresh sample was either preheated for ½ hr or the oxidized surface was repolished and used with no preheating. For ZrC, the sample was preheated for ½ hr for each run.

Flow rates.—Runs were done with O_2 flow rates of 100, 50, and 20 ml/min, at 1056°C in order to determine the effect of flow rate on the reaction, and the rate constants (parabolic) obtained in these cases are reported in Table II. It is evident from this table that the rate of oxidation of ZrB_2 is independent of the flow rate of O_2 in the system in the range studied, within experimental error.

Effect of oxygen partial pressure.—Figure 3 presents the parabolic plot of the results obtained at various O_2 partial pressures (102–744 mm of mercury, mixed with helium gas) for the oxidation of

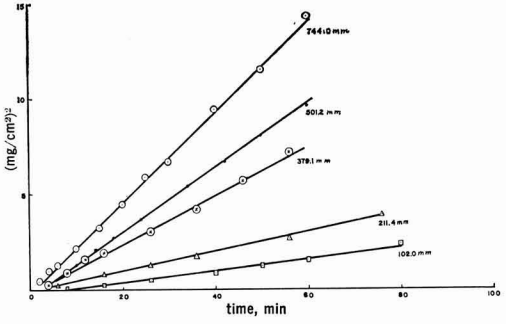

Fig. 3. Parabolic plot for the oxidation of ZrB_2 at various oxygen partial pressures. Temperature, 1056°C.

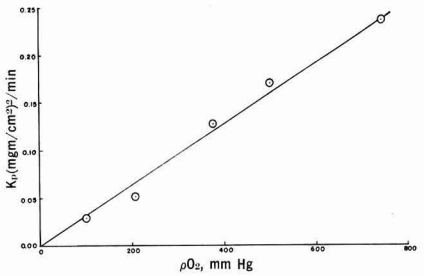

Fig. 4. Effect of O_2 partial pressure on the oxidation of ZrB_2. Temperature, 1056°C.

ZrB_2 at 1056°C. The oxidation rate increases with increasing partial pressure of O_2, and the increase in the parabolic rate constant is directly proportional to the partial pressure of O_2 as indicated by Fig. 4 which is a plot of the rate constants against the partial pressure.

Effect of temperature.—In order to obtain the activation energy for the reaction between ZrB_2 and O_2, experiments were carried out at various temperatures ranging from 945° to 1256°C at a pressure of 740 ± 5 mm and an O_2 flow rate of 100 ± 5 ml/min. The parabolic rate constants calculated in each case are listed in Table III. The Arrhenius plot of the results is linear with an activation energy of 19.8 ± 1.0 kcal/mole, calculated by a least-square method. Because of the volatility of boron oxide, one would expect the rate constant to fall off in the log k *vs.* $1/T$ plot at higher temperatures. This is apparently not the case, possibly, because the loss in weight by evaporation of B_2O_3 is compensated for by an increased oxidation due to less thickness in the protective oxide film. The activation energy of 19.8 kcal is in contrast to the value 66 kcal obtained by Berkowitz, although the rate constants in both this investigation and hers at about 1256°C were in excellent agreement (10). The variation in the activation energy must arise because of a change in the mechanism of oxidation. This point is further confirmed by the recent investigation of Berkowitz (11) who obtained an activation energy of 25 ± 6 kcal/mole in the temperature range below 1400°K for the oxidation of ZrB_2. The oxidation product was x-ray analyzed and was found to contain zirconium dioxide. The ethyl borate test showed the presence of boron oxide in the scales.

Table III. Parabolic rate constants for the oxidation of ZrB_2 at various temperatures
O_2 Pressure, 740 ± 5 mm; flow rate, 100 ml/min

Temperature, °C	Parabolic rate constant, $(mg/cm^2)^2/min$
945	0.1019
962	0.1190
975	0.1435
998	0.1653
1056	0.2459
1056	0.2368
1166	0.3899
1256	0.5625

ΔE_a = 19.8 ± 1.0 kcal/mole

Presence of water vapor in the oxygen gas.—In one of the experiments, oxygen was bubbled through distilled water and passed into the combustion tube containing ZrB_2 at 1056°C, to study the effect of moist oxygen on the reaction. A parabolic reaction rate was observed and the rate constant in this run [0.20 $(mg/cm^2)^2/min$] was identical, within experimental error with that for dry oxygen under similar conditions [0.24 $(mg/cm^2)^2/min$]. The slight decrease in the rate might be attributed to: (*i*) a reduction in the partial pressure of oxygen from 744 to 719 mm due to the presence of water vapor, and (*ii*) the formation of boric acid which is more volatile than B_2O_3, which would cause a further decrease in the observed rate of weight gain. Glistening white crystals of boric acid were observed on the cooler parts of the combustion tube. It was further noticed, unlike in other cases, that the ZrB_2 became very brittle after being exposed to moist oxygen. It should be mentioned that Brown (1) reported a greater rate in moist air than in dry air.

Oxidation of Zirconium Carbide

Zirconium carbide is more susceptible to oxidation than zirconium diboride and at lower temperatures. Pieces of zirconium carbide were found to break up immediately in contact with O_2 at 1000°C or even lower. Berkowitz (12) also has observed the same phenomenon. Gangler (13) found excessive oxidation of ZrC in air at 980°C and Watt, Crockett, and Hall (6), rapid oxidation in air at 800°C. In order to find a workable temperature range for studying the oxidation kinetics, a piece of ZrC was heated slowly from room temperature in an atmosphere of oxygen. The sample began to crumble at about 700°C and broke up into several pieces at about 850°C, so that the maximum workable temperature was about 650°C. Even at this temperature, samples started crumbling after about an hour of oxidation. A porous film of zirconium oxide (identified by x-ray diffraction) was formed on the sample. The results of the successful runs at 554°-652°C are presented graphically in Fig. 5. It is clear that the reaction follows a linear rate law at 740 ± 5 mm pressure of O_2 and a flow rate of 100 ± 5 ml/min. The linear rate constants at various temperatures are given in Table IV. The activation energy calculated in this case from the Arrhenius plot is 16.7 ± 1.7 kcal/mole. This activation energy is lower than the 45.7 kcal/mole reported by

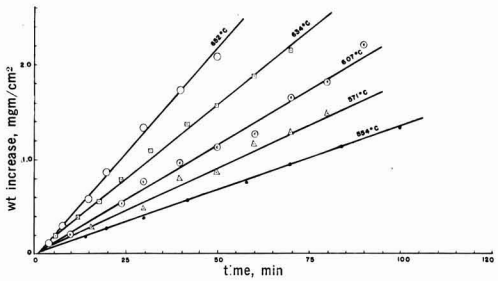

Fig. 5. Linear plot for the oxidation of ZrC at various temperatures. O_2 pressure, 740 ± 5 mm; O_2 flow rate, 100 ml/min.

Table IV. Rate constants for the ZrC-O_2 reaction at various temperatures
Oxygen pressure, 740 ± 5 mm

Temperature, °C	Linear rate constant, k_l, $mg/cm^2/min$
554	0.01371
571	0.01818
607	0.02320
634	0.03153
652	0.04444

ΔE_a = 16.7 ± 1.7 kcal/mole

Bartlett *et al.* (5) from their study of the oxidation rate of powdered ZrC over the range 450°-580°C. Bartlett (14), in his thesis, notes that the temperature-dependence above 580°C is noticeably lower so that a change in reaction mechanism is again implied. One might suspect that the spalling off of flakes of ZrC or ZrO_2 as oxidation occurs could cause an apparently slow reaction, but this would have been detected by the sensitive balance used unless the particles are extremely small. An alternative suggestion is that a diffusion-controlled oxidation process through a protective Zr-O-C film predominates at low temperatures while a linear process which produces a porous ZrO_2 and gaseous CO_2 takes over in the range above 580°C.

Conclusions

The oxidation of zirconium diboride, between the temperatures 945° and 1256°C follows a parabolic rate law over the first hour of oxidation. The oxidation products seem to be the oxides of Zr and boron, with the boron oxide present as a molten layer on the surface. Part of the boron oxide slowly vaporizes at high temperatures as indicated by a white deposit on the cooler parts of the combustion tube after several runs. Variations in flow rate of oxygen in the experimental system from 20-100 ml/min have practically no effect on the rate of oxidation (at 1056°C) but a direct dependence on the partial pressure of O_2 (mixed with helium) was observed. The Arrhenius plot of the rate constants for the oxidation of ZrB_2 between 945° and 1256°C is linear and gives an activation energy of 19.8 kcal/mole.

The oxidation of zirconium carbide follows a linear rate law at 554°-652°C, and at higher tem-

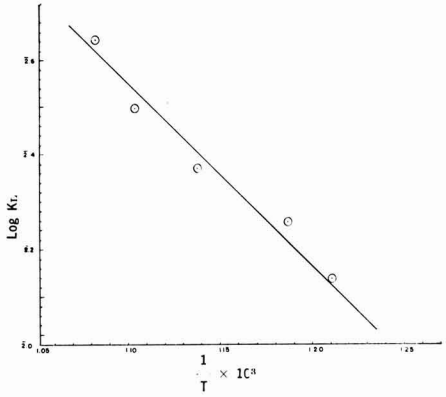

Fig. 6. Arrhenius plot for ZrC-O_2 reaction. O_2 pressure, 1 atm

peratures, a destructive oxidation of the material takes place in pure O_2. The activation energy for the oxidation of ZrC based on data at 554°-652°C is 16.7 kcal/mole.

Acknowledgments

The authors are pleased to acknowledge the financial support of this work by the United States Air Force through Contract No. AF 33(616)-7472 administered by Dr. Leslie McClaine for A. D. Little, Inc. The samples of ZrB_2 and ZrC were prepared by Dr. George Feick, of A.D. Little, Inc., and were typical high-purity zone-refined materials like those being currently used for heat of formation (15) and heat capacity studies (16, 17). Computer time and facilities of the Numerical Analysis Laboratory were made available through the Wisconsin Alumni Research Foundation.

Manuscript received March 27, 1963; revised manuscript received Nov. 1, 1963.

Any discussion of this paper will appear in a Discussion Section to be published in the June 1965 JOURNAL.

REFERENCES

1. F. H. Brown, Jr., Progress Report No. 20-252, Jet Propulsion Laboratory, Pasadena, California, February 25, 1955.
2. J. Berkowitz-Mattuck, "Thermodynamic and Kinetic Studies for a Refractory Materials Program," ASD-TDR 62-204 Part II, May 1963.
3. G. A. Meerson, G. V. Samsonov, R. B. Kotel'nikov, M. S. Voinova, I. P. Evteeva, and S. D. Krasnenkova, *Sbornik Nauch. Trudov. Nauch.-Tekh. Obshchestva Tsvetnoi Met., Moskov. Inst. Tsvetn. Metal. Zolota*, 1959, No. 29, 323-8; *C. A.*, **54**, 10781e (1960).
4. G. S. Markevich and L. Ya. Markovskii, *Zh. Prikl. Khim.*, **33**, 1008 (1960).
5. R. W. Bartlett, M. E. Wadsworth, and I. B. Cutler, *Trans. Met. Soc., AIME*, **227**, 467 (1963).
6. J. Berkowitz-Mattuck, "Kinetics of Oxidation of Refractory Metals and Alloys at 1000°-2000°C," ASD-TDR-62-203, Part II, March 1963.
7. W. Watt, G. H. Crockett, and A. R. Hall, *Metaux Corr-Ind.*, **28**, 222 (1953).
8. N. R. Thielke, WADC, TR54-467, Pennsylvania State University.
9. J. Hinnüber and O. Rüdiger, *Arch. Eisenhüttenw.*, **24**, 267 (1953).
10. Leslie A. McLaine, A. D. Little, Inc., San Francisco, California, Private communication, June 12, 1963.
11. J. Berkowitz-Mattuck, "Thermodynamic and Kinetic Studies for a Refractory Materials Program," Progress Report to Air Force Materials Laboratory, Aeronautical System Divisions, August 1963.
12. J. Berkowitz-Mattuck, "Thermodynamic and Kinetic Studies for a Refractory Materials Program," Progress Report to Aeronautical Systems Division, August 1962.
13. J. J. Gangler, Amer. Ceramic Soc. 52nd Annual Meeting, Preprint, 1950 (as cited in P. Schwartzkopf and R. Kieffer, "Refractory Hard Metals," MacMillan Publishing Co., New York, 1953) p. 195.
14. R. W. Bartlett, Ph.D. Thesis, University of Utah, 1961, p. 110.
15. G. Johnson, E. Greenberg, W. Hubbard, and J. Margrave, Abstracts, 145th American Chemical Society Meeting, New York City, September 13, 1963.
16. E. F. Westrum, Jr. and G. Feick, *J. Chem. Engr. Data*, **8**, 176, 193 (1963).
17. R. Mezaki, R. Valentine, T. Jambois, and J. Margrave, *ibid.*, (1963).

"Oxygen" Adsorption and Double Layer Capacities; Gold in Perchloric Acid

G. M. Schmid and R. N. O'Brien

Department of Chemistry, University of Alberta, Edmonton, Alberta, Canada

ABSTRACT

The "oxygen" adsorption on polycrystalline Au in 1*N* $HClO_4$ was studied between 0.4 and 1.43v *vs.* SCE at 5°, 25°, and 50°C, using cathodic galvanostatic stripping and rapid single pulse differential capacity measurements. A potential arrest at 0.5v is ascribed to surface Au-OH and/or Au-O formation, a plateau at 1.0v to surface oxidation to Au_2O_3, probably occurring in patches. The appearance of a maximum in the differential capacity-potential curve during the adsorption process is explained on the basis of an additional capacity, C_{ads}, of the inner double layer due to the presence of the charges of the (specifically) adsorbed species. It is shown that C_{ads} should be proportional to the slope of a plot of amount adsorbed *vs.* potential. The model proves satisfactory for surface "Au-OH" build-up to 1/3 of a monolayer, and on decomposition from a monolayer.

Adsorption and desorption processes on metal electrodes are frequently accompanied by a large maximum in the capacity-potential curve (1). It was shown by Lorenz (2) that the capacity maximum decreases with increasing measuring frequency but does not disappear even at 700 kc. At such frequencies the capacity can reasonably be assumed to be free of faradaic effects and to represent the capacity of the ionic double layer only.

In previous papers (3, 4) the electrical double layer (edl) differential capacities of gold in $HClO_4$ were reported as a function of potential. A rapid single pulse technique (5) was used to exclude the influence of the faradaic impedance. The zero point of charge was determined to be close to 0.0v on the saturated calomel electrode (SCE) scale (including a saturated KCl-$HClO_4$ junction potential) (4, 6). A number of maxima in the capacity-potential curve were attributed to hydrogen adsorption, some specific ClO_4^- adsorption, and to the adsorption of an unknown, oxygen-containing species.

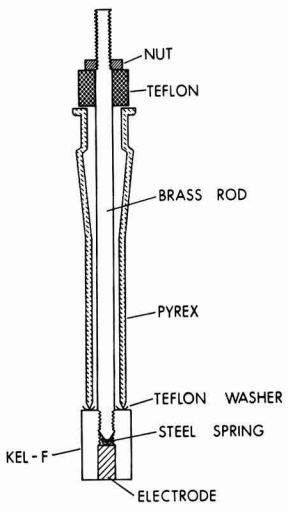

Fig. 1. Electrode assembly

An attempt to explain the behavior of the capacity of the ionic double layer on the basis of a change in dielectric constant due to the adsorbed species was made by Devanathan (7). In the present investigation the appearance of a capacity maximum on adsorption (or desorption) is attributed to the presence of the charge of the (polarized or charged) adsorbed species in the inner double layer.

The gold-"adsorbed oxygen" system was chosen because of the ease with which both the amount adsorbed (or desorbed) and the edl capacity can be measured, thus making possible a ready comparison between the two quantities.

Experimental

The electrodes were polycrystalline mint gold purchased from Engelhard Industries, Inc., Newark, New Jersey. Rods were pressure-sealed into Kel-F, cut to expose a cross-section of 0.086 cm^2 apparent area, and joined to a Pyrex glass holder using a Teflon washer, brass rod, and nut (Fig. 1). Before each experiment, the electrodes were abraded with 4/0 emery paper, washed with distilled water, degreased with acetone in a Soxhlet, and washed with conductivity water.

Conductivity water was prepared by redistilling tap distilled water from an alkaline permanganate solution in a Pyrex still, followed by distillation in a Heraeus two-stage quartz still. The electrolyte, 1*N* $HClO_4$ in all cases, was prepared from 70% reagent grade $HClO_4$ by appropriate dilution with conductivity water. Before each run it was purified by pre-electrolysis between Pt electrodes with a minimum of 35 coulombs/ml, and degassed by passing a steady stream of Grade A Helium for at least 12 hr.

The all Pyrex cell contained, in addition to the Au electrode, a cylindrical platinized Pt wire gauze as counter electrode, and two SCE's, the latter being connected to the main compartment by closed, ungreased stopcocks and capillaries. The cell had a

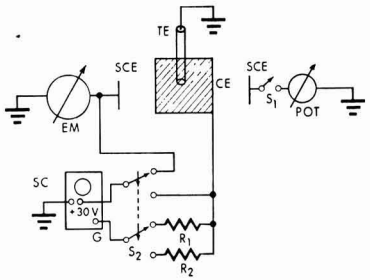

Fig. 2. Circuit diagram. TE, test electrode; CE, counter electrode; SCE, saturated calomel electrode; EM, Keithley 610A electrometer; POT, Sensitive Research Instr. Corp. PV potentiometer; SC, Tektronix 535A oscilloscope; G, gate; R_1, R_2, series resistor; S_1, S_2, switch. A stripping curve is being taken.

water jacket and was thermostated at 5°, 25°, and 50°C to ±0.1°C with a Colora Ultra Thermostat.

The test electrodes were polarized with a Hickling potentiostat (8). In the low current density region ($i < 0.1$ μa, +0.2 to +1.43v) the potentiostat did not give satisfactory results and was replaced by a Sensitive Research Instrument Corp. Model PV potentiometer applied between test electrode and a SCE. The potential was monitored with a Keithley 610A electrometer (input impedance 10^{14} ohms) applied between test electrode and the second SCE. The potentials are reported with respect to SCE at 25°C.

For the edl differential capacity measurements a rapid single pulse technique was used, as described elsewhere (5). The method essentially consists of measuring the slope of the potential-time curve of the test electrode at the onset, or a time very close to it, of a fast rise, rectangular current pulse. The potential-time curves were displayed on a Tektronix Type 535A oscilloscope, operated on "single sweep," with a Type D preamplifier, and connected between test and counter electrode (Fig. 2). The traces were photographed with a Tektronix Type C-12 Polaroid camera. Approximately +30v appear at the gate of the oscilloscope for the duration of the push button triggered sweep. The current pulse, of a length up to 50 μsec, was taken from this gate and dropped through a suitable resistor to give 617 μa. In the investigated potential range (0.4 to 1.4v) the potential-time curve was a straight line over at least the first 40 μsec, indicating the absence of a faradaic impedance during this period. The desired slope could be measured about 1 μsec after the onset of the pulse. The measurement thus corresponds to an a-c determination with a base frequency of more than 500 kc and represents the differential capacity of the ionic double layer only. The accuracy of the measurement is limited by the non-linearity of the oscilloscope amplifiers to ±3%.

The coverage with oxygen-containing adsorbed species was determined by constant current cathodic stripping. For this purpose the oscilloscope was connected between test electrode and SCE, and the gate of the oscilloscope, through a series resistor, between test and counter electrode (Fig. 2). The potential of the test electrode was set to the desired value. The potentiometer was then switched off and the oscilloscope triggered simultaneously. All stripping was done with 121 μa. The low input impedance of the oscilloscope (1 megohm) causes an iR drop of 30 mv at 1.4v to appear between test electrode and SCE (as measured with the Keithley). A corresponding correction was applied to all potentials reported.

Reproducible results were obtained only after repeated anodic and cathodic cycling to the highest anodic potential used in this study (+1.43v) and to −0.5v. This pretreatment presumably removes oxidizable and reduceable impurities from the electrode surface (9). It also seems to introduce roughening of the surface until a constant state is reached. After cycling, capacity data were taken, beginning at about +0.4v through +1.4v and back to the starting point. The potential was changed in steps of 100 mv every 10 min, except in the vicinity of the maximum where the steps were 50 mv only. The capacity reaches a constant value after 2-5 min and does not change over a period of up to 1 hr. Stripping curves were then taken in steps of approximately 100 mv, starting from cathodic potentials through +1.43v, allowing 10 min at each potential for the adsorption to come to a steady state. The potential was then set to +1.43v for 10 min, changed to a less anodic potential, and a stripping curve taken from there 10 min later. This procedure was repeated for successively less anodic potentials, always allowing the electrode to come to a steady state at +1.43v first.

All data reported are referred to the estimated true surface area. From freshly prepared electrode to freshly prepared electrode the reproducibility of the capacity data was ±15%. This was attributed to difficulties in reproducing a definite roughness factor. The capacity curves were normalized to an (arbitrary) capacity of 16 μf/cm² at the capacity minimum just before the rise to the anodic adsorption maximum. The procedure was tantamount to using a roughness factor varying between 2.1 and 2.5. The reproducibility of the capacity data was then ±5%. The stripping data were reproducible to ±10% as calculated with an average roughness factor of 2.3.

Results

Figure 3a shows the coverage with "oxygen-containing" species obtained on a Au electrode in 1*N* $HClO_4$ at three different temperatures. Adsorption starts at around 0.5v and increases up to 1.43v without any indication of reaching a constant magnitude. Average values at 1.43v are 1440, 1200, and 1100 μcoulomb/cm² for 5°, 25°, and 50°C, respectively. The adsorption is highly irreversible and this can be seen in Fig. 3b which shows the residual coverage after holding the potential at 1.43v, and then at the anodic starting potential for 10 min each. Desorption of the adsorbed species occurs in two very pronounced steps at about 1.0 and 0.5v.

The charge involved in the step at 1.0v can be separated from the charge involved in the step at 0.5v on the basis of the oscilloscope traces obtained during cathodic stripping, both for adsorption (increasing potentials) and for desorption (decreasing potentials). The duration of the plateau at 1.0v was taken from the beginning of the trace to the inflection point following the potential arrest; of the

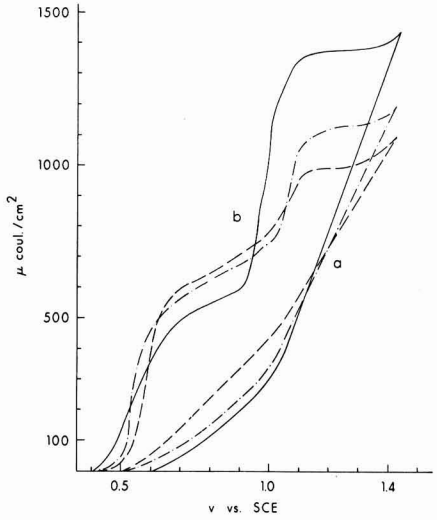

Fig. 3. "Oxygen" coverage as a function of potential. Au in 1*N* $HClO_4$. 5°C, ——; 25°C, — · —; 50°C, — — —. a. For increasing potentials; b, for decreasing potentials after steady state at 1.43v.

plateau at 0.5v from the inflection point before to the inflection point after the arrest. The potential rise to the plateau took less than 0.05 sec in most cases, the error involved in this procedure is therefore small, but may account partly for the reproducibility being ±10% only.

The results are shown in Fig. 4. Adsorption starts at approximately 0.5 and 1.0v respectively and shows no tendency to level off even at 1.43v (except perhaps at 5°C in Fig. 4a). The irreversibility already evident in Fig. 3 is again visible in Fig. 4. A pronounced negative temperature coefficient becomes apparent for the plateau at 1.0v, whereas the coverage causing the plateau at 0.5v increases with

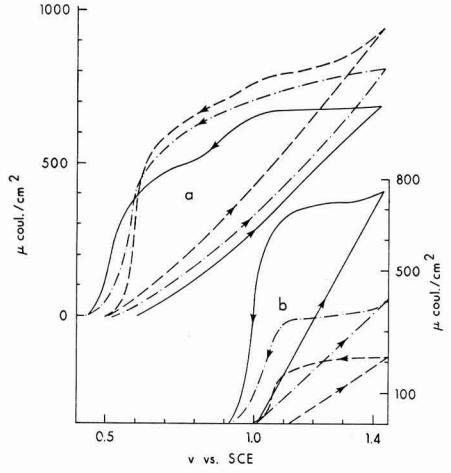

Fig. 4. "Oxygen" coverage as a function of potential. Au in 1*N* $HClO_4$. 5°C, ——; 25°C, — · —; 50°C, — — —. a, Plateau at 0.5v; b, plateau at 1.0v; both for increasing and decreasing potentials.

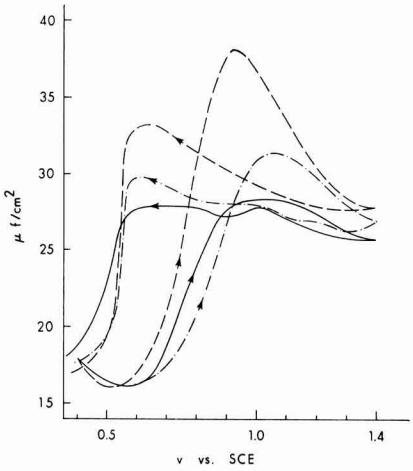

Fig. 5. Differential capacity as a function of increasing and decreasing potentials. Au in 1*N* $HClO_4$. 5°C, ——; 25°C, — · —; 50°C, — — —.

temperature. The potential plateaus on the oscilloscope traces (not shown) are displaced by about 100 mv to more cathodic values as compared to the corresponding drops in coverage shown in Fig. 3 and 4. This is due to overvoltage caused by the relatively high stripping current (121 μa, ≈550 μa/cm²).

Comparison of the adsorption-desorption behavior outlined above with the capacity data shown in Fig. 5 reveals that the onset of adsorption (increasing potentials) at about 0.5v closely corresponds to the beginning of the rise of the capacity to the adsorption maximum. The desorption step (decreasing potentials) at 0.5v causes a sharp drop in capacity, whereas desorption at 1.0v seems to have little or no influence on the capacity-potential behavior. After desorption is completed, at about 0.4v, the capacity returns to approximately the values encountered before adsorption. This indicates that the adsorption-desorption process leaves the surface essentially unaltered after a constant roughness factor has been achieved by cathodic-anodic cycling.

The influence of temperature on the capacity is quite pronounced, the maximum being 38.2 μf/cm² at 50°C, and 28.3 μf/cm² at 5°C. With increasing temperature the potential at which the maximum occurs shifts to less noble values, the maximum becoming sharper at the same time. The irreversibility in the adsorption-desorption behavior finds its expression in the capacity hysteresis. The desorption peaks (Fig. 5, decreasing potentials) are at potentials at least 300 mv more cathodic than the adsorption peaks (Fig. 5, increasing potentials).

Discussion

Adsorption-desorption behavior.—The gold-"adsorbed oxygen" system has been studied repeatedly (10). It is generally assumed that a Au-O layer is formed first which is later converted to Au_2O_3 with time and at more anodic potentials (11-14). It is then surprising that on cathodic decay only one potential arrest is reported (11, 12, 14, 15). One would

rather expect two plateaus, and this was indeed found here.

If the model outlined above is correct, the adsorption step beginning at 0.5v and causing, on desorption, the plateau at 0.5v (Fig. 4a) may be associated with the formation of Au-O, or some similar oxygen-containing species, on the surface. Perhaps the assumption of a species Au-OH (12), formed by oxidation of an adsorbed water dipole, is more reasonable since it requires the transfer of only one electron. The formation of Au-O and/or Au-OH is in agreement with the small positive temperature coefficient observed for this step, and with the strong influence on the capacity behavior (see below), which would both be expected for chemisorption-type adsorption.

The amount of "Au-OH" formed on the surface does not reach saturation even at 1.43v, although the observed value of 950 μcoulomb/cm^2 at 50°C is higher than what is normally considered to be a monolayer on the basis of one electron per surface atom of Au ($\approx$500 μcoulomb/cm^2), even if a large error was made in estimating the roughness factor. It is interesting to note that the desorption behavior after steady state at 1.43v (Fig. 4a) shows a gradual reduction of the amount of "Au-OH" present, until, at approximately 0.65v, about one monolayer is left which is then removed within 100 mv or so. Adsorbed OH radicals in excess of one monolayer may be converted to adsorbed (atomic) oxygen, may form multilayers, and/or may be adsorbed on oxidized portions of the Au surface.

It should be pointed out that the possibility of the plateau at 0.5v being caused by adsorption of H_2O_2 could be made highly unlikely, but could not be excluded all together. H_2O_2 may be formed during preelectrolysis, during anodic-cathodic cycling, and during the normal polarization procedures used during a run. Omission of pre-electrolysis and cycling still gave plateaus at 0.5v, although of rather irreproducible length. Also, keeping the electrolyte at 50°C for several hours should remove most of the H_2O_2 eventually present and should lead to a decrease in the amount adsorbed, whereas an increase was actually found.

The adsorption step beginning at 1.0v can be identified with oxide formation, *e.g.*, by further oxidation of "Au-OH" to Au_2O_3. The latter is more difficult to form at higher temperatures (16), consequently a negative temperature coefficient for this adsorption step would be expected and is found. The assumption finds further support in the observation that a visible oxide film can be formed on the electrode by keeping the potential at 1.4v for 24 hr. The maximum value of 760 μcoulomb/cm^2 observed at 5°C and 1.43v is too small to account even for a monolayer of Au_2O_3. The oxidation seems to occur in patches (17), leaving a considerable part of the surface covered with OH radicals only.

The oxidation-reduction-potential behavior of the surface-Au_2O_3 resembles closely that of the adsorbed species found by Laitinen and Chao (12). These authors did not report the presence of a second adsorbate. However, as can be seen from their Fig. 3, not all the "oxygen" adsorbed is removed at the plateau at 1.0v, the total coverage not being reduced to zero until at about 0.4v.

Differential capacity—theoretical.—The theory of the edl on metals was originally developed for ideally polarizable electrodes (1). It is generally assumed to hold for intermediate cases also, a viewpoint which will be adopted here.

The differential capacity of the edl is defined as the derivative of the (electronic) charge on the metal with respect to potential (1). Because of the electroneutrality requirement, the charge on the metal must be equal and opposite in sign to the sum of the excess charges of the anions and cations on the solution side of the interface. In the potential region in which an adsorption (or desorption) process occurs, the sum of these excess charges, considered as a function of potential, undergoes a change, as does the charge on the metal, and with it the edl capacity. It may be expected that the capacity gives a strong indication of an adsorption process only for species entering the inner double layer (specific adsorption), the capacity of the outer double layer being very large and having little influence on the total capacity of the series combination.

The differential capacity is a function of the dielectric constant in the inner double layer region and of the (effective) distance between metal surface and inner Helmholtz plane. It will be assumed in this discussion that both these parameters are constant during the adsorption process [see however (7)]. This is equivalent to assuming that the adsorbate has the same polar character and effective physical size as the water dipoles replaced. Although this assumption is open to debate, here it is perhaps not an unreasonable one. With the adsorbed water dipole already distorted to give a dielectric constant of $\epsilon < 10$ (7), due to the presence of the water-metal bond, the proton(s) missing in surface Au-O and/or Au-OH should not account for a considerable additional change in ϵ.

For an adsorption process, the differential capacity can be written as

$$C = \mathrm{d}(q + k'q')/\mathrm{dE} = C_o + C_{ads} \quad [1]$$

where q represents the charge on the metal in the absence of an adsorption (or desorption) step, q' the increase in charge in the inner double layer due to adsorption, and k' the fraction of the charge q' that is reflected as an increase in charge on the metal, the fraction $1 - k'$ being compensated for by a net increase of opposite charges in the outer double layer. C_o is the differential capacity in the absence of adsorption, C_{ads} the increase in capacity due to the adsorption process

$$C_{ads} = k'(\mathrm{d}q'/\mathrm{dE}) \quad [2]$$

The charge in the inner double layer due to adsorption, q', is not easily accessible to measurement. What can be measured frequently is the charge, q_{ads}, necessary to reduce, or oxidize, the adsorbed species. If the interaction between adsorbed molecules is

negligible (for small coverage), q' is a fraction, k'', of q_{ads}

$$q' = k'' q_{ads} \quad [3]$$

so that

$$C_{ads} = k(dq_{ads}/dE) \quad [4]$$

with

$$k = k'k''$$

The dimensionless quantity k is taken as a constant, independent of potential, although this is probably a first approximation only. It contains k' which converts the charge q' to the ensuing increase in charge on the metal. The coefficient k' will depend on the electrode material, the state of the electrode surface, and the bond established between surface and adsorbate. A determination of k' requires detailed knowledge of the components of charge of the edl which is available for some mercury systems (18), but not for solid electrodes at the present time.

One might assume that for adsorption steps accompanied by a charge transfer, q_{ads}, the magnitude of the charge present in the inner double layer, q', and with it k' depends on the nature of the adsorbed species, that is whether they can be considered a charged species, of type M^+_{ads}, or a neutral entity, such as M_{ads}. Further discussion of k' and k'' must await a more detailed knowledge of the state of the adsorbed species and the adsorptive bonds.

According to Eq. [4], C_{ads} is proportional to the slope of a plot of q_{ads} *vs.* potential and will go through a maximum during the adsorption (or desorption) step. For symmetrical, S-shaped q_{ads} *vs.* potential curves, the capacity maximum will be established at a potential corresponding to ½ of the final coverage. In potential regions where maximum adsorption has been reached, the capacity returns to C_o, or to a new, fairly constant value, consistent with the geometrical relationships and the dielectric constant of the fully covered (or uncovered) surface (2, 19). This behavior is represented schematically in Fig. 6. An average value for k can be obtained if C_o stays constant in the potential range involved.

The model outlined above explains the presence and position of maxima in potential-differential capacity curves caused by adsorption and desorption processes. It is assumed that the dielectric constant in the inner double layer does not change significantly in the region of the capacity maxima, and that the change in capacity is brought about by the presence of additional charged or dipolar species in the inner double layer.

Differential capacity—experimental.—The capacity data for 25°C reported here are in very good agreement with values previously found on (100) and (110) single crystal electrodes for this temperature (3). They do not agree with results obtained for polycrystalline electrodes (4), where the relative height of the anodic adsorption peaks was considerably smaller. This discrepancy is the result of the anodic and cathodic cycling used as pretreatment in the present work. The small amount of oxidation and redeposition caused by the cycling procedure leads to an increase in roughness factor, as judged from the general increase in capacity, and also seems to lead to a surface more susceptible to adsorption, as judged from the relative height of the adsorption maximum. The latter phenomena could be caused for example by re-deposition onto preferred crystal faces leading to a preferred surface orientation (12). No x-ray analysis was performed with the electrodes used in the present work.

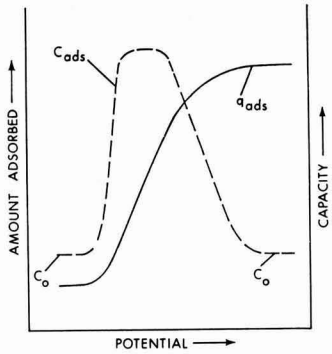

Fig. 6. Expected behavior of the capacity-potential function during an adsorption process. C_o, differential capacity before and after the adsorption step; C_{ads}, additional capacity due to adsorption; q_{ads}, charge equivalent of amount adsorbed.

Although the capacities measured tended to decrease with temperature, much overlapping was caused by the irreproducibility of the roughness factor. Normalization of the capacity data to 16 $\mu f/cm^2$ at the minimum just before the rise to the anodic adsorption maximum (Fig. 5) allows comparison of the capacity-adsorption (or desorption) behavior at the various temperatures used here. The 16 $\mu f/cm^2$ chosen is a reasonable value for a metal surface free of adsorbed species (1).

The capacity-potential behavior during an adsorption step outlined above can be expected to hold for the formation of a surface Au-OH and/or Au-O, that is, a chemisorbed species. It will not hold for surface oxidation to Au_2O_3. Moreover, the model is not expected to hold for adsorption exceeding a monolayer. Comparison of Fig. 4 with Fig. 5 shows that the capacity maxima are in the vicinity of beginning Au_2O_3 formation rather than at potentials with an "OH" coverage of about 250 μcoulomb/cm^2 (½ monolayer). Interference of Au-OH multilayer buildup and/or Au-O formation, and surface oxidation cannot be excluded. Metal oxide surfaces have an edl capacity considerably lower than "free" metal surfaces (20). The appearance of oxide patches, growing in area with potential would in itself lead to a capacity maximum. The decrease in height of the maximum with temperature is brought about by a corresponding increase in oxidation to Au_2O_3.

Similar interference can be expected for the desorption step shown in Fig. 4 and 5. Here, coming from higher potentials, the rise in capacity is caused by a gradual conversion of a low capacity oxide into a high capacity "Au-OH" with simultaneous desorption of excess Au-OH and/or Au-O. However, the capacity maximum is positioned at or near a residual coverage with ½ of a monolayer. There-

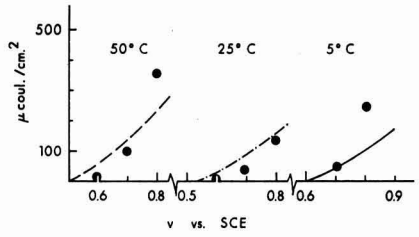

Fig. 7a. Formation of surface "Au-OH." Points calculated with Eq. [1] and [4]; $C_o = 16$, $\mu f/cm^2$, $k = 2.5 \times 10^{-3}$.

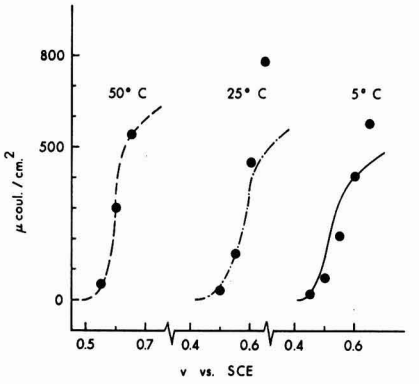

Fig. 7b. Decomposition of surface "Au-OH." Points calculated as in Fig. 7a.

fore, the capacity-adsorption model should hold for desorption of "Au-OH" from the monolayer level.

In Fig. 7 experimental coverage data are compared with values calculated from the integrated form of Eq. [1] and [4] with $C_o = 16$ $\mu f/cm^2$ and $k = 2.5 \times 10^{-3}$. As expected, the adsorption step is described satisfactorily only to about 1/3 of a monolayer, whereas the desorption from a monolayer is represented reasonably well.

Summary

The amount of "oxygen" adsorbed on Au in 1*N* $HClO_4$ was studied between 0.40 and 1.43v *vs.* SCE at 5°, 25°, and 50°C, and compared with the differential capacity of the ionic double layer. Coverage data were obtained from cathodic galvanostatic stripping curves; a rapid single pulse technique was used to measure the capacity.

The stripping curves show two potential plateaus, at 0.5v and at 1.0v. The arrest at 0.5v is attributed to surface Au-OH and/or Au-O formation on the basis of a small positive temperature coefficient, expected for chemisorption, and a pronounced influence on the capacity, expected for adsorption processes involving the inner double layer. For this species, the coverage of 950 μcoulomb/cm² measured at 1.43v and 50°C exceeds monolayer coverage as calculated for the transition of one electron per surface atom of Au (≈500 μcoulomb/cm²). This is explained by multilayer buildup or conversion of Au-OH to Au-O. The arrest at 1.0v is caused by surface oxidation to Au_2O_3, as judged from a negative temperature coefficient of formation. The oxidation reaches 760 μcoulomb/cm² at 1.43v and 5°C and probably occurs in patches.

The differential capacity exhibits a maximum in the "oxygen" adsorption region. The appearance of such a maximum during a (specific) adsorption process is explained on the basis of an additional capacity, C_{ads}, of the inner double layer, due to the presence of the charges of the adsorbed species, at constant dielectric constant. It is shown that C_{ads} should be proportional to the slope of a plot of "amount adsorbed" *vs.* potential. The capacity-adsorption model is tested for "Au-OH" adsorption and desorption. A value of $k = 2.5 \times 10^{-3}$ for the proportionality constant gives satisfactory results for adsorption up to 1/3 of a monolayer, and for desorption from a monolayer, which is the range for which the model is expected to hold.

Manuscript received Aug. 4, 1963; revised manuscript received March 2, 1964.

Any discussion of this paper will appear in a Discussion Section to be published in the June 1965 JOURNAL.

REFERENCES

1. For reviews see: D. C. Grahame, *Chem. Rev.*, **41**, 441 (1947); A. N. Frumkin, *This Journal*, **107**, 461 (1960); B. B. Damaskin, *Uspekhi Khim.*, **30**, 220 (1961).
2. W. Lorenz, *Z. physik. Chem.* (NF), **26**, 424 (1960).
3. G. M. Schmid and Norman Hackerman, *This Journal*, **109**, 243 (1962).
4. G. M. Schmid and Norman Hackerman, *ibid.*, **110**, 440 (1963).
5. J. S. Riney, G. M. Schmid, and Norman Hackerman, *Rev. Sci. Instruments*, **32**, 588 (1961).
6. M. Green and H. Dahms, *This Journal*, **110**, 466 (1963).
7. M. A. V. Devanathan, *Proc. Roy. Soc. (London)*, **A267**, 256 (1962).
8. A. Hickling, *Electrochim. Acta*, **5**, 161 (1961).
9. S. Gilman, *J. Phys. Chem.*, **66**, 2657 (1962).
10. K. J. Vetter, "Elektrochemische Kinetik," p. 502, Springer Verlag, Berlin (1961).
11. K. J. Vetter and D. Berndt, *Z. Elektrochem.*, **62**, 378 (1958).
12. H. A. Laitinen and M. S. Chao, *This Journal*, **108**, 726 (1961).
13. J. P. Hoare, *ibid.*, **110**, 245 (1963).
14. A. Hickling, *Trans. Faraday Soc.*, **42**, 518 (1946).
15. F. G. Will and C. A. Knorr, *Z. Elektrochem.*, **64**, 270 (1960).
16. "Handbook of Chemistry and Physics," p. 1825, Chemical Rubber Publishing Co., Cleveland (1958).
17. S. Barnartt, *This Journal*, **106**, 722 (1959).
18. D. C. Grahame and B. A. Soderberg, *J. Chem. Phys.*, **22**, 449 (1954).
19. W. Lorenz and W. Mueller, *Z. physik. Chem.* (NF), **25**, 161 (1960).
20. J. J. McMullen and Norman Hackerman, *This Journal*, **106**, 341 (1959).

Electrodialytic Demineralization Using Permselective Membranes

I. Energy Consumption and Production Rate

W. G. B. Mandersloot

Chemical Engineering Group, South African Council for Scientific and Industrial Research, Pretoria, South Africa

ABSTRACT

Equations were derived for the energy consumption and production rate in electrodialytic demineralization, based on a simple empirical relation between the apparent compartment pair resistance and the electrolyte concentration in the desalting stream. The equations are independent of the compartment dimensions parallel to the membranes and of flow velocity. Special attention is given to the detrimental effect of water transport and an "over-all efficiency" is introduced which covers the nonideality of the membranes, salt diffusion, and water transport. The equations are compared with experimental results.

The principle of electrodialytic demineralization (1, 2) using ion-selective membranes in a multicompartment apparatus (Fig. 1) in which flow disturbing devices (2, 3) are placed in the compartments to combat concentration polarization (4-6) finds increasing technical application. A number of transport processes occur simultaneously in the membranes (Fig. 2), of which only counterion transport brings about the desired effect. These transport processes occur in a medium in which the concentrations of counterions and fixed ions are usually in the range of 1-6*M*; a good deal of interaction must therefore occur.

The optimum compartment thickness, arrived at through a balance of electrical resistance and hydraulic resistance, is approximately 1 mm. The electrolyte concentration in the brine should be high to achieve a low resistance of the compartment pair, but limitations are set by (*a*) the presence of precipitate forming ions; (*b*) the fact that the concentration difference across the membranes constitutes

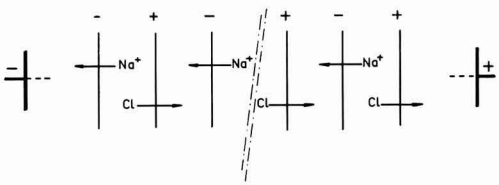

Fig. 1. Membrane arrangement in a membrane stack for electrodialytic water demineralization. The cation and anion selective membranes are indicated by — and +, respectively.

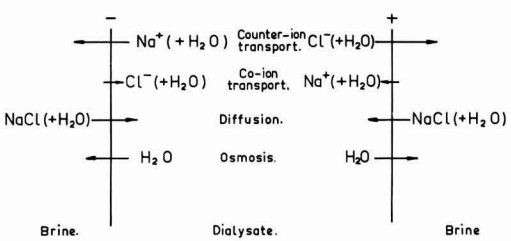

Fig. 2. Transport processes occurring simultaneously through the membranes.

the driving force for most of the detrimental processes indicated in Fig. 2; (*c*) electrical leakage through the brine stream.

In the design of electrodialytic demineralization plants the cost of membrane surface area (approximately inversely proportional to the applied electric potential gradient) and the cost of electrical energy consumed (approximately proportional to this gradient) should be balanced to arrive at an economic optimum. Relations between these two variable cost-determining factors and the initial and final dialysate concentrations are therefore required. They are derived from the relation between compartment pair resistance and the dialysate concentration. For small demineralization ranges the average compartment pair resistance can be determined (7, 8) or calculated from the resistances of the component parts (9). The latter method requires an estimate of the effect of that part of concentration polarization which cannot be eliminated and of the screening effect of spacer materials and membrane potentials should be taken into account as well. A measurement of the apparent resistance of the complete assembly is, of course, much more accurate. We therefore decided on a method applicable to large desalting ranges as well, in which the relation between compartment pair resistance and dialysate concentration is determined in a laboratory size electrodialysis apparatus with components identical to those used in a technical installation (except dimensions parallel to the membranes).

Mathematical Description of the Process

When serious concentration polarization is avoided by using an appropriate flow velocity in the compartments the apparent electrical resistance of a unit surface area of a compartment pair is a linear function of the reciprocal of the electrolyte concentration in the dialysate

$$r = a + b/C \qquad [1]$$

In a given compartment pair assembly a and b are dependent on the temperature and composition of the electrolyte, and the relation is valid for the range of C for which electrodialytic demineralization

is usually considered ($0.01 < C < 0.6$), provided no large variation in the brine concentration occurs. When, as usual, a constant voltage per compartment pair is applied

$$i = E/(a + b/C) \qquad [2]$$

The salt transport j per square centimeter of membrane pair is then

$$j = \psi' E/F(a + b/C) \qquad [3]$$

and the rate at which salt is removed from the dialysate is

$$dN/dt = -jA = -\psi' AE/F(a + b/C) \qquad [4]$$

At any time

$$N = VC \qquad [5]$$

and therefore

$$dN = VdC + CdV \qquad [6]$$

If it is assumed that for each gram equivalent of salt removed from the dialysate the volume of the dialysate changes by H liter and that this figure includes osmotic water transport, then

$$dV = HdN \qquad [7]$$

and a material balance gives:

$$V = V_T(1 - HC_T)/(1 - HC) \qquad [8]$$

Combining Eq. [4], [6],[7], and [8] and taking $(1 - HC)^2 = 1 - 2HC$, the concentration change in the dialysate can be described by

$$dC/dt = -\psi' AE(1 - 2HC)/FV_T(1 - HC_T)(a + b/C) \qquad [9]$$

After integration (assuming ψ' to be constant) the production rate of the process is given by

$$V_T/T = 2\psi' AEH/F(1 - HC_T)(a \ln[(1 - 2HC_T)/(1 - 2HC_o)] + 2bH \ln[C_o(1 - 2HC_T)/C_T(1 - 2HC_o)] \qquad [10]$$

and the energy consumption per liter of product of concentration C_T obtained through the integration

$$W' = AE \int_0^T idt/V_T \qquad [11]$$

is

$$W' = EF(1 - HC_T)\ln[(1 - 2HC_T)/(1 - 2HC_o)]/2\psi' H \qquad [12]$$

It should be noted that a and b do not appear in Eq. [12]

Simplification Using "Over-all Efficiency"

The coulomb efficiency ψ' incorporated the non-ideality of the membranes, the effect of diffusional salt transfer, and the effect of the small amount of usually unavoidable interstream leakage. We may, however, replace ψ' by the over-all efficiency ψ, which incorporates in addition the effect of water transfer. Equation [9] then changes to

$$dC/dt = -\psi AE/FV_T(a + b/C) \qquad [9a]$$

the production rate is then given by

$$V_T/T = \psi AE/F(C_o - C_T)(a + b/C_{\ln \text{ mean}}) \qquad [10a]$$

and the energy consumption per liter of product of concentration C_T by

$$W' = EF(C_o - C_T)/\psi \qquad [12a]$$

The slope of this linear relation between W' and C_T (*i.e.*, the energy consumption per gram equivalent removed per liter) is

$$W'' = -EF/\psi \qquad [13a]$$

and the energy consumption per volt per compartment pair and per gram equivalent removed per liter is

$$W = F/\psi \qquad [14a]$$

Equation [14a] can be expressed in more practical units by

$$W = 2.68 \times 10^{-2}/\psi \text{ kwh/g-equiv. volt} \qquad [15a]$$

In the American literature on electrodialysis reference is often made to a quantity called the Power Index, which is the energy consumption per unit volume over the production rate per unit area

$$\text{Power Index} = F^2(C_o - C_T)^2(a + b/C_{\ln \text{ mean}})/\psi^2 \qquad [16a]$$

Effect of Water Transport

The detrimental effect of water transport on the efficiency of the process can be shown by combining Eq. [11] and [11a]

$$\psi/\psi' = (1 - 2HC)_{\ln \text{ mean}}/(1 - HC_T) \qquad [17a]$$

A graphical illustration of Eq. [17a] for various values of H and C_o and for $C_T = 0.01$ (drinking water) is given in Fig. 3. Values for $H < 0.2$ are not indicated as this value corresponds with the primary hydration of the ions. Figure 3 clearly indicates that the over-all efficiency of electrodialytic demineralization can never be high when solutions of near sea water concentration are demineralized to a drinking water level.

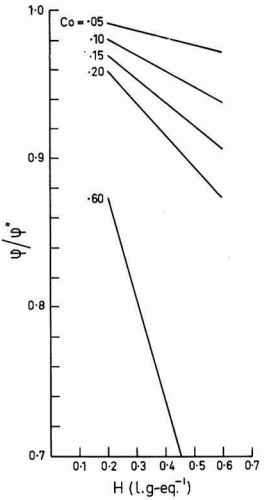

Fig. 3. The ratio ψ/ψ', for various values of H and C_o, when $C_T = 0.01$; Eq. [17a].

Average Current Density

In electrodialytic demineralization it is often required to consider the effect of one dialysate pass through the apparatus; in some technical installations a pass length of up to several yards is used. The externally measured total current can be expressed only as an average current density $\bar{i}$. Making the reasonable assumption that each compartment is at one electric potential over its whole area, $\bar{i}$ can be related to the ingoing and outgoing dialysate concentrations. If it takes the dialysate T sec to complete one pass, then

$$\bar{i} = \int_0^T i dt/T \qquad [18]$$

By combining Eq. [2], [9a], and [10a] we obtain

$$\bar{i} = E/(a + b/C_{\ln \text{ mean}}) \qquad [19a]$$

and this equation can be used to predict the electric current in a technical installation from flow rate and a laboratory measurement of a and b.

Optimization of Cost

To optimize the cost of the process, the costs of compartment surface area and power consumption must be balanced (12, 13), and Eq. [10a] and [12a], or their more intricate equivalents, may be used to determine the optimum E with respect to cost (rather than an optimum average current density). The cost of installed compartment pair area per liter of product can be expressed as

$$S_A = qF(C_o - C_T)(a + b/C_{\ln \text{ mean}})/\psi E \qquad [20a]$$

and the energy cost per liter of product by

$$S_{W'} = pEF(C_o - C_T)/\psi \qquad [21a]$$

if allowance is made in the factor p for rectifying losses and also for the required pump energy. The total cost S, variable with E is

$$S = S_A + S_{W'} \qquad [22]$$

and the optimum E can be obtained from $dS/dE = o$

$$E_{\text{optimum}} = [q(a + b/C_{\ln \text{ mean}})/p]^{0.5} \qquad [23a]$$

It may occur that E_{optimum} is higher than the maximum allowable value for E with respect to concentration polarization and scaling.

Experimental

The electrodialysis multicell was composed of 21 Klingerit[1] gaskets, 0.08 cm thick, with a central cutaway section 16 x 8 cm forming 11 brine and 10 dialysate compartments with a surface area of 128 cm^2 each. The membrane alternating with the gaskets were supported across this area by corrugated perforated spacers, the corrugations making an angle of 22° with the vertical long axis of the compartments. The assembly was clamped between Perspex[2] plates backed by steel plates, and a graphite cathode and a platinized titanium anode[3] were placed either in or adjacent to the Perspex plates. Liquid flow was upwards in all compartments, a multislot feeding and withdrawal system being used (Fig. 4). The conduits formed by corresponding holes in gaskets and membranes were interconnected in one of the Perspex plates on which external connections were supplied. A flow diagram is given in Fig. 5. The batch of dialysate was contained in a 10 l aspirator with a calibrated glass on top and all liquids were pumped with nonmetallic pumps. The by-pass in the dialysate system allowed quick mixing in the aspirator. A branch of this by-pass contained a conductivity cell.[4] All lines returning to the calibrated glass with which the dialysate volume was measured ended in a length of glass tubing, the lower end of which was placed on the meniscus when a volume reading was taken.

The brine and electrode rinse systems were thermostated, which sufficed also to keep the dialysate at the required temperature, all flows being measured with rotameters.[5] The direct current was

[1] Klingerit, compressed asbestos steam jointing, Klinger & Co., England.

[2] Perspex, Lucite, Plexiglass.

[3] Imperial Chemical Industries.

[4] Radiometer, Kopenhagen, type CDM2c with cell CDC114.

[5] Fischer & Porter, flowrators.

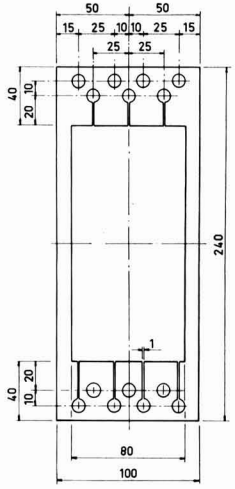

Fig. 4. Gasket to form dialysate compartments (and brine compartments by turning 180°); sizes in mm.

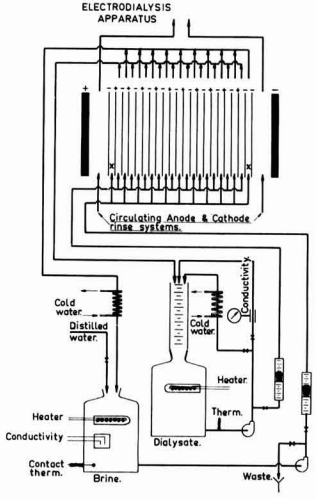

Fig. 5. Flow diagram of experimental set-up. The compartments marked "x" have a calomel probe electrode inserted.

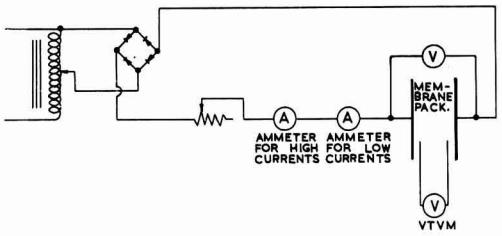

Fig. 6. Wiring diagram

obtained from a selenium rectifier;[6] a wiring diagram is given in Fig. 6. The membrane pack voltage was measured with probe electrodes inserted in the first and last brine compartments. Best results were obtained with calomel electrodes connected to a vacuum tube voltmeter.[7] The calomel electrodes were put under an air pressure slightly exceeding the pressure in the brine compartments.

The desalting experiments were usually carried out by selecting a temperature, brine concentration, and initial dialysate concentration and composition. By applying a constant electric potential as measured on the probe electrodes the batch of dialysate was desalted taking frequent volume, conductivity and current readings. The liquid flows were kept at 10 cm/sec in brine and dialysate compartments and 14 cm/sec in the electrode compartments. When mixed electrolytes were used intermediate samples of the dialysate were taken to determine individual ion concentrations.

Salt diffusion rates in the membrane pack were determined in a currentless experiment with the dialysate concentration at approximately 0.01*N*. On a number of single membranes diffusion rates were measured separately in a small stirred diffusion cell placed in a thermostat at 25°C. The low concentration was again 0.01*N*.

[6] Standard Telephones and Cables, Type 22JE293.

[7] Marconi Instruments, Model TF1300.

Results and Discussion

Resistance.—The validity of Eq. [2] is demonstrated in Fig. 7 and 8, in which for three constant voltages per compartment pair $1/i$ is plotted against $1/C$. The linear relations hold over large concentration ranges. Values for a and b derived from Fig. 7 and a number of similar plots are included in Table I. The spread in the values for a and b for each series of experiments (certain membrane pair, temperature, brine concentration, and electrolyte composition) illustrates the poor reproducibility of membrane pack resistance, a fact well known to workers in this field. The application of the individual values for a

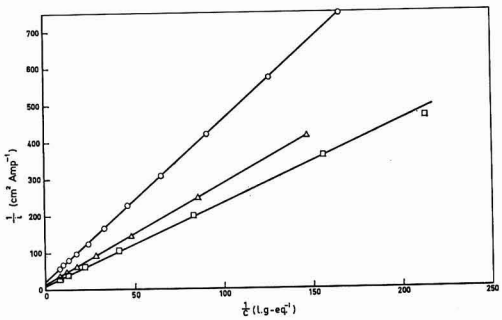

Fig. 7. Reciprocal of the current density *vs.* reciprocal of the concentration in the dialysate. T.N.O.-A60 and C60[8] membranes at 25°C. ○, 0.50v; △, 0.76v; □, 1.00v.

Table I. Production rates (10^{-6} l sec^{-1} cm^{-2} volt^{-1}) calculated according to Eq. [10*a*], the effect of water transport calculated according to Eq. [17*a*], and experimental values

Cation selective membrane	Anion selective membrane	C_o	C_T	E	a	b	ψ	ψ'	H	ψ/ψ' Eq. [17a]	ψ/ψ' Observed	V_T/ATE Eq. [10a]	V_T/ATE Observed	B	Temp, °C	Experiment
		0.152	0.012	0.50	11	2.2	0.805	0.835	0.45	0.93	0.96	1.17	1.17	1.0	35	1
		0.146	0.010	0.75	13	1.6	0.805	0.870	0.35	0.95	0.93	1.40	1.41	1.0	35	2
3129B-56[9]	3129B-96[9]	0.167	0.010	1.00	12	1.5	0.805	0.850	0.32	0.94	0.95	1.39	1.27	1.0	35	3
		0.163	0.010	0.50	14	2.1	0.825	0.858	0.35	0.94	0.96	1.08	1.00	0.5	35	4
		0.154	0.010	0.75	12	2.0	0.825	0.862	0.30	0.95	0.96	1.22	1.16	0.5	35	5
		0.100	0.005	0.70	32	2.1	0.947	1.000	0.36	0.96	0.95	1.07	1.09	0.25	20	6
		0.100	0.005	1.00	20	2.4	0.947	0.979	0.36	0.96	0.97	1.08	1.03	0.25	20	7
		0.100	0.005	1.40	20	2.4	0.947	0.946	0.36	0.96	1.00	1.09	0.99	0.25	20	8
		0.100	0.005	0.50	12	2.2	0.880	0.918	0.44	0.95	0.96	1.19	1.11	0.25	25	9
C-60[8]	A-60[8]	0.100	0.005	0.76	12	2.1	0.880	0.931	0.41	0.96	0.95	1.20	1.18	0.25	25	10
		0.100	0.005	1.00	12	2.2	0.880	0.901	0.41	0.96	0.98	1.16	1.11	0.25	25	11
		0.100	0.005	0.50	14	1.3	0.853	0.851	0.50	0.95	1.00	1.65	1.57	0.25	30	12
		0.100	0.005	1.00	10	1.6	0.853	0.897	0.45	0.95	0.95	1.54	1.46	0.25	30	13
		0.050	0.003	0.80	—	—	0.840	0.844	0.44	0.98	0.99	—	1.46	0.25	20	14
C-60[8]	TA[12]	0.050	0.003	0.80	—	—	0.840	0.856	0.51	0.97	0.98	—	1.72	0.25	20	15
C-20[11]	A-20[11]	0.250*	0.020	0.40	18	1.4	0.83	0.903	0.39	0.89	0.92	—	1.29	0.50	30	16
		0.250*	0.020	0.80	16	1.1	0.83	0.867	0.35	0.91	0.96	—	1.24	0.50	30	17
		0.250*	0.020	0.40	11	1.8	0.86	0.927	0.46	0.87	0.87	—	1.53	0.50	30	18
C-60[8]	A-60[8]	0.250*	0.020	0.80	12	1.2	0.79	0.854	0.39	0.89	0.89	—	1.33	0.50	30	19
		0.250*	0.020	1.00	7	1.9	0.73	0.850	0.40	0.88	0.86	1.17	1.26	0.50	30	20

* Initially equal equivalents of $CaCl_2$ and NaCl.

[8] Central Technical Institute, T.N.O. (Netherlands); commercially available at AMFion A60 and C60 membranes from the American Machine and Foundry Company.

[9] American Machine and Foundry Company.

[10] Asahi Chemical Industry Co.

[11] The Permutit Co. Ltd.

[12] South African C.S.I.R.

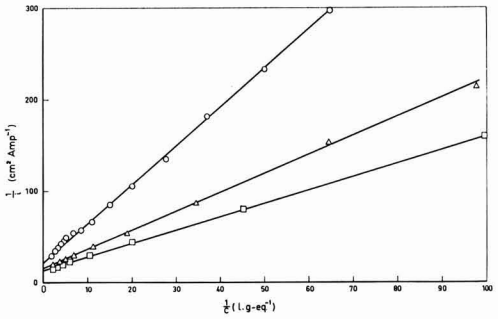

Fig. 8. Reciprocal of the current density *vs.* reciprocal of the concentration in the dialysate. A.M.F. 3129-B-56 and 96[9] membranes at 35°C. ○, 0.50v; △, 0.75v; □, 1.00v.

and b in the derived equations led to good agreement with experimental values.

Salt diffusion.—In Eq. [3] it was assumed that the coulomb efficiency ψ' is constant. For most practical cases this is an acceptable approximation for the calculation of production rate and energy consumption. However, a check should always be made so that even at the end of the desalting range the back diffusion of salt from brine to dialysate remains acceptable in comparison with the current density. Practical salt diffusion rates (including a small amount of leakage) from brine towards an 0.01*N* dialysate appear to be proportional to the brine concentration, as illustrated in Fig. 9.

The results of diffusion measurements on single membranes are shown in Fig. 10 for a number of anion and cation selective membranes. From a simple "Donnan equilibrium" (14) it would be expected that the diffusion rates increase with the second power of the high concentration on one side of the membrane, as the amount of sorbed electrolyte in the membrane is then proportional to the square of the external concentration. The actual power, however, varies between 1.13 and 1.54 for the various membranes. Glueckauf and Watts (15) attributed the deviation from 2 to heterogeneity in the crosslinking of the resin, for which evidence was also obtained from electrolyte uptake data. The interaction of electrolyte diffusion and the simultaneously occurring osmosis in the opposite direction is the subject

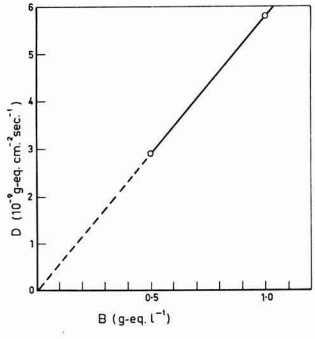

Fig. 9. Salt diffusion rate through a membrane pair at two brine concentrations; dialysate concentration approximately 0.01*N*; 35°C, A.M.F. 3129-B[9] membranes.

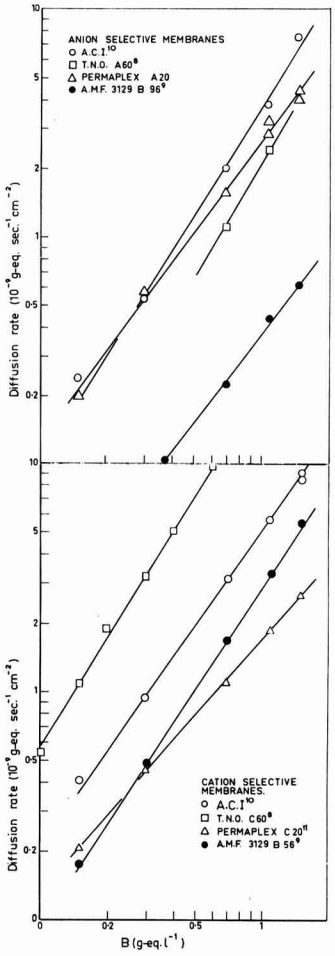

Fig. 10. Sodium chloride diffusion rate through a number of ion selective membranes; 0.01*N* NaCl solution on one side.

of a current investigation in this laboratory (16). It should be noted that the slopes for the data on the mechanically heterogeneous Permaplex membranes in Fig. 10 indicate lower powers than for the majority of the "homogeneous" membranes.

Water transport.—A check on Eq. [8] is presented in Table II; the experimental data were taken from experiment 20.

Production rate.—The production rates calculated according to Eq. [10] and [10*a*] are compared in

Table II. Calculated and experimental values for the dialysate volume; $H = 0.4$

C	V, observed	V, Eq. [8]
0.25	12.81	12.82
0.20	12.53	12.56
0.15	12.28	12.30
0.10	12.02	12.03
0.05	11.77	11.80
0.02	11.63	11.64
0.01	11.60 ⟷	11.60

Table III. Production rates (10^{-6} l $sec^{-1}cm^{-2}$ $volt^{-1}$) calculated according to the derived equations, and experimental values

C_T	V_T/AET Eq. [10]	Eq. [10a]	Observed
0.20	10.09	9.72	9.76
0.15	4.69	4.51	4.91
0.10	2.82	2.69	2.89
0.05	1.78	1.72	1.84
0.02	1.26	1.19	1.26
0.01	1.04	0.96	1.04

Table IV. Energy consumption (kwh/m^3) calculated according to Eq. [12] and [12b], and experimental values

C_T	W', kwh/m^3 Eq. [12]	Eq. [12b] and experimental
0.20	1.83	1.80
0.15	3.58	3.61
0.10	5.30	5.48
0.05	7.05	7.34
0.02	8.11	8.45
0.01	8.46	8.75

Table III with experimental values from experiment 20. The following values for the constants were used in the calculations: a, 7; b, 1.92; H, 0.4; E, 1.0; A, 1280; B, 0.5; ψ', 0.85; ψ, 0.73; F, 96,500; C_o, 0.25. Calculated and experimental values are in good agreement, even when the most simplified Eq. [10a] is used. Comparison of experimental and calculated production rates on a number of complete desalting experiments is included in Table I. The observed values for ψ/ψ' in Table I can also be compared with values in Fig. 3.

Energy Consumption.—The energy consumption calculated according to Eq. [12] and [12a] and experimental values obtained from experiment 20 are compared in Table IV. The constants used were the same as for Table III. As the concept of "over-all efficiency" originated in energy consumption data, values calculated according to Eq. [12a] and the experimental values in Table IV are the same. A separate check of the validity of Eq. [12a] can be found in a plot of energy consumption per volume of dialysate *vs.* the electrolyte concentration in the dialysate. Such plots are shown in Fig. 11 for a number of experiments on mixed $NaCl/CaCl_2$ solutions. Linear relations were obtained and the slopes of these relations have been plotted *vs.* E in Fig. 12. Again linear relations were obtained showing the validity of Eq. [13a]. In Fig. 12 the line for $\psi = 1$ is also indicated and ψ is now the ratio of the slopes of this line and of an experimental line.

Power Index.—In Eq. [16a] it has been shown that the Power Index is a complicated function of C_o. Linear plots of log P.I. *vs.* log C_o with a slope of 1.86 have been reported (17) for desalting to drinking water concentration ($C_T = 0.01$) from $0.04 < C_o < 0.6$. It can be shown that such linear relations correspond to rather large values for the basic resistance of the compartment pair.

Conclusion

The use of the concept of "over-all efficiency" allows a mathematical description of the process with relatively simple equations which are in good agreement with experimental results and which can be used for the prediction of the operation of large scale equipment from laboratory compartment pair d-c resistance measurements because the equations are independent of the compartment dimensions parallel to the membranes. The equations can also be used for the optimization of E with respect to cost. The "over-all efficiency" incorporates the effect of water transport, which is an important detrimental factor in electrodialytic demineralization when other than short brackish desalting ranges, using reasonably high current densities, are considered.

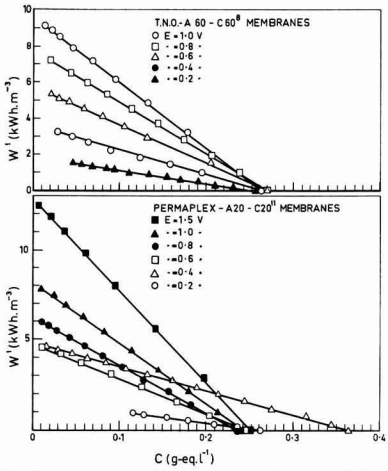

Fig. 11. Energy consumption per unit volume *vs.* dialysate concentration.

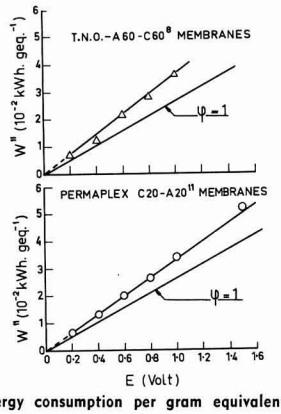

Fig. 12. Energy consumption per gram equivalent *vs.* compartmental voltage.

Acknowledgment

The assistance of Mr. J. Venlet and Mr. L. R. J. van Vuuren is gratefully acknowledged.

Manuscript received July 30, 1962.

Any discussion of this paper will appear in a Discussion Section to be published in the June 1965 JOURNAL.

REFERENCES

1. "Demineralization by Electrodialysis," J. R. Wilson, Editor, Butterworths, London (1960).
2. H. J. Cohan, *Chem. & Eng. Prog.*, **57** [2], 72 (1961).

3. Ref. (1), pp. 216, 240.
4. D. A. Cowan and J. H. Brown, *Ind. & Eng. Chem.*, **51**, 1445 (1959).
5. Ref. (1), p. 13.
6. B. A. Cooke, *Electrochim. Acta*, **3**, 307 (1961); **4**, 179 (1961); **5**, 216 (1961).
7. E. Wegelin, Central Technical Institute, T.N.O. (Netherlands), Publ. 59, p. 4 (1960).
8. Ref. (1), p. 324.
9. M. van Ments, *Ind. & Eng. Chem.*, **52**, 149 (1960).
10. T. R. E. Kressman and F. L. Tye, *Trans. Faraday Soc.*, **55**, 1441 (1959).
11. W. G. B. Mandersloot, *Electrochim. Acta*, **9**, 395 (1964).
12. D. A. Cowan, *Advances in Chemistry*, Series No. 27, 224 (1960).
13. Ref. (1), p. 234.
14. F. Helfferich, "Ionenaustauscher," Vol. 1, p. 320, Verlag Chemie, Weinheim (1959).
15. E. Glueckauf and R. E. Watts, *Nature*, **191**, 904 (1961).
16. G. Eder, *Z. phys. Chem. N.F.*, **39**, 218 (1963).
17. P. M. Rapier, W. K. Baker, and S. A. Weiner, University of California, Institute of Engineering Research, Series No. 75, Issue No. 29 (1962).

SYMBOLS

r Resistance of 1 cm^2 of compartment pair, ohm-cm^2
a Constant ($a = r$ at $C = \infty$), ohm-cm^2
b Proportionality factor, ohm-cm^2, g-eq. 1^{-1}
C Electrolyte concentration in dialysate, g-eq. 1^{-1}
i Current density, amp cm^{-2}
E Electric potential gradient per compartment pair, volt
j^2 Effective salt transport rate per cm^2, g-eq. sec^{-1}, cm^2
ψ' Coulomb efficiency
F 96,500, coul. g-eq.$^{-1}$
N Total number of g-eq. in the batch of dialysate, g-eq.
t Time, sec
A Available total compartment pair area, cm^2
V Volume of the batch of dialysate, liter
H Water transport factor, l.g-eq.$^{-1}$
T Time required to desalt from C_o to C_T, sec
W' Energy consumption per liter of product, watt sec 1^{-1}
ψ Over-all efficiency
W'' Energy consumption per g-eq. (removed per liter), watt sec g-eq.$^{-1}$
W Energy consumption per g-eq. (removed per liter) and per volt applied on each compartment pair, amp sec g-eq.$^{-1}$
$\bar{i}$ Average current density, amp cm^{-2}
q (Depreciation) cost of 1 cm^2 of compartment pair, per sec, \$. cm^{-2}, sec^{-1}
p Cost of energy, \$. Watt^{-1}, sec^{-1}
S Cost per liter of product, \$. 1^{-1}
B Electrolyte concentration in brine, g-eq. 1^{-1}
D Salt diffusion rate through a membrane pair, g-eq. cm^{-2}, sec^{-1}

Subscripts o and T refer to $t = o$ and $t = T$, respectively.
Subscript "ln mean" indicates the logarithmic mean of the values at $t = o$ and at $t = T$.

Theoretical Calculations of the Separation Factors in the Hydrogen Evolution Reaction for the Slow Discharge Mechanism

John O'M. Bockris and S. Srinivasan

The Electrochemistry Laboratory, The University of Pennsylvania, Philadelphia, Pennsylvania

ABSTRACT

Theoretical calculations of the electrolytic separation factors (S) for the slow discharge mechanism were carried out following the lines of earlier calculations by Horiuti *et al.* Previous calculations neglected the effect on S of (i) the step following the discharge step, (ii) the real stretching frequency of the transition state, and (iii) tunneling corrections. The presently calculated S values differ from previous results mainly due to the inclusion of the real stretching frequency of the transition state. The H-T separation factors are more useful than the H-D separation factors in determining the mechanism.

Calculations of electrolytic separation factors for the slow discharge mechanism have been carried out by Keii and Kodera (1) (H/D separation factors), Conway (2) (H/D separation factors), and by Kodera and Saito (3) (H/T separation factors). The Japanese authors based their calculations on those of earlier calculations of Horiuti *et al.* (4-6) for other mechanisms. Conway carried out his calculations for various mechanisms of the evolution reactions, assuming that the isotopic effects were related in part to the difference of heats of activation measured with respect to the zero point energy levels for the isotopic reactants and products, as treated by Bockris (7). In further papers (8, 9) approximate estimates of isotope effects on the energy of the transition state were made in calculations of the ratio of the hydrogen and deuterium exchange currents. The ratios of exchange currents on various metals were measured experimentally by Conway (8) and discussed in terms of calculated separation factors for the various mechanisms.

There are two important differences in these approaches. The first presents a difference in the model of the activated complex. Horiuti's calculations follow the Eyring treatment (10) in which the transition state complex is considered as a stable molecule having its own vibrational frequencies. Hence, differences of zero point energies of the isotopic activated complexes make an important contribution to the separation factor.

Conway's calculations imply that the transition state complex is transient, *i.e.*, it is sufficiently short lived so that vibrational frequencies of the activated complex do not affect the activation energy, which is

hence measured from the zero point energy of the initial state to the intersection point of the Morse curves.

A second difference is one of convenience. In Conway's calculations, the ratio of concentrations of isotopic species in the initial state is calculated from theoretical considerations of equilibrium in solution. In Horiuti's calculations it is possible to avoid these considerations by introducing an experimental equilibrium constant between isotopic species in solution and corresponding molecules in the gas phase. This latter feature of the Horiuti approach appears preferable to that of Conway's because it reduces uncertainties in calculating partition functions of species in solution.

In both treatments, the influence of the electrochemical desorption step on the separation factor for a slow discharge mechanism was neglected. Tunneling effects, which were first pointed out by Bawn and Ogden (11) were also not considered in either treatment. However, Conway (12) had previously concluded that appreciable tunneling would lead to a high dependence of S on potential and to anomalous Tafel slopes which are not observed experimentally. Nevertheless, it is the authors' opinion that calculations should include tunneling corrections, if possible, since these are certainly important in hydrogen atom and ion transfer reactions (13). In the calculation of the ratio of activities of isotopic oxonium ions ($a_{H_3O^+}/a_{H_2DO^+}$), Conway assumed incorrectly the equality of the deuteron affinity of water and the proton affinity of HDO. The slopes of Morse curves for H^+-OH_2 and D^+-OH_2 were also calculated to be different and hence to contribute to the isotope effect. This difference arose because the observed vibration frequencies of the O-H and O-D bonds were related to "a" values of the Morse equations using the usual approximate assumption (13, 14) that the H^+-OH_2 interaction could be treated by an analogous formula relevant to that for a diatomic molecule. In order to facilitate many calculations in isotope effect work, such an approximation is useful. However, its application to calculate different "a" values for the Morse curves, implies that the potential energy distance functions for the stretching of bonds exhibits isotope effects. This is not consistent with the usual opinion which is based on the consideration that in the Schroedinger equation set up in a discussion of the bond, the relevant mass is the reduced mass of the electron and the nucleus, *i.e.*, influence of nuclear mass is small (16).

Keii and Kodera and also Kodera and Saito have not included the isotope effect due to the real stretching frequency of the activated complex H_2O----H----M. [The H_2O molecule is treated as a pseudo atom as in previous work (14).] They also used 263 kcal $mole^{-1}$ (solvation energy of a proton) as the dissociation energy of the H^+-OH_2. It is more appropriate to use the proton affinity of water. This change should also affect the Morse constant of the H^+-OH_2 molecule. In the present calculations, the Eyring assumption regarding the transition state complex (cf. Conway's transient assumption) has been used largely on grounds of the greater consistency of the resultant calculations with experiment. Further, the easier way of calculating ionic concentration ratios in solution and their partition function ratios was used. The latter method is, however, more complex than that of Conway due to difficulties of evaluating potential energy surfaces of the transition state complex for calculating vibrational frequencies.

Present Calculations

Discharge Followed by Recombination

Expression for separation factor.—The H/D separation factor (S_D) is given by

$$S_D = \left(\frac{C_H}{C_D}\right)_g \Big/ \left(\frac{C_H}{C_D}\right)_s \qquad [1]$$

where $(C_H/C_D)_g$ and $(C_H/C_D)_s$ are the ratios of atomic concentrations of H to D in the gas and solution, respectively. Under the condition that $a_{H_2O,l} >> a_{HDO,l}$ (where $a_{H_2O,l}$ and $a_{HDO,l}$ are the activities of H_2O and HDO in solution) Eq. [1] reduces to

$$S_D = \frac{1}{2}\left(\frac{C_H}{C_D}\right)_g \left(\frac{a_{HDO,l}}{a_{H_2O,l}}\right) \qquad [2]$$

It may easily be shown (17)[1] that both for the case in which the recombination step is treated as in equilibrium or not so treated that

$$\left(\frac{C_H}{C_D}\right)_g = \frac{i_{1,H}}{i_{1,D}} \qquad [3]$$

where $i_{1,H}$ and $i_{1,D}$ are the discharge currents for the isotopic reactions

$$H_3O^+ + e_o + M \rightarrow MH + H_2O \qquad [4]$$

$$H_2DO^+ + e_o + M \rightarrow MD + H_2O \qquad [5]$$

respectively,

$i_{1,H}$ and $i_{1,D}$ are given by

$$i_{1,H} = k_{1,H} a_{H_3O^+} (1 - \theta_H - \theta_D) e^{-\beta VF/RT} \qquad [6]$$

$$i_{1,D} = k_{1,D} \frac{a_{H_2DO^+}}{3} (1 - \theta_H - \theta_D) e^{-\beta VF/RT} \qquad [7]$$

where $k_{1,H}$ and $k_{1,D}$ are the respective rate constants, when the metal-solution potential difference (V) is zero; $a_{H_3O^+}$ and $a_{H_2DO^+}$ are the activities of the H_3O^+ and H_2DO^+ ions at the double layer. The factor (1/3) in Eq. [7] arises, since it is assumed that only one out of three H_2DO^+ molecules is suitably oriented for D^+ discharge. Dividing Eq. [6] by Eq. [7], we have

$$\frac{i_{1,H}}{i_{1,D}} = \frac{k_{1,H}}{k_{1,D}} \cdot \frac{a_{H_3O^+}}{\frac{a_{H_2DO^+}}{3}} \qquad [8]$$

Expressing the ratio $k_{1,H}/k_{1,D}$ in terms of the standard chemical potentials of the activated and

[1] Equation [3] follows from the equation

$$\frac{C_H}{C_D} = \frac{2(i_{2,H} - i_{-2,H}) + (i_{2,D} - i_{-2,D})}{(i_{2,D} - i_{-2,D})}$$

and the use of the stationary state hypothesis for the intermediates, *i.e.*, adsorbed atomic hydrogen and deuterium.

initial states and ratio of the tunneling factors $(\Gamma_{1,H}/\Gamma_{1,D})$[2] for the isotopic reactions, we have

$$\frac{i_{1,H}}{i_{1,D}} = \frac{\Gamma_{1,H}}{\Gamma_{1,D}} \cdot \frac{e^{-\mu_H{}^{o\neq}/RT}}{e^{-\mu_D{}^{o}/RT}} \cdot \frac{e^{-\mu_{H_2DO^+}{}^{o}/RT}}{e^{-\mu_{H_3O^+}{}^{o}/RT}} \cdot \frac{a_{H_3O^+}}{\frac{a}{3}H_2DO^+} \quad [9]$$

$$= \frac{\Gamma_{1,H}}{\Gamma_{1,D}} \cdot \frac{e^{-\mu_H{}^{o\neq}/RT}}{e^{-\mu_D{}^{o\neq}/RT}} \cdot \frac{e^{-\mu_{H_2DO^+}/RT}}{e^{-\mu_{H_3O^+}/RT}} \quad [10]$$

The latter Eq. [10] is obtained using the relations

$$\mu_{H_3O^+} = \mu_{H_3O^+}{}^{o} + RT \ln a_{H_3O^+} \quad [11]$$

$$\mu_{H_2DO^+} = \mu_{H_2DO^+}{}^{o} + RT \ln \frac{a_{H_2DO^+}}{3} \quad [12]$$

$\mu_{H_3O^+}$ and $\mu_{H_2DO^+}$ are the chemical potentials of the H_3O^+ ion and the H_2DO^+ ion (with D^+ oriented suitably for its discharge) at the double layer respectively.

Considering the following steps which are in equilibrium

$$H_3O^+{}_B \rightleftharpoons H_3O^+ \quad [13]$$

$$H_2DO^+{}_B \rightleftharpoons H_2O - D^+ \quad [14]$$

we have

$$\mu_{H_3O^+{}_B} = \mu_{H_3O^+} \quad [15]$$

$$\mu_{H_2DO^+{}_B} = \mu_{H_2DO^+} \quad [16]$$

B refers to the bulk of the solution.

In addition, the following equilibrium reactions may be considered

$$H_3O^+{}_B + HDO_l \rightleftharpoons H_2DO^+{}_B + H_2O_l \quad [17]$$

$$H_2O_l + HDO_g \rightleftharpoons HDO_l + H_2O_g \quad [18]$$

We may thus write

$$\frac{e^{-\mu_{H_2DO^+{}_B}/RT}}{e^{-\mu_{H_3O^+{}_B}/RT}} = \frac{e^{-\mu_{HDO_g}/RT}}{e^{-\mu_{H_2O_g}/RT}} \quad [19]$$

The suffixes l and g refer to the liquid and gaseous phase, respectively.

Using Eq. [15], [16], [18], and [19], Eq. [10] may be rewritten as

$$\frac{i_{1,H}}{i_{1,D}} = \frac{\Gamma_{1,H}}{\Gamma_{1,D}} \cdot \frac{e^{-\mu_H{}^{o\neq}/RT}}{e^{-\mu_D{}^{o\neq}/RT}} \cdot \frac{e^{-\mu_{HDO_g}/RT}}{e^{-\mu_{H_2O_g}/RT}} \quad [20]$$

We also have the relations

$$\mu_H{}^{o\neq} = -RT \ln f_H{}^{\neq} \quad [21]$$

[2] The quantum mechanical rate constant, (k_q) is related to the classical rate constant (k_c) by the relation $k_q = \Gamma k_c$, where Γ is the tunneling correction to the classical rate.

$$\mu_{H_2O_g} = -RT \ln f_{H_2O_g} + RT \ln a_{H_2O_g} \quad [22]$$

and

$$\mu_{HDO_g} = -RT \ln f_{HDO_g} + RT \ln a_{HDO_g} \quad [23]$$

Hence, the equation for $(i_{1,H}/i_{1,D})$ may be expressed in another form

$$\frac{i_{1,H}}{i_{1,D}} = \frac{\Gamma_{1,H}}{\Gamma_{1,D}} \cdot \frac{f_H{}^{\neq}}{f_D{}^{\neq}} \cdot \frac{f_{HDO_g}}{f_{H_2O_g}} \cdot \frac{a_{H_2O_g}}{a_{HDO_g}} \quad [24]$$

With Eq. [2], [3], and [24], S_D is expressed as

$$S_D = \frac{1}{2} \frac{\Gamma_{1,H}}{\Gamma_{1,D}} \cdot \frac{f_H{}^{\neq}}{f_D{}^{\neq}} \cdot \frac{f_{HDO_g}}{f_{H_2O_g}} \cdot K_D \quad [25]$$

where K_D is the equilibrium constant for reaction [18].

Similarly, the H/T separation factor (S_T) is given by

$$S_T = \frac{1}{2} \cdot \frac{\Gamma_{1,H}}{\Gamma_{1,T}} \cdot \frac{f_H{}^{\neq}}{f_T{}^{\neq}} \cdot \frac{f_{HDO_g}}{f_{H_2O_g}} \cdot K_T \quad [26]$$

where K_T is the equilibrium constant for the reaction

$$H_2O_l + HTO_g \rightleftharpoons HTO_l + H_2O_g \quad [27]$$

Numerical calculations of separation factors (S_D and S_T).—Equilibrium constant (K_D or K_T).—The equilibrium constant, K_D, was measured over a wide range of temperatures by Ikusima and Azakami (18). Its value at 25°C is 1.07. This value differs by only 2% from that of Horiuti and Okamoto (19).

Sepall and Mason (20) have measured K_T at temperatures ranging from 0° to 90°. Its value at 25°C is 1.093. The results of these workers are in complete agreement with that of Brown (21).

Partition function ratio of isotopic water molecules in gas phase ($f_{HDO_g}/f_{H_2O_g}$ and $f_{HTO_g}/f_{H_2O_g}$).—The partition function ratio $(f_{HDO_g}/f_{H_2O_g})$ is given by

$$\frac{f_{HDO_g}}{f_{H_2O_g}} = \frac{\sigma_{H_2O}}{\sigma_{HDO}} \left(\frac{m_{HDO}}{m_{H_2O}}\right)^{3/2} \frac{(I_A I_B I_C)_{HDO}{}^{1/2}}{(I_A I_B I_C)_{H_2O}{}^{1/2}} \cdot \frac{\prod^{3} \sinh(h\nu_i/2kT)_{H_2O}}{\prod^{3} \sinh(h\nu_i/2kT)_{HDO}} \quad [28]$$

A similar expression may be written for the ratio $(f_{HTO_g}/f_{H_2O_g})$. Using the spectroscopic data of Benedict, Gailer, and Plyer (22), $f_{HDO_g}/f_{H_2O_g}$ is 59.16 at 25°C and that of Libby (23), $f_{HTO_g}/f_{H_2O_g}$ is 289.54. Together with K_D and K_T, given in the previous subsection, we have

$$\frac{1}{2} K_D \frac{f_{HDO_g}}{f_{H_2O_g}} = 31.68 \quad [29]$$

$$\frac{1}{2} K_T \frac{f_{HTO_g}}{f_{H_2O_g}} = 158.23 \quad [30]$$

Partition function ratio of isotopic activated complexes ($f_H{}^{\neq}/f_D{}^{\neq}$ and $f_H{}^{\neq}/f_T{}^{\neq}$).—Complete partition function ratio.—It may be assumed that the activated complex, H2O----H----M (or its isotopes) is analogous to a linear triatomic molecule, as has been done previously by Parsons and Bockris (14).

The partition function ratio of the isotopic activated complexes is given by

$$\frac{f_H^{\neq}}{f_D^{\neq}} = \frac{f_{t,H}^{\neq}}{f_{t,D}^{\neq}} \cdot \frac{f_{r,H}^{\neq}}{f_{r,D}^{\neq}} \cdot \frac{f_{v,H}^{\neq}}{f_{v,D}^{\neq}} \quad [31]$$

where $f_t^{\neq}$, $f_r^{\neq}$, and $f_v^{\neq}$ represent the translational, rotational, and vibrational contributions, respectively, of the indicated isotopes.

Translational partition function ratio.—The activated complex may be regarded as immobile. Under these conditions, the translational partition function ratio is unity. Even if the translational motion were treated as restricted, no isotope effect arises, since the heavy metal atom forms a part of the isotopic activated complexes.

Rotational partition function ratio.—A small isotope effect exists due to the restricted rotation of the isotopic activated complexes about the two axis through the center of gravity of the activated complex and mutually perpendicular to the axis of the molecule. The partition function ratio due to this restricted rotation is expressed as

$$\frac{f_{r,H}^{\neq}}{f_{r,D}^{\neq}} = \frac{\sinh^2 h\nu_D/2kT}{\sinh^2 h\nu_H/2kT} \quad [32]$$

Since the observed vibrational frequencies are small (*e.g.*, for water 600 cm^{-1} at room temperature), and are inversely proportional to the square roots of the corresponding moments of inertia

$$\frac{f_{r,H}^{\neq}}{f_{r,D}^{\neq}} = \frac{I_H^{\neq}}{I_D^{\neq}} \quad [33]$$

where $I_H^{\neq}$ and $I_D^{\neq}$ are the moments of inertia of the H and D activated complexes, respectively, about an axis, perpendicular to the axis of the molecule and through their respective centers of gravities. The calculated rotational partition function ratios are

$$\frac{f_{r,H}^{\neq}}{f_{r,D}^{\neq}} = 0.983 \quad [34]$$

Similarly

$$\frac{f_{r,H}^{\neq}}{f_{r,T}^{\neq}} = 0.962 \quad [35]$$

Vibrational partition function ratios.—For a linear triatomic molecule, there are four degrees of vibrational freedom. Since one of these is imaginary for the activated complex, three frequencies are to be considered in calculating the vibrational partition function ratio of the isotopic activated complexes (7), which is given by

$$\frac{f_{v,H}^{\neq}}{f_{v,D}^{\neq}} = \frac{\sinh(h\nu_D/2kT)_s}{\sinh(h\nu_H/2kT)_s} \cdot \frac{\sinh^2(h\nu_D/2kT)_b}{\sinh^2(h\nu_H/2kT)_b} \quad [36]$$

The suffixes, s and b stand for stretching and bending frequencies, respectively.

The bending frequency (ν) of a linear triatomic molecule, XYZ, is given by (24)

$$\lambda = 4\pi^2\nu^2 = \frac{1}{l_1^2 l_2^2}\left[\frac{l_1^2}{m_z} + \frac{l_2^2}{m_x} + \frac{(l_1+l_2)^2}{m_y}\right] k_\delta \quad [37]$$

where l_1 and l_2 are the distances of X and Z from the central atom Y; m_x, m_y, and m_z are the masses of the atoms X, Y, and Z, respectively, and k_δ is the bending force constant. In the case under consideration, X = M, Y = H, D, or T, and Z = H_2O.

Assuming that force constants are invariant upon isotopic substitution and also that $m_x >> m_y$ and $m_z >> m_y$, it follows from Eq. [37] that

$$\frac{\nu_D}{\nu_H} = \left(\frac{m_H}{m_D}\right)^{1/2} \quad [38]$$

and

$$\frac{\nu_T}{\nu_H} = \left(\frac{m_H}{m_T}\right)^{1/2} \quad [39]$$

Generally bending frequencies are small (<600 cm^{-1}). We may hence assume that

$$\frac{\sinh^2(h\nu_D/2kT)_b}{\sinh^2(h\nu_H/2kT)_b} = \frac{\nu_D^2}{\nu_H^2} = \frac{m_H}{m_D} = \frac{1}{2} \quad [40]$$

$$\frac{\sinh^2(h\nu_T/2kT)_b}{\sinh^2(h\nu_H/2kT)_b} = \frac{\nu_T^2}{\nu_H^2} = \frac{m_H}{m_T} = \frac{1}{3} \quad [41]$$

as has been done by Melander (16)

For the calculation of the stretching vibrational frequencies, it is necessary to know the force constants of the respective bonds in the activated complex (Fig. 1). The potential energy of the system can then be expressed as a function of displacements from the saddle point by the equation

$$V = V_o + \frac{1}{2}k_{11}(r_1 - r_1^{\neq})^2 + \frac{1}{2}k_{22}(r_2 - r_2^{\neq})^2 + k_{12}(r_1 - r_1^{\neq})(r_2 - r_2^{\neq}) \quad [42]$$

where k_{11} is the force constant for the stretching of the bond between the water molecule and H^+ ion, k_{22} that for the stretching of the bond between the hydrogen and metal atoms, and k_{12} is a coupling constant. The kinetic energy of the system is given by

$$T = \frac{1}{2}m_1\dot{r}_1^2 + \frac{1}{2}m_2\dot{r}_2^2 + \frac{1}{2}m_3\dot{r}_3^2 \quad [43]$$

where m_1, m_2, and m_3 are the masses of the water molecule, hydrogen, and metal atoms, respectively.

Using Lagrange's equation of motion, it can then be shown that the stretching frequencies are given by the equation

$$\lambda^2 - \lambda\left[\left(\frac{1}{m_1}+\frac{1}{m_2}\right)k_{11} + \left(\frac{1}{m_2}+\frac{1}{m_3}\right)k_{22} - \frac{2}{m_2}k_{12}\right] + \frac{m_1+m_2+m_3}{m_1m_2m_3}(k_{11}k_{22} - k_{12}^2) = 0 \quad [44]$$

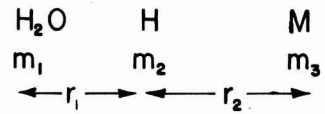

Fig. 1. Activated complex for slow discharge mechanism

where

$$\lambda = 4\pi^2\nu^2 \qquad [45]$$

As pointed out earlier, one of these frequencies is imaginary for the activated complex. An absolute calculation of the partition function ratio of the isotopic activated complexes, due to the real stretching frequencies presents a number of difficulties. Two of the approximate methods used will be described in the following subsections.

Method 1, Case of low real stretching frequencies.—According to Westheimer (25), if the imaginary frequency be taken as zero, (one vibration becomes translation along reaction path), the last term in Eq. [44] can be set equal to zero.

$$\therefore\ k_{11}\,k_{22} = k_{12}^2 \qquad [46]$$

Under these conditions, the real frequency of the activated complex is given by

$$\lambda = 4\pi^2\nu^2 = \frac{k_{11}}{m_1} + \frac{k_{22}}{m_3} + \frac{k_{11} + k_{22} - 2k_{12}}{m_2} \qquad [47]$$

Using Eq. [46], Eq. [47] becomes

$$\lambda = 4\pi^2\nu^2 = \frac{k_{11}}{m_1} + \frac{k_{22}}{m_3} + \frac{k_{11} + k_{22} - 2\sqrt{k_{11}k_{22}}}{m_2} \qquad [48]$$

If we now make the assumption that $m_1 >> m_2$, $m_3 >> m_2$, and $k_{11} >> k_{22}$, Eq. [48] reduces to

$$\lambda = 4\pi^2\nu^2 = \frac{k_{11} + k_{22} - 2\sqrt{k_{11}k_{22}}}{m_2} \qquad [49]$$

It is clear from Eq. [49] that the ratio of vibrational frequencies for the H to D (or H to T) activated complexes is equal to the ratio of the square roots of the masses of the D to H (or T to H) atoms. Further, if we assume that these frequencies are small, the vibrational partition function ratio of the H to D (or H to T) activated complexes is equal to the ratio of the corresponding frequencies. Thus

$$\frac{f_{V,H}^{\neq}}{f_{V,D}^{\neq}} = \frac{m_H^{1/2}}{m_D^{1/2}} = \frac{1}{\sqrt{2}} \qquad [50]$$

$$\frac{f_{V,H}^{\neq}}{f_{V,T}^{\neq}} = \frac{m_H^{1/2}}{m_T^{1/2}} = \frac{1}{\sqrt{3}} \qquad [51]$$

Using Eq. [34], [35], [40], and [41], the complete partition function ratio is

$$\frac{f_H^{\neq}}{f_D^{\neq}} = 0.3479 \qquad [52]$$

$$\frac{f_H^{\neq}}{f_T^{\neq}} = 0.1851 \qquad [53]$$

The use of this method for the calculation of the vibrational partition function ratio gives an upper limit for the separation factors.

Method 2, Case of moderate or high frequencies, the method of Eyring *et al.* (10).—In this method, the potential energy of the linear three atom system (Fig. 1, H_2O is treated as a single atom) is given by the Heitler-London expression, *viz.*

$$V = K_{12} + K_{23} + K_{31} - \left[\frac{1}{2}\{(J_{12} - J_{23})^2 + (J_{23} - J_{31})^2 + (J_{31} - J_{12})^2\}\right]^{1/2} \qquad [54]$$

where K's are the coulombic and J's the exchange contributions to the total energies for interactions between H_2O and H^+, H and M, and M and H_2O.[3] As in the method of Eyring *et al.*, the reference state for the energy was taken as that of the separated atoms $H_2O + H + M$ and Morse functions were used to express variation of potential energy with distance.

The potential energy of the initial state $H_2O - H^+ + e_{o,M} + M$, expressed as a function of the distance between H^+ ion and H_2O molecule (pseudo atom) can then be obtained by considering the following Born-Haber cycle (14)

$$H + H_2O + M \rightarrow H^+ + H_2O + M + e \quad I \qquad [55]$$

$$H^+ + H_2O + e + M \rightarrow H_3O^+ + e_M + M \quad D_{12} - \phi \qquad [56]$$

Adding

$$H + H_2O + M \rightarrow H_3O^+ + e_M + M \quad V_{12} \qquad [57]$$

$$\therefore\ V_{12} = K_{12} + J_{12} = I + D_{12} - \phi \qquad [58]$$

where I is the ionization energy of the H atom, ϕ is the electronic work function of the metal, D_{12} is the energy of the H^+-OH_2 interaction as a function of the internuclear distance and is given by

$$D_{12} = D_{12}^{o}[1 - e^{-a(r_1 - r_1^{o})}]^2 - L \qquad [59]$$

L is the heat of solvation of a proton and D_{12}^{o} is the proton affinity of water.

Similarly, the potential energy of the final state MH + H_2O, expressed as a function of the distance between the M and H atoms, is obtained by considering the reaction

$$H + M + H_2O \rightarrow MH + H_2O \qquad D_{23} \qquad [60]$$

where

$$D_{23} = D_{23}^{o}[e^{-2a_2(r_2 - r_2^{o})} - 2e^{-a(r_2 - r_2^{o})}] = V_{23} = K_{23} + J_{23} \qquad [61]$$

Since the metal atom and water molecule are relatively far apart for all values of r_1 and r_2, and also because the interaction between M and H_2O is considerably less than between H and M or H^+ and H_2O, the M-H_2O interaction was taken as zero for all distances of separation, *i.e.*

$$V_{31} = K_{31} + J_{31} = 0 \qquad [62]$$

As in the method of Eyring *et al.*, a certain percentage of each of the energies V_{12}, V_{23}, and V_{31} was assumed to be coulombic and the balance exchange, for all distances of separation. Thus, the total en-

[3] In a normal chemical reaction of the type A + BC → AB + C, where A, B and C are atoms, all atoms maintain the same electronic state throughout the reaction path. In our case, it is necessary to treat the central particle as an ion for interaction with water and as an atom for interaction with M, since the initial state of the discharge step is $H_2O - H^+ + M + e_{o,M}$ and the final state is M − H + H_2O. Although not strictly correct, the approximation may be considered as satisfactory, since for small displacements from the equilibrium position of the H^+ and H_2O, the interaction energy is mainly that of H^+-OH_2, while the M-H interaction energy is small and vice versa for the case of small displacements of the H from the M-H equilibrium position. In the activated state, the central atom may be considered as partly neutralized, since in the initial state it is totally ionic, whereas in the final state it is an atom.

Table I. Physical constants used in calculation of potential energy of system for slow discharge mechanism

D_{12}°	D_{23}°	I	L	ϕ	r_1°	r_2°	a_1	a_2
187	57	313	263	104	1.05	1.74	1.375	1.20
	kcal · mole^{-1}				Å		Å^{-1}	

ergy of the system H_2O----H----M was calculated, using Eq. [54], as a function of r_1 and r_2.

All calculations were carried out with M = Hg. The constants used in the calculation of V_{12} and V_{23} with the aid of Eq. [58], [59], and [61] are given in Table I and were obtained from the paper of Parsons and Bockris (14) except for D_{12}° and a_1. Parsons and Bockris used the figure of 263 kcal mole^{-1} for D_{12}°, which is the heat of solvation of a proton. D_{12}° represents the dissociation energy of the H_2O-H^+ into H_2O and H^+ and the more appropriate figure is the proton affinity for water (187 kcal mole^{-1}). Due to this change in D_{12}°, a_1 is also altered.

Three calculations were carried out varying the percentage coulombic energies, ρ_1 and ρ_2, in V_{12} and V_{23}, respectively. In the first calculation, ρ_1 and ρ_2 were taken as 20%. The energy V, given by Eq. [54] was calculated as a function of the variable distances r_1 and r_2, using an I.B.M. 7090 computer. From the table of values of V as a function of r_1 and r_2, the reaction path and saddle point were determined. It was found that $r_1^{\neq} = 1.05$Å and $r_2^{\neq} = 3.40$Å. This calculation also showed that the classical activation energy excluding zero point energies is 2 kcal mole^{-1}. The force constants k_{11}, k_{22}, and k_{12}, appearing in Eq. [42] were then calculated by evaluating the second derivatives of V (Eq. [54]) at the saddle point. The coupling constant, k_{12}, is zero for the present model since the interaction between M and H_2O was ignored. The stretching vibrational frequencies, calculated using Eq. [44], for the isotopic activated complexes (H, D, and T) in this case and the subsequent two calculations are given in Table II.

In the second calculation, the percentage coulombic energy used for each interaction was reduced to 5% since the first calculation gave too small an activation energy. The activation energy increased to 6 kcal mole^{-1} in this case. This calculation and the subsequent one were also carried out to check any variation in the vibrational partition function ratio (due to stretching) of the isotopic activated complexes.

In the last calculation, the percentage coulombic energy for the O-H$^+$ bond was taken as 39% and 3% for the Hg-H bond. These figures were obtained from the relationship between percentage ionic character of a bond and the difference in electronegativities of the atoms forming the bond (26).

The results of all three calculations, including partition function ratios of the isotopic activated complexes are given in Table II. ρ_1 and ρ_2 are the percentage coulombic energies of the O-H$^+$ and H-Hg bonds respectively, $r_1^{\neq}$ and $r_2^{\neq}$ are the O-H$^{\oplus}$ and Hg-H internuclear distances respectively in the activated complex, $E^{\neq}$ is the activation energy $\dfrac{\sinh(h\nu_D/2kT)_s}{\sinh(h\nu_H/2kT)_s}$ and $\dfrac{\sinh(h\nu_T/2kT)_s}{\sinh(h\nu_H/2kT)_s}$ the partition function ratios of the isotopic activated complexes due to the real stretching frequencies.

Table II reveals that the variation in percentage coulombic energy has little influence on the real vibrational frequencies (ω_H, ω_D, ω_T) of the activated complexes. Further, the calculated activation energies are considerably less than the experimentally observed values. This discrepancy is probably due to the neglect of the H_2O-Hg interaction in the calculation of V. The real frequency for the H activated complex is of the order of the frequency of the bond O-H$^+$, which is the highest possible value. This high value may be expected, since it is found that in the activated complex the O-H bond is not stretched from the equilibrium value in H_2O-H$^+$ in any of the calculations. Thus, the partition function ratios, $f_H^{\neq}/f_D^{\neq}$ and $f_H^{\neq}/f_T^{\neq}$, in Table II, may be considered as the lower limits for these ratios.

Tunneling factor ratios ($\Gamma_{1,H}/\Gamma_{1,D}$ and $\Gamma_{1,H}/\Gamma_{1,T}$).— The tunneling factor ratios depend on potential. The calculations of Christov (27) refer to the reversible potential. The H/T separation factors on Hg were determined (28) at a current density of 10^{-2} amp cm^{-2}. Hence the tunneling factor ratios are now calculated at the barrier height corresponding to this current density. The overpotential (η) at this current density is about 1v. The activation energy ($E^{\neq}$) may be obtained by using the relation

$$E^{\neq} = E_o^{\neq} - \beta\eta \qquad [63]$$

where $E_o^{\neq}$ is the activation energy at the reversible potential and β is the symmetry factor.

Using $E_o^{\neq} = 21.5$ kcal mole^{-1} and $\beta = \frac{1}{2}$, $E^{\neq} = 10$ kcal mole^{-1}.

Two proton (or isotopic ions) transfer distances are possible, depending on the model chosen. If it is assumed that the proton transfer takes place from

Table II. Force constant (k's), stretching vibrational frequencies (ω's), partition function ratios (f_H/f_D and f_H/f_T) of isotopic activated complexes for the slow discharge mechanism

Parameter	Calculation number 1	2	3
ρ_1 (%)	20	5	39
ρ_2 (%)	20	5	3
$r_1^{\neq}$ (Å)	1.05	1.05	1.05
$r_2^{\neq}$ (Å)	3.40	2.92	3.30
$E^{\neq}$ (kcal mole^{-1})	2	6	4
k_{11} (kcal mole^{-1} Å^{-2})	688.6	635.1	654.8
k_{22} (kcal mole^{-1} Å^{-2})	−3.9	−12.7	−10.6
k_{12} (kcal mole^{-1} Å^{-2})	0	0	0
ω_H (cm^{-1})	2906	2773	2820
ω_D (cm^{-1})	2110	2015	2048
ω_T (cm^{-1})	1763	1686	1714
$\omega_H^{\neq}$ (cm^{-1})	52 i	90 i	84 i
$\omega_D^{\neq}$ (cm^{-1})	50 i	88 i	83 i
$\omega_T^{\neq}$ (cm^{-1})	50 i	89 i	81 i
$\dfrac{\sinh(h\nu_D/2kT)_s}{\sinh(h\nu_H/2kT)_s}$	0.1465	0.1605	0.1552
$\dfrac{\sinh(h\nu_T/2kT)_s}{\sinh(h\nu_H/2kT)_s}$	0.0633	0.0725	0.0672
$(f_H^{\neq}/f_D^{\neq})$ 10^2	7.207	7.897	7.636
$(f_H^{\neq}/f_T^{\neq})$ 10^2	2.030	2.325	2.155

a hydroxonium ion specifically adsorbed on the electrode, the proton transfer distance is 1.15Å. The other possible proton transfer distance follows from the model of Bockris, Devanathan, and Müller (29), where a layer of water molecules is assumed between the electrode surface and the Helmholtz plane. In this case, the proton transfer distance is 2.86Å. This distance corresponds to the width of the equivalent Eckart barrier (4.75Å) used by Christov at the reversible potential.

Tunneling factors were obtained both for the symmetrical Eckart and parabolic barriers. In the former case, they were obtained from the tunneling factors tabulated as a function of the barrier height and frequency at the top of the barrier [which can easily be related to the barrier height and width (17)] by Johnston and Rapp (30). In the latter case, the method of Bell (31) was followed, assuming in this calculation the same barrier height and curvature at the top of the barrier as the equivalent Eckart barrier.

For the smaller proton transfer distance, the tunneling factor ratios, $\Gamma_{1,H}/\Gamma_{1,D}$ and $\Gamma_{1,H}/\Gamma_{1,T}$, for a symmetrical Eckart barrier are 4.8 and 8.4, respectively. The corresponding values for a parabolic barrier are 14 and 33. It has been pointed out earlier that when the degree of tunneling is high, the use of the parabolic barrier overestimates the tunneling factor ratios.

For the higher proton transfer distance, the tunneling factor ratios, $\Gamma_{1,H}/\Gamma_{1,D}$ and $\Gamma_{1,H}/\Gamma_{1,T}$ are 1.24 and 1.35, respectively, for a symmetrical Eckart barrier. These values are in excellent agreement with the corresponding ratios of 1.25 and 1.34 obtained for a parabolic barrier.

Separation factors.—Separation factors excluding tunneling corrections (S_D^* and S_T^*).—Excluding tunneling corrections, the separation factors[4] were calculated for the two methods of obtaining vibrational partition function ratios due to the real stretching frequencies (cases of low and moderate/high real frequencies). For this purpose, the Eq. [25], [26], [29], [30], [52], [53] and data in Table II were made use of. The separation factors are tabulated in Table III. The first method (low real stretching frequencies) gives an upper limit whereas the second (moderate or high frequencies—Eyring's method) a lower limit for the separation factor. The values obtained by the latter method, with variation of percentage coulombic and exchange energies are consistent to within 10%.

The values of S_D^* and S_T^*, calculated here, are significantly different from the earlier values of Keii and Kodera (1) for S_D^* of 12-14, and of Kodera and Saito (3) for S_T^* of 33-37, mainly because of the inclusion of the isotope effect due to the real stretching frequency in the present work.

Separation factors including tunneling corrections.—Table III shows that if we use $2l_E = 1.90$Å ($2l_E$ is the width of the equivalent Eckart barrier, corresponding to a proton transfer distance of 1.15Å), the separation factors obtained including tunneling corrections for both methods of calculation of partition function ratios of activated complexes, are considerably higher than the experimental separation factors. For $2l_E = 4.75$Å, with the second method of calculation of vibrational partition function ratios due to the real stretching frequencies, S_D and S_T are in the region of experimentally determined separation factors.

It may also be added that with $2l_E = 4.75$Å the separation factors, obtained for the case of low real stretching frequencies of the isotopic activated complexes, are considerably higher than the experimentally observed separation factors (even for the case of the linked discharge-electrochemical desorption mechanism, as seen below). We may thus conclude that the approximate method (for low real stretching frequencies) is not valid in our case.

Table III. Separation factors for the slow discharge fast recombination mechanism

Separation factors excluding (S^*) or including tunneling corrections (S)	Methods of calculation of $f_H^{\neq}/f_D^{\neq}$ or $f_H^{\neq}/f_T^{\neq}$			
	Method 1	Method 2—Moderate or high real stretching frequency		
		Calculation 1	Calculation 2	Calculation 3
S_D^*	11.0	2.3	2.5	2.4
S_T^*	29.3	3.2	3.7	3.4
$S_D(2l_E = 1.90\text{Å})$	53.0	11.1	12.0	11.6
$S_D(2l_E = 4.75\text{Å})$	13.6	2.9	3.1	3.0
$S_T(2l_E = 1.90\text{Å})$	245.2	26.8	31.0	28.5
$S_T(2l_E = 4.75\text{Å})$	39.6	4.3	5.0	4.6

Discharge followed by electrochemical desorption at low and intermediate overpotentials.—Expression for separation factor.—The discharge steps [4] and [5] are followed by

$$H_3O^+ + e_o + MH \rightarrow H_2 + H_2O + M \qquad [64]$$

$$H_3O^+ + e_o + MD \rightarrow HD + H_2O + M \qquad [65]$$

$$H_2DO^+ + e_o + MH \rightarrow HD + H_2O + M \qquad [66]$$

It follows from Eq. [1] and [2] that S_D is given by

$$S_D = \frac{c_{H_2}}{c_{HD}} \cdot \frac{a_{HDO_l}}{a_{H_2O_l}} \qquad [67]$$

for the condition that $(c_H)_s >> (c_D)_s \cdot c_{H_2}/c_{HD}$ is the ratio of concentrations of the electrolytic gases H_2 to HD. Since the electrochemical desorption steps may be considered to be in equilibrium at low and intermediate overpotentials, when the discharge step is rate-determining, we have from Eq. [64] and [66] the following equilibrium

$$H_3O^+ + HD \rightleftharpoons H_2DO^+ + H_2 \qquad [68]$$

In addition to this equilibrium reaction, we also have the equilibrium reactions [13], [14], and [17], from which it follows that

$$H_2O_l + HD \rightleftharpoons HDO_l + H_2 \qquad [69]$$

The ratio, c_{H_2}/c_{HD}, may now be expressed as

$$\frac{c_{H_2}}{c_{HD}} = K_{HD} \cdot \frac{a_{H_2O_l}}{a_{HDO_l}} \qquad [70]$$

[4] Inclusion of anharmonicity corrections in the partition function ratios of (a) isotopic water molecules in the gas phase and (b) isotopic activated complexes has an effect of less than 10% on the separation factors. The authors wish to thank one of the reviewers for pointing out the effect of anharmonicity corrections on the former partition function ratio.

where K_{HD} is the equilibrium constant for reaction [69]. Use of Eq. [70] in [67] gives the interesting result

$$S_D = K_{HD} \quad [71]$$

and similarly we have

$$S_T = K_{HT} \quad [72]$$

where K_{HT} is the equilibrium constant for the reaction

$$H_2O_l + HT \rightleftharpoons HTO_l + H_2 \quad [73]$$

Numerical values of separation factors (S_D and S_T).—The equilibrium constants K_{HD} and K_{HT} are 3.8 [Farkas and Farkas (32)] and 6.2 [Libby (33)], respectively, at room temperature. The calculated and experimental results of these equilibrium constants are in excellent agreement. Thus, for the case of the slow discharge mechanism followed by the fast electrochemical desorption step, with the latter treated as in equilibrium, the H/D and H/T separation factors are equal to these values at room temperature.

Discharge followed by electrochemical desorption of high overpotentials.—Expression for separation factor.—At high overpotentials the reverse currents of the electrochemical desorption steps may be neglected. During electrolysis, the ratio $(c_H/c_D)_g$ is hence given by

$$\left(\frac{c_H}{c_D}\right)_g = \frac{2i_{3,H_2} + i_{3,HD}}{i_{3,HD}} \quad [74]$$

where i_{3,H_2} and $i_{3,HD}$ are the partial currents for H_2 and HD evolution, respectively. Since $(c_H)_s >> (c_D)_s$, $i_{3,H_2} >> i_{3,HD}$ and Eq. [74] reduces to

$$\left(\frac{c_H}{c_D}\right)_g = \frac{2i_{3,H_2}}{i_{3,HD}} \quad [75]$$

Using Eq. [2] and [75], we have

$$S_D = \frac{a_{HDO_l}}{a_{H_2O_l}} \cdot \frac{i_{3,H_2}}{i_{3,HD}} \quad [76]$$

$i_{3,HD}$ is composed of two further partial currents, since there are two paths [65] and [66] for HD evolution. We may, therefore, write

$$i_{3,HD} = i_{3,D,H} + i_{3,H,D} \quad [77]$$

where $i_{3,D,H}$ and $i_{3,H,D}$ are the partial currents according to paths [65] and [66] respectively. The electrochemical desorption currents may be expressed as

$$i_{3,H_2} = k_{3,H_2}\, a_{H_3O^+}\, \theta_H\, e^{-\beta VF/RT} \quad [78]$$

$$i_{3,D,H} = k_{3,D,H}\, a_{H_3O^+}\, \theta_D\, e^{-\beta VF/RT} \quad [79]$$

$$i_{3,H,D} = k_{3,H,D} \frac{a}{3} H_2DO^+\, \theta_H\, e^{-\beta VF/RT} \quad [80]$$

$$\therefore \quad \frac{i_{3,HD}}{i_{3,H_2}} = \frac{i_{3,D,H} + i_{3,H,D}}{i_{3,H_2}} \quad [81]$$

$$= \frac{k_{3,D,H}}{k_{3,H_2}} \cdot \frac{\theta_D}{\theta_H} + \frac{k_{3,H,D}}{k_{3,H_2}} \cdot \frac{\frac{1}{3} a_{H_2DO^+}}{a_{H_3O^+}} \quad [82]$$

It is now necessary to evaluate the ratio θ_D/θ_H. Using the stationary state hypothesis for θ_H and θ_D, we have

$$k_{1,H}\, a_{H_3O^+}(1 - \theta_H - \theta_D) - k_{3,H_2}\, a_{H_3O^+}\, \theta_H - k_{3,H,D} \frac{1}{3} a_{H_2DO^+}\, \theta_H = 0 \quad [83]$$

and

$$k_{1,D} \frac{1}{3} a_{H_2DO^+}\, (1 - \theta_H - \theta_D) - k_{3,D,H}\, a_{H_3O^+}\, \theta_D = 0 \quad [84]$$

Solving the simultaneous Eq. [83] and [84] for θ_H and θ_D,

$$\frac{\theta_D}{\theta_H} = \frac{k_{3,H2}\, a_{H_3O^+}\, k_{1,D} \frac{1}{3} a_{H_2DO^+} + k_{3,H,D} \frac{1}{3} a_{H_2DO^+}\, k_{1,D} \frac{1}{3} a_{H_2DO^+}}{k_{1,H}\, a_{H_3O^+}\, k_{3,D,H}\, a_{H_3O^+}} \quad [85]$$

The second term in the numerator on the right hand side of Eq. [85] is very small compared to the first, since

$$a_{H_3O^+} >> a_{H_2DO^+} \quad [86]$$

and

$$k_{3,H_2} > k_{3,H,D} \quad [87]$$

Equation [85], thus reduces to

$$\frac{\theta_D}{\theta_H} = \frac{k_{3,H_2}}{k_{1,H}} \cdot \frac{k_{1,D}}{k_{3,D,H}} \cdot \frac{\frac{1}{3} a_{H_2DO^+}}{a_{H_3O^+}} \quad [88]$$

Using Eq. [88] in [82], we have

$$\frac{i_{3,HD}}{i_{3,H_2}} = \frac{k_{3,HD}}{k_{3,H_2}} \cdot \frac{\frac{1}{3} a_{H_2DO^+}}{a_{H_3O^+}} + \frac{k_{1,D}}{k_{1,H}} \cdot \frac{\frac{1}{3} a_{H_2DO^+}}{a_{H_3O^+}} \quad [89]$$

It follows from Eq. [76] and [89] that

$$S_D = \frac{a_{HDO_l}}{a_{H_2O_l}} \cdot \frac{a_{H_3O^+}}{\frac{1}{3} a_{H_2DO^+}} \cdot \frac{1}{\left(\frac{k_{3,H,D}}{k_{3,H_2}} + \frac{k_{1,D}}{k_{1,H}}\right)} \quad [90]$$

$$= \frac{1}{\frac{1}{S_{D,E_1}} + \frac{1}{2S_{D,1}}} \quad [91]$$

where

$$S_{D,1} = \frac{1}{2} \frac{k_{1,H}}{k_{1,D}} \cdot \frac{a_{H_3O^+}}{\frac{1}{3} a_{H_2DO^+}} \cdot \frac{a_{HDO_l}}{a_{H_2O_l}} \quad [92]$$

and

$$S_{D,E_1} = \frac{k_{3,H_2}}{k_{3,H,D}} \cdot \frac{a_{H_3O^+}}{\frac{1}{3} a_{H_2DO^+}} \cdot \frac{a_{HDO_l}}{a_{H_2O_l}} \quad [93]$$

It may be noted that Eq. [92] is also obtained from Eq. [2], [3], [6], and [7] and is numerically

Table IV. Separation factors for the slow discharge fast electrochemical desorption mechanism at high overpotentials

Calculation (27) No. for S_{D,E_1} or S_{T,E_1}	Percentage coulombic energy (ρ)			Separation factors excluding tunneling corrections			Separation factors including tunneling corrections		
	ρ_{M-H}	$\rho_{H^+-OH_2}$	ρ_{H-H}	$S_{D,1}^*$	S_{D,E_1}^*	S_D^*	$S_{D,1}$	S_{D,E_1}	S_D
3	100	100	100	2.4	11.8	3.4	3.0	13.0	4.1
4	20	20	15	2.4	14.9	3.6	3.0	16.4	4.4
				$S_{T,1}^*$	S_{T,E_1}^*	S_T^*	$S_{T,1}$	S_{T,E_1}	S_T
3	100	100	100	3.4	27.9	5.4	4.6	29.5	7.0
4	20	20	15	3.4	34.1	5.7	4.6	39.5	7.5

equal to the separation factor worked out in an earlier subsection. It is also shown in a separate paper (33) that S_{D,E_1} is pseudo separation factor for the electrochemical desorption step according to paths [64] and [66] only.

Numerical calculation of separation factors.—Separation factors excluding tunneling corrections (S_D^* and S_T^*).—With the average of the $S_{D,1}^*$ values, 2.4, using the second method for the calculation of the partition function ratio of the isotopic activated complexes due to the real stretching frequencies (earlier subsection) and the value of S_{D,E_1}^* (11.8) assuming a 100% coulombic energy for all interactions, Eq. [91] shows that S_D^* is 3.4. A similar calculation, using $S_{T,1}^* = 3.4$ and $S_{T,E_1}^* = 25.5$ gives a value of 5.4 for S_T^* at 25°C.

Assuming at 20% coulombic energy for the H^+-OH_2 and also for the M-H interactions and a 15% coulombic energy for the H-H interaction, in the calculation of S_{D,E_1}^* and S_{T,E_1}^*, their respective values are 14.9 and 34.1. With these values and the values used earlier for $S_{D,1}^*$ and $S_{T,1}^*$, S_D^* and S_T^* are 3.6 and 5.7, respectively.

Separation factors including tunneling corrections (S_D and S_T).— These values are summarized in Table IV along with the corresponding S^* values.

Conclusions

It may be seen from Table V that the separation factor for a slow discharge mechanism depends on the desorption step as well. For a desorption step by the combination of adsorbed hydrogen atoms, the separation factor is solely determined by the ratio of rate constants for the discharge step. For a desorption by the electrochemical mechanism the separation factors depend on whether this step is treated as in equilibrium or not in equilibrium. In the former case, the separation factors (S_D and S_T) become the respective equilibrium constants of the H_2/HDO_l and H_2/HTO_l interchange reactions. In the latter case, the separation factors are the same as for a coupled discharge-electrochemical desorption mechanism.

Table V. Theoretical separation factors for the slow discharge mechanism

Mechanism	Separation factors excluding tunneling corrections		Separation factors including tunneling corrections	
	S_D^*	S_T^*	S_D	S_T
Slow discharge-fast recombination	2.4	3.4	3.0	4.6
Slow discharge-fast electrochemical	3.8	6.2	3.8	6.2
Linked discharge-electrochemical				
(i) Coulombic energy—100% for all interactions	3.4	5.4	4.1	7.0
(ii) Coulombic energy—20% for M-H and H^+-OH_2, 15% for H-H interactions	3.6	5.7	4.4	7.5

The H/D separation factors are not sufficiently separated to be of value in determining the desorption step. The H/T separation factors may be useful for this purpose.

A slow discharge-fast electrochemical desorption mechanism cannot be distinguished from a fast discharge-slow electrochemical desorption mechanism [as seen in a subsequent paper (33)] at high overpotentials when the reverse currents of the discharge and electrochemical desorption steps may be neglected in comparison to their forward currents. The only way of distinguishing between these two mechanisms is by a determination of degree of coverage (θ) of atomic hydrogen on the electrode since $\theta \to 0$ for a slow discharge mechanism and $\theta \to 1$ for a slow electrochemical desorption mechanism.

The tunneling corrections may be somewhat overestimated. In this case, the H/T separation factors for the three cases are nearly equal.[5] There are two possible ways of examining the tunnel effect (i) influence of potential on the separation factors [*cf.*, Conway, ref. (11)], and (ii) influence of temperature on the separation factor at constant potential. Assuming no change of mechanism, with variation of potential, there should be no change of separation factor with current density if the desorption step is the electrochemical desorption mechanism and is treated as in equilibrium. The other mechanisms will be affected since the tunneling factors change with potential. Temperature effect of S will also distinguish the slow discharge-fast electrochemical desorption mechanism (with the latter treated as in equilibrium) from the others.

Acknowledgments

Financial support from the Aeronautical Systems Command, Air Force Systems Command, United States Air Force, Contract 33 (657)-8823, is gratefully acknowledged. The authors also wish to thank Drs. E. R. Nixon, E. R. Thornton, T. E. Sharp, H.

[5] The authors wish to thank Mr. D. B. Matthews for making these suggestions.

Carlmichael, and K. Thormalingam, and Messrs. D. B. Matthews and R. Haynes for helpful theoretical discussions. Mathematical assistance from Mr. C. Vaseekaran and part of the computer facilities afforded by Dr. L. Nanis are also greatly appreciated.

Manuscript received Aug. 5, 1963; revised manuscript received Dec. 11, 1963. This paper is from work carried out in partial fulfillment of requirements for the degree of Ph.D.

Any discussion of this paper will appear in a Discussion Section to be published in the June 1965 JOURNAL.

REFERENCES

1. T. Keii and T. Kodera, *J. Research Inst. Cat.*, **5**, 105 (1957).
2. B. E. Conway, *Proc. Roy. Soc.*, **A247**, 400 (1958).
3. T. Kodera and T. Saito, *J. Research Inst. Cat.*, **7**, 5 (1959).
4. G. Okamoto, J. Horiuti, and K. Hirota, *Sci. Papers Inst. Phys. Chem. Research (Tokyo)*, **29**, 223 (1936).
5. J. Horiuti, T. Keii, and K. Hirota, *J. Research Inst. Cat.*, **2**, 1 (1951).
6. J. Horiuti and T. Nakamura, *ibid.*, **2**, 73 (1951).
7. J. O'M. Bockris, "Modern Aspects of Electrochemistry," vol. I, chap. IV, Butterworths, London (1954).
8. B. E. Conway, *Proc. Roy. Soc.*, **A256**, 128 (1960).
9. B. E. Conway, "Transactions Symposium on Electrode Processes," chap. 15, The Electrochemical Society, John Wiley & Sons, New York (1961).
10. S. Glasstone, K. J. Laidler, and H. Eyring, "The Theory of Rate Processes," McGraw Hill Book Co., New York (1941).
11. C. E. H. Bawn and G. Ogden, *Trans. Faraday Soc.*, **30**, 432 (1934).
12. B. E. Conway, *Can. J. Chem.*, **37**, 178 (1959).
13. H. S. Johnston, "Advances in Chemical Physics," vol. III, p. 131, Interscience Publishers, New York (1961).
14. R. Parsons and J. O'M. Bockris, *Trans. Faraday Soc.*, **47**, 914 (1951).
15. B. E. Conway, J. O'M. Bockris, and B. Lovrecek, "Proceedings C.I.T.C.E., Sixth Meeting," p. 207, Butterworths, London (1955).
16. L. Melander, " Isotope Effects on Reaction Rates," Ronald Press, New York (1960).
17. S. Srinivasan, Thesis, University of Pennsylvania (1963).
18. M. Ikusima and S. Azakami, *J. Chem. Soc. Japan*, **59**, 40 (1938).
19. J. Horiuti and G. Okamoto, *Bull. Chem. Soc. Japan*, **10**, 503 (1935).
20. O. Sepall and S. G. Mason, *Can. J. Chem.*, **38**, 2024 (1960).
21. G. Brown, Referred to in ref. (20).
22. W. S. Benedict, N. Gailer, and E. K. Plyer, *J. Chem. Phys.*, **24**, 1139 (1956).
23. W. F. Libby, *ibid.*, **11**, 101 (1943).
24. G. Herzberg, "Infra Red and Raman Spectra of Polyatomic Molecules," p. 173, Van Nostrand, New York (1945).
25. F. H. Westheimer, *Chem. Rev.*, **61**, 265 (1961).
26. L. Pauling, "The Nature of the Chemical Bond," Cornell University Press, New York (1962).
27. St. G. Christov, *Electrochim. Acta*, **4**, 194 (1961).
28. J. O'M. Bockris and S. Srinivasan, To be published in *Electrochem. Acta*.
29. J. O'M. Bockris, M. A. V. Devanathan, and K. Müller, *Proc. Roy. Soc.*, **A274**, 55 (1963).
30. H. S. Johnston and D. Rapp, *J. Am. Chem. Soc.*, **83**, 1 (1961).
31. R. P. Bell, *Trans. Faraday Soc.*, **55**, 1 (1959).
32. A. Farkas and L. Farkas, *J. Chem. Phys.*, **2**, 468 (1934).
33. J. O'M. Bockris and S. Srinivasan, *This Journal*, **111**, 853 (1964).

Theoretical Calculations of the Separation Factors in the Hydrogen Evolution Reaction for the Slow Electrochemical Desorption Mechanism

John O'M. Bockris and S. Srinivasan

The Electrochemistry Laboratory, The University of Pennsylvania, Philadelphia, Pennsylvania

ABSTRACT

Separation factors (S) for the slow electrochemical desorption mechanism at low and intermediate overpotentials are calculated for Ni. The S values are distinctly separated from those for all other mechanisms. The results are consistent with variation of percentage coulombic energy of all interactions. The separation factor method alone cannot be used to distinguish between either of the rate-determining steps in a linked discharge electrochemical desorption mechanism. A knowledge of the degree of coverage is also required.

Calculations of electrolytic separation factors are of value in examination of mechanism of hydrogen evolution and are discussed elsewhere (1). Of the mechanisms cogent in this discussion, the electrochemical desorption mechanism is one of importance. The theoretical values, associated with this mechanism, are calculated in this paper.

In previous calculations of the separation factor for this mechanism (2), the rate of only one of the two paths for HD evolution

$$H_3O^+ + e_o + MD \rightarrow HD + H_2O + M \quad [1a]$$

$$H_2DO^+ \; e_o + MH \rightarrow HD + H_2O + M \quad [1b]$$

was compared with the rate of H_2 evolution according to

$$H_3O^+ + e_o + MH \rightarrow H_2 + H_2O + M \quad [2]$$

That HD evolution could occur by the two parallel paths [1a] and [1b] was considered by the author of the previous paper, who concluded however that HD evolution by step [1b] would lead to separation fac-

tors less than unity, which is in conflict with experimental observations. Since the total quantity of HD in the electrolytic gas is evolved according to the two parallel paths, it is necessary to compare the rates of both paths simultaneously with the rate of path [2]. Further refinements on the previous calculations are possible through inclusion of the zero point energy differences of the isotopic activated complexes (which were assumed sufficiently short lived that their vibrational frequencies do not contribute to the activation energy), and of tunneling corrections [as there is still some question as to the conditions under which these contribute significantly to the separation factors (3, 4)].

For mechanisms involving adsorbed species in the rate determining step, the ratio of adsorbed atomic hydrogen to deuterium (θ_H/θ_D) is a particularly important quantity. In the previous separation factor calculations, this ratio was worked out for a steady-state situation, allowing for isotopic differences of free energies of activation in the forward and backward directions of the discharge step. The result of assuming that θ_H/θ_D is approximately equal to the ratio of activities of the isotopic ions H_3O^+ and H_2DO^+ was also considered. Since an isotope effect exists in the primary discharge step, this latter assumption is not correct.

Present Calculations

Slow Electrochemical Desorption at Low and Intermediate Overpotentials

Expression for separation factor.—Under these conditions, the discharge steps may be considered to be in equilibrium. They are represented by

$$H_3O^+ + e_o + M \rightleftharpoons MH + H_2O \qquad [3]$$

$$H_2DO^+ + e_o + M \rightleftharpoons MD + H_2O \qquad [4]$$

and are followed by [1], [2] and

$$H_3O^+ + e_o + MH \rightarrow H_2 + H_2O + M \qquad [5]$$

If $a_{H_2O_l} >> a_{HDO_l}$, the separation factor is given by

$$S_D = \frac{1}{2}\left(\frac{C_H}{C_D}\right)_g \cdot \frac{a_{HDO_l}}{a_{H_2O_l}} \qquad [6]$$

where $(C_H/C_D)_g$ is the ratio of atomic concentrations of H to D in the electrolytic gas. During electrolysis, $(C_H/C_D)_g$ may be expressed as

$$\left(\frac{C_H}{C_D}\right)_g = \frac{2i_{3,H_2} + i_{3,HD}}{i_{3,HD}} \qquad [7]$$

where i_{3,H_2} is the electrochemical desorption current according to path [5] and $i_{3,HD}$ is the total current for HD evolution according to the two parallel paths [1] and [2]. Since $i_{3,H_2} >> i_{3,HD}$, S_D is given by

$$S_D = \frac{a_{HDO_l}}{a_{H_2O_l}} \cdot \frac{i_{3,H_2}}{i_{3,HD}} \qquad [8]$$

The currents i_{3,H_2} and $i_{3,HD}$ may be represented as

$$i_{3,H_2} = k_{3,H_2}\, a_{H_3O^+}\, a_{MH}\, e^{-\beta VF/RT} \qquad [9]$$

$$i_{3,HD} = i_{3,H,D} + i_{3,D,H} \qquad [10]$$

where

$$i_{3,H,D} = k_{3,H,D}\frac{a}{3} H_2DO^+\, a_{MH}\, e^{-\beta VF/RT} \qquad [11]$$

$$i_{3,D,H} = k_{3,D,H}\, a_{H_3O^+}\, a_{MD}\, e^{-\beta VF/RT} \qquad [12]$$

$i_{3,D,H}$ and $i_{3,H,D}$ are the partial currents according to paths [1] and [2], respectively; k's are the respective rate constants; a_{MH} and a_{MD} are the activities of the adsorbed hydrogen and deuterium atoms respectively, on the surface; and V is the metal solution potential difference.

It follows from Eq. [9] to [12] that

$$\frac{i_{3,HD}}{i_{3,H_2}} = \frac{i_{3,H,D} + i_{3,D,H}}{i_{3,H_2}} \qquad [13]$$

$$= \frac{k_{3,H,D}}{k_{3,H_2}} \cdot \frac{\frac{1}{3} a_{H_2DO^+}}{a_{H_3O^+}} + \frac{k_{3,D,H}}{k_{3,H_2}} \cdot \frac{a_{MD}}{a_{MH}} \qquad [14]$$

$$= \frac{\Gamma_H}{\Gamma_D} \cdot \frac{f_{H,D}^{\neq}}{f_{H_2}^{\neq}} \cdot \frac{f_{H_3O^+}}{f_{H_2DO^+}} \cdot \frac{\frac{1}{3} a_{H_2DO^+}}{a_{H_3O^+}} + \frac{\Gamma_H}{\Gamma_D} \cdot \frac{f_{D,H}^{\neq}}{f_{H_2}^{\neq}} \cdot \frac{f_{MH}}{f_{MD}} \cdot \frac{a_{MH}}{a_{MD}} \qquad [15]$$

$$= \frac{\Gamma_H}{\Gamma_D} \cdot \frac{f_{H,D}^{\neq}}{f_{H_2}^{\neq}} \cdot \frac{e^{-\mu_{H_3O^+}/RT}}{e^{-\mu_{H_2DO^+}/RT}} + \frac{\Gamma_H}{\Gamma_D} \cdot \frac{f_{D,H}^{\neq}}{f_{H_2}^{\neq}} \cdot \frac{e^{-\mu_{MH}/RT}}{e^{-\mu_{MD}/RT}} \qquad [16]$$

Γ, f, μ with the appropriate suffices are the tunneling factor, partition function, and chemical potential, respectively, of the indicated isotopes.

By considering the equilibrium reactions [3] and [4] and also between the isotopic oxonium ions and water molecules in the liquid phase and then in the gaseous phase (5), Eq. [16] may be written as

$$\frac{i_{3,HD}}{i_{3,H_2}} = \left(\frac{f_{H,D}^{\neq}}{f_{H_2}^{\neq}} + \frac{f_{D,H}^{\neq}}{f_{H_2}^{\neq}}\right) \frac{\Gamma_H}{\Gamma_D} \cdot \frac{e^{-\mu_{H_2O_g}/RT}}{e^{-\mu_{HDO_g}/RT}} \qquad [17]$$

It follows from Eq. [8] and [17] that

$$S_D = \frac{\Gamma_H}{\Gamma_D} \cdot \frac{f_{HDO_g}}{f_{H_2O_g}} K_D \left[\frac{f_{H,D}^{\neq}}{f_{H_2}^{\neq}} + \frac{f_{D,H}^{\neq}}{f_{H_2}^{\neq}}\right]^{-1} \qquad [18]$$

Equation [18] may also be expressed in the form

$$\frac{1}{S_D} = \frac{1}{S_{D,E_1}} + \frac{1}{S_{D,E_2}} \qquad [19]$$

where

$$S_{D,E_1} = \frac{\Gamma_H}{\Gamma_D} \cdot \frac{f_{H_2}^{\neq}}{f_{H,D}^{\neq}} \cdot \frac{f_{HDO_g}}{f_{H_2O_g}} K_D \qquad [20]$$

and

$$S_{D,E_2} = \frac{\Gamma_H}{\Gamma_D} \cdot \frac{f_{H_2}^{\neq}}{f_{D,H}^{\neq}} \cdot \frac{f_{HDO_g}}{f_{H_2O_g}} K_D \qquad [21]$$

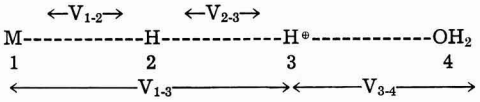

Fig. 1. Activated complex for slow electrochemical desorption mechanism.

K_D is the equilibrium constant for the reaction

$$H_2O_l + HDO_g \rightleftharpoons H_2O_g + HDO_l \qquad [22]$$

The H/T separation factor for the fast discharge-slow electrochemical desorption mechanism at low and intermediate overpotentials is given by an expression, similar to [19].

Numerical Calculations of Separation Factors

Product of equilibrium constant (K_D or K_T) *and partition function ratio of isotopic water molecules in the gas phase* (f_{HDOg}/f_{H2Og} *or* f_{HTOg}/f_{H2Og}).—In a previous paper (3), it was shown

$$K_D \cdot \frac{f_{HDOg}}{f_{H2Og}} = 63.36 \qquad [23]$$

$$K_T \cdot \frac{f_{HTOg}}{f_{H2Og}} = 316.48 \qquad [24]$$

Partition function ratios of isotopic activated complexes ($f_{H,D}^{\neq}/f_{H_2}^{\neq}$, $f_{H,T}^{\neq}/f_{H_2}^{\neq}$, $f_{D,H}^{\neq}/f_{H_2}^{\neq}$, *and* $f_{T,H}^{\neq}/f_{H_2}^{\neq}$).—It may be assumed that the activated complex has a configuration in which the centers of the metal atom, hydrogen atom, partially neutralized hydrogen ion and water molecule are collinear, as shown in Fig. 1.

For the calculation of $f_{H,D}^{\neq}/f_{H_2}^{\neq}$, isotopic substitution occurs at position 3 in Fig. 1, whereas for calculating $f_{D,H}^{\neq}/f_{H_2}^{\neq}$, isotopic substitution is at position 2. The activated complexes may be regarded as immobile, under which conditions their translational partition function ratio is unity. The contribution to the isotope effect due to restricted rotation about the two axes, mutually perpendicular to the axis of the molecule is insignificant, due to the heavy end atoms. Thus, the partition function ratios of the isotopic activated complexes reduce to

$$\frac{f_{H_2}^{\neq}}{f_{H,D}^{\neq}} = \frac{\prod_i^5 \sinh(h\nu_i/2kT)_{H,D}}{\prod_i^5 \sinh(h\nu_i/2kT)_{H_2}} \qquad [25]$$

$$\frac{f_{H_2}^{\neq}}{f_{D,H}^{\neq}} = \frac{\prod_i^5 \sinh(h\nu_i/2kT)_{D,H}}{\prod_i^5 \sinh(h\nu_i/2kT)_{H_2}} \qquad [26]$$

To determine the coordinates of the central atoms (or its isotopes) in the activated complex, the potential energy of the system (V) was treated as a four atom problem (6). V is given by

$$V = K_{12} + K_{23} + K_{34} + K_{13} - \left[\frac{1}{2}\{(\alpha-\beta)^2 + (\beta-\gamma)^2 + (\gamma-\alpha)^2\}\right]^{1/2} \qquad [27]$$

where

$$\alpha = J_{12} + J_{34} \qquad [28]$$

$$\beta = J_{13} \qquad [29]$$

$$\gamma = J_{23} \qquad [30]$$

and

$$V_{ij} = K_{ij} + J_{ij} \qquad [31]$$

according to the Heitler-London method. V_{ij} is the potential energy due to interactions between atoms i and j with varying internuclear distance; K_{ij} and J_{ij} are the respective coulombic and exchange contributions to the total energy.

The M-H_2O and H-H_2O interactions were neglected since their respective internuclear distances are relatively far apart and also because these interactions are considerably less than the others where strong chemical bonding exists.

As in the method of Eyring *et al.*, the reference state for the energy was taken as that of the separated atoms 2H + M + H_2O [H_2O is treated as a pseudo atom (7)]. The sum of the energies, ($V_{12} + V_{34}$), represent the potential energy of the intial state as a function of the M-H and H^+-OH_2 distances. For this calculation, the respective Morse functions were used.

The potential energy ($V_{12} + V_{34}$) was expressed as a function of the distance between the H^+ ion (position 1) and H_2O molecule and also between the metal atom and H atom (position 2) by considering the following Born-Haber cycles (8).

$$2H + H_2O + M \rightarrow H^+ + H_2O + M + H + e_o \quad (I) \qquad [32]$$

$$H^+ + H_2O + H + M + e_o \rightarrow H_3O^+ + e_M + H + M \quad (D_{12} - \phi) \qquad [33]$$

$$H_3O^+ + e_M + H + M \rightarrow H_3O^+ + e_M + MH \quad (D_{34}) \qquad [34]$$

Adding

$$2H + H_2O + M \rightarrow H_3O^+ + e_M + MH \quad (V_{12} + V_{34}) \qquad [35]$$

$$V_{12} + V_{34} = I + D_{12} - \phi + D_{34} \qquad [36]$$

with

$$D_{12} = D_{12}^o[1 - e^{-a_{12}(r_{12} - r_{12}^o)}]^2 - |L| \qquad [37]$$

and

$$D_{34} = V_{34} = D_{34}^o[e^{-2a_{34}(r_{34} - r_{34}^o)} - 2e^{-a_{34}(r_{34} - r_{34}^o)}] \qquad [38]$$

L and D_{12}^o are the heat of solvation of a proton and the proton affinity for a water molecule in the gas phase, respectively, as used in the slow discharge mechanism calculations (5). V_{23} is the energy of the final state, H_2, as a function of the H-H distance and is given by the Morse function of the final state. In the absence of spectroscopic data for the M-H^+ interaction, the Morse function of M-H was used for the V_{13} energy. (Spectroscopic data for Hg-H and Hg-H^+ are practically the same.) As in the slow discharge mechanism calculation, the hydrogen ion is assumed to be an ion, where interactions with the water molecule are concerned and as an atom for interaction with the other hydrogen atoms. However, the energy of the electron has been accounted for through the chosen reference state. Further, when the hydrogen ion is sufficiently separated from the water molecule, the H^+-OH_2 interaction is small and the H-H energy is predominant and it is likely that in this position the hydrogen

Table I. Physical constants in calculation of potential energy of system (V)

Parameter	Interaction		
	H-H	Ni-H	H^+-OH_2
D^o kcal mole^{-1}	109.52	60.00	187.00
a Å^{-1}	1.94	1.60	1.375
r_e Å	0.74	1.48	1.05

ion is fully neutralized. Thus, the assumption is not seriously in error.

As in the slow recombination mechanism calculation (9), the metal atom was considered as fixed. In addition, the position of the water molecule, with respect to the metal atom, was also considered to be fixed for purposes of simplifying the calculation of vibrational frequencies. The error involved in the calculation of the vibrational frequencies, due to the latter assumption, is small since the water molecule is heavy compared to the hydrogen or deuterium atoms and also because the motion of the water molecule is restricted due to hydrogen bonding with surrounding water molecules.

The potential energy of the system was then calculated as a function of the coordinates of the two hydrogen atoms with respect to the metal atom using a computer. Four calculations were carried out for nickel. The constants, used in the calculation of V, are shown in Table I. In the first two calculations, an Ni-H_2O distance of 3.5Å was used, as in the calculation of Conway and Bockris (8). No saddle point was obtained when the total energy was assumed to be 100% coulombic for all interactions nor for the case of 20% coulombic energy for the Ni-H, H^+-OH_2 interactions and 15% coulombic for the H-H interaction. The results of these two calculations indicate that the electrochemical desorption mechanism can take place readily for the assumed distance between the Ni atom and water molecule.

In the third and fourth calculations, the distance between the Ni atom and water molecule was taken as 5.4Å. This distance follows from the model of the double layer according to Bockris, Devanathan, and Müller (10) in which a layer of water molecules separates the metal surface from the first layer of ions. In the third calculation, the total energy of the system was assumed to be coulombic. In the fourth calculation 20% of the H^+-OH_2, Ni-H interactions and 15% of the H-H interactions were assumed to be coulombic. Saddle points were obtained in the two calculations. Let the coordinates of the H atom (position 2) and H ion (position 3) at the saddle point be (x_o,D,D) and (y_o,O,O). (The axis of the activated complex is the x axis, the y and the z axis are the two axes mutually perpendicular to the x axis).

The potential energy in the neighborhood of the saddle point may be expanded by a Taylor series and is given by

$$V = V_o + \frac{1}{2}\sum_{x}^{\zeta} a_{xx}(x - x_o)^2 + a_{x\xi}(x - x_o)(\xi - \xi_o) + a_{y\eta}y\eta + a_{z\zeta}z\zeta \quad [39]$$

Since the activated complex is linear, the other cross terms vanish. The terms a_{xx}----$a_{z\zeta}$ were obtained by a determination of the corresponding second derivatives ($\partial^2V/\partial x^2$----$\partial^2V/\partial_z\partial_\zeta$) of the potential function at the saddle point. They were then used in the secular equations

$$\begin{vmatrix} a_{xx} - 4m_1\lambda, a_{x\xi} \\ a_{x\xi}, a_{\xi\xi} - 4m_2\lambda \end{vmatrix} = 0 \quad [40]$$

$$\begin{vmatrix} a_{yy} - 4m_1\lambda, a_{y\eta} \\ a_{y\eta}, a_{\eta\eta} - 4m_2\lambda \end{vmatrix} = 0 \quad [41]$$

$$\begin{vmatrix} a_{zz} - 4m_1\lambda, a_{z\zeta} \\ a_{z\zeta}, a_{\zeta\zeta} - 4m_2\lambda \end{vmatrix} = 0 \quad [42]$$

where $\lambda = 4\pi^2\nu^2$, m_1 and m_2 are the masses of hydrogen (or its isotopes) at positions 2 and 3, respectively. One of the frequencies is imaginary. The bending frequencies are doubly degenerate due to the cylindrical symmetry of the potential function around the saddle point. The results of the two calculations including partition function ratios of the activated complexes are summarized in Table II.

The fourth calculation gave an activation energy ($E^{\neq}$) considerably higher than the third. The experimentally observed $E^{\neq}$ for the hydrogen evolution reaction on Ni in acid solutions (11) is 7 kcal mole^{-1} and this figure is also much less than the

Table II. Force constants (a's) vibrational frequencies (ω's) partition function ratios ($f_{H_2}{}^{\neq}/f_{H,D}{}^{\neq}$, etc.) of isotopic activated complexes for the slow electrochemical desorption mechanism

Parameter	Percentage coulombic energy for Ni-H, H^+-OH_2 and H-H interactions (ρ) and calculation number in parentheses	
	$\rho_{Ni-H} = \rho_{H^+-OH_2} = \rho_{H-H} = 100$ 3	$\rho_{Ni-H} = \rho_{H^+-OH_2} = 20$ $\rho_{H-H} = 15$ 4
$r_{12}{}^{\neq}$ Å*	2.40	2.74
$r_{23}{}^{\neq}$ Å*	1.88	1.58
$r_{34}{}^{\neq}$ Å*	1.12	1.08
$E^{\neq}$ kcal mole^{-1}*	21.1	50.8
a_{xx} kcal mole^{-1} Å^{-2}	—109.52	—191.39
a_{yy} kcal mole^{-1} Å^{-2}	39.47	22.94
a_{zz} kcal mole^{-1} Å^{-2}	39.47	22.94
$a_{\xi\xi}$ kcal mole^{-1} Å^{-2}	448.84	298.18
$a_{\eta\eta}$ kcal mole^{-1} Å^{-2}	61.10	27.96
$a_{\zeta\zeta}$ kcal mole^{-1} Å^{-2}	61.10	27.96
$a_{x\xi}$ kcal mole^{-1} Å^{-2}	70.84	152.68
$a_{y\eta}$ kcal mole^{-1} Å^{-2}	—22.07	—14.65
$a_{z\zeta}$ kcal mole^{-1} Å^{-2}	—22.07	—14.65
ω for Ni - - - H - - - $H^{\oplus}$ - - - OH_2 (cm^{-1})	588i, 1156, 468, 274, 468, 274	829i, 999, 343, 176, 343, 176
ω for Ni - - - H - - - $D^{\oplus}$ - - - OH_2 (cm^{-1})	584i, 823, 387, 234, 387, 234	806i, 726, 295, 145, 295, 145
ω for Ni - - - D - - - $H^{\oplus}$ - - - OH_2 (cm^{-1})	418i, 1151, 440, 206, 440, 206	600i, 975, 310, 137, 310, 137
ω for Ni - - - H - - - $T^{\oplus}$ - - - OH_2 (cm^{-1})	571i, 675, 366, 202, 366, 202	794i, 596, 286, 124, 286, 124
ω for Ni - - - T - - - $H^{\oplus}$ - - - OH_2 (cm^{-1})	341i, 1149, 433, 171, 433, 171	496i, 964, 301, 116, 301, 116
$f_{H_2}{}^{\neq}/f_{H,D}{}^{\neq}$	0.1864	0.2359
$f_{H_2}{}^{\neq}/f_{D,H}{}^{\neq}$	0.4411	0.4411
$f_{H_2}{}^{\neq}/f_{H,T}{}^{\neq}$	0.08048	0.1077
$f_{H_2}{}^{\neq}/f_{T,H}{}^{\neq}$	0.2828	0.2845

* $r_{12}{}^{\neq}$, $r_{23}{}^{\neq}$ and $r_{34}{}^{\neq}$ are the Ni-H, H-$H^{\oplus}$ and $H^{\oplus}$-OH_2 internuclear distances in the activated complex; $E^{\neq}$ is the activation energy.

Table III. Separation factors for the slow electrochemical desorption mechanism at low and intermediate overpotentials

Calculation No.	Percentage coulombic energy (ρ) S			Separation factors excluding tunneling corrections			Separation factors including tunneling corrections		
	ρ_{N1-H}	$\rho_{H^+-OH_2}$	ρ_{H-H}	S_{D,E_1}^*	S_{D,E_2}^*	S_D^*	S_{D,E_1}	S_{D,E_2}	S_D
3	100	100	100	11.8	27.9	8.3	13.0	30.7	9.1
4	20	20	15	14.9	27.9	9.7	16.4	30.7	10.7
				S_{T,E_1}^*	S_{T,E_2}^*	S_T^*	S_{T,E_1}	S_{T,E_2}	S_T
3	100	100	100	27.9	89.5	19.8	29.5	103.8	23.0
4	20	20	15	34.1	90.0	24.7	39.5	104.4	28.7

value obtained in the third calculation. The partition function ratios in the two calculations are, however, not significantly different. The value obtained in the third calculation is preferable since $E^{\neq}$ in this calculation is closer to the experimental activation energy. It may be expected that the correct partition function ratios of the activated complexes may be slightly less than the values of calculation 3. The isotope effect is greater when the isotopic substitution is at position 2 rather than position 3 (see Fig. 1).

Tunneling factor ratios (Γ_H/Γ_D *and* Γ_H/Γ_T).—The tunneling factor ratios were obtained for hydrogen ion or atom (or its isotopes) transfer distances of 2.13Å [5.40 − (1.48 + 1.05 + 0.74)]. Calculations for both parabolic and Eckart barriers (5, 12) were in good agreement. Γ_H/Γ_D is 1.09 for a parabolic and 1.10 for an Eckart barrier, the corresponding Γ_H/Γ_T ratios being 1.13 and 1.16, respectively.

Separation Factors

Separation factors excluding tunneling corrections (S_D^* *and* S_T^*).—Using Eq. [19] to [21], [23], [24] and the data in Table II, S_D^* and S_T^* were calculated and are given in Table III. The values obtained in calculation 3 are closer to the correct values, since the activation energy obtained in this calculation is closer to the experimental activation energy than that of calculation 4.

Separation factors including tunneling corrections (S_D *and* S_T).—The separation factors including tunneling corrections are also given in Table III. It is probable that the tunneling factors are somewhat overestimated in view of the low barrier height at an overpotential of 0.4v on Ni and thus the separation factors, excluding tunneling corrections are the preferred values for this mechanism.

Table IV. Separation factors for the slow electrochemical desorption mechanism at all overpotentials

Overpotential region	Percentage coulombic energy (ρ)			Separation factors excluding tunneling corrections		Separation factors including tunneling corrections	
	ρ_{N1-H}	$\rho_{H^+-OH_2}$	ρ_{H-H}	S_D^*	S_T^*	S_D	S_T
Low and intermediate	100	100	100	8.3	19.8	9.1	23.0
Low and intermediate	20	20	15	9.7	24.7	10.7	28.7
High	100	100	100	3.4	5.4	4.1	7.0
High	20	20	15	3.6	5.7	4.4	7.5

Slow Electrochemical Desorption Mechanism at High Overpotentials

Expression for separation factor.—At high overpotentials, the reverse currents of the discharge steps 3 and 4 may be neglected. The separation factor expression for this case was worked out previously (5) as

$$\frac{1}{S_D} = \frac{1}{2S_{D,1}} + \frac{1}{S_{D,E_1}} \qquad [43]$$

where S_{D_1} is the separation factor expression for the discharge step and is given by

$$S_{D,1} = \frac{1}{2} \cdot \frac{f_{H^{\neq}}}{f_{D^{\neq}}} \cdot \frac{f_{HDO_g}}{f_{H_2O_g}} \cdot K_D \qquad [44]$$

This equation holds for a linked discharge-electrochemical desorption mechanism. However, at high overpotentials, if the coverage of the electrode with adsorbed atomic hydrogen (θ) is low, the mechanism is rate determined by the discharge step, whereas if θ is high, the electrochemical desorption step is rate-determining. Equation [43] was obtained in the general case but holds equally well for the two special cases of low and high degree of coverage, the determination of which distinguishes the alternate rate-determining steps.

Numerical values of separation factors.—The numerical values of separation factors were worked out previously and are given in Table IV, along with the S values for the slow electrochemical desorption mechanism at low and intermediate overpotentials.

Conclusions

At low and intermediate overpotentials, when the discharge step can be treated as in equilibrium, the calculated S values are distinctly separated from the corresponding values for all other mechanisms.

The theoretical separation factors, using a 100% coulombic energy for all interactions, are closer to the true S values, since the experimental activation energy is closer to the calculated activation energy for this case than for the case where the coulombic energy is taken at 20% for the Ni-H and H^+-OH_2 bonds and 15% for the H-H bond. It is not possible to reduce the calculated values any further, since the separation factors in both the presently calculated cases are not much different even though the calculated activation energies differ by as much as 30 kcal mole^{-1}.

At high overpotentials the separation factor is given by that for a linked discharge-electrochemical

desorption mechanism. Thus, the separation factor method cannot be used to distinguish between a rate-determining discharge and a rate-determining electrochemical desorption mechanism at high overpotentials. The only way of distinguishing between these two mechanisms is by a determination of the degree of coverage of adsorbed hydrogen on the electrode, since the coverage is low for a slow discharge mechanism and is high for a slow electrochemical desorption mechanism.

Some aspects of separation factor calculations.— It may be thought that there are inaccuracies in such calculations [ref. (5, 9) and this paper]. The statistical mechanical treatment of reaction rates is quite satisfactory. The only doubt arises in the calculation of vibrational frequencies of transition state which is vital. Defects of calculation are those of the semiempirical method of Eyring *et al.* The Heitler-London treatment for H bonds is used in the present calculations as well. The inaccuracies of the calculations are much less than is thought, as has been shown by a variation of parameters: metal, M-M distance, percentage coulombic energy. In any case, many defects are present in absolute calculation of reaction rates, they are particularly useful in conjunction with isotope effects (3).

The separation factors for the slow electrochemical desorption mechanism at low and intermediate overpotentials and the slow discharge mechanism are distinctly separated, mainly due to the high real stretching frequencies in the activated complex of the slow discharge step. Thus, the separation factor method has proved useful in distinguishing between these two mechanisms on a number of metals (1) in which cases other methods (*e.g.*, stoichiometric numbers, variation of degree of coverage with potential) are inapplicable (12).

Acknowledgments

Financial support from the Aeronautical Systems Command, Air Force Systems Command, United States Air Force, Contract 33(657)-8823, is gratefully acknowledged. The authors also wish to thank Drs. E. R. Nixon and K. Tharmalingam for helpful theoretical discussions. Mathematical assistance from Mr. C. Vaseekaran and computer facilities afforded by the Physics Department are greatly appreciated.

Manuscript received Aug. 9, 1963; revised manuscript received Dec. 11, 1963. This paper is from work carried out in partial fulfillment of requirement for the degree of Ph.D.

Any discussion of this paper will appear in a Discussion Section to be published in the June 1965 JOURNAL.

REFERENCES

1. J. O'M. Bockris and S. Srinivasan, *Electrochim. Acta*, in press.
2. B. E. Conway, *Proc. Roy. Soc.*, **A247**, 400 (1958).
3. J. O'M. Bockris and S. Srinivasan, *This Journal*, **111**, 858 (1964).
4. B. E. Conway, *Can. J. Chem.*, **37**, 178 (1959).
5. J. O'M. Bockris and S. Srinivasan, *This Journal*, **111**, 858 (1964).
6. S. Glasstone, K. J. Laidler, and H. Eyring, "The Theory of Rate Processes," p. 121, McGraw Hill Book Co., New York (1941).
7. R. Parsons and J. O'M. Bockris, *Trans. Faraday Soc.*, **47**, 914 (1951).
8. B. E. Conway and J. O'M. Bockris, *Can. J. Chem.*, **35**, 1124 (1957).
9. J. O'M. Bockris and S. Srinivasan, *This Journal*, **111**, 844 (1964).
10. J. O'M. Bockris, M. A. V. Devanathan, and K. Müller, *Proc. Roy. Soc.*, **A274**, 55 (1963).
11. J. O'M. Bockris and E. C. Potter, *J. Chem. Phys.*, **20**, 614 (1952).
12. S. Srinivasan, Ph.D. Thesis, University of Pennsylvania (1963).
13. J. Bigeleisen and M. Wolfsberg, in "Advances in Chemical Physics," vol. I, chap. II, Interscience Publications, New York (1960).

Theoretical Calculations of the Separation Factors in the Hydrogen Evolution Reaction for the Slow Recombination Mechanism

John O'M. Bockris and S. Srinivasan

The Electrochemistry Laboratory, The University of Pennsylvania, Philadelphia, Pennsylvania

ABSTRACT

The theoretical calculations of H/D and H/T separation factors have been carried out on the metals Ni and Pt, following the lines of earlier calculations by Okamoto *et al.* The effect of variations in the metal-metal internuclear distances and the coulombic exchange energy ratio on the separation factor was small. Tunneling corrections were also made. The calculated H/T separation factor on Pt is in agreement with the experimentally determined value. The theoretically predicted separation factors for a slow molecular hydrogen diffusion mechanism are not distinctly separated from the values for a slow recombination mechanism. Separation factor determinations on the platinum group of metals or the temperature coefficients of separation factors on these metals should be useful to distinguish between the two mechanisms.

Earlier calculations (1-3) of the separation factors for the slow recombination mechanism are contradictory. In the original calculations (1, 2), the longer of the two possible M-M distances for Ni and Pt surfaces were used. Recent overpotential measurements in Ni (4) showed that the most closely packed plane has the smallest overvoltage and it is hence more appropriate to use the closer M-M dis-

tances in the determination of the coordinates of the saddle point and the vibrational frequencies of the activated state therefrom. Wigner's tunneling correction was also used and this is applicable only for very small degrees of tunneling. Since hydrogen or its isotopes are the masses involved in the reaction, larger tunneling corrections are to be expected.

Considerations in the most recent calculations of the zero point energy differences of the isotopic activated complexes and of the concentration ratio of adsorbed atomic hydrogen to deuterium have been discussed in the previous paper of this series (5).

Present Calculations

Expression for Separation Factor

Under the conditions that $a_{H_2O_l} >> a_{HDO_l}$, the H/D separation factor is given by

$$S_D = \frac{1}{2}\left(\frac{c_H}{c_D}\right)_g \frac{a_{HDO_l}}{a_{H_2O_l}} \qquad [1]$$

where $(c_H/c_D)_g$ is the ratio of atomic concentrations of H to D in the electrolytic gas; $a_{H_2O_l}$ and a_{HDO_l} are the activities of H_2O and HDO in solution.

During electrolysis, the ratio $(c_H/c_D)_g$ is given by

$$\left(\frac{c_H}{c_D}\right)_g = \frac{2i_{H_2} + i_{HD}}{i_{HD}} \qquad [2]$$

where i_{H_2} and i_{HD} are the recombination currents for the isotopic reactions

$$2MH \rightarrow 2M + H_2 \qquad [3]$$

and

$$MH + MD \rightarrow 2M + HD \qquad [4]$$

respectively. Since $i_{H_2} >> i_{HD}$, we have

$$S_D = \frac{i_{H_2}}{i_{HD}} \cdot \frac{a_{HDO_l}}{a_{H_2O_l}} \qquad [5]$$

using Eq. [1] and [2]. The currents i_{H_2} and i_{HD} may be expressed as

$$i_{H_2} = k_{H_2}\, a_{MH}^2 \qquad [6]$$

$$i_{HD} = k_{HD}\, a_{MH}\, a_{MD} \qquad [7]$$

where k_{H_2} and k_{HD} are the respective recombination rate constants for the isotopic reactions, a_{MH} and a_{MD} are the activities of H and D atoms adsorbed on the electrode.

Dividing Eq. [6] by [7], we have

$$\frac{i_{H_2}}{i_{HD}} = \frac{k_{H_2}}{k_{HD}} \cdot \frac{a_{MH}}{a_{MD}} \qquad [8]$$

Expressing the rate constants in terms of statistical mechanical functions, we have

$$\frac{i_{H_2}}{i_{HD}} = \frac{\Gamma_H}{\Gamma_D} \cdot \frac{f_H^{\neq}}{f_D^{\neq}} \cdot \frac{f_{MD}}{f_{MH}} \cdot \frac{a_{MH}}{a_{MD}} \qquad [9]$$

where Γ_H/Γ_D is the ratio of the tunneling factors for the isotopic reactions, $f_H^{\neq}/f_D^{\neq}$ is the ratio of partition functions of the isotopic activated complexes and f_{MD}/f_{MH} is the ratio of partition functions of an MD molecule to an MH molecule.

The reference state, used in the definition of partition functions for isotopic species, is the minima of potential energy curves and not the zero point energy level.

If f, a, μ are the partition function, activity, and chemical potential of a species respectively, then $f/a = e^{-\mu/RT}$. Thus, Eq. [9] becomes

$$\frac{i_{H_2}}{i_{HD}} = \frac{\Gamma_H}{\Gamma_D} \cdot \frac{f_H^{\neq}}{f_D^{\neq}} \cdot \frac{e^{-\mu_{MD}/RT}}{e^{-\mu_{MH}/RT}} \qquad [10]$$

The discharge steps

$$H_3O^+ + e_o + M \rightleftharpoons MH + H_2O \qquad [11]$$

$$H_2DO^+ + e_o + M \rightleftharpoons MD + H_2O \qquad [12]$$

may be considered to be in equilibrium when the recombination step is rate-determining. Hence,

$$\frac{e^{-\mu_{MD}/RT}}{e^{-\mu_{MH}/RT}} = \frac{e^{-\mu_{H_2DO^+}/RT}}{e^{-\mu_{H_3O^+}/RT}} \qquad [13]$$

It was shown in an earlier paper (6) that

$$\frac{e^{-\mu_{H_2DO^+}/RT}}{e^{-\mu_{H_3O^+}/RT}} = \frac{e^{-\mu_{HDO_g}/RT}}{e^{-\mu_{H_2O_g}/RT}} \qquad [14]$$

Using Eq. [5], [10], [13], and [14], we have

$$S_D = \frac{a_{HDO_l}}{a_{H_2O_l}} \cdot \frac{\Gamma_H}{\Gamma_D} \cdot \frac{f_H^{\neq}}{f_D^{\neq}} \cdot \frac{e^{-\mu_{HDO_g}/RT}}{e^{-\mu_{H_2O_g}/RT}} \qquad [15]$$

$$= \frac{\Gamma_H}{\Gamma_D} \cdot \frac{f_H^{\neq}}{f_D^{\neq}} \cdot \frac{f_{HDO_g}}{f_{H_2O_g}} \cdot K_D \qquad [16]$$

where $f_{HDO_g}/f_{H_2O_g}$ is the partition function ratio of the isotopic water molecules in the gas phase and K_D is the equilibrium constant of the reaction

$$H_2O_l + HDO_g \rightleftharpoons H_2O_g + HDO_l \qquad [17]$$

The suffixes l and g stand for the liquid and gas phase, respectively.

The H/T separation factor is given by a similar expression.

Numerical Calculation of Separation Factors

Product of equilibrium constant (K_D or K_T) and partition function ratio of isotopic water molecules in the gas phase ($f_{HDO_g}/f_{H_2O_g}$ or $f_{HTO_g}/f_{H_2O_g}$).—In a previous paper (6) it was shown that

$$K_D \cdot \frac{f_{HDO_g}}{f_{H_2O_g}} = 63.36 \qquad [18]$$

$$K_T \cdot \frac{f_{HTO_g}}{f_{H_2O_g}} = 316.48 \qquad [19]$$

Partition function ratio of isotopic activated complexes ($f_H^{\neq}/f_D^{\neq}$ or $f_H^{\neq}/f_T^{\neq}$).—At low coverages, interactions between adsorbed hydrogen atoms may be neglected. The activated complex may be regarded as planar and also to have a plane of symmetry through the right bisector of the line joining the two metal

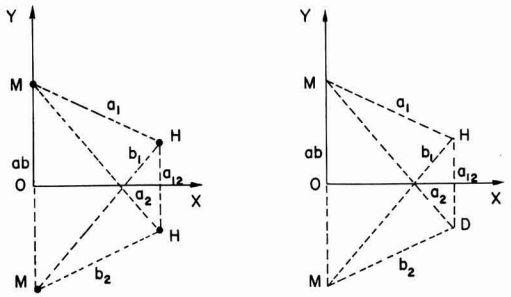

Fig. 1. Activated complex for slow recombination mechanism

atoms and perpendicular to the plane of the molecule (1, 7).

In the activated state, the hydrogen atoms may be considered to be immobile. The translational and rotational partition function ratio are unity, apart from a symmetry factor and hence

$$\frac{f_H^{\neq}}{f_D^{\neq}} = \frac{\sigma_D}{\sigma_H} \cdot \frac{\prod^{5}[\sinh(h\nu_i/2kT)]_D}{\prod^{5}[\sinh(h\nu_i/2kT)]_H} \qquad [20]$$

The activated complex has five real frequencies.

To determine the coordinates of the H atoms (or its isotopes) in the activated complex, the potential energy of the system was treated as a four electron problem, *cf.* Eyring *et al.* (8). The potential energy of the system (V) is given by

$$V = K_{ab} + K_{12} + K_{a1} + K_{b2} + K_{a2} + K_{b1} - \left[\frac{1}{2}\{(\alpha-\beta)^2 + (\beta-\gamma)^2 + (\gamma-\alpha)^2\}\right]^{1/2} \qquad [21]$$

with

$$\alpha = J_{ab} + J_{12} \qquad [22]$$

$$\beta = J_{a1} + J_{b2} \qquad [23]$$

$$\gamma = J_{a2} + J_{b1} \qquad [24]$$

where K's are the coulombic and J's the exchange contributions to the total energies of interactions M-M, H-H and M-H (see Fig. 1).

As in the method of Eyring, a certain percentage of each interaction was assumed to be coulombic for all distances of separation.

Three calculations were carried out, two on nickel and one on platinum. The constants, used in the calculation of V, are given in Table I. In the first calculation on Ni, the physical constants used are the same as in the calculation of Okamoto *et al.* (1). In the second calculation on Ni and the one on Pt, the shorter of the two possible M-M distances was used.

As in previous work (1, 7) a fixed distance was assumed between the two metal atoms in all calculations. This assumption may be considered as valid, since the metal atoms are much heavier than the hydrogen atoms and thus the hydrogen atoms only move in the formation of the activated complex. The potential energy of the system (V) was then expressed as a function of two coordinates, the distance between the two hydrogen atoms ($2y$) and that between the centers of the two metal atoms and the two H atoms (x), in keeping with the assumption that the activated complex is symmetrical. V was calculated as a function of x and y on a computer and from the table of these V values, the coordinates of the saddle point where determined.

Following the treatment of Okamoto *et al.* (1) let the coordinates of the H atoms in any arbitrary position be (x_1, y_1, z_1) and (x_2, y_2, z_2). [The OZ axis is perpendicular to the plane of the paper through O; Fig. 1]. Introducing a change of coordinates to simplify the subsequent treatment, we have

$$x = \frac{x_1 + x_2}{2} \qquad \xi = \frac{x_1 - x_2}{2}$$

$$y = \frac{y_1 + y_2}{2} \qquad \eta = \frac{y_1 - y_2}{2}$$

$$z = \frac{z_1 + z_2}{2} \qquad \zeta = \frac{z_1 - z_2}{2}$$

At the saddle point, $x = x_o$, $y = y_o$, and $z = \xi = \eta = \zeta = 0$. The potential energy in the neighborhood of the saddle point may be expanded by a Taylor series and is given by

$$V = V_o + \frac{1}{2}\sum_{x}^{\zeta} a_{xx}(x-x_o)^2 + a_{xy}(x-x_o)(y-y_o) + a_{\xi\eta}\,\xi\eta \qquad [25]$$

Due to the symmetry of the activated complex, the other cross terms are zero. The terms $a_{xx} \ldots a_{\xi\eta}$ were obtained by a determination of the corresponding second derivatives ($\partial V^2/\partial x^2 \ldots \partial^2 V/\partial\xi\,\partial\eta$) of the expression [21] at the saddle point.

$a_{xx} \ldots a_{\xi\eta}$ were used in the secular equations

$$\begin{vmatrix} a_{xx}(m_1+m_2) - 4m_1m_2\lambda, a_{\xi\xi}(m_1-m_2), a_{xy}(m_1+m_2), a_{\xi\eta}(m_1-m_2) \\ a_{xx}(m_1-m_2), a_{\xi\xi}(m_1+m_2) - 4m_1m_2\lambda, a_{xy}(m_1-m_2), a_{\xi\eta}(m_1+m_2) \\ a_{xy}(m_1+m_2), a_{\xi\eta}(m_1-m_2), a_{yy}(m_1+m_2) - 4m_1m_2\lambda, a_{\eta\eta}(m_1-m_2) \\ a_{xy}(m_1-m_2), a_{\xi\eta}(m_1+m_2), a_{yy}(m_1-m_2), a_{\eta\eta}(m_1+m_2) - 4m_1m_2\lambda \end{vmatrix} = 0 \qquad [26]$$

$$\begin{vmatrix} a_{zz}(m_1+m_2) - 4m_1m_2\lambda, a_{\zeta\zeta}(m_1-m_2) \\ a_{zz}(m_1-m_2), a_{\zeta\zeta}(m_1+m_2) - 4m_1m_2\lambda \end{vmatrix} = 0 \qquad [27]$$

Table I. Physical constants used in calculation of potential energy of system for slow recombination mechanism

	Interaction and calculation number							
	H-H		Ni-Ni		Ni-H		Pt-Pt	Pt-H
Parameter	1	2 and 3	1	2	1	2	3	3
D^o kcal mole^{-1}	109.10	109.52	20.60	20.00	60	74.24	21.55	65.52
a Å^{-1}	1.95	1.94	—	—	1.60	1.45	—	1.63
r_e Å	0.74	0.74	3.52	2.49	1.48	1.48	2.77	1.62
ρ	11	14	37	30	24	20	40	27

Table II. Force constants (a's) vibrational frequencies (ω's) and partition function ratios ($f_H^{\neq}/f_D^{\neq}$ and $f_H^{\neq}/f_T^{\neq}$ of isotopic activated complexes for the slow recombination mechanism

Parameter	Metal, d_{M-M} and calculation number in parenthesis		
	Ni, d_{Ni-Ni} = 3.52Å 1	Ni, d_{Ni-Ni} = 2.49Å 2	Pt, d_{Pt-Pt} = 2.77Å 3
x_o Å*	1.06	1.74	1.48
y_o Å*	0.69	0.39	0.63
$E^{\neq}$ kcal mole^{-1}*	14.2	36.0	15.8
a_{xx} kcal mole^{-1} Å^{-2}	232.75	—57.55	400.06
a_{yy} kcal mole^{-1} Å^{-2}	—155.09	546.65	—393.58
a_{zz} kcal mole^{-1} Å^{-2}	0.96	0.23	1.61
$a_{\xi\xi}$ kcal mole^{-1} Å^{-2}	276.66	138.69	452.19
$a_{\eta\eta}$ kcal mole^{-1} Å^{-2}	267.09	26.65	131.79
$a_{\zeta\zeta}$ kcal mole^{-1} Å^{-2}	38.38	124.02	41.33
a_{xy} kcal mole^{-1} Å^{-2}	—193.09	194.41	—101.33
$a_{\xi\eta}$ kcal mole^{-1} Å^{-2}	—221.30	36.23	—179.70
$\omega_{H_2}^{\neq}$ cm^{-1}	1170i, 1696, 1355, 543, 473, 75.	818i, 1876, 933, 305, 850, 36.	1539i, 1762, 1551, 547, 491, 91.
$\omega_{HD}^{\neq}$ cm^{-1}	998i, 1554, 1049, 446, 406, 62.	690i, 1635, 776, 249, 737, 30.	1322i, 1663, 1166, 448, 426, 79.
$\omega_{HT}^{\neq}$ cm^{-1}	924i, 1531, 879, 390, 387, 53.	627i, 1553, 692, 216, 695, 26.	1232i, 1653, 963, 391, 392, 68.
$f_H^{\neq}/f_D^{\neq}$	0.1715	0.187	0.1550
$f_H^{\neq}/f_T^{\neq}$	0.07153	0.0827	0.05934

* x_o and $2y_o$ are the distances of the line joining the 2 hydrogen atoms from the line joining the 2M atoms and the distance between the 2 hydrogen atoms in the activated complex; $E^{\neq}$ is the activation energy.

where $\lambda = 4\pi^2\nu^2$. Of the six frequencies, one is imaginary, corresponding to motion along the reaction coordinate.

The results of all three calculations, including partition function ratios of the activated complexes, are given in Table II. The first calculation on nickel gives values of partition function ratios of activated complexes lower than the corresponding values of Horiuti *et al.* (1, 2), although the same input parameters were used in both calculations. The discrepancy is probably due to an inaccurate location of the saddle point in the earlier work. Further, the calculation of the force constant, a_{xx}, appears to be inexact since a negative value is reported, though it is clearly positive, as indicated in the corresponding energy map. The procedure of calculating the force constants in the present work (viz., by evaluating the corresponding second derivatives at the saddle point) may also be thought to be more accurate than that carried out by Horiuti *et al.* (viz., from potential energy maps).

$f_H^{\neq}/f_D^{\neq}$ and $f_H^{\neq}/f_T^{\neq}$, obtained in the second calculation on Ni, with variation of Ni-Ni distance, coulombic exchange energy ratio and Morse constants, are in reasonable agreement with the corresponding values of the first calculation.

$f_H^{\neq}/f_D^{\neq}$ and $f_H^{\neq}/f_T^{\neq}$ on Pt are also lower than the values obtained by Horiuti and Nakamura (2). In addition to the above possible explanations, this discrepancy may be due to the different Pt-Pt distances used (2.77Å in this work and 3.92Å in the former work).

Tunneling factor ratios.—The tunneling factor ratios on Ni were obtained for a hydrogen atom transfer distance of 2.48Å (3.52-0.74) in the first calculation and 1.75Å (2.49-0.74) in the second calculation. Bell's method of calculation for a parabolic barrier (9). [which gives good agreement with calculations for an Eckart barrier, when the tunneling corrections are small (10)] was used. This method of calculating tunneling corrections was first applied to the separation factor problem by Bawn and Ogden (10), and more recently by Conway (11).

The height of the barrier, $E^{\neq}$, at η = 0.4v was calculated as 2.4 kcal mole^{-1}, using equation

$$E^{\neq} = E_o^{\neq} - \beta\eta F \qquad [28]$$

with β = 1/2 and $E_o^{\neq}$ = 7 kcal mole^{-1} (13). The ratios Γ_H/Γ_D are 1.07 and 1.15 according to the first and second calculations, respectively. The corresponding values of Γ_H/Γ_T are 1.09 and 1.20, respectively.

For Pt, a hydrogen atom transfer distance of 2.03Å (2.77-0.74) was used. $E^{\neq}$ calculated at η = 0.05v, using Eq. [28] with β = 2.0 and $E_o^{\neq}$ = 5.2 kcal mole^{-1} (14) is 2.9 kcal mole^{-1}. Γ_H/Γ_D is 1.13 and Γ_H/Γ_T is 1.18.

It is probable that these tunneling factors are overestimated in view of the fact that the barrier heights are small.

Separation factors.—Separation factors excluding tunneling corrections (S_D^* *and* S_T^*).—Using Eq. [18], [19], and the partition function ratios in Table II, S_D^* and S_T^*,[1] arising in the three calculations are given in Table III. Though the H/D separation factors differ by about 10%, whereas the H/T separation factors differ by about 16% in the two calculations and both sets of results are somewhat higher than the results on Pt, we may conclude that the separation factors do not significantly depend on the metal, the interatomic distances and the coulombic-exchange energy ratios, but they de-

[1] Inclusion of anharmonicity corrections in the partition function ratios of (a) isotopic water molecules in the gas phase and (b) isotopic activated complexes has an effect of less than 10% on the separation factors. The authors wish to thank one of the reviewers for pointing out the effect of anharmonicity corrections on the former partition function ratio.

Table III. Separation factors for the slow recombination mechanism

Separation factors excluding (S^*) or including tunneling (S)	Metal and calculation number		
	Ni 1	Ni 2	Pt 3
S_D^*	5.4	5.9	4.9
S_T^*	11.3	13.1	9.4
S_D	5.8	6.4	5.5
S_T	13.0	15.7	11.1

pend mainly on the mechanism. Of the two results on Ni, for both H/D and H/T separation factors, the lower values are preferable since for a Ni-Ni distance of 3.52Å, the activation energy is considerably lower than for the Ni-Ni distance of 2.49Å. This result was also reported by Okamoto *et al.* (1) but is contrary to the conclusions reached by Piontelli *et al.* from overpotential measurements on Ni single crystals. The present calculations on Pt also yield considerably lower S values than those of Horiuti and Nakamura ($S_D = 7.2$, $S_T = 16.1$ with no tunneling corrections). From the results on Ni for the two interatomic distances, we may expect still lower values on Pt for a Pt-Pt distance of 3.92Å as used by Horiuti *et al.*

Separation factors including tunneling corrections (S_D and S_T).—The separation factors, including tunneling corrections are also given in Table III. Calculations 1 and 3 give results in reasonable agreement with each other. The results of calculation 2 are somewhat higher. Due to a higher activation energy for a Ni-Ni distance of 2.49Å, as compared with 3.52Å, we may conclude that the separation factor on polycrystalline nickel is more likely to correspond to the value obtained in the first calculation for a slow recombination mechanism.

Conclusion

Due to the higher calculated activation energy for a Ni-Ni distance of 2.49Å than that for 3.52Å, it is probable that most of the reaction takes place on two adjacent Ni atoms 3.52Å apart for a slow recombination mechanism.

On Pt, it is probable that the reaction takes place on 2Pt atoms 3.92Å apart, but since the calculated activation energy for a Pt-Pt distance of 2.77Å is itself fairly low, S values for the higher Pt-Pt distance are not likely to be much different, although they may be somewhat lower (since there was a decrease in S with decrease of activation energy on Ni).

In some experimental determinations of H/T separation factors (S_T), an increasing trend or a small scatter was observed with each successive measurement (15). This variation in S_T was probably due to certain preferred sites being used up.

The values of S_T for the recombination mechanism are distinctly separated from S_T for a slow discharge or for a coupled discharge-electrochemical desorption mechanism. S_D values for a slow recombination and coupled discharge-electrochemical desorption mechanism are not markedly separated.

The H/D separation factor for a slow molecular hydrogen diffusion mechanism is

$$S_D = K_D \left(\frac{\mu_D}{\mu_H}\right)^{1/2} \quad [29]$$

where K_D is the equilibrium constant for reaction

$$HD + H_2O \rightleftharpoons H_2 + HDO \quad [30]$$

and μ_H or μ_D is the reduced mass of an H_2 or HD and H_2O molecules (15). The H/T separation factor is given by a similar expression. With K_D as 3.8 (16) and K_T as 6.2 (17), S_D and S_T are 4.5 and 8.2, respectively. Unfortunately, these values are not distinctly separated from the corresponding values for the slow recombination mechanism on platinum. It is on the platinum group of metals that this mechanism was proposed. However, for a slow recombination mechanism, there should be a slight dependence of S on the metal, whereas for a diffusion mechanism, there should be no dependence of S on the metal. Thus, from the experimental S values on the platinum group of metals, we may be able to distinguish the two mechanisms. The temperature coefficient of the separation factors should also prove useful in distinguishing between a slow recombination and slow molecular hydrogen diffusion mechanism.

Acknowledgments

Financial support from the Aeronautical Systems Command, Air Force Systems Command, United States Air Force, Contract 33(657)-8823, is gratefully acknowledged. The authors also wish to thank Drs. E. R. Nixon, E. R. Thornton, T. E. Sharp, H. Carlmichael, and K. Tharmalingam for valuable theoretical discussions. Mathematical assistance from Mr. C. Vaseekaran and part of the computer facilities afforded by Dr. L. Nanis are also greatly appreciated.

Manuscript received Aug. 29, 1963; revised manuscript received Dec. 12, 1963. This paper is from work carried out in partial fulfillment of requirement for the degree of Ph.D.

Any discussion of this paper will appear in a Discussion Section to be published in the June 1965 JOURNAL.

REFERENCES

1. G. Okamoto, J. Horiuti, and K. Hirota, *Sci. Papers Inst. Phys. Chem. Research (Tokyo)*, **29**, 223 (1936).
2. J. Horiuti and T. Nakamura, *J. Research Inst. Cat.*, **2**, 73 (1951).
3. B. E. Conway, *Proc. Roy. Soc.*, **A247**, 400 (1958).
4. R. Piontelli, L. Peraldo Bicelli, and A. LaVecchia, *Rend. accad. naz.* Lincei, VIII, **27**, 312 (1959).
5. J. O'M. Bockris and S. Srinivasan, *This Journal*, **111**, 844 (1964).
6. J. O'M. Bockris and S. Srinivasan, *ibid.*, **111**, 853 (1964).
7. A. Sherman, C. E. Sun, and H. Eyring, *J. Chem. Phys.*, **3**, 49 (1934).
8. S. Glasstone, K. J. Laidler, and H. Eyring, "The Theory of Rate Processes," p. 121, McGraw-Hill Book Co., New York (1941).
9. R. P. Bell, *Trans. Faraday Soc.*, **55**, 1 (1959).

10. T. E. Sharp and H. S. Johnston, *J. Chem. Phys.*, **37**, 154 (1962).
11. C. E. H. Bawn and G. Ogden, *Trans. Faraday Soc.*, **30**, 432 (1934).
12. B. E. Conway, *Can. J. Chem.*, **37**, 178 (1959).
13. J. O'M. Bockris and E. C. Potter, *J. Chem. Phys.*, **20**, 614 (1952).
14. R. Parsons, *Trans. Faraday Soc.*, **56**, 1340 (1960).
15. S. Srinivasan, Ph.D. Thesis, University of Pennsylvania (1963).
16. A. Farkas and L. Farkas, *J. Chem. Phys.*, **2**, 468 (1934).
17. W. F. Libby, *ibid.*, **11**, 101 (1943).

The Mechanism of the Electro-Oxidation of Acetylene on Platinum

James W. Johnson, Halina Wroblowa, and John O'M. Bockris

The Electrochemistry Laboratory, The University of Pennsylvania, Philadelphia, Pennsylvania

ABSTRACT

The increasing interest in hydrocarbon oxidation reactions connected with the development of electrochemical energy conversion makes the investigation of the influence of the relations between structure of the oxidized compound and the mechanism of the reaction of primary importance. The study of oxidation reactions of several olefins has been reported elsewhere. This paper is concerned with the mechanism of acetylene oxidation.

Experimental

Cell and apparatus.—The electrolytic cell and electrical apparatus were similar to that described previously (1, 2) unless otherwise stated. The test electrode was a planar rectangle of platinized 52 mesh platinum gauze of geometric area 11.7 cm^2. The auxiliary electrode (cathode) was of similar platinized gauze (47 cm^2). The procedure for platinization and activation of the electrodes has been reported (1, 2). The reference electrodes were saturated calomel for alkaline and 1*N* mercury-mercurous sulfate for acid solutions.

Coulombic efficiency.—Acid solution.—This was measured galvanostatically in a three compartment cell with closed stopcocks between the compartments. The effluent gases from the anodic compartment were passed through an absorber containing barium hydroxide solution. For a measurement, 300 ml of saturated solution (~ 30g $Ba(OH)_2$/liter) were initially filtered into the absorber; 50 ml were withdrawn and titrated with 0.200*N* HCl using phenolphthalein indicator. Precautions were taken so that air did not contact the solutions. All containers were nitrogen-flushed, and nitrogen was used to pass the solutions from one container to another.

The cell was first operated for a sufficient length of time at constant current to saturate the anolyte with carbon dioxide. During this time, the gases were vented to the atmosphere via a three-way stopcock and a bubbler. Immediately following, the gases were diverted through the absorber. A low flow rate of gases (~ 5 $cm^3\ min^{-1}$ at STP) and glass bead packing in the absorber were used to increase the gas-liquid contact. (A second absorber indicated no carbon dioxide was passing out of the first.)

After the carbon dioxide had been collected for the desired length of time (cell always operated at the original constant current), the absorber was disconnected from the cell. Another 50 ml sample was withdrawn and titrated as described above.

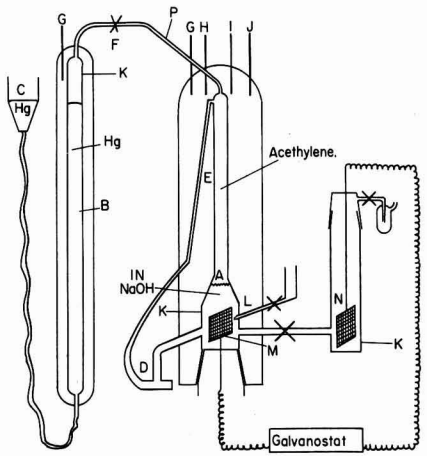

Fig. 1. Diagram of apparatus for measurement of coulombic efficiency in alkaline solution. A, anode compartment; B, gas buret; C, leveling bulb; D, circulation pump; E, water jacket; F, three-way stopcock; G, thermometer; H, thermoregulator; I, heater; J, stirrer; K, gas inlet; L, Luggin capillary; M, anode; N, cathode; P, water cooled condenser.

Separate experiments indicated that the barium hydroxide could be titrated accurately in the presence of barium carbonate.

Alkaline solution.—A diagram of the apparatus is shown in Fig. 1. The change in volume of gaseous acetylene contained in a closed anodic compartment A above the anolyte is measured at constant pressure with a mercury-filled buret B and leveling bulb C which are integral parts of the compartment. The carbon dioxide produced during the oxidation is absorbed by the alkaline anolyte. A small magnetically driven glass centrifugal pump D circulates the anolyte causing it to flow down column E (approximately 12 in. in length). This gives a sufficient gas-liquid contact area to keep the anolyte saturated with acetylene.

When making a consumption determination, the cell was filled with electrolyte and the circulation pump D started. The mercury level in the buret was raised near to the three-way stopcock F and nitrogen vigorously bubbled through the anode and cathode compartments to remove oxygen from the cell. After about 1 hr of bubbling, the nitrogen passing through the anode compartment was stopped and acetylene flow started. This was continued for 1 to 2 hr to saturate the anolyte and replace the other gases in the compartment with acetylene. Next, stopcock F was turned so as to connect the gas buret to the anode compartment and the mercury displaced by acetylene until the desired amount was contained in the buret. The system was allowed to equilibrate, the buret reading noted, and the current started at a value to keep the potential within the linear Tafel region. The run was continued (with frequent adjustment of the leveling bulb) until a desired volume of acetylene had been consumed.

Reagents.—Sulfuric acid, "Baker Analyzed" reagent; sodium sulfate, "Fisher Certified" reagent; sodium hydroxide, "Baker Analyzed" reagent; acetylene, Air Reduction Company, purified (> 99.5% purity, impurities largely water and nitrogen); nitrogen, Matheson, prepurified (99.996% purity); water-distilled; gas mixtures of acetylene and prepurified nitrogen were supplied in cylinders and analyzed by Matheson.

Results

Rest potentials.—All potentials are given on the normal hydrogen scale ($e^{\circ}_{H_2} = 0$ at 80°C). The correction for the reference electrode being at room temperature was made as described previously (2).

Oxygen was removed from the electrolyte by vigorously passing nitrogen through the anode and cathode compartments for 1 to 2 hr. Acetylene (or the mixtures with nitrogen) was then passed through the anolyte at a rate of 90 cm^3 (STP)/min. The rest potentials were found to be − 0.58 in 1*N* NaOH and + 0.26v in 1*N* H_2SO_4. These values were attained almost immediately after admitting the acetylene and remained constant for periods of 1-2 hr. For more prolonged periods, the potentials slowly became more positive. The rest potentials varied by 60-70 mv per unit pH (Table I) and were independent of the partial pressure of acetylene in the range 10^{-4} to 1 atm.

Coulombic efficiency.—Acid solution.—The amount of electricity q per mole of CO_2 produced during the time t by current i is

$$q = \frac{2V_s\, it}{N\, V_a\, (V_o - V_e)}$$

Table I. Rest potentials for acetylene at 80°C

pH	V_{rest}, v
12.6	−0.58
11.9	−0.45
8.7	−0.36
1.2	+0.19
0.3	+0.26

where V_s is the volume of samples titrated, ml; V_a the volume of barium hydroxide solution in absorber, ml; V_o the volume of hydrochloric acid for initial titration, ml; V_e the volume of hydrochloric acid for final titration, ml; and N the concentration of hydrochloric acid, mole/ml.

For acetylene oxidation in 1*N* H_2SO_4 (in the Tafel region), it was found that $(4.8 \pm 0.2) \times 10^5$ coulombs of electricity was produced per mole of CO_2 as compared with the theoretical value of 4.82×10^5 coulombs according to the equation: $C_2H_2 + 4H_2O \rightarrow 2CO_2 + 10H^+ + 10\bar{e}$.

Alkaline solution.—The amount of electricity q produced per mole of acetylene consumed was directly calculated by the formula

$$q = \frac{22{,}400\, it}{\Delta V_{corr}}$$

where ΔV_{corr} is the volume of acetylene consumed corrected to standard temperature and pressure.

For acetylene oxidation in 1*N* NaOH, the Faradaic equivalence was found to be $(9.1 \pm 0.5) \times 10^5$ coulombs per mole of acetylene, as compared with the theoretical value of 9.65×10^5 coulombs. The error in this determination is much higher than in the first method; it is connected with the measurement of the volume and correction for the water vapor pressure (the presence of the temperature gradient between A and B, Fig. 2) and amounts to about 5%.

Analysis of electrolyte.—An analysis[1] was made of the 1*N* NaOH anolyte to determine the presence of any organic substances that might be the products of branching reactions. Previous to the analysis an anodic oxidation of acetylene was carried out for approximately 100 hr in the electrolyte.

An ultraviolet spectrum of the electrolyte showed no significant absorption, indicating no conjugated unsaturation, such as might be suspected for polymerization reactions.

Infrared spectrograms of samples obtained by extracting portions of the electrolyte with benzene,

[1] Analysis performed by Sadtler Research Laboratories, Philadelphia, Pennsylvania.

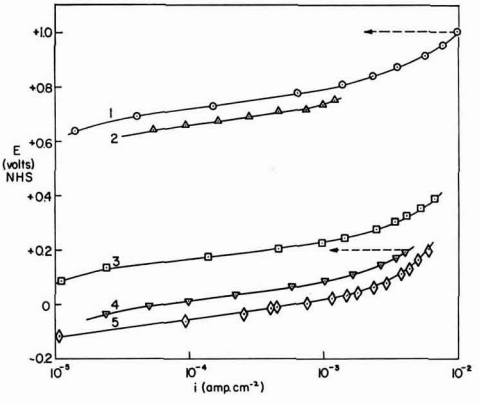

Fig. 2. Current-potential relation ($\overline{P}_A = 1$ atm) as a function of pH = curve 1, 0.3; curve 2, 1.2; curve 3, 8.7; curve 4, 11.9; curve 5, 12.6.

ethyl ether, and n-hexane revealed nothing other than sodium carbonate.

Water was removed from a sample neutralized with hydrochloric acid. The sample was then extracted with anhydrous ethyl alcohol. No organic residue could be demonstrated.

Current-potential relation.—These were determined both galvanostatically and potentiostatically. A linear Tafel region was found at potentials 450-500 mv more positive than the rest potentials (Fig. 2). This region extended over about one and a half decades of current and had a slope of 65-75 mv/decade. Below the linear region the current was quite small and nearly independent of potential. Above the linear region the slope increased rapidly, with passivation (2) occurring at potentials V = 0.2v and 1.0v for 1N NaOH and 1N H_2SO_4, respectively. Reproducibility of the current values at constant potential was within 10%.

Time effects and electrode activation.—The variation of current with time depended on the electrode potential as related to the linear Tafel region. At potentials below the linear region, the current decreased steadily with time and reached a quasi-steady state only after several hours at a constant potential. In the lower section of the linear region, the current increased with time reaching a steady value in 30-90 min. (The time necessary to reach the steady state decreased as the potential increased.) In the upper part of this region, steady currents were attained almost immediately. At potentials still higher by about 200 mv, a passivation region was found, but no consistent behavior noted. The electrode might passivate immediately on switching the potential to this region or it might function quite normally for periods up to 45 min before suddenly passivating. The electrode could be re-activated by interrupting the current and allowing the rest potential to be re-established. This normally required 1-2 hr. (At potentials below the passivation region, the rest potential was re-established rapidly after opening the circuit.) Once a steady current was attained in the linear Tafel region, it remained constant with almost no perceptible change for periods in excess of 24 hr.

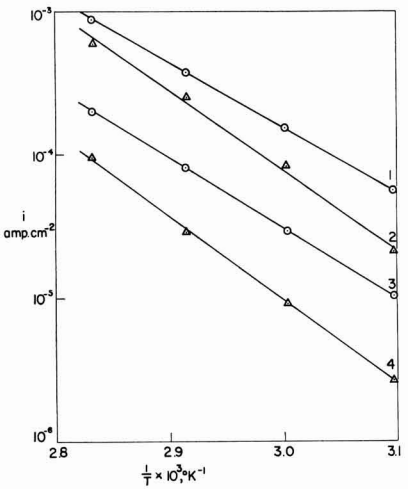

Fig. 3. Current-temperature relation as a function of potential: 1, 0.790v, 1N H_2SO_4; 2, 0.740v, 1N H_2SO_4; 3, 0.005v, 1N NaOH; 4, 0.055v, 1N NaOH.

Table II. Activation energies for the anodic oxidation of acetylene on platinized platinum electrodes

Electrolyte	Potential (V), v	Activation energy (E_A), kcal mole^{-1}
1N H_2SO_4	0.790	21.2
1N H_2SO_4	0.740	22.4
1N NaOH	—0.005	25.4
1N NaOH	—0.055	26.7

pH effect.—The effect of pH at constant ionic strength is shown in Fig. 2. A linear Tafel region with the same slope (b = 70 mv) was found in each case over approximately the same current range. The only effect was that the lines were shifted in the positive direction along the potential axis as the pH decreased, $(dV/dp\mathrm{H})_i \sim -50$ mv.

Temperature effect.—The effect of temperature on current was measured potentiostatically in both 1N NaOH and 1N H_2SO_4 solutions at potentials within the linear Tafel region. Results are shown in Fig. 3. Activation energies were calculated and are shown in Table II. The shift in activation energy with potential is ~ -25 kcal/volt as compared with the theoretical value $d(E_A)/dV = \alpha F = -23.06$ kcal/v for $\alpha = 1$.

From the above values the heat of activation at reversible potential was calculated $E_{A\mathrm{rev}} = E_{A(\eta)} + \eta F = 42$ kcal mole^{-1} for acidic, and 48 kcal mole^{-1} for alkaline solutions.

Pressure effect.—Acetylene of a given partial pressure (mixed with prepurified nitrogen) was passed through the cell. The electrode was held at constant potential and, after a steady state had been obtained, the pressure was changed to another value. The i-p curves thus attained in 1N sulfuric acid are shown in Fig. 4. For acetylene pressures between 0.04 and 1.0 atm it can be seen that the current increases inversely with pressure. The Tafel lines at various pressures are laterally shifted hav-

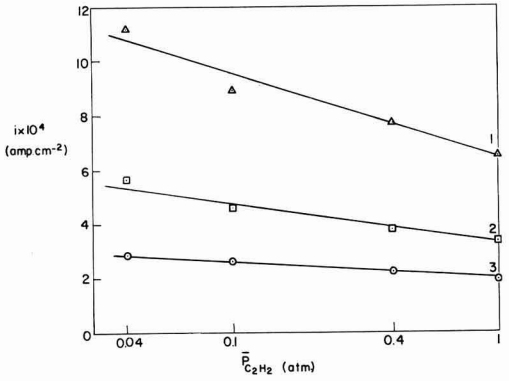

Fig. 4. Current-pressure relation (1N H_2SO_4) as a function of potential: curve 1, 0.775v; curve 2, 0.750v; curve 3, 0.725v.

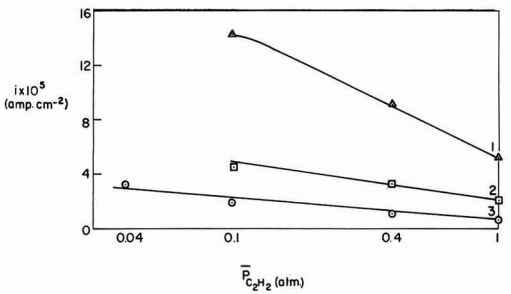

Fig. 5. Current-pressure relation (1*N* NaOH) as a function of potential: curve 1, 0.005v; curve 2, 0.030v; curve 3, 0.055v.

ing approximately the same slope but different intercepts. At pressures lower than 0.04 atm, limiting currents (influenced by the rate of stirring) are observed at very low current densities, and no Tafel lines could be obtained. The pressure effect in 1*N* NaOH is shown in Fig. 5. The effect was similar but more pronounced than in sulfuric acid.

Discussion

Adsorption of Acetylene

In a recent paper (2) adsorption of ethylene from aqueous solutions under anodic conditions had been discussed. The adsorption isotherm was formulated as

$$\frac{\theta_E}{(1-\theta_E)^4} = K_{c_E}\ c_E$$

where θ_E is the fractional coverage by ethylene, c_E the concentration of ethylene (mole cm^{-3}). The order of magnitude of K_{c_E} estimated by two independent methods give a range of 10^6-10^8 cm^3 $mole^{-1}$. No data are available which would allow an independent evaluation of the isotherm constant K_c for acetylene adsorption on Pt from solution. The evidence from the gas phase (4) shows that the heat of adsorption of acetylene is independent of coverage. Taking this into account, as well as the fact that the coverage of acetylene is probably even higher than that of ethylene (4), which in turn is already high (2), Langmuir conditions are assumed. A very rough estimation of K_c can then be made on the following basis.

The most probable mode of acetylene adsorption is

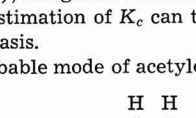

The evidence from the gas phase adsorption suggests that acetylene forms an immobile layer (4) by means of covalent bonds with d-band electrons (5). Since one Pt atom may supply 0.5 of d-electrons, one molecule of acetylene requires 4 adjacent surface sites to adsorb. Thus, the adsorption isotherm is of the same type as in the case of ethylene, *i.e.*,

$$\frac{\theta_A}{(1-\theta_A)^4} = K_{c_A}\ c_A = K_{p_A}\ p \qquad [1]$$

The similarity of the ethylenic and acetylenic radicals allows one to assume analogous adsorption behavior of the two hydrocarbons and to calculate roughly the value of $K_{c_A} \equiv Ke^{-\Delta G^\circ/RT}$, where ΔG_A° is the standard free energy of adsorption of acetylene, and the K value includes energy changes connected with the displacement of water. The free energy of adsorption of ethylene and acetylene will differ by a value which consists of the following contributions:

1. The difference connected with the energy of breaking one C—C bond in a double and a triple bond. The values of energies reported in the literature (6-8) differ; the best estimate of $\Delta G_1 = \Delta G_{c=c} - \Delta G_{c\equiv c} = 6$ kcals $mole^{-1}$ seems to be that given by Bond (4).

2. The difference in free energies of adsorption due to different adsorbate-solution interactions. This difference may be roughly estimated (9) as

$$\Delta G_2 = \Delta G^\circ{}_{S_E} - \Delta G^\circ{}_{S_A} = RT \ln a_E/a_A$$

where $\Delta G^\circ{}_{S_E}$ and $\Delta G^\circ{}_{S_A}$ are the standard free energies of solution of ethylene and acetylene, respectively, and a_E and a_A are the activities of saturated solutions at 1 atm partial pressure of the respective hydrocarbons. Assuming activity coefficients to be 1 and introducing $c_E \cong 0.1\ c_A$,[2] $\Delta G_2 \simeq -1.6$ kcal, thus $K_{c_A} = K_{c_E}\ e^{\Delta G_1 + \Delta G_2/RT} = 5.5.10^8$ to $5.5.10^{10}$ cm^3 $mole^{-1}$ and the limits of the corresponding K_{p_A} values are 10^4-10^6 atm^{-1} (K_{p_A} is the adsorption constant for isotherm relating coverage to partial pressure of acetylene).

Reaction Mechanism

General nature.—(*A*) The efficiency of CO_2 production is 100 ± 1% in acid and 95 ± 5% in alkaline solutions. Thus, it is assumed that no branching leading to products other than CO_2 and water (or protons) occurs to an appreciable extent. The results of ultraviolet and infrared spectroscopy of the anolyte confirm this result. However, a branching reaction occurring with < 1% of the total current cannot be excluded by these measurements even in acid solution.

(*B*) The high value of the heat of activation $E_a \simeq 40$ kcal $mole^{-1}$ precludes terminal desorption of CO_2 as a rate-determining step (1).

(*C*) The observed Tafel slopes, $b = 0.065 - 0.075$v (Fig. 2) are consistent with the value of $b = 2.3\ RT/F$. For a consecutive sequence of reactions, such as must exist in acetylene oxidation to CO_2, the slope $b = 2.3\ RT/F$ must be associated under Langmuir conditions with a chemical reaction following the first charge transfer, or following any later charge transfer in which the reactant is at full coverage as can easily be shown by a treatment of the consecutive reaction kinetics in the usual way (10). For the latter case, however, no pressure effect could be expected. Thus, the value of $b = 2.3\ RT/F$, together with the fact that $di/dp < 0$, fix the

[2] Data were not available for determining the ratio of c_E/c_A directly for 1*N* H_2SO_4 at 80°C. The value $c_E/c_A \simeq 0.1$ is for the ratio of the solubilities of the gases in water at 80°C. Data available at lower temperatures indicated the solubilities of each gas in 1*N* H_2SO_4 to be about 80% of their respective values in water.

location of the r.d.s. as one of the chemical reactions between the first and the second charge transfer.

(*D*) The negative pressure effect, $di/dp < 0$, shows that the r.d.s. must include a substance other than the adsorbing acetylene, or a radical derived from acetylene.

Reaction sequence and reaction rate.—The requirements listed above allow one to formulate the reaction path up to the r.d.s., and the nature of the latter.

The substance other than acetylene, or a radical derived therefrom and adsorbed on the surface, may be only OH^- or OH radical. Since all kinetic parameters are the same in acidic and alkaline solutions, the same mechanism may be assumed for both. This points to the OH radical being the entity in question. This in turn (in acidic solutions) may arise only from water discharge (2). Thus the charge transfer preceding the r.d.s. is assumed to be water discharge:

$$H_2O \rightarrow OH + H^+ + \bar{e} \qquad [2]$$

The rate-determining chemical reaction involves apart from OH either adsorbed acetylene, or a radical derived therefrom, in a chemical reaction. (Any dissociation into H atoms would involve ionization into $H^+ + \bar{e}$ and contribute to the Tafel slope.) Thus, the radical derived from acetylene can be only CH or an addition product involving acetylene and water.

The adsorption of acetylene followed by splitting, *i.e.*,

$$\begin{array}{cccccc} H & H & & H & & H \\ | & | & & | & & | \\ C=C & \rightarrow & 2\,C: & \text{or} & 2\,C. & \\ | & | & & | & & \| \\ Pt & Pt & & Pt & & Pt \end{array} \qquad [3]$$

would require additional energy connected with breaking of the double bond of about 146 kcal $mole^{-1}$. Even if each carbon atom were to form not one, but two covalent bonds with Pt, the extra energy needed would be about 80 kcal $mole^{-1}$.[3] Therefore, the possibility of CH being the radical seems unlikely.

It is impossible to distinguish whether the radical in question is adsorbed acetylene or a product of water addition since both would give similar kinetic parameters. Absence of polymerization products and of acetaldehyde in the electrolyte indicate there is no hydrolysis in solution. Thus, the radical is assumed to be adsorbed acetylene.

The reaction path may be now formulated as

$$C_2H_2 = C_2H_2\,(ads) \qquad [4]$$

$$H_2O = OH\,(ads) + H^+ + e, \text{ or} \qquad [5a]$$

$$OH^- = OH\,(ads) + e \qquad [5b]$$

[3] The energy of C-Pt bond was calculated as:

$$E_{C\text{-}Pt} = 1/2\,(E_{C\text{-}C} + E_{Pt\text{-}Pt}) - 23.06\,(X_C - X_{Pt})^2$$

where X = electronegativity value, $E_{C\text{-}C}$ = 83 kcal $mole^{-1}$, $E_{Pt\text{-}Pt}$ = 20.3 kcal $mole^{-1}$, X_C = 2.5, X_{Pt} = 2.2 (6).

Table III. Comparison of theoretical and experimental kinetic parameters

Kinetic parameter Tafel slope	Theoretical value 2.3 RT/F = 70 mv	Experimental value 65-75 mv (Fig. 2)
pH dependence, assuming $\theta_A \neq f(pH)$ at constant ionic strengths	$\left(\frac{\partial \log i}{\partial pH}\right)_V = 1$	0.8*
	$\left(\frac{\partial V}{\partial pH}\right)_i = -70$ mv	−50 mv (Fig. 2)
	$\left(\frac{\partial \log i_o}{\partial pH}\right) = 0$	~0 (See below, "Exchange current")

* The coefficient $\left(\frac{\partial \log i}{\partial pH}\right)_V$ was obtained by extrapolating the Tafel lines (Fig. 2) so that the current could be obtained at the same potential for various pH values, and by plotting log i *vs.* pH (Fig. 6).

$$C_2H_2\,(ads) + OH\,(ads) \xrightarrow{\text{r.d.s.}} C_2H_2OH, \text{ or } C_2H^{\cdot} + H_2O \qquad [6]$$

$$C_2H_2OH \ldots \xrightarrow{H_2O} 2CO_2 + 9H^+ + 9e$$

From the quasi-equilibrium in reaction [5]

$$\theta_{OH} = K_5\,(1 - \theta_T)\,a_{H^+}{}^{-1}\,e^{FV/RT}$$

where K_5 represents either $K_{5a}\,a_{H_2O}$ for 5*a* or $K_{5b}\,K_W\,A_{H_2O}$ for 5*b*, and K_W is the ionization constant of water.

The coverage of OH radicals is very low (11) and the coverage of all other intermediates may be neglected in comparison with θ_A, since they occur in the reaction sequence after the rate-determining step, and are not in equilibrium because of the constant removal of the final product, CO_2. Thus the total coverage θ_T may be approximated as $\theta_T \simeq \theta_A$.

The rate of anodic oxidation of acetylene may then be expressed as

$$i = nFK_5\,k_6\,a_{H^+}{}^{-1}\,\theta_A\,(1 - \theta_A)\,e^{FV/RT} \qquad [7]$$

See Table I for a comparison of theoretical and experimental kinetic parameters.

Pressure dependence.—The dependence of the steady-state reaction rate on the acetylene pressure (Fig. 4 and 5) can be stated in terms of the coefficient $Z \equiv (\partial i/\partial \log P)$. The values of Z are given in Fig. 7. They depend on potential, $d \log Z/dV$ being

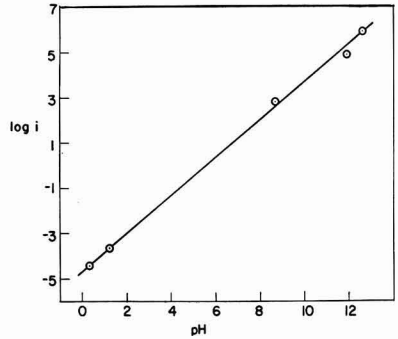

Fig. 6. Dependence of current on pH at constant potential V = 0.40v.

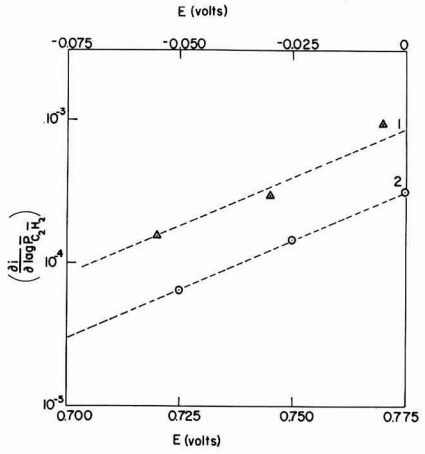

Fig. 7. Dependence of $Z \equiv \left(\frac{\partial i}{\partial \log p}\right)_V$ on potential curve 1 1*N* NaOH (use potential scale at top), curve 2 1*N* H_2SO_4 (use potential scale at bottom).

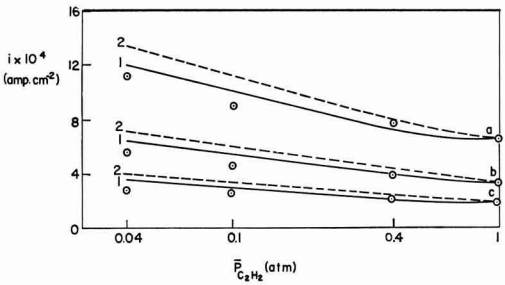

Fig. 8. Theoretical dependence of current on pressure as a function of potential: (a) 0.775v, (b) 0.750v, (c) 0.725v; curve 1 for $K_{\bar{P}_A} = 10^4$ atm^{-1}, curve 2 for $K_{\bar{P}_A} = 10^6$ atm^{-1}, ⊙ experimental points.

equal to ~ 13.5 v^{-1}, as calculated from Fig. 7.

Qualitatively, two types of explanation may be considered for the inverse pressure effect: (i) It could be due to increasing adsorption of a poison, either present in the C_2H_2, or produced by a side branching reaction of current efficiency too low to be detected by the methods employed. A polymerization of a reactant or product might also lead qualitatively to the effects observed. However, this explanation is not consistent with a number of facts, as discussed elsewhere (12). (ii) Aceteylene blocks partly the area available for reaction. A detailed treatment of such effects, in terms of poisoning, and hydrocarbon adsorption model, is published elsewhere (12). It is shown here that the observations are consistent with the type (ii) model according to the mechanism suggested in Eq. [7].

To compare the experimental data with the theoretical dependence of current on pressure at various potentials, the calculated limits of $K_p \simeq 10^4 - 10^6$ atm^{-1} (cf. section on Adsorption of Acetylene above), were inserted in Eq. [1]. By plotting the term $\theta(1-\theta)$ *vs.* p, the values of $\theta(1-\theta)$ at any given pressure may be read. Inserting those values into Eq. [7] and calibrating the term $ka^{-1}{}_{H^+}\, e^{FV/RT}$ for one value of current for $\bar{p}_A = 1$ atm, the theoretical i — log p curves for 3 potential values were obtained (Fig. 7, curve 1, $K_p = 10^4$ atm^{-1}; curve 2, $K_p = 10^6$ atm^{-1}). The experimental results obtained in 1*N* H_2SO_4 for these potentials are also shown in Fig. 8. It may be seen that a better fit would be obtained for somewhat lower K_p values than 10^4 atm^{-1}. However in view of the very rough calculation of K_p, the agreement is considered satisfactory.

The theory also yields the coefficient $d \log Z/dV$ as $F/2.3\ RT \simeq 14$ v^{-1} in fair agreement with the experimental value of 13.5 v^{-1}.

For 1*N* NaOH solution the change of current with pressure at constant potential is about 2-3 times higher than that predicted by theory. Variation of K_p to values considerably outside those deduced earlier does not cover the observed discrepancy. The coefficient $d \log Z/dV$ (Fig. 7) and all other kinetic parameters are in agreement with the suggested mechanism. This strongly points to a similar mechanism for the oxidation reaction in both acidic and alkaline solutions, but with a different type of adsorption isotherm, in that the amount of sites occupied by one adsorbed acetylenic radical in alkaline solution would be less than in acidic solution, since the value of $\left(\frac{d[\theta(1-\theta)]}{d \log p}\right)_V = \left(\frac{di}{d \log p}\right)_V$ would then be higher. Two explanations of this possible difference in surface occupancy by acetylene in H_2SO_4 and NaOH solutions may be suggested:

1. In NaOH, a rearrangement occurs, so that the adsorbed species are

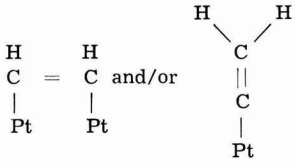

giving rise to a decreased occupancy per 1 acetylenic radical.

2. Acetylene does not form covalent bonds with d-electrons as assumed above, and on the basis of steric considerations it will occupy only two adjacent sites. In H_2SO_4, however, adsorption occurs along with hydration, according to the equation

$$C_2H_2\ (g) + H_2O \rightleftharpoons CH_2 = CHOH$$

and the resulting radical occupies an area covering approximately four surface sites.

Behavior at potentials above Tafel region.—Acetylene behaves here similarly to ethylene, and diffusion limiting currents are observed for $p_A \leq 0.4$. At higher pressures the potential of about + 1v, where the current rapidly decreases to negligible value is reached earlier than the limiting current value. The observed passivation of the electrode had been interpreted elsewhere (2) in terms of accumulation of surface oxide resulting from the reaction between the OH radicals which at the above potential becomes sufficiently fast. The resulting oxide is unable to oxidize the hydrocarbon.

Exchange current.—From the thermodynamic data, the standard reversible potential of the C_2H_2/CO_2 couple is

$$E^{\circ}_{80} = -\frac{\Delta G^{\circ}_{25} - \Delta S^{\circ}\,(80-25)}{10F} = -0.0503\text{v}$$

Taking into account the solubility of carbon dioxide [cf. ref. (1)] and the actual value of pH, the reversible potential at 1 atm acetylene partial pressure is

-0.11v in 1*N* H_2SO_4 (pH = 0.3)
and -0.97v in 1*N* NaOH (pH = 12.6)

solutions. The exchange currents obtained by extrapolation of the Tafel lines to those potential values are

4.5×10^{-18} and 6.6×10^{-18} amp cm^{-2} (geom.), respectively. The model proposed indicates equality of i_o in acid and alkaline solutions (cf. Table III).

Rest potentials.—The rest potential observed on Pt in presence of acetylene in solution is about 350 mv more positive than the reversible potential, for the acetylene oxidation to CO_2. Similar differences between the rest and reversible potentials have been reported for other hydrocarbons (1-3).

It is of interest to consider the possible nature of this potential. The principal facts with which an interpretation must be consistent are the following: 1, It is linearly dependent on pH: $dE/dp\text{H} \simeq -2.3\,RT/F$. 2, It is independent of the nature of the hydrocarbon used. 3, The partial pressure of hydrocarbon has no effect. 4, The potential concerned differs little from that which exists in the nitrogen saturated solution before the ingress of the hydrocarbon. The average effect of adding the hydrocarbon is to make the rest potential at the zero current flow more negative by approximately 20 mv. 5, Purification of the solution has no effect. 6, Temperature coefficient $dE/dT < 0$. 7, Stirring has no effect.

Possible interpretations of this potential are:

1. It may be a mixed potential set up between the reduction of oxygen to water on hydrogen peroxide and the oxidation of the hydrocarbon to CO_2. This theory would agree with the sign of the dependence of rest potential on pH and with the lack of effects of hydrocarbon pressure and temperature coefficient. However, it is unlikely that the nature of the hydrocarbon would then have a small effect, because acetylene and ethylene, at least, have very largely different exchange current values. Correspondingly, for the oxygen concentration present, it can be shown that the potential would be stirring dependent.

2. It may be a mixed potential between the oxidation of the unsaturated hydrocarbon to CO_2 and its reduction to the corresponding saturated hydrocarbon. This theory might be consistent with the absence of partial pressure effects in the hydrocarbon and stirring. Although neither the exchange current densities nor Tafel slopes for the reduction of the hydrocarbons are known, consideration of a mixed potential diagram shows that a mixed potential at the constant value observed, independent of the nature of the hydrocarbon, would require certain unlikely differences between the Tafel slopes and exchange current densities in the reduction of ethylene and acetylene. Furthermore, the small change brought about upon the introduction of the hydrocarbon into the nitrogen-saturated solution makes this theory unlikely.

3. Another possibility is the interference of the ethylene oxidation reaction by some redox process connected with the presence of impurities. This seems unlikely, however, because of the fact that calculations show that the impurities have to be present at a concentration having an order of magnitude of 10^{-5} moles/liter. If the rest potential at zero current flow is to be independent of stirring, this is an improbably high concentration of impurities to have present. A constant value independent of purification is also a strong point against this view.

4. Last, it is possible to regard the potential as that corresponding to the reversible equilibrium of water with hydroxyl radicals according to the reaction $H_2O \rightleftharpoons OH^{\cdot} + H^+ + e_o^-$. A reaction similar to this has been discussed by Bockris and Oldfield (13). Attempts to calculate the potential utilizing a PtOH bond, gives values which are approximately 0.5v too high. However, such calculations are uncertain. The theory would be consistent with the absence of stirring effects and with the negative temperature coefficient of the reversible potential. It might, however, be thought that the introduction of the hydrocarbon would play a large effect, for it would presumably reduce the concentration of hydroxyl radicals, on which the potential (according to this view) would be linearly dependent.

At the present time it is not possible to elucidate the mechanism of this rest potential, but the above remarks may serve as a beginning to such work.

Effect of the Triple Bond

The mechanisms proposed for olefin oxidation involves a rate-determining water discharge reaction, whereas that for acetylene involves a rate determining reaction between adsorbed acetylene and OH radicals. That the systems have a difference in mechanisms arises probably from a higher value of the heat of adsorption of acetylene as compared to that of ethylene as a result of the triple bond in the former (4).

For the case of ethylene, the specific rate of the reaction

$$\begin{array}{l} \quad H \quad H \\ \quad | \quad | \\ H-C-C-H + OH \rightarrow R-OH, \text{ or } R' + H_2O \\ \quad | \quad | \\ \quad Pt \quad Pt \end{array}$$

is higher than that of water discharge, whereas for acetylene, the specific rate of the reaction

$$\begin{array}{l} H \quad H \\ | \quad | \\ C=C + OH \rightarrow R'' - OH, \text{ or } R''' + H_2O \\ | \quad | \\ Pt \quad Pt \end{array}$$

is less than that of water discharge. This results in a change of the Tafel slope from $2RT/F$ to RT/F and a reduced i_o value.

Summary

The acetylene oxidation reaction on platinized platinum has been studied at 80°C in solutions of H_2SO_4 + Na_2SO_4 and NaOH of constant ionic strength. Reaction rates were measured as a function of potential, pH, and partial pressure of acetylene. Coulombic efficiency was determined by measurements of CO_2 production in acidic solutions and of C_2H_2 consumption in alkaline solutions. An improved apparatus for consumption measurements is described.

The following parameters have been found

$$\left(\frac{\partial V}{\partial \log i}\right)_p = 70 \text{ mv}, \left(\frac{\partial \log i}{\partial \text{pH}}\right)_V \simeq 0.8,$$

$$\left(\frac{\partial \log i_o}{\partial \text{pH}}\right) \simeq 0, \left(\frac{\partial i}{\partial p}\right)_V < 0,$$

$$\frac{\partial \log \left(\frac{\partial i}{\partial \log p}\right)_V}{\partial V} \simeq 13.5V^{-1}$$

Coulombic efficiency is 100 ± 1% in acidic and 95 ± 5% in alkaline solutions. $i_o \simeq 10^{-18}$ amp cm^{-2} for both solutions. The heat of activation at the reversible potential, $\Delta H^\circ \simeq 42$ kcal $mole^{-1}$ in acidic and $\simeq 46$ kcal $mole^{-1}$ in alkaline solutions. At $V \simeq 1V$ in $1N$ H_2SO_4 $\simeq 0.3V$ in $1N$ NaOH, "passivation" due to oxide formation occurs.

The reaction mechanism in the Tafel range was interpreted in terms of the following sequence

$$C_2H_2 \rightleftharpoons C_2H_2 \text{ (ads)}$$
$$H_2O \rightleftharpoons OH \text{ (ads)} + H^+ + e$$
$$C_2H_4 \text{ (ads)} + OH \text{ (ads)} \xrightarrow{\text{r.d.s.}} \ldots$$

over the entire pH range investigated (pH = 0.3 — 12.6). The inverse pressure effect observed could also be quantitatively accounted for in terms of the suggested mechanism.

Acknowledgments

The authors' thanks are due to Dr. Allan R. Day for helpful discussions, Alan Saunders for construction of the cells, and to Pratt and Whitney Division of United Aircraft Corporation for support of this work.

Manuscript received Sept. 19, 1963.

Any discussion of this paper will appear in a Discussion Section to be published in the June 1965 JOURNAL.

REFERENCES

1. M. Green, J. Weber, and V. Drazic, *This Journal*, **111**, 721 (1964).
2. H. Wroblowa, B. J. Piersma, and J. O'M. Bockris, *J. Electroanal. Chem.*, **6**, 401 (1963).
3. H. Wroblowa, B. J. Piersma, and J. O'M. Bockris, In course of publication.
4. G. C. Bond, "Catalysis by Metals," Academic Press, London, New York (1962).
5. B. M. V. Trapnell, "Chemisorption," Butterworths, London (1955).
6. C. A. Coulson, "Valence," Oxford University Press, London (1961).
7. L. Pauling, "The Nature of the Chemical Bond," Cornell University Press (1960).
8. E. A. Moelwyn-Hughes, "Physical Chemistry," Pergamon, New York, London (1961).
9. E. Blomgren, J. O'M. Bockris, and C. Jesch, *J. phys. Chem.*, **65**, 2000 (1961).
10. J. O'M. Bockris, *J. Chem. Phys.*, **24**, 1956.
11. H. Dahms and J. O'M. Bockris, *This Journal*, **111**, 728 (1964).
12. H. Wroblowa and J. O'M. Bockris, In course of publication.
13. J. O'M. Bockris and L. F. Oldfield, *Trans. Faraday Soc.*, **51**, 249 (1955).

Technical Notes

Growth Twins and Branching of Electrodeposited Copper Dendrites

Fielding Ogburn

National Bureau of Standards, Washington, D. C.

It is not unusual to see electrodeposited dendrites or trees which are branched in one plane only. That is, all the branches and the main stalk lie in the same plane, the whole dendrite being flat. Such dendrites of lead, tin, and copper were described by Wranglen (1), but he gave no explanation for the growth being restricted to one plane. From crystallographic considerations one would not predict this restricted growth if the dendrite were a single crystal. Branching would be expected to appear also in other planes passing through the main stalk.

Faust and Johns (2) reported twinning boundaries in electrodeposited dendrites of aluminum, copper, gold, lead, and silver. They showed that twinning can play a dominant role in the electrolytic growth of dendrites and cite references showing the same dominant role for growth other than electrolytic. The twinning boundary provides a re-entrant groove, and this groove may be self-perpetuating if two or more twin planes occur close together.

Consideration of these two pieces of information leads to the proposal that branching in one plane only is directly related to the occurrence of growth twins and that at least one twinning boundary extends throughout the dendrite and is parallel to the plane of the dendrite. The reasoning is that, if the twinning boundary facilitates the growth of the deposit by providing a re-entrant groove, then the dendrite should grow fastest at or close to the re-entrant groove. Growth at a distance from the groove would proceed more slowly or not at all. Thus, a platelet would form with the twinning boundary sandwiched between two thin layers of metal. Within the plane of the dendrite, the rate of growth would be different in different crystallographic directions, and one would expect the usual dendritic pattern. The net effect is to produce a fern-like shape with a twinning boundary extending throughout the stalk and each of its branches.

To test this hypothesis, copper dendrites were selected which were branched in one plane only and examined metallographically and by x-ray diffraction. These dendrites had been grown in a solution of 2g of cuprous chloride, 15g of sodium chloride, and 1 ml of concentrated hydrochloric acid in 80 ml of distilled water. All the chemicals were reagent grade. The deposition was carried out potentiostatically with 150 mv between the cathode deposit and a reference electrode. The latter was a copper wire in a Luggin capillary with the tip of the capillary within 5 mm of the cathode. The rate of growth of the dendrite is estimated to have been about 1 mm/hr or less judging from rate measurements made under similar conditions. The dendrites were free to grow in all directions.

Figure 1 shows an x-ray Laue transmission diffraction pattern taken of a copper dendrite 1 or 2 mm long with several branches, all in one plane. The plane common to the stalk and its branches was normal to the x-ray beam in each case. The pattern shows a sixfold symmetry which is characteristic of diffraction patterns of twinned face-centered cubic metals for which the (111) twinning plane is normal to the x-ray beam. The six Laue spots nearest the center of the pattern are 311 reflections.

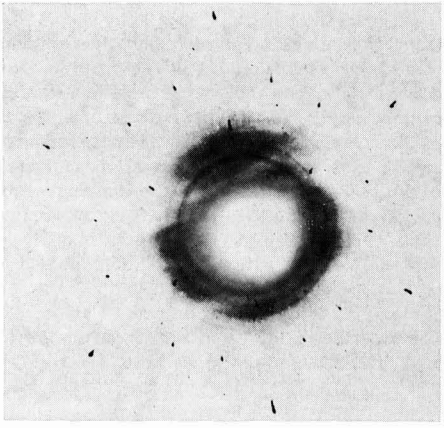

Fig. 1. Laue transmission pattern of copper dendrite. X-ray beam perpendicular to plane of dendrite.

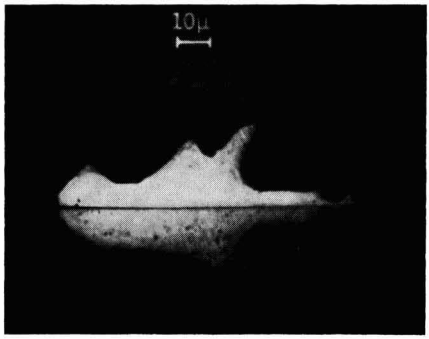

Fig. 2. Section through dendrite of Fig. 1 showing boundary between growth twins; etchant, ammonium hydroxide with hydrogen peroxide.

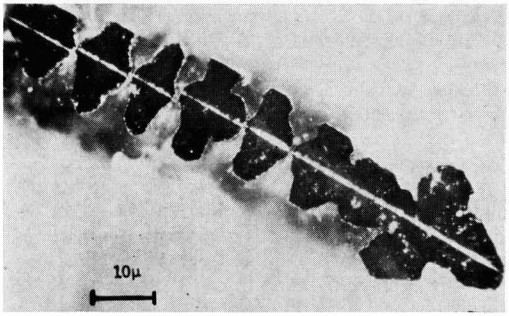

Fig. 3. Section through dendrite showing boundary between growth twins which extends through branches and main stalk. Section is perpendicular to branches and oblique to stalk. Polarized light; etchant, ammonium hydroxide with hydrogen peroxide.

The dendrite was mounted in plastic, sectioned, polished, and etched with a solution of dilute ammonium hydroxide and hydrogen peroxide. Figure 2 shows an etched section of the main stalk. It shows what appears to be the boundary between a pair of crystals in twin orientation and the plane of the twinning boundary is essentially parallel to the branches of the dendrite.

Figure 3 shows a similar section of a second dendrite grown simultaneously with the dendrite of Fig. 1 and 2. This section passes through the main stalk and the branches and is essentially perpendicular to the branches. Here again it appears that a twinning boundary extends throughout the dendrite, but with a slight displacement. Successive sections showed that the displacement disappears as the section approaches the junctions of the branches with the stalk.

To summarize, x-ray diffraction and metallographic examinations of copper dendrites which are branched in one plane only show them to be twinned with the twinning boundary extending the length of the stalks and branches. This appears to be an example of a growth twin and one which exerts a substantial influence on the growth of the dendrite. This is to be compared with the apparent influence of growth twins in polycrystalline electrodeposits of copper (3).

Acknowledgment

The author is indebted to Theodore Orem for the diffraction pattern and to the Advanced Research Projects Agency, Department of Defense, which helped support the work described.

Manuscript received Dec. 31, 1963.

Any discussion of this paper will appear in a Discussion Section to be published in the June 1965 JOURNAL.

REFERENCES

1. G. Wranglen, *Trans. Roy. Inst. Tech.*, **94** (1955).
2. J. W. Faust, Jr., and H. F. Johns, *This Journal*, **108**, 109 (1961); **110**, 463 (1963).
3. F. Ogburn and C. Newton, *ibid.*, **110**, 1148 (1963).

Evidence for Oxidation Growth at the Oxide-Silicon Interface from Controlled Etch Studies

W. A. Pliskin and R. P. Gnall

Components Laboratory, International Business Machines Corporation, Poughkeepsie, New York

The purpose of this paper is to show how a dilute selective etch can be used in the study of various glass and oxide film systems. We shall show, as an example, the details for only one specific application, in particular its usefulness for the study of silicon oxidation. Ligenza and Spitzer have shown by infrared spectroscopy using isotopic oxygen that, with high pressure steam, the oxidation occurs at the silicon-silicon dioxide interface (1). The controlled etch technique described here, is a simpler method of showing that oxidation occurs at the silicon-silicon dioxide interface with both atmospheric steam and dry oxygen oxidation. This technique depends on the ability of the selective etch, consisting of 15 parts hydrofluoric acid (49%), 10 parts nitric acid (70%), and 300 parts water, to etch various type glass and mixed oxide layers much more rapidly than silicon dioxide. The selective nature of this etch, referred to as P etch, is shown in Fig. 1. A silicon dioxide film was exposed to a phosphorus diffusion process to form a mixed SiO_2 + P_2O_5 layer on top of a pure silicon dioxide layer as shown on the left. The film thicknesses[1] were measured after etching for various times with P etch and plotted as shown on the right. The film thickness measurements were accurate to tens of Angstroms.

It is thus seen that the etch rate is much faster for the SiO_2 + P_2O_5 layer than for pure SiO_2, and the demarcation is clearly visible. Similar results have been observed with various type glasses on silicon dioxide, and this technique has been used for studying the penetration of glass films and glazes into underlying silicon dioxide films. (3).

[1] Thicknesses were measured with Vamfo, an interference microscope developed for accurate, nondestructive, film thickness measurements. (2).

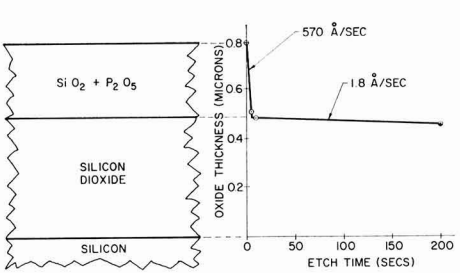

Fig. 1. Etch rates after exposure of an SiO_2 film to phosphorus diffusion.

Table I. Etch rates (Å/sec) for P_2O_5-SiO_2 and SiO_2 (23°C)

	P_2O_5-SiO_2 layer Thickness, Å	P etch, Å/sec	NH_4F-HF, Å/sec	SiO_2 P etch, Å/sec	NH_4F-HF, Å/sec
After phosphorus diffusion					
A	2960	570	270	1.8	9.5
B	1940	390	110	—	—
C	1310	220	—	—	9.0
After reoxidation (steam at 970°C)					
A	3930	35.1	33.2	1.7	9.0
B	2460	27.6	—	1.8	—
C	1860	18.3	28.5	1.8	10.3

Etch data for phosphosilicate films formed on silicon dioxide after exposure to different phosphorus diffusion conditions[2] is shown in Table I, where we have compared the etch rate of P etch with that of an ammonium fluoride buffer etch.[3] For the purpose of delineation of films, the etch rate ratio between the phosphosilicate layer and the silicon dioxide layer should be as large as possible. For P etch, this ratio is 100 to 300 after the phosphorus diffusion, whereas, with the NH_4F-HF buffered solutions, it is only about 10 to 30, about one order of magnitude less. After reoxidation, the ratio for P etch is about 10-20 and for NH_4F-HF it is only 3-4. Thus it is seen that the P etch is much better for delineation than is the ammonium fluoride buffer etch.

Table I also shows the thicknesses of the phosphosilicate layer on SiO_2 before and after reoxidation. This layer increases in thickness during reoxidation due to further penetration of the P_2O_5 into the SiO_2, thus diluting the concentration of P_2O_5 and decreasing the etch rate. At the same time, a small quantity of P_2O_5 outdiffuses resulting in a slightly slower etch rate within a few hundred Angstroms of the outer surface.

Evidence that the oxidation occurs at the oxide-silicon interface is given in Fig. 2. After the phosphorus diffusion, the phosphosilicate layer extended

[2] The phosphorus diffusion process used P_2O_5 in nitrogen carrier gas at either 1050° or 1100°C for various times.

[3] The buffer etch consists of one part hydrofluoric acid to ten parts of ammonium fluoride solution which was made by mixing 1 lb of NH_4F with 680 cc water.

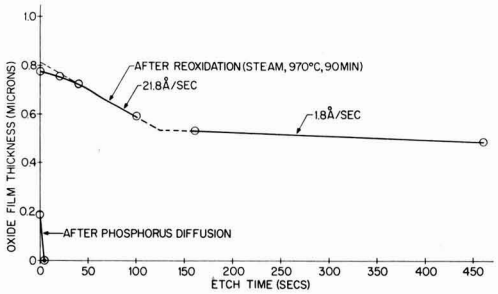

Fig. 2. P etch rate before and after steam oxidation

to the silicon as shown by the lower film thickness-etch time plot. The wafer was then oxidized in steam at atmospheric pressure for 90 min at 970°C. If the diffusing species were silicon, then Si atoms would diffuse out through the $SiO_2 + P_2O_5$ layer to form the SiO_2 layer on the outer surface. An etch rate plot of such a film should show a slow etch rate at the surface and a faster etch rate near the oxide-silicon interface. On the other hand, if the diffusing species were the oxidizing species diffusing through the phosphosilicate layer, then the new oxide would form at the oxide-silicon interface and the phosphosilicate layer would be at the outer surface. The etch rate plot would then show a fast etch rate followed by a slower etch rate corresponding to that of silicon dioxide. As shown in Fig. 2, this is exactly what is observed. It is concluded that in steam at atmospheric pressure the oxide forms at the oxide-silicon interface in agreement with the infrared isotopic studies of high pressure steam oxidation carried out by Ligenza and Spitzer.

Since in dry oxygen the oxidation rates are much slower, greater precautions are necessary. These precautions consist of limiting the phosphorus concentration and thickness of the phosphosilicate layer. This was accomplished by exposing a 1900Å SiO_2 film (on a 0.9 ohm-cm P-type wafer) to a diffusion condition which limited the phosphosilicate layer above ~ 100Å of the silicon surface. The film thickness after the phosphorus diffusion was 2380Å. The wafer was then subjected to dry nitrogen at 970°C for 90 min. The etch rate of this film was found to be 100Å/sec, and it extended to the bare silicon as shown by thermal probe and infrared carrier absorption. Since this layer would be too thick for

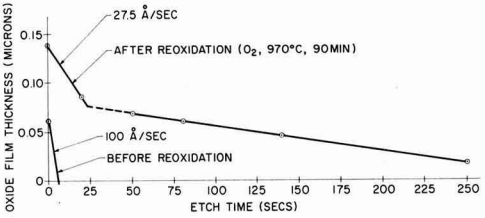

Fig. 3. P etch rate before and after dry oxygen oxidation

the subsequent reoxidation experiment, most of the phosphosilicate layer was removed by etching for 16.8 sec in P etch, leaving a 620Å phosphosilicate film as shown in Fig. 3. The wafer was oxidized in dry oxygen at atmospheric pressure at 970°C for 90 min. The upper plot was obtained by etching for various times with P etch.[4] It shows the phosphosilicate layer on top of a 700Å SiO_2 layer thus verifying the hypothesis that dry oxygen oxidation also occurs at the oxide-silicon interface. Similar results were obtained with various phosphosilicate layers and a borosilicate layer containing approximately 10% B_2O_3.

In conclusion, these results show how a dilute selective etch can be used in the study of film systems and, particularly, by simple techniques show that in thermally oxidized silicon by atmospheric steam or dry oxygen, oxidation occurs at the oxide-silicon interface.

Acknowledgment

The authors wish to thank Dr. J. A. Perri, Dr. J. Riseman, and Mr. H. S. Lehman for helpful discussions during the course of this work.

Manuscript received Jan. 23, 1964. This paper was presented at the Pittsburgh Meeting, April 15-18, 1963.

Any discussion of this paper will appear in a Discussion Section to be published in the June 1965 JOURNAL.

REFERENCES

1. J. R. Ligenza and W. G. Spitzer, *J. Phys. Chem. Solids*, **14**, 131 (1960).
2. W. A. Pliskin and E. E. Conrad, Paper presented at International Colloquium on the Optics of Thin Solid Layers, Marseille, France, Sept. 9, 1963; *IBM J. Res. & Dev.*, **8**, 43 (1964).
3. W. A. Pliskin, Unpublished work.

[4] The thicknesses of thinner oxide films were obtained from the intensity of the 9.2μ SiO_2 absorption band in the infrared spectra of the silicon wafer. The oxidized wafer was compared with a comparable thickness nonoxidized wafer in a Perkin-Elmer model 221G spectrophotometer.

Note on Calcium-Orthovanadate

L. H. Brixner, P. A. Flournoy, and Keith Babcock

Pigments, Engineering Physics, and Central Research Departments,

Experimental Station, E. I. du Pont de Nemours & Company, Inc., Wilmington, Delaware

Although calcium orthovanadate $Ca_3(VO_4)_2$ has been known since 1925, when Tammann (1) obtained it by solid-state reaction between CaO and V_2O_5, there is no publication on its structure. One reason for this may be that $Ca_3(VO_4)_2$ is isomorphic with neither the corresponding phosphate nor with the vanadates of strontium and barium. Therefore, the lattice parameters could not readily be derived from powder patterns and required the availability of large single crystals.

We have grown single crystals of $Ca_3(VO_4)_2$ up to 10 cm long and 1.25 cm in diameter by the Czo-

chralski (2) technique, employing a 25 kw Westinghouse radio-frequency generator, 450 kc/sec. An automatic radio-frequency voltage controller, regulating to 2.5%, was used in conjunction with the generator. The melt was contained in a 60% Pt-40% Rh crucible and the temperature observed with an optical pyrometer. The apparent melting point was 1430°C. An occasional check with a Pt/Pt 13% Rh thermocouple indicated that the optical measurement was about 40°C too low; hence, the true melting point is about 1470°.

The starting material was obtained by interacting $CaCO_3$ with $Ca_2V_2O_7$, which had been prepared by precipitation from purified solutions of calcium nitrate and ammonium metavanadate. While $Ca_2V_2O_7$ is a distinct lemon-yellow color, $Ca_3(VO_4)_2$ in the polycrystalline state is practically colorless. The pulled single crystals always had a very light orange-yellow color, which thus far has not been associated with any specific impurity. Spectroscopic as well as x-ray fluorescence analysis, in comparison with a "glass clear" sample of $CaMoO_4$, indicated only such elements as Sr and Ba present in greater quantities than in the absolutely colorless $CaMoO_4$. X-ray fluorescence analysis gave: CaO, 48.20% V_2O_5 = 52.05% (calc.: CaO, 48.05; V_2O_5, 51.95) for the composition of a grown crystal.

We suspect, therefore, that the VO_4^{-3} group may indeed be slightly colored intrinsically. In view of the decreasing intensity of color of the neighboring isoelectric anion groups, MnO_4^{-1} and CrO_4^{-2}, this conclusion appears quite reasonable.

X-ray examination by oscillation and Weissenberg methods of a section cut from a 10 cm crystal gave the following parameters: $a_o = 8.35$Å; $b_o = 10.77$Å; $c_o = 7.00$Å; $\beta = 95.0°$. The most probable space group is C_{2h}^6 C 2/c. The x-ray density is 3.55 $g \cdot ml^{-1}$, which checks closely with the pycnometrically determined density of 3.49 $g \cdot ml^{-1}$.

Pure $Ca_3(VO_4)_2$ does not fluoresce at room temperature in either 2537 or 3660Å ultraviolet radiation. However, when irradiated at −196°C, yellow fluorescence is observed.

Since the ionic radius of Ca^{+2} is about the same as the average of the trivalent rare earths, the latter can be readily introduced in the lattice of $Ca_3(VO_4)_2$ if electroneutrality is restored by compensation with Na^{+1} as in the typical compound $Ln_x{}^{+3}Na_x{}^{+1}Ca_{3-2x}(VO_4)_2$ or with Ti^{+4} as in a compound of the general type $Ln_{2x}Ca_{3-2x}(V_{1-x}Ti_xO_4)_2$.

Studies of the fluorescent emission of various rare earth ions in $Ca_3(VO_4)_2$ will be the subject of a future and more detailed publication. An intense fluorescence emission at 1.063μ is observed at −196°C from Nd^{3+} doped $Ca_3(VO_4)_2$ when sodium compensation is used. The emission lines are narrower and fewer in number than those observed for neodymium in $CaWO_4$ and $CaMoO_4$. Experiments to produce laser quality crystals of $Ca_3(VO_4)_2$ are now under way.

Manuscript received March 28, 1964.

Any discussion of this paper will appear in a Discussion Section to be published in the June 1965 JOURNAL.

REFERENCES

1. G. Tammann, *Z. anorg. u. Allgem. Chem.*, **149**, 68 (1925).
2. J. Czochralski, *Z. physik. Chem.*, **29**, 219 (1917).

The Preparation of Semi-Insulating Gallium Arsenide by Chromium Doping

G. R. Cronin and R. W. Haisty

Texas Instruments Incorporated, Dallas, Texas

The preparation of high resistivity or semi-insulating[1] GaAs has been reported by several laboratories using a variety of methods (1-12). For example, it has been prepared by compensation involving copper diffusion, by addition of oxygen, by extensive purification, that is, by vertical zoning, and by doping with iron, cobalt, or nickel. These methods, however, have not been amenable to the preparation of material with resistivity as high as 10^6 ohm-cm by crystal pulling techniques. Attempts to pull single crystal semi-insulating GaAs by oxygen doping at this laboratory have not been entirely successful mainly due to the formation of oxides on the melt surface.

[1] The term "semi-insulating" was first used by Allen (2) to describe materials whose resistivities are so high that the term "semiconductor" seems inappropriate. For a more precise definition, we propose for the purpose of this paper to define as "semi-insulating," material whose resistivity lies in the range 10^4-10^{12} ohm-cm. This range is the upper half of the 10^{-4}-10^{12} ohm-cm arbitrary limits between conductors and insulators suggested by Spenke (13).

Experimental Results

Our experiments have shown that semi-insulating GaAs with room temperature resistivity at 10^8 ohm-cm can be pulled consistently by doping with chromium. The minimum amount of chromium required is that concentration which just exceeds the concentration of the usual residual n-type impurities such as sulfur, tellurium, or silicon. Only on one occasion was low resistivity material obtained after the introduction of chromium. This crystal was grown before an effective segregation coefficient for chromium had been measured and was shown by spectrographic analysis to contain a higher than normal silicon content. Subsequent crystals were grown with chromium contents on the order of a few parts per million or less and have all been of the semi-insulating variety.

Table I. Properties of chromium-doped GaAs at 300°K

Crystal	Cr analysis (ppm by wt)	R_H (cm^3/coulomb)	R_H/ρ (cm^2/v-sec)	ρ (ohm-cm)	Type By Hall coefficient	Type By thermal probe
3-37	0.2-0.3	1.2×10^{11}	1130	1.06×10^{8}	n	p
3-41	0.4	2.8×10^{2}	2120	1.34×10^{-1}	n	n
3-42	0.2-0.5	8.8×10^{10}	256	3.43×10^{8}	n	p
3-44	0.4	3.5×10^{11}	630	5.61×10^{8}	n	p
3-45*	0.4-0.5	3.0×10^{8} 4.0×10^{11}	—	3.30×10^{8}	n	n
555-215	1.8	3.2×10^{11}	1120	2.84×10^{8}	n	p
555-216	3.5	2.9×10^{11}	693	4.17×10^{8}	n	p
3-50	360-400	1.3×10^{10}	614	2.15×10^{8}	n	p

* Crystal 3-45 inhomogeneous. Two values for Hall coefficient are measurements at each end of sample.

The crystals were all pulled on the (111) direction from melts compounded in the crystal puller. The details of this apparatus and its manipulation have been described previously (14). The chromium, in pellet form, was added directly to the gallium which was contained in an alumina crucible surrounded by a SiC-coated graphite susceptor. The purity of the gallium was 99.9999% while the arsenic was an equivalent grade made at Texas Instruments. The total charge weight was about 90g which included about 10% excess of arsenic over the stoichiometric quantity. The chromium content of each charge was between 100 and 200 mg.

The material was compounded slowly over a period of about 1 hr. Crystals were pulled at a withdrawal rate of 1.5 in./hr with a rotation speed of 25 rpm. The crystals tend to grow in what is approximately a tetrahedral shape and up to about 75% of the charge weight can be pulled. The crystals were cooled slowly to room temperature and their surface which was bright and shiny was apparently oxide free. Crystals grown under these same conditions but without addition of chromium have consistently been low resistivity n-type with excess carrier concentrations in the low 10^{16} cm^{-3} range.

Some data taken from a series of chromium-doped crystals are shown in Table I. The chromium content was obtained by emission spectrographic analysis. With the exception of crystal 3-41, referred to earlier, all of the crystals are semi-insulating. It is interesting to note that while sign of the Hall coefficient indicates n-type material in every case, the sign of the thermoelectric power determined by electrometer measurement indicates p-type material in all cases but one. The same result was obtained whether contact was made directly to the sample or by melting indium dots on the sample surface at about 375°C. Similar measurements on semi-insulating samples which were not doped with chromium have consistently checked n-type by thermoelectric power in agreement with the sign of the Hall coefficient. The difference in conduction type as measured by Hall coefficient and thermoelectric power for the chromium-doped samples would ordinarily be expected to occur only when the hole and electron concentrations are nearly equal, but due to the large mobility difference between holes and electrons in GaAs there is a wider range of hole and electron concentrations over which this effect can occur, since the mobility ratio enters as the square in determining the sign of the Hall coefficient. In agreement with this possible explanation we do find that the Hall mobilities are generally low as would be predicted from this model. Another possible explanation for this anomalous behavior of conduction type would be the existence of small n-type regions in the predominantly p-type samples which influence the sign of the Hall coefficient due to the greater mobility of electrons. This seems unlikely, however, in view of the uniform distribution of chromium as shown by the autoradiograms.

Table II. Cr^{51} in GaAs crystal 217 (300°K)

	Cr content (cm^{-3})	R_H (cm^3/coulomb)	R_H/ρ (cm^2/v-sec)	ρ (ohm-cm)
Slice No. 5	1.03×10^{17}	9.7×10^{11}	1920	5.1×10^{8}
Slice No. 5	1.56×10^{17}	1.5×10^{11}	395	3.8×10^{8}

In order to measure the effective segregation coefficient and the uniformity of distribution of chromium across the diameter, crystal 217 was grown with the addition of 211 mg of Cr^{51} enriched chromium in about 83g of material. Approximately half of the total melt was pulled. The crystal was cut perpendicular to the growth direction into 17 slices, numbered from top to bottom, and the chromium content of each slice was counted. Data from two slices near the top and bottom of the crystal are shown in Table II. Again the resistivity is in the 10^8 ohm-cm range while the chromium content varies by a factor of about 1.5 between these two slices representing total fractions solidified of 0.03 and 0.37, respectively. Autoradiograms of two of the slices in this crystal show that the distribution of chromium across the diameter of this particular crystal was very uniform with no evidence of "faceting" effects. A plot of log C/C_o *vs.* log $(1-X)$, where C and C_o refer to the chromium concentration in each slice and the initial melt respectively and X is the fraction solidified, yields an "effective segregation coefficient" of 6.4×10^{-4}.

In one instance a larger amount of chromium (about 1.5g) was added to the melt to determine whether the electrical properties would be affected. The resulting crystal, 3-50, had electrical properties similar to those containing a part per million or less chromium although, as shown in Table I, this crystal contained at least 400 ppm chromium. This high chromium concentration is difficult to reconcile with such a small segregation coefficient and therefore suggests the presence of a second phase. In this case the spectrographic analysis was checked and substantiated by wet chemical analysis. Metallographic examination of a section of this crystal disclosed the presence of small inclusions, metallic in appearance, which we believe are precipitates of chromium or a chromium compound. Attempts to confirm their identity with electron diffraction techniques have not yet been successful. Similar metal-

lographic examinations of crystals whose chromium content are in the low part per million range showed no evidence of these precipitates.

Discussion

Chromium doping is a convenient and very reliable method for producing semi-insulating GaAs. While we cannot as yet with certainty identify the mechanism by which this occurs, we can rule out some of the possible explanations.

If chromium introduced a deep donor level one should still observe low resistivity n-type material, since these crystals would have been low resistivity n-type without adding chromium. Thus the fact that chromium always produces semi-insulating material is an indication that it either introduces an acceptor or reduces the donor concentration enough to expose a deep level. To test this hypothesis further, crystal 3-59 was grown doped with both tellurium and chromium. Sufficient tellurium was added to the charge to produce a crystal whose excess n-type carrier concentration should range from 10^{16} cm^{-3} to 10^{17} cm^{-3}. The correct melt concentration had been determined from many previous tellurium-doped crystals. An amount of chromium calculated to exceed the tellurium concentration at the first to freeze portion of the crystal was also added. Most of the resulting crystal was again semi-insulating, and the electrical data shown in Table III indicate little if any difference between this crystal and those grown doped only with chromium. Near the very bottom, this crystal abruptly changed to low resistivity n-type, presumably where the tellurium concentration exceeded the chromium concentration as a result of the limited solubility of the latter. Similar attempts to counter dope with a shallow acceptor, for example, manganese or zinc, in melts containing chromium have not produced semi-insulating material (Table III), although analysis of the crystals shows that chromium was present in amounts in excess over other impurities. The hole concentrations in the p-type materials obtained were somewhat lower than expected. This effect, possibly the result of complex formation involving chromium, is under investigation and will be the subject of another paper.

There are at least three other possible explanations for the role of chromium in GaAs which should be considered.

1. Chromium, by gettering, reduces the concentration of shallow donors to expose an existing deep donor level when $N_D < N_A$ and $N_{DD} > (N_A - N_D)$.

2. Chromium is a relatively shallow acceptor which compensates the shallow donors to expose an existing deep donor level when $N_A > N_D$ and $N_{DD} > (N_A - N_D)$.

Table III. Properties of Cr-doped GaAs counter-doped with Te and Mn, at 300°K

Crystal	Analysis (ppm by wt)	R_H (cm^3/coulomb)	R_H/ρ (cm^2/v-sec)	ρ (ohm-cm)	$1/R_He$ (cm^{-3})
3-59	5Cr, 2Te*	6.5×10^{11}	1.7×10^3	3.9×10^8	
3-60	8Cr, 1Mn	6.5×10^3	1.6×10^2	4.1×10^1	9.6×10^{14}

* Te and Cr content of crystals 3-59 determined by solids mass spectrographic analysis.

3. Chromium introduces a deep acceptor, (N_{AA}) possibly in combination with a defect or other impurity which is revealed when $N_{AA} > (N_D - N_A)$ provided that $N_D > N_A$.

At this time we feel the evidence weighs against a gettering action such as has been ascribed to tantalum in the growth of high resistivity AlSb by Shaw and McKell (15), for example. The evidence they got for this mechanism was a lowering of the hole concentration accompanied by an increase in mobility with the addition of tantalum, indicating removal of scattering centers rather than compensation. In our case the mobilities in the chromium-doped semi-insulating GaAs are much lower than expected, and in the low resistivity n-type crystal (3-41) which did contain some chromium the mobility was 2100 cm^2/v-sec, also a rather low value for pulled crystals with this carrier concentration.

The next two explanations involving chromium as an acceptor are somewhat more plausible. If chromium were a relatively shallow acceptor it would actually be a secondary cause of semi-insulating material, the primary cause being a deep level already present. In support of this explanation is the fact that plots of log resistivity *vs.* reciprocal temperature for several samples of chromium doped material show slopes corresponding to energies ranging from 0.73 to 0.80 electron volts. This is remarkably close to that reported for semi-insulating GaAs which contained no chromium (4, 5). However, calculations have shown that if the deep level already present is a donor, chromium, as a shallow acceptor must compensate the donors present rather exactly. Since we expect some variation in both shallow and deep donor concentrations, it seems unlikely that we would obtain such consistent results, unless some automatic compensation mechanism as discussed by Allen (2) were operative.

Chromium as a deep acceptor would not require such close compensation and perhaps is a more straightforward explanation. A deep level is certainly present and chromium behaves as if it were an acceptor. The exact location of the chromium level however is still uncertain and will require further investigation, possibly luminescence, photoconductivity, and infrared absorption measurements.

Regardless of the exact nature of the mechanism involved, the preparation of semi-insulating GaAs by chromium doping has several advantages:

1. The doping can be carried out easily in vertical crystal pulling equipment and thus provides a source of large single crystals of controlled orientation.

2. Under reasonable precautions which maintain purity, the doping concentration which achieves semi-insulating material is not a really critical factor, it being necessary only to exceed the concentration of the usual residual n-type impurities.

Acknowledgments

The authors would like to thank the Semiconductor Physics branch of our laboratory for the Hall measurements, the Analytical branch for the chromium analyses, and G. Larrabee for the tracer work. We also acknowledge the support of the Electronic

Technology Laboratory of the Research and Technology Division, Air Force Systems Command, United States Air Force, under Contract Number AF 33(657)-9196 for part of this work.

Manuscript received Dec. 13, 1963. This paper was presented at the New York Meeting, Sept. 29-Oct. 3, 1963.

Any discussion of this paper will appear in a Discussion Section to be published in the June 1965 JOURNAL.

REFERENCES

1. J. Blanc, R. H. Bube, and H. E. MacDonald, *J. Appl. Phys.*, **32**, 1666 (1961).
2. J. W. Allen, *Nature*, **187**, 403 (1960).
3. J. Blanc and L. R. Weisberg, *ibid.*, **192**, 155 (1961).
4. R. W. Haisty, E. W. Mehal, and R. Stratton, *J. Phys. Chem. Solids*, **23**, 829 (1962).
5. C. H. Gooch, C. Hilsum, and B. R. Holeman, *J. Appl. Phys.*, **32**, 2069 (1961).
6. R. H. Bube, *ibid.*, **31**, 315 (1960).
7. F. A. Cunnell and R. Wickham, *J. Sci. Instruments*, **37**, 410 (1960).
8. J. M. Whelan and G. H. Wheatley, *J. Phys. Chem. Solids*, **6**, 169 (1958).
9. L. R. Weisberg, F. D. Rose, and P. G. Herkart, in "Properties of Elemental and Compound Semiconductors," Vol. 5, pp. 25-66, Interscience Publishers, New York (1959).
10. J. F. Woods and N. G. Ainslie, *J. Appl. Phys.*, **34**, 1469 (1963).
11. N. G. Ainslie, S. E. Blum, and J. F. Woods, *ibid.*, **33**, 2391 (1962).
12. W. J. Turner, G. D. Pettit, and N. G. Ainslie, *ibid.*, **34**, 3274 (1963).
13. E. Spenke. "Electronic Semiconductors," p. 3, McGraw-Hill Publishing Co., New York (1958).
14. G. R. Cronin, M. E. Jones, and O. W. Wilson, *This Journal*, **110**, 582 (1963).
15. D. Shaw and H. D. McKell, *Brit. J. Appl. Phys.*, **14**, 295 (1963).

Polycrystalline Silicon Films on Foreign Substrates

W. J. McAleer, M. A. Kozlowski, and P. I. Pollak

Electronic Chemicals Department, Merck Sharp & Dohme Research Laboratories, Rahway, New Jersey

Layers of silicon with crystallites up to 0.3 x 0.7 cm were prepared on graphite by a zone melting technique. Vapor deposition of silicon on foreign substrates by a chemical decomposition reaction (1, 2) yields layers with very small crystallites ranging from 2 to 200μ across (Fig. 1). Substantial increases in the size of the crystallites (Fig. 2) can be realized by passing a molten zone through the deposited layer and effecting a controlled recrystallization in the layer. The zone melting is accomplished using a 2.5 kw r.f. generator as power source, and the melting step is carried out in argon. Although the initial deposition step can be carried out with virtually any graphite, the melting step was much more critical in this regard. A variety of graphites were tested and found wanting, due to penetration of the molten silicon into the substrate which produced fractioning of the support. A graphite[1] with a scleroscope hardness of 72 and moderate density (1.65) was found to react with molten silicon at the graphite surface forming a SiC film. Residual silicon remained on the surface forming a semiconductor layer.

[1] United Carbon-UT 1.

All graphites tested produced silicon layers with varying acceptor (p-type) levels undoubtedly due to group III impurities in the graphite. To produce uniformly and heavily n-doped layers the graphite slabs were pretreated with P_2O_5 in methylcellosolve. Employing this technique, layers could be produced with the following characteristics: n-type, 1-2 ohm-cm resistivity, $\mu = 190$ cm^2 v^{-1} sec^{-1} and $\tau = 0.5$-1 μsec. The very low mobility presumably arises from the general imperfection and contamination of the layers.

Preparation of Devices

Mesa diodes.—To the polycrystalline silicon layer was applied a solution of B_2O_3 in cellosolve (50%), and the layer was inserted into a quartz diffusion

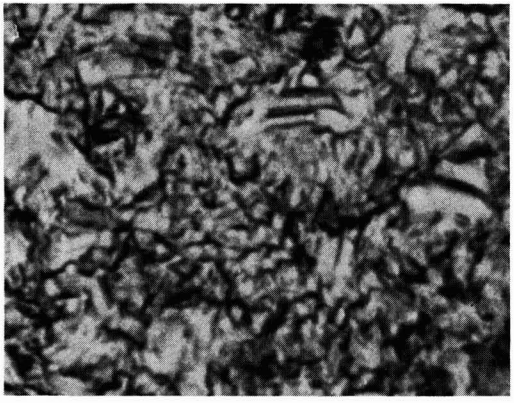

Fig. 1. Photomicrograph of surface of vapor deposited silicon layer on graphite. Magnification.

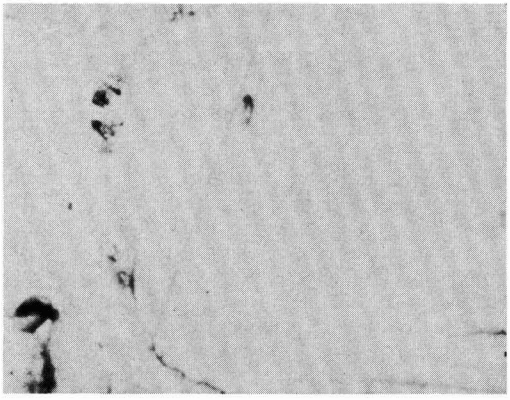

Fig. 2. Photomicrograph of zone melted silicon layer showing enlarged crystallites. Magnification.

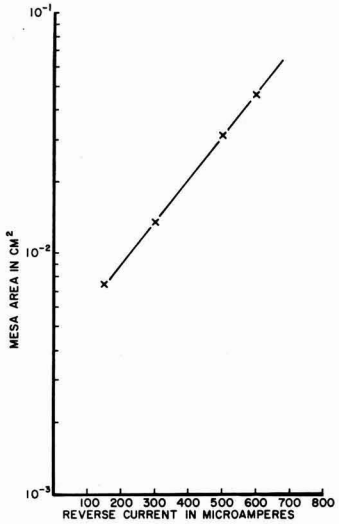

Fig. 3. Reverse currents as a function of mesa diode area

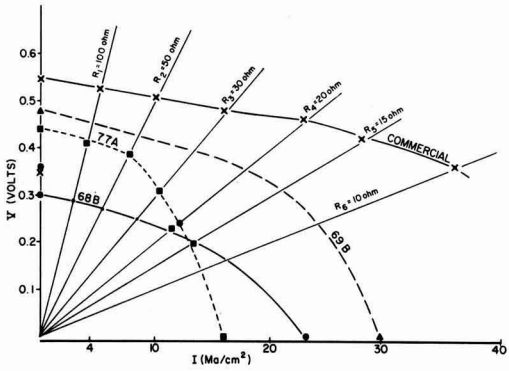

Fig. 4. Voltages and currents of photovoltaic diodes at various loads

apparatus. The assembly was purged with N_2 for 15 min, closed off, and inserted into a Globar furnace set to 1523°K. Diffusion was continued for 17 hr. The assembly was removed from the furnace and allowed to cool to room temperature.

The layer was treated with hydrofluoric acid for 30 to 60 sec to remove a neutral glass-like film which forms during the diffusion operation. Following this operation the silicon was thermally probed and was found to be strongly p-type, demonstrating that boron diffusion had occurred. The freshly etched surface was covered with 1-2 mm dots of an acid resistant wax (Apiezon W) dissolved in toluene, and the layer was exposed to an IR heat lamp to drive off the solvent leaving the dry wax. The assembly was etched in modified CP-4 ($5HNO_3$: 3HF : 3HOAc) for 1 to 2 min and immediately quenched in distilled water. The wax was removed from the etch produced mesa with toluene, and the layer was finally washed with distilled water and air dried. Reverse characteristics were measured dynamically using an oscilloscope. The mesas exhibited PIV's ranging from 40 to 90v with leakage currents as low as 100μa. In the forward direction mesas 2 mm in diameter (0.03 cm^2) were found to pass 1.2 amp at 1v. This would be equivalent to $>$ 30 amp/cm^2 at 1v.

The mesa area was found to affect critically the reverse characteristics of the diode. Figure 3 is a plot of reverse current (leakage) *vs.* area for four mesas formed on one layer of polycrystalline silicon. Leakage current varied from 150 μa for a mesa of 0.0075 cm^2 to 600 μa at 0.05 cm^2. Mesas larger than 0.05 cm^2 gave progressively poorer reverse characteristics, and at an area of 0.2 cm^2 rectification was virtually eliminated.

Photovoltaic cells.—The silicon on graphite piece was placed in a quartz apparatus which was evacuated to 1 mm Hg pressure. Gaseous BCl_3 was introduced into the system pressure of 150 mm Hg, and the sealed ampule was inserted into a Globar furnace held at 1323°K. The diffusion was continued for 5 hr. Following the diffusion the assembly was removed from the furnace and allowed to cool naturally to room temperature. The piece was cut into several 1 cm^2 sections, and the edges were abraided and etched (CP-4) to avoid short-circuiting of the p-layer to the graphite contact. Edge contacts were provided to the p-layer by chemically plating nickel strips on the upper surface taking care to leave the largest portion of the layer free for illumination.

Leads were then provided from the photovoltaic cell to a Triplett multimeter (Model 630-NA) and various resistors were inserted in the circuit in parallel with the cell to enable one to examine the performance of the cells under different loading conditions. Figure 4 shows the results obtained with 3 polycrystalline cells and a standard single crystal cell (~9% efficient). The current-voltage characteristics were determined at 100, 50, 30, 15, and 10 ohms resistance under identical illumination conditions (100 watt lamp mounted 12 cm from the cell). Referring to Fig. 4, it can be seen that the power output (IxV) of the polycrystalline cells most closely approaches the single crystal cell at high loads (100-50 ohms) and thereafter falls off very rapidly. The maximum power output varies for each cell illustrated in Fig. 4 falling at around 15 ohms for cell No. 69B (6.5 mw/cm^2) and approximately at 30 ohms for cell No. 77A (3.1 mw/cm^2).

Acknowledgment

The authors express their thanks to Professor H. P. Kallmann for his helpful advice and discussions and to Drs. Conrad and Rosenberg for assistance in electrical and metallurgical examinations.

Manuscript received March 24, 1964.

Any discussion of this paper will appear in a Discussion Section to be published in the June 1965 JOURNAL.

REFERENCES

1. C. K. Teal, J. R. Fisher, and A. W. Trystow, *J. Appl. Phys.*, **17**, 879 (1946).
2. J. F. Elliott, R. E. Hysell, and C. L. Kolbe, Final Report 1/29/60-1/28/61, Contract No. DA36-039 sc 85286 ARPA Order No. 80-59, U.S. Army Signal Res. & Dev. Labs, Fort Monmouth, N. J.

A Kinetic Study of the System Si-$SiCl_4$

R. R. Monchamp,[1] W. J. McAleer,[2] and P. I. Pollak[2]

Electronic Chemicals Division, Merck & Company, Incorporated, Rahway, New Jersey

As an adjunct to the development of epitaxial programs several investigators have reported upon the kinetics of the hydrogen reduction of $SiCl_4$ (1-4) and $SiCl_3H$ (5, 6). In all of these studies flow-type systems of one or more designs were used and, with the exception of Bylander's work, no direct study was made of the etching reaction.

$$Si(s) + SiCl_4(g) = 2SiCl_2(g) \qquad [1]$$

Schäfer (7) has studied the $SiCl_4$-Si system to determine the equilibrium constant as a function of temperature by means of a manometric method. From his equilibrium experiments Schäfer concluded that the only important gaseous species in equilibrium with solid silicon were $SiCl_4$ and $SiCl_2$ over the temperature range 1125°-1300°C. No study of the equilibrium of the $SiCl_4$-H_2-Si system, *i.e.*, the hydrogen reduction of $SiCl_4$

$$SiCl_4(g) + 2H_2(g) = Si(s) + 4HCl(g) \qquad [2]$$

has ever been reported. However, sufficient thermodynamic data are available to calculate equilibrium constants.

In their studies Theuerer (1) and Steinmaier (4) have shown that, as the ratio of $SiCl_4/H_2$ increases, the rate of deposition increases to a maximum and then decreases until the rate actually becomes negative. Considering the work of Schäfer it is reasonable to assume that the observed deposition rates are actually the net rate for two competing reactions [1] and [2]. Such a situation would explain the observed maximum and final negative rate, although no attempt has been made to modify the reduction data in these terms.

Second, because of the nature of flow systems the results of these investigations can only be interrelated by means of a system variable. Heinecke and Ing (8) in their study of the etching rates of germanium by elemental iodine found that they could not get reproducible kinetic data using an atmospheric flow type reactor. As a result they resorted to a low-pressure system from which they obtained "true kinetic data."

Similar results were obtained in this laboratory in some initial experiments. Using helium as a carrier gas for the $SiCl_4$ an activation energy of ~5 kcal was obtained which indicated that a mass transport phenomenon was the rate-controlling step. Furthermore, it was observed that the etch rate was significantly affected by the wafer orientation in the reactor. Therefore in order to investigate the $SiCl_4$-$SiCl_3H$-H_2 kinetics systematically, a low-pressure static system was devised to avoid the problems and variables associated with flow-type reactors. Considering all possible reactions which could be studied the simplest reaction, [1], was used as a starting point, and it is the kinetics of this reaction which are reported in this paper.

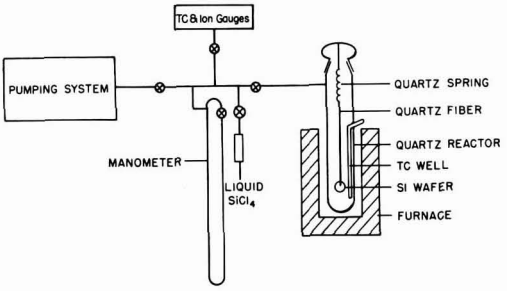

Fig. 1. Low pressure static system apparatus used to study $SiCl_4$-Si kinetics.

Experimental

The apparatus as shown in Fig. 1 was constructed from Pyrex glass with the exception of the reactor itself which was made of quartz. The pumping stage consisted of a fore pump, diffusion pump, and liquid nitrogen-cooled trap. The thermocouple and ion gauges were NRC types 501 and 518, respectively. The furnace was constructed from an Alundum core and heavy Nichrome winding. The temperature was measured with a Pt-Pt:13% Rh thermocouple seated in a well within the reactor and with a L&N potentiometer for reading the emf. In setting up the reactor the thermocouple was positioned opposite the center of the wafer.

In operation silicon wafers which had been mechanically lapped with 600 mesh aluminum oxide were chemically polished with CP-4 etchant, washed, rinsed with absolute methanol, and dried in the reactor under vacuum. The wafers were 8 mils thick and 20 mm in diameter, having a 1 mm hole just off center for suspension. In this series only <111> ± 1/2° oriented wafers were used, and they were p-type, 89-116 ohm-cm. The wafer was suspended from calibrated quartz spring (Worden Laboratory) by means of a thin quartz fiber. The springs had sensitivities of 5-7 mg/mm. The system was evacuated to ca. 2×10^{-4} Torr and then 0.5 atm of high-purity dry hydrogen was admitted to the reactor chamber. The furnace was then raised and the wafer heated in the hydrogen atmosphere for 1 hr. The system was evacuated again to 2×10^{-4} Torr. $SiCl_4$ was then admitted to a pressure of 30-260 Torr, and the spring displacement was measured by means of a cathetometer as a function of time. Two sets of experiments were performed, one to

[1] Present address: Airtron, Division of Litton Industries, Morris Plains, New Jersey.

[2] Present address: Merck Sharp & Dohme Research Laboratories, Division of Merck & Company, Inc.

determine the pressure dependency at a particular temperature and the other to determine the temperature dependency at a particular pressure.

Since the upper part of the reactor is much colder, the reverse reaction

$$2SiCl_2(g) = SiCl_4(g) + Si(s) \qquad [3]$$

takes place in the cooler portions just above the furnace. By means of reaction [3] $SiCl_4$ is continuously being generated and can migrate to the silicon surface again to be reacted with it. As a consequence of these reactions [1] and [3] the reactor operates under steady-state conditions. The slope of the line of a plot of weight loss *vs.* time is the rate for that $SiCl_4$ pressure and temperature. For most of the runs only 5-10% of the total wafer weight was consumed with no reduction in wafer diameter being noted.

Discussion

Unlike the decomposition reaction of $SiCl_4$, where the question has been raised as to whether or not the reaction occurs on or just near the silicon surface, the etching reaction must involve the silicon surface. The $SiCl_4$ pressure dependence for this reaction can be written most simply as follows

$$R = Kp^n \qquad [4]$$

where R is the rate, K a constant, p the $SiCl_4$ pressure in the system, and n is the pseudoreaction order.

Figure 2 shows a log log plot of the pressure *vs.* rate data from which the slope of the line or n has been determined to be one-half. The equation derived from the data is

$$R = 1.41 \times 10^{17}\, p^{0.49} \quad (T = 1110°C) \qquad [5]$$

where R is expressed as at./cm^2 sec and p is in atmospheres.

An interpretation of the observed results is that the surface is partially covered by adsorbed reactant molecules since the value of n is one-half. For a zero order reaction, one which is pressure independent, n would thus equal zero indicating complete surface coverage by adsorbed reactant molecules. The other case which might have been anticipated is that the surface would be bare or sparsely covered by reactant molecules, in which case the reaction would be expected to demonstrate a first order-type pressure dependency, and the value of n would be one. Thus, the conclusion, based on an intermediate value of n, must be that the surface is partially covered by adsorbed molecules. This value of n should then vary with temperature and approach one at higher temperatures where adsorption decreases and conversely approach zero at lower reaction temperatures. An alternate interpretation of the results rests in the possibility that the reaction products, $SiCl_2$ molecules, may be involved in the rate-determining step. In this case the reaction is retarded by the adsorbed products strongly held on the surface.

The general rate equation which may then be written is

$$R = K \frac{P_{\text{reactant}}}{P_{\text{product}}} \qquad [6]$$

If it is assumed that equilibrium conditions are approached near the surface of the wafer, then the equilibrium expression

$$K = \frac{P_{SiCl_2}{}^2}{P_{SiCl_4}} \qquad [7]$$

may be solved for P_{SiCl_2} and this quantity substituted in the rate equation to give the following rate expression

$$R = K' P_{SiCl_4}{}^{1/2} \qquad [8]$$

This alternate approach is in excellent agreement with the observed rate-pressure dependency.

The assumption of near equilibrium attainment close to the surface is not unreasonable when it is considered that the system is a static type in which the products must diffuse or be convected to the cold regions rather than be swept away by fresh unreacted gases.

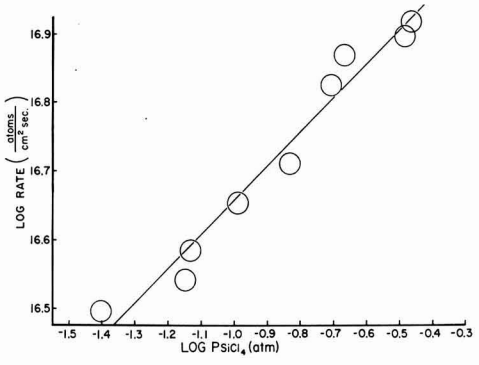

Fig. 2 Log rate *vs.* log P_{SiCl_4} plot for etching study at 1110°C; rate = $1.41 \times 10^{17}\, p^{0.49}$; T = 1110°C.

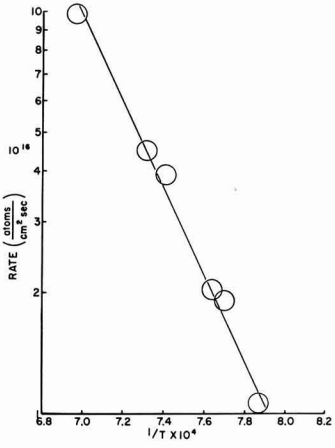

Fig. 3. Arrhenius plot of rate data at P_{SiCl_4} = 112 Torr; rate = $10^{24.5}\, e^{-49{,}100/RT}$.

Figure 3 shows the rate *vs.* $1/T$ relationship from which an activation energy of 49 kcal was calculated for the reaction.

Equation [9] was calculated by the least mean square method to represent the data

$$R = 3.16 \times 10^{24} e^{-49100/RT} \quad [9]$$

The activation energy of 49 kcal when viewed in accordance with heterogeneous rate theory is in agreement with either of the proposed mechanisms. However, for a chemical reaction controlled mechanism this activation energy is on the high side (8-10), whereas a desorption controlled mechanism would be expected to have an activation energy in this range (10).

Unfortunately there is not sufficient molecular constant data in the literature for $SiCl_2$ to allow a theoretical calculation to be made for either of the mechanisms.

Manuscript received Dec. 20, 1963; revised manuscript received Jan. 24, 1964.

Any discussion of this paper will appear in a Discussion Section to be published in the June 1965 JOURNAL.

REFERENCES

1. H. C. Theuerer, *This Journal*, **108**, 649 (1961).
2. S. K. Tung, "The Influence of Process Parameters on the Growth of Epitaxial Silicon," in "Metallurgy of Semiconductor Materials, Metallurgical Society Conferences," J. B. Schroeder, Editor, **15**, pp. 87-102, Interscience Publishers, New York (1961).
3. E. G. Bylander, *This Journal*, **109**, 1171 (1962).
4. W. Steinmaier, *Philips Research Repts.*, **18**, 75 (1963).
5. J. M. Charig and B. A. Joyce, *This Journal*, **109**, 957 (1962).
6. R. Glang and E. S. Wajda, "Status of Vapor Growth in Semiconductor Technology," in "Metallurgy of Semiconductor Materials, Metallurgical Society Conferences," J. B. Schroeder, Editor, **15**, pp. 22-47, Interscience Publishers, New York (1961).
7. H. Schäfer and J. Nickl, *Z. anorg. allgem. Chem.*, **274**, 250 (1953).
8. W. J. Heinecke and S. Ing, Jr., *J. Appl. Phys.*, **32**, 1498 (1961).
9. J. I. Carasso and I. Stelzer, *J. Chem. Soc.*, 1797 (1960).
10. E. A. Moelwyn-Hughes, "Physical Chemistry," 2nd ed., pp. 1186-1199, Pergamon Press, New York (1961).

Epitaxial Growth of Silicon Carbide

R. W. Brander

Central Research Laboratories, The General Electric Company Limited,

Hirst Research Centre, Wembley, England

Single crystal silicon carbide is normally grown by the vapor phase sublimation technique, devised by Lely (1). This requires the use of very high temperatures, usually 2500°C, and a cavity, at least partially closed, in order to retain silicon vapor. Elaborate heat shields and accurately designed heaters are required to obtain the close control of temperature gradient necessary for the growth of flat platelets of single polytype.

Silicon carbide consists of layers of tetrahedrally bonded silicon and carbon atoms, stacked in such a way as to give cubic, rhombohedral, and/or hexagonal symmetry. The c-dimension of the hexagonal unit cell in the various polytypes depends on the exact number of layers necessary for the arrangement to repeat itself.

In order to obtain good quality growth it is essential to control the furnace conditions so as to produce only a slight supersaturation of the ambient, thus allowing the material striking the surface to migrate to lattice sites rather than nucleate to form new crystals. Too low a degree of saturation will allow the crystal surface to decompose. With a binary compound it is also necessary to provide the correct quantities of the two elements. An excessive quantity of one species settling on the surface will tend to result in the formation of inclusions in the grown layer.

The necessary vapors can be produced either by decomposing silicon carbide, or by cracking compounds such as $SiCl_4$ and CCl_4, or by vaporizing the elements silicon and carbon. The first mentioned method resembles closely the vapor phase growth technique of Lely and has been used by Hergenrother *et al.* (2). It did not offer sufficiently variable conditions for the present experiments. The second method is similar to that used in the growth of β-silicon carbide or in silicon epitaxy and appears to require the presence of hydrogen. The third method is simpler to use and most variables can be altered independently, hence this technique was employed.

Material Preparation

Hexagonal silicon carbide crystals grown by the vapor phase technique were used throughout this work. The crystals were either obtained from the Norton Co., Arendal Co., or were grown in this Laboratory (3) by a technique similar to that described by Lely (1). Both flat parallel sided platelets and bulky crystals with one terraced face were used. Lapping, polishing, and etching were carried out as required.

The structure of silicon carbide results in opposite {0001} crystal faces being terminated in different atomic layers. It has been observed by Faust (4) and others that these opposite faces etch differently, one face exhibiting hexagonal pits while the other becomes "wormy." In this work the crystal face which exhibits the hexagonal pits will be referred to as the "p" face, and other as the "q" face. The growth on both {0001} faces was studied and the effect of substrate quality on the perfection of growth examined. Surfaces with various degrees of flatness were obtained by either lapping with 800

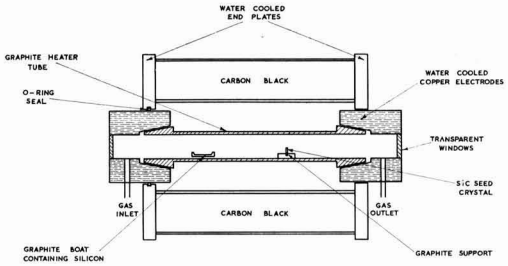

Fig. 1. Schematic diagram of furnace

Norbide, polishing with 1200 alumina or 1μ diamond, or chemically etching in 50% KOH/KNO_3 or NaOH. The untreated surfaces of flat platelets grown by the vapor phase technique were also examined as substrates. All substrates were chemically cleaned before use to remove oxide, etc.

Crystal polytype and perfection were determined prior to growth by x-ray techniques and by etching to ascertain the etch pit density. The latter was carried out by etching in either NaOH, Na_2CO_3 or borax at temperatures in the range 800°-1000°C. Two types of hexagonal pit can be observed, flat bottomed pits due to macroscopic imperfections at the surface, and tapering pits which occur where dislocations intersect the surface (5). The densities of these untruncated pits found on our seed crystals varied from 10 to 10^3 per cm^2. The grown layers were similarly investigated for perfection.

Growing Technique

The furnace (Fig. 1) consisted of a long graphite tube of ¾ in. bore and 12 in. long heated by the passage of a high current. The crystal substrate was situated in or near the hottest part of the tube, the temperature of which could be varied up to 2700°C. The crystal surface was allowed to radiate freely to the ends or to the walls of the tube. The silicon source was contained in a boat of high density graphite situated in the cooler part of the tube in a position which could be controlled externally but was often fixed prior to the run. The vapor pressure of Si in the tube could thus be controlled within the range 10^{-4}-10^{-1} mm Hg.

Carbon vapor was supplied from the walls of the tube and the necessary vapor pressure above the specimen controlled by adjusting the position of the specimen and the maximum temperature of the tube. Carbon vapor pressures in the range 10^{-6}-10^{-2} mm Hg could be obtained in the absence of silicon. The vapors were carried over the specimen in a stream of argon at a rate of 0.05 to 1 liters/min. The degree of supersaturation above the crystal was regulated either by increasing the tube and source temperatures or by altering the position and temperature of the substrate. The exact nature of the molecular species transported was not determined, but it is most likely to consist of SiC_2 and Si_2C and Si (6).

The crystal substrates were mounted in a high density graphite holder in such a manner as to expose only one face to the vapors. In this way the growth on individual faces could be investigated without any influence from the other face either during the run or in subsequent measurements.

A number of experiments were performed in which one single crystal was broken in two and then mounted in such a way that the same crystallographic face was turned towards the gas flow and away from it.

A similar arrangement was also employed in order to ascertain the growth rates on different crystal faces. In this case the crystal was broken and then mounted so that opposite crystallographic faces were facing the same direction with respect to the gas flow.

Results

Initial growth runs indicated that it was necessary to have the temperature of the carbon source about 600°-800°C higher than that of the silicon source in order to prevent the formation of silicon globules on the growing surface and silicon inclusions in the grown layer. It would appear from published vapor pressure data that this temperature difference ensures approximately equal vapor pressures from the two sources.

Growth rates.—The rate of growth of silicon carbide layers was found to vary with the orientation of the crystal in the furnace. Fastest growth was observed when the gas stream was directed onto the crystal face. The rate of growth fell off rapidly as the crystal was rotated towards the tube wall and was approximately 1/5th of the fastest rate when the crystal face was parallel to the direction of flow. Growth on the face shielded from the gas stream was slower still, being about 1/10th that of the fastest rate.

Growth rate could be easily varied by altering the various parameters of the system and rates from 0.05 to 5 μ/min were examined. Growth of 5 μ/min was achieved with the substrate at a temperature of 2200°C facing a gas flow of 500 cc/min, with silicon and carbon source temperature of 1800° and 2500°C, respectively. In this case the vapor pressures of the two elements would be of the order of 10^{-3} mm Hg. It was found that suitable reduction of the various temperatures and flow rate could produce any desired growth rate below this value. The above temperatures were measured optically and have not been corrected for emissivity.

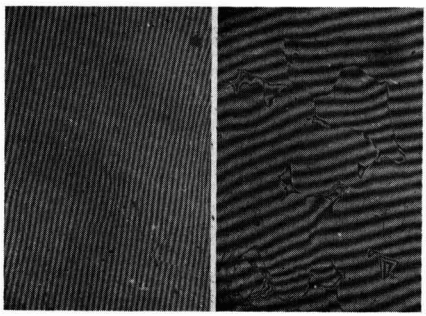

Fig. 2. Interference patterns on SiC epitaxial layer (slow growth rate). Magnification approximately 20X.

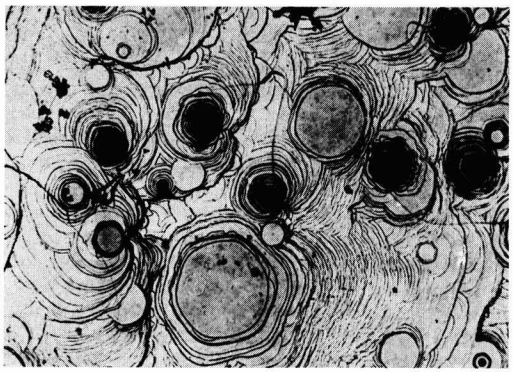

Fig. 3. Growth features on SiC epitaxial layer (fast growth rate). Magnification approximately 50X.

The above growth rates were measured on the p crystal face. The rate growth on the opposite {0001} face was also examined and this was found to be approximately half that of the growth rate on the p face under identical conditions of growth and substrate preparation. This fast growing face has also been observed to etch faster than face q (7).

Quality of growth.—Examination of the grown layers under a polarizing microscope, magnification 500X, showed that the three smooth substrates obtained with polished, etched, or untreated platelets produced layers of similar appearance when grown under similar conditions. At rates of 0.5 μ/min or less it was found possible to grow layers on sheltered crystal faces which were flat to better than 1000Å over an area of a few square millimeters (Fig. 2). Some areas had an irregular stepped structure of the type shown in Fig. 2b. Faster growth rates, exposure to the direct gas stream, or a rough substrate surface, resulted in uneven growth, an extreme example of which is shown in Fig. 3. Here the surface is composed of "hills" ranging up to 0.3 mm across and 10μ high.

The quality of growth was also investigated by etch pit studies. Observations showed that layers of the type shown in Fig. 3 had extremely large dislocation densities compared with that of the original crystal and often exceeded 10^3/cm^2. The slowly grown flat layers showed appreciably fewer etch pits, the density being of the same order, or slightly greater than that on the seed.

X-ray examination of the grown layers showed that they were of a single polytype without any observable random stacking disorder. For growth temperatures above 1900°C the polytype was always identical to that of the seed crystal for the polytypes investigated, namely 4H, 6H, 15R, 33R, and 51R. The polytype of layers grown at lower temperatures was not so easily reproduced and a few layers of different polytype to the seed were observed. In all cases the layers were found to be single crystals over the whole area of the seed.

Conclusions

The experiments described in this paper show that good quality single crystal layers can be grown on silicon carbide seeds by a simple vapor phase technique without the need to obtain pure polycrystalline silicon carbide starting charges, or the necessity of cracking volatile compounds.

Good quality growth can be achieved at rates of 0.5 μ/min as long as the vapor stream does not impinge on the growing face. With an impinging vapor stream rates of less than 0.1 μ/min are necessary to produce relatively smooth surfaces.

Layers grown above 1900°C show perfect polytype reproduction of the substrate. Below this temperature the polytypism is often different to that of the seed, and if the temperature is sufficiently low polycrystalline cubic material may nucleate. Since the various crystallographic modifications are known to have different energy gaps, their controlled growth could be used as a method of producing heterojunctions.

It was also observed during these experiments that opposite {0001} faces grow at a markedly different rate under identical conditions of preparation and growth. In this case the hexagonal pitted face, which etches fastest in molten KOH/KNO_3, was the fast growing face.

Manuscript received Aug. 12, 1963.

Any discussion of this paper will appear in a Discussion Section to be published in the June 1965 JOURNAL.

REFERENCES

1. J. A. Lely, *Ber. dent. keram. Ges.*, **32**, 229 (1955).
2. K. M. Hergenrother, S. E. Mayer, and A. I. Mlavsky, "Silicon Carbide," p. 60, Pergamon Press, New York (1960).
3. R. W. Brander and J. R. Martin, To be published by I.E.E.
4. J. W. Faust, Jr., "Silicon Carbide," p. 403, Pergamon Press (1960).
5. S. Amelinckx and G. Strumane, *ibid.*, p. 162.
6. J. Drowart and G. De Maria, *ibid.*, p. 16.
7. R. W. Brander, To be published.

Ta_2O_5 Films Formed with Nonsteady Potentials

D. A. Vermilyea

Research Laboratory, General Electric Company, Schenectady, New York

This note reports two characteristics of anodic Ta_2O_5 films formed with nonsteady potential and an observation of a new type of film formed with alternating potential. The first characteristic of films formed with nonsteady potential is observed for films formed by applying either an alternating voltage or a pulsating direct voltage to a cell containing platinum and tantalum electrodes immersed in any of several aqueous solutions. Such films are thinner for a given peak formation voltage than films formed at a steady voltage equal to the peak voltage. For example, films were formed by apply-

ing half-wave rectified 60 cycle alternating voltage to a cell shunted by a resistance which reduced the potential to zero between pulses. The formation field (voltage applied 2 min) was 0.077 v/Å, while the corresponding value for films formed 2 min at a steady voltage was 0.0625 v/Å. If the pulsating potential was applied for 1 hr the field was 0.0726 v/Å, while for steady voltage it was 0.053 v/Å. The platinum potential measured against the saturated calomel electrode was +0.3v and did not change with either the pulsating or steady potential. With an alternating voltage of 10v maximum the field was about 0.08 v/Å. Films formed by one type of potential (for instance pulsating) to one thickness and then formed further with the other type of potential (for instance steady) had a formation field characteristic of the final type of potential.

The second characteristic is that films formed with nonsteady potential dissolve more slowly in hydrofluoric acid. For example films formed with either pulsating direct potential or alternating potential dissolved in 50% HF at about 12.5 Å/sec. Films formed one way and then another showed dissolution at a rate characteristic of the final type of formation.

Both of these characteristics, slower attack by HF and the requirement of a higher field for ion motion, are characteristic of films which have been annealed after formation (1, 2). Such annealing occurs even at room temperature and is accelerated by applied fields smaller than those required for ion motion. It is suggested that films formed with nonsteady potential are annealed during the portions of each cycle when the field is within the range of 100-75% of the maximum field.

When alternating potentials are applied in certain solutions a new type of film is formed. The solutions in which this phenomenon occurs are those containing alkali ions at fairly high concentrations. For example, with a 1M lithium chloride solution and an alternating potential of 10v maximum (20v peak to peak) the film formed on a ¼x1 in. tantalum coupon showed several orders of interference colors indicating thicknesses varying from 1000Å to 3500Å (at 10v a film formed at constant voltage was ~160Å thick). The figure shows a black-and-white photograph of the specimen; the colors indicated a thicker film at the edges where the current density was highest. Indeed, a high current density favors the effect, for in tenth molar solutions the effect was greatly reduced. Similar effects occur with lithium solutions containing other anions and is somewhat more pronounced in the order $NO_3^- < Cl^- < ClO_4^-$, possibly because of differences in the conductivities of the various solutions. Greater differences exist among the alkali cations, the effect increasing in the order $Rb^+ \sim K^+ < Na^+ < Li^+$. In NH_4Cl, KCH_3COO plus 0.5M CH_3COOH, Mg_2SO_4, $(C_2H_5)_4NCl$, and in solutions of Li^+ or K^+ at *p*H $< \sim 0.5$ the effect is absent. Apparently a condition for the occurrence of this phenomenon is the development of a high *p*H at the electrode surface during the portion of the cycle when tantalum is negative. In solutions containing buffers (NH_4^+, acetic acid) or in solutions in which high *p*H cannot be reached because of precipitation of a hydroxide (Mg^{++}) or ion decomposition [$(C_2H_5)_4N^+$] the effect is absent. The capacitance of both the multicolored films and those formed in buffered solutions is the same and corresponds to a film about 160Å thick. These multicolored films dissolve completely on immersion for 2 sec in 50% HF. Underneath the multicolored film is a thin film which etches at the 12.5 Å/sec characteristic of films formed with pulsating potential. No such multicolored films were formed during pulsating direct potential formation.

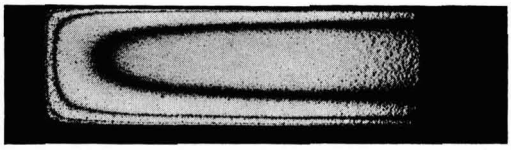

Fig. 1. Tantalum oxide film formed with an alternating potential of 10v maximum.

Probably the anodic oxidation in the very high *p*H solution at the surface immediately following the half cycle in which the tantalum is negative forms soluble tantalates (3). As the pH falls these tantalates would hydrolyze to give Ta_2O_5 which would precipitate on the electrode. Such Ta_2O_5 would probably be gelatinous or porous and is evidently an electrical conductor rather than a dielectric. The properties of these multicolored films resemble strongly those of films formed during illumination with ultraviolet light (4).

Manuscript received Dec. 11, 1963.

Any discussion of this paper will appear in a Discussion Section to be published in the June 1965 JOURNAL.

REFERENCES

1. D. A. Vermilyea, *This Journal*, **104**, 427 (1957).
2. D. A. Vermilyea, *ibid.*, **104**, 485 (1957).
3. W. H. Nelson and R. S. Tobias, *Inorg. Chem.*, **2**, 985 (1963).
4. L. Young, "Anodic Oxide Films," p. 135, Academic Press, New York (1961).

Orientation of Stacking Faults and Dislocation Etch Pits in β-SiC

W. K. Liebmann

IBM-Laboratories, Boeblingen, Germany

SiC crystallizes in several modifications which exhibit either hexagonal, rhombohedral, or cubic crystal symmetry. All crystal modifications are identical with respect to their nearest neighbor arrangement and differ only with respect to the stacking sequence of SiC-tetrahedra in the direction of the hexagonal crystal axis (1). Epitaxial growth of one SiC modification on another along a plane normal to the hexagonal axis is thus possible without the incorporation of too many lattice defects at the interface.

In the preparation of SiC-single crystals by the Lely method (2) it is often found that hexagonal α-SiC crystals possess a thin epitaxial coating of cubic β-SiC. Fused salt etching (3) and subsequent optical microscopy have revealed markings in these cubic layers which are reminiscent of the stacking faults in epitaxial Si (4, 5), and which will consequently be called stacking faults below. Figure 1 shows an example of such a stacking fault triangle on a {111} β-SiC surface. All closed stacking fault triangles on a specific crystal are of the same size, indicating that the stacking faults nucleate at the sample depth, evidently at the α-β-interface. Aside from stacking fault triangles straight line segments are found, as shown, *e.g.*, at A in Fig. 2. These segments probably correspond to two very closely spaced extrinsic-intrinsic stacking fault pairs as found by Finch *et al.* (4) in epitaxial Si.

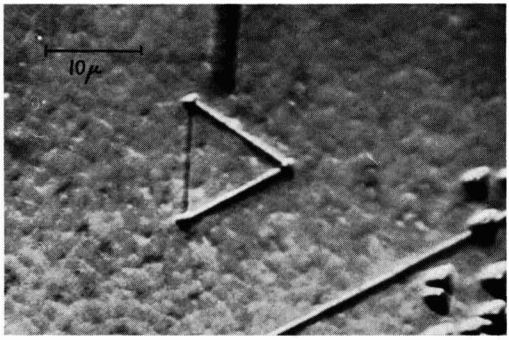

Fig. 1. Stacking fault triangle in β-SiC. Thickness of the epitaxial layer: 10μ; etched with $NaNO_2$ + 10% Na_2O_2 at 500°C for 10 min.

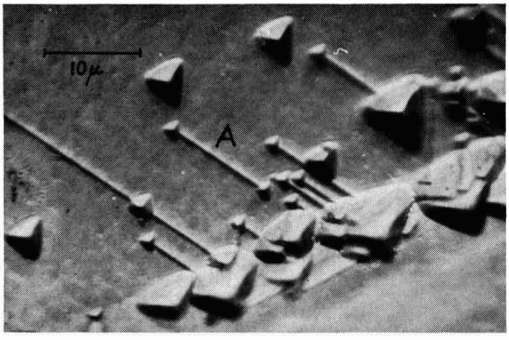

Fig. 2. Straight line stacking fault segment at A

Triangular dislocation etch pits are formed at the corners of the stacking fault triangles and at the termination points of the straight stacking fault segments, marking the intersection points between the connecting stair-rod dislocations and the {111} observation plane. Figure 3 demonstrates that both extrinsic and intrinsic stacking faults are possible. The two interacting stacking faults do not annihilate along their junction, but form a new fault terminating on both sides with dislocations.

It is interesting to note that the orientation of the stacking fault triangles and the triangular dislocation etchpits is reversed, even though both intersect with the {111} observation plane along <110> direactions. This means that either the stacking faults or the side faces of the dislocation etch pits do not consist of {111} planes.

In the zincblende structure, the lowest energy plane which can lead to a stacking fault or an etch pit of opposite orientation from a {111} fault is the {311} plane. There are three sets of {311} planes

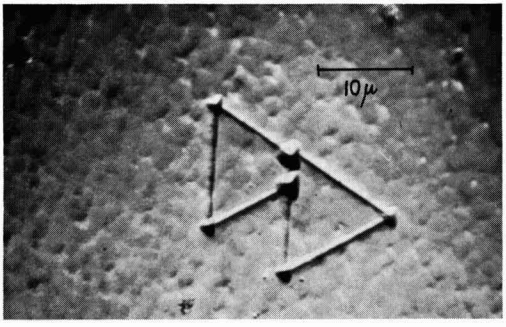

Fig. 3. Two interacting stacking fault triangles

Table I. Possible orientations of etch pits and stacking faults

	Etch pit orientation	Stacking fault orientation	h/a For stacking fault pyramids
A	{311} 29° plane	{111}	0.81
B	{311} 79° plane	{111}	0.81
C	{111}	{311} 29° plane	0.16
D	{111}	{311} 79° plane	1.6

intersecting with the {111} observation plane with intersection angles equal to 29° 30′, 58° 31′, and 79° 59′. Out of these three sets of planes only the 29° 30′ and the 79° 59′ planes are inclined opposite to the corresponding {111} plane and can thus form etch pits or stacking faults of the opposite orientation. Only these two planes intersect with the {111} plane along a <110> direction, while a pyramidal defect formed by three 58° planes would be slightly misoriented with respect to a {111} defect.

Assuming that the {311} plane is involved in the formation of the observed defects, the configurations listed in Table I are possible. The stacking fault orientations can be easily tested by computing the altitude "h" of the various possible stacking fault pyramids from their altitude to base ratio, h/a, and comparing it to the thickness of the epitaxial β-SiC layer. The values for (h/a) are also listed in Table I, and it can be seen that they are sufficiently different to use this method of differentiation. The thickness of the epitaxial layers was measured by angle lapping and subsequent etching, and in all cases very close agreement between the h/a ratio for a {111} stacking fault pyramid and the measured layer thickness was obtained. This establishes that the stacking fault planes are parallel to {111}, eliminating possibilities C and D. B would lead to a very steep etch pit, with a depth to side length ratio of 1.6, if the etch pit sides are not terraced. A, on the other hand, would lead to a very shallow etch pit, with a depth of side length ratio of 0.16. This ratio is actually found when measuring the depth of the etch pits by focussing a light microscope to their edge and to their bottom. This indicates that the etch pits are actually formed by three 29° {311} planes, even though electron microscope examinations will have to establish whether the etch pit side actually corresponds to a lattice plane or whether it is terraced.

The formation of etch pits involving {311} planes can be understood if one uses the same criteria for the etching process which Sangster (6) developed to determine the most favorable growth direction. Following his arguments, the greatest etching rate will not occur in crystallographic directions normal to the most stable plane, but in directions normal to planes where the removal of individual atoms will not alter the net number of "dangling" covalent bonds, so that the formation of the first hole in a perfect crystallographic plane will not represent a serious energetic problem. In the zincblende lattice the {311} plane is the lowest energy plane where this condition is satisfied.

It is interesting to note that also in silicon thermal etching in vacuum produces triangular etchpits which are rotated 180° with respect to the orientation of stacking fault triangles (7). It thus appears that the {311} plane is of similar importance in elemental semiconductors and that also the formation of etchpits on the {111} planes of III-V compounds should receive further attention.

Acknowledgment

The author wishes to thank Dr. B. A. Unvala for suggesting the {311} plane, and Dr. H. G. Jansen for many helpful discussions.

Manuscript received Feb. 24, 1964.

Any discussion of this paper will appear in a Discussion Section to be published in the June 1965 JOURNAL.

REFERENCES

1. H. Jagodzinski and H. Arnold, Proc. Conf. Silicon Carbide Boston 1959, p. 136, Pergamon Press, New York.
2. J. A. Lely, *Ber. dtsch. Keram. Ges.*, **32**, 229 (1955).
3. J. W. Faust, Proc. Conf. Silicon Carbide, Boston 1959, p. 403, Pergamon Press, New York.
4. R. H. Finch, H. J. Queisser, G. Thomas, and J. Washburn, *J. Appl. Phys.*, **34**, 406 (1963).
5. T. L. Chu and J. R. Gavaler, in "Metallurgy of Advanced Electronic Materials," G. E. Brock, Editor, Interscience Publishers, Inc., New York (1963).
6. R. C. Sangster, in "Compound Semiconductors," Vol. I, R. K. Willardson and H. L. Goering, Editors, p. 241, Reinhold Publishing Co., New York (1962).
7. G. R. Booker and B. A. Unvala, submitted for publication to *Phil. Mag.*

The Effect of Orientation on the Electrical Properties of Epitaxial Gallium Arsenide

Forrest V. Williams

Central Research Department, Monsanto Chemical Company, St. Louis, Missouri

The anisotropic segregation of impurities in semiconductors has been well established. A dependence of the segregation coefficient on orientation has been reported for germanium by Hall (1) and by Dikhoff (2), for indium antimonide by Hulme and Mullin (3), and for gallium antimonide by Hall (4) and by Willardson (5). Apparently, the effect is general for the III-V compounds and has been reported for a variety of solutes in the case of indium antimonide (6) and germanium (2). In the above cited examples the segregation being referred to is for the case of a solid-liquid interface; that is, a crystal growing in contact with its melt. In the present paper are reported some data which indicate anisotropic segregation of impurities at a solid-vapor interface.

Briefly, epitaxial layers of gallium arsenide were deposited on seed crystals of gallium arsenide oriented on <100>, <110>, <111>A, and <111>B planes. (The <111>B plane terminates with arsenic atoms.) An open tube system using hydrogen chloride as a transporting agent was employed. This method has been described in detail (7). The epitaxial layers were doped by either the use of doped gallium arsenide as a source or the use of a separate reservoir of the doping element in the vapor transport system. The chemically polished seed crystals were undoped, high resistivity (>10^3 ohm-cm) material which permitted the electrical properties of the epitaxial layer to be determined directly since the resistivities of the epitaxial layers were many factors smaller than the resistivity of the substrate. Wherever possible, seeds with different orientations were cut from the same high resistivity ingot. To eliminate the effect of slight run to run variations in flow rates, growth rates, and other variables, substrates with at least two different orientations were present in all experiments; four different orientations were present in some experiments.

Some representative data which have been obtained are summarized in Table I. Only net carrier concentrations are reported in this table, but the same differences are noted for the other electrical properties. This is shown for two experiments in Table II. The relative growth rates of epitaxial layers on the four orientations studied are shown in Table III. Comparison of the growth rates with the data of Table I indicates no relation between purity and the growth rate of the epitaxial layer. Thus, comparable carrier levels are obtained on epitaxial layers grown on <100> and <110> oriented substrates while the growth rates differ by a factor of about seven. On the other hand, widely different carrier levels are obtained on epitaxial layers grown on <111>B and <110> oriented substrates which have nearly equivalent growth rates. Clearly, the electrical properties obtained on epitaxial layers are governed by the crystal orientation of the substrate.

Table I. Net carrier concentration of epitaxial GaAs as a function of substrate orientation

Run	Dopant	Carrier conc, at./cc <110>	<111>A	<100>	<111>B
1	None*	9.6×10^{15}	1.8×10^{16}	4.2×10^{16}	2.7×10^{17}
2	None*			3.0×10^{16}	3.4×10^{17}
3	S			3.7×10^{18}	5.8×10^{18}
4	Sn			3.0×10^{18}	7.6×10^{18}
5	Zn	9.0×10^{17}	2.2×10^{18}	1.5×10^{18}	5.8×10^{17}
6	Zn			7.3×10^{18}	3.2×10^{18}
7	Te	4.6×10^{16}	3.7×10^{16}	9.0×10^{16}	6.7×10^{17}
8	Te			1.4×10^{18}	1.1×10^{19}
9	Se	3.6×10^{17}		2.2×10^{17}	1.6×10^{18}

* Undoped runs gave n-type epitaxial layers.

Table II. Effect of substrate orientation on electrical properties of epitaxial GaAs

Run	Orientation	n	μ	ρ
10	<100>	2.3×10^{16}	4420	0.062
	<111>B	1.7×10^{17}	3310	0.011
11	<100>	2.7×10^{17}	3090	0.008
	<111>B	1.5×10^{18}	1660	0.002

Table III. Relative growth rates of epitaxial GaAs on different orientations

Orientation	Growth rate
<100>	1.0
<111>A	0.9
<110>	0.14
<111>B	0.10

The following conclusions are evident from the data of Table I.

1. There is a marked difference in electrical properties of epitaxial layers grown on <111>B oriented substrates and layers grown on the other three orientations, <100>, <110>, and <111>A.

2. In the case of n-type doped layers, the doping level is much higher in layers grown on <111>B oriented substrates.

3. In the case of p-type doped layers, the doping level is lower in layers grown on <111>B oriented substrates than those grown on the other three orientations. Further, the magnitude of the differences between the orientations is smaller in the case of p-type dopants.

4. For n-type doped layers, the difference in doping levels on <111>B and <100> oriented substrates decreases in the order Te > Se > Sn > S.

These conclusions are more apparent from the data presented in Table IV which show the ratio of the carrier levels obtained in the four orientations as a function of dopant. Actually, this ratio can be viewed as the ratio of the segregation coefficients of the various impurities between the solid and vapor phase.

There are some striking similarities between the effects described here and those which have been reported for anisotropic segregation in the solid-melt systems referred to initially. These similarities are illustrated in Table V, in which some data are compared for the anisotropic segregation of impurities in crystals of InSb and GaSb grown from the melt and crystals of GaAs grown epitaxially from the vapor (data from Table IV). Anisotropic segregation of tellurium in a melt grown crystal of GaAs has been recently reported (11). The ratio of the segregation coefficient in the <111> facet to the segrega-

Table IV. Ratio of carrier concentrations on different orientations as a function of dopant

Dopant	n <111>B / <100>	<111>B / <111>A	<111>B / <110>
None	11.0 (6)	15 (1)	28 (1)
Zn	0.43 (7)	0.20 (1)	0.49 (2)
Te	7.4 (8)	~20 (3)	~15 (1)
Se	6.3 (3)	—	4.4 (1)
Sn	2.3 (2)	—	—
S	1.4 (2)	—	—

Numbers in parentheses refer to the number of experimental runs.

Table V. Comparison of anisotropic segregation of impurities in crystals grown from the melt and from the vapor

Impurity	k<111>B/<100> InSb (melt)	GaSb (melt)	GaAs (vapor)
Zn	1.3		0.4
S	3.1		1.4
Sn	3.9		2.3
Se	5.4, 6.1, 5.7	1.5	6.3
Te	6.1, 8.9, 5.9	2.0	7.4

InSb, ref. (6); GaSb, ref. (5); GaAs, Table IV, this paper.

tion coefficient "on the surrounding material" was 2.6.

Several theories have been postulated to account for the orientation dependence of segregation coefficients. Originally, Hall (1) postulated that the incorporation of impurities into the crystal depended on specific adsorption of the impurities at the different growth interfaces. Others (6, 8) have attempted to rationalize the effect by consideration of the detailed mechanism of the growth process for the different orientations. Burton *et al.* (9) have proposed a transport theory to account for the variation of segregation coefficient with growth rate and orientation. An impurity diffusion layer at the growth interface is postulated in this theory. The segregation coefficient is a function of the thickness of this diffusion layer. Since the thickness of the impurity diffusion layer is also a function of stirring, this theory has proved useful in explaining the variation of segregation coefficients with stirring. This theory, however, has difficulty accounting for the variation of segregation coefficient with orientation. A dependence of the impurity diffusion layer on orientation is then invoked.

Gatos (10) has pointed out that adsorption phenomena alone can account for the anisotropy of segregation coefficients. The results of the experiments reported in the present paper support the original adsorption theory of Hall (1). The same general features of the phenomenon in the solid-melt interface system are observed in the solid-vapor interface system, where transport processes in the vapor should be negligible.

Of particular interest are the cases of the segregation of gallium in germanium and zinc in gallium arsenide. Dikhoff (2) found that gallium is incorporated less readily on the <111> planes of germanium than the other planes. As indicated earlier in this paper, zinc is less readily incorporated into the <111>B plane of gallium arsenide than the other orientations. These are the only reported examples of ratios of the segregation coefficient on the <111> to <100> orientation less than unity. However, there is no need, in the adsorption theory, to postulate that preferential adsorption is exhibited by the <111>B planes for all impurities. It is reasonable to assume that other examples will be discovered which display behavior similar to zinc and gallium.

The results of this paper imply that more pure GaAs could be prepared by the Czochralski technique if the seed crystal were oriented in the <100> or <110> direction. This result has been confirmed for the case of <110> oriented seeds in this laboratory.

Manuscript received Feb. 10, 1964. This paper was presented at the Toronto Meeting, May 3-7, 1964.

Any discussion of this paper will appear in a Discussion Section to be published in the June 1965 JOURNAL.

REFERENCES

1. R. N. Hall, *J. Phys. Chem.*, **57**, 836 (1953).
2. J. A. M. Dikhoff, *Solid State Electron.*, **1**, 202 (1960).
3. J. B. Mullin and K. F. Hulme, *J. Phys. Chem. Solids*, **17**, 1 (1960).
4. R. N. Hall and J. H. Racette, *J. Appl. Phys.*, **32**, 856 (1961).
5. R. K. Willardson, "Compound Semiconductors," Vol. 1, "Preparation of III-V Compounds," p. 189, Reinhold Publishing Co., New York (1962).
6. J. B. Mullin, *ibid.*, p. 378.
7. R. L. Newman and N. Goldsmith, *This Journal*, **108**, 1127 (1961); F. V.Williams and R. A. Ruehrwein, *ibid.*, **108**, 177C (1961).
8. W. P. Allred and R. T. Bate, *This Journal*, **108**, 258 (1961).
9. J. A. Burton, R. C. Prim, and W. P. Slichter, *J. Chem. Phys.*, **21**, 1987 (1953); H. E. Bridgers and E. D. Kolb, **25**, 648 (1956).
10. M. D. Banus and H. C. Gatos, *This Journal*, **109**, 829 (1962).
11. C. Z. Lemay, *J. Appl. Phys.*, **34**, 439 (1963).

A Thermal Probe for Segregation Detection

J. H. Westbrook, A. U. Seybolt, and A. J. Peat

Research Laboratory, General Electric Company, Schenectady, New York

Physical property measurement techniques which will permit detection of compositional variation over micron distances are still few in number. Some success has been achieved recently in the application of microhardness measurements for the detection of grain boundary segregation of solute elements in a variety of base materials (1-5). A limitation of this method is that for most materials the hardness indentation itself is of the order of 5-50μ diameter and the region strained by the indenter a multiple of 2-3 times this. Thermal emf probes have sometimes been suggested for sorting of unknown samples (6), measurement of diffusion gradients (7), or identification of inclusions (8). In the latter case several features were provided by the authors to facilitate the measurement and adapt it to problems requiring high resolution: an electrolytically sharpened tungsten probe tip, use of a microhardness tester for applying the probe to the sample, and heating one leg of the thermocouple, *i.e.*, the probe itself, rather than the test sample. The present article reports the adaptation of this

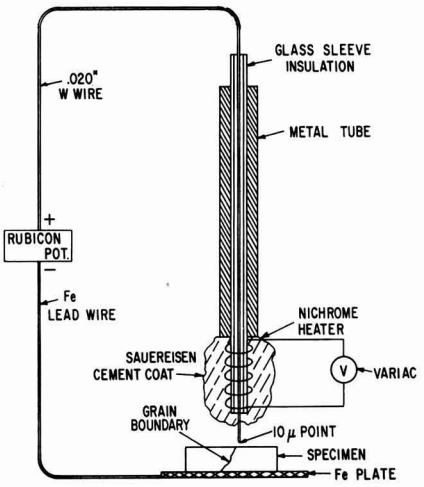

Fig. 1. Schematic drawing of thermal emf probe and associated equipment.

technique to the detection of grain boundary segregation.

Figure 1 shows a schematic drawing of the test equipment and the detail of the probe itself. The probe was formed by electrolytically etching a 0.020 in. W wire in a NaOH bath (9, 10). The wire was insulated with a woven glass sleeve, and this assembly was placed in a metal tube for rigid support. The heater was a 0.010 in. diameter Nichrome wire wound around the lower section of the insulated probe. This section of the probe was then coated with Sauereisen cement to hold the heater in place and to insulate the heater. The complete assembly was then mounted on a Kentron Microhardness Tester in place of the usual diamond indenter. Connections between probe and sample and measuring potentiometer were iron thermocouple wire. A small Variac provided variable power to the nichrome heating element.

Bicrystals, or coarse-grained polycrystals, of several intermetallic compounds (NiGa, NiAl, and AgMg) containing dissolved oxygen and dilute alloys of lead and of nickel were examined. Sample surfaces were prepared metallographically with a chemical polish or an electropolish as the final treatment. In a typical experiment a bicrystal of the compound NiGa, known to contain grain boundary segregated oxygen (3), was used as the test sample. A few preliminary experiments established that suitable experimental conditions were of the order of 10μ probe tip diameter, 10g load on probe tip, and 5-20v on the heater. At heater voltages of this order negligible heating of the sample surface occurs since the probe temperature is estimated to be less than 200°C, and furthermore, the contact between the probe and specimen is only a few microns diameter. The sample and the thermoelectric circuit were protected from drafts by plexi-glass shields.

Typical experimental results are shown in Fig. 2a, which also presents a hardness profile for the

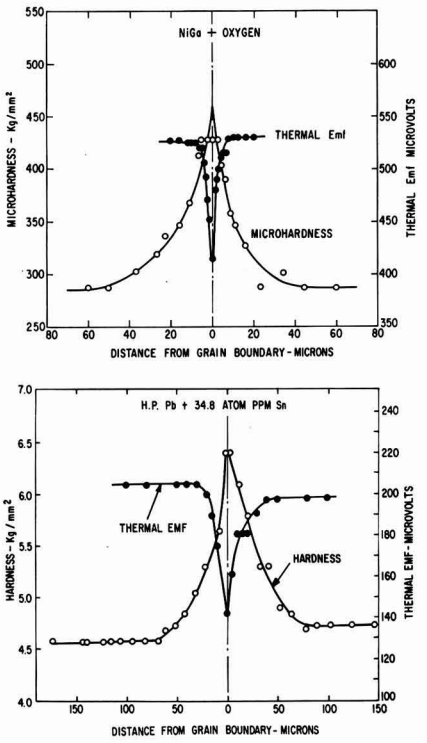

Fig. 2. Comparison of thermal emf and microhardness profiles at grain boundaries in (a) (top) NiGa (52 a/o Ga) containing oxygen and (b) (bottom) zone-refined lead with 34.8 at. ppm tin.

same specimen. The thermal emf is observed to fall about 25% in the vicinity of the grain boundary. The width of the affected region is somewhat smaller than that deduced from the hardness measurements, as would be expected from the greater resolving power of the finer probe. Figure 3 shows that the mean thermal emf increases in a regular manner as the heater voltage is increased, while

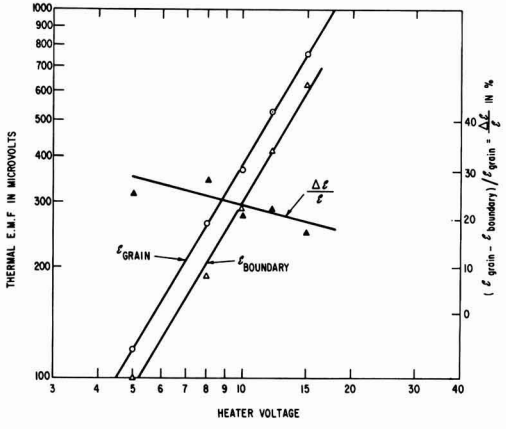

Fig. 3. Effect of temperature (heater voltage) on absolute and relative thermal emf in an oxygen contaminated grain boundary in NiGa containing 52 a/o Ga.

the relative change in thermal emf, grain *vs.* grain boundary, decreases only slightly.

Since the amount and distribution of grain boundary segregated oxygen in the intermetallic compound samples are not known, further experiments were carried out on bicrystals of zone-refined lead, some of which contained substitutional solute in parts per million concentrations. The zone-refined lead bicrystals with no added solute had previously been demonstrated to have extremely mobile grain boundaries whose microhardness was the same as that of the contiguous crystals. It is, therefore, inferred that impurity segregation in these samples is very slight. Thermal probe traverses across such a grain boundary gave an emf constant to within ± 5 μv. On the other hand similar traverses across a bicrystal of the same zone-refined lead to which about 35 atom ppm Sn had been added exhibited sharp minima in thermal emf (about 60 μv change) and sharp maxima in microhardness as shown in Fig. 2b.

Previous investigations (2-5) have shown that quenching from a high temperature eliminates the grain boundary hardness peak, and from this it is inferred that the local gradient in the hardening agent is removed at the high temperature. Accordingly pairs of samples of the intermetallic compounds NiGa and NiAl containing oxygen at grain boundaries were both quenched and slowly cooled from high temperature. Comparison of thermal probe traverses showed that for quenched specimens the thermal emf was low and essentially constant over the length of the traverse whereas slowly cooled specimens showed a higher level of thermal emf together with a sharply cusped minimum at the grain boundary.

A peculiarity of the time dependence of thermal emf was observed in the tests. Upon initial contact of the probe with the specimen surface a certain potential could be measured almost instantaneously. This potential would then drift slowly higher for many seconds until a steady-state emf was reached of the order of 15-20% above the initial value. In surveys in which both the initial and steady-state emf were recorded as a function of distance from the grain boundary, parallel curves were obtained with both emf parameters exhibiting minima at the grain boundary.

Continued experience with this testing technique disclosed some difficulties. First, in attempts to calibrate the thermal emf with composition in a series of homogeneous specimens, no regular correlation was obtained. Next it was found that even on a single specimen the level of thermal emf was sensitively dependent on the method of preparation of the surface, on the time of exposure to room temperature air following polishing, and on the load applied to the probe. Although the regular decrease observed in room temperature thermal emf with time of exposure to air at room temperature (Pb) or elevated temperature (NiAl) suggests that oxide film thickness is of critical importance, attempts to standardize these conditions for calibration purposes were not notably successful. Nonetheless traverses

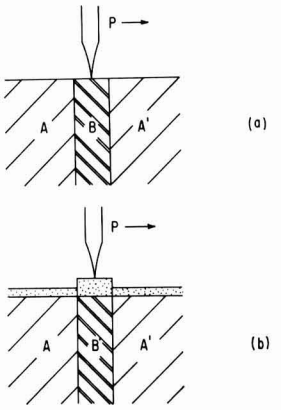

Fig. 4. Section through a grain boundary region showing schematically a composition change at the grain boundary, without (a) and with (b) oxide film formation.

on zone-refined lead or quenched intermetallics containing oxygen always showed constant emf across grain boundaries and slowly cooled specimens containing solutes always showed grain boundary minima in emf-distance curves.

Although the system is admittedly complex and the experiments inadequate to identify unambiguously the operative mechanism, an attempt will be made at least to describe the physical processes contributing to the observed results. For simplicity assume that the sample in the region of a grain boundary is a sandwich as in Fig. 4a, wherein a layer of material B at the grain boundary has one set of physical and chemical properties and the contiguous grain volumes A and A′ another set of physical and chemical properties. A thermal probe, P, traversing such a region perpendicular to the grain boundaries should then develop an emf which for a number of reasons is dependent on its position.

First, this emf is primarily the Seebeck effect which will depend on the temperature difference ΔT between probe and sample and on the thermoelectric characteristics of the materials in the circuit. The temperature difference for a given power applied to the probe heater will depend on the thermal diffusivity or conductivity and the surface heat transfer coefficient. Since both these factors and the thermoelectric characteristics are expected to vary, A as against B, the over-all Seebeck emf will be expected to vary as the probe traverses the ABA′ sandwich.

Since the thermal conductivity of the presumably more highly alloyed material, B, would be expected to be lower than that of A, a higher ΔT and hence a higher steady-state emf is to be expected at the grain boundary from this variable alone. The fact that only minima are observed indicates either (*a*) that cases are comparatively rare for which the variation in thermoelectric coefficient does not more than compensate for the effects of the variation in thermal conductivity, or (*b*) that some other dominating factor enters in. One such possibility is that in Fig. 4b, which illustrates schematically the for-

mation of oxide films of various thickness depending on the chemical characteristics of the substrates A and B. If B oxidizes faster than A, the film thickness at B will be greater than at A and, in accordance with the above observations on progressively oxidized surfaces, the resultant thermal emf from the probe less at B than at A. The slow increase in emf following initial contact of the probe might result from local build up of surface oxide about the tip of the hot probe insulating it and raising the effective ΔT. The model of a differential film thickness dominating the net thermal emf is also consistent with the observed difficulties in reproducibility, calibration, and deterioration.

Although it is obvious that much further work will be required to establish the details of the mechanism, the technique is attractive for several reasons. These reasons include: the fact that the measurement depends on a different group of properties than those of other grain boundary probe methods, the improved resolution, and the possibility of automated profile display on an x-y recorder.

Manuscript received Dec. 31, 1963.

Any discussion of this paper will appear in a Discussion Section to be published in the June 1965 JOURNAL.

REFERENCES

1. J. H. Westbrook and D. L. Wood, *Nature*, **192**, 1281 (1961).
2. J. H. Westbrook and D. L. Wood, *J. Inst. Metals*, **91**, 174 (1963).
3. A. U. Seybolt and J. H. Westbrook, *Acta Met.*, **12**, 449 (1964).
4. J. H. Westbrook and K. T. Aust, *ibid.*, **11**, 1151 (1963).
5. P. J. Jorgensen and J. H. Westbrook, *J. Am. Ceram. Soc.*, In press.
6. Antony Doschek, *J. Soc. Non-Destructive Testing*, **10**, 22 (1951).
7. B. I. Boltaks and V. P. Zhuze, *Zhur. Tekh. Fiz.*, **18**, 1459 (1948).
8. V. N. Novogrudskii and I. G. Fadikov, "Determination of Electromotive Force with a Modified Microhardness Tester," *Phys. Met. and Met.*, **7**, 99 (1959-1960) (Eng.) *Fiz. Met. i Met.*, **7**, 903 (1959) (Russian).
9. W. G. Pfann, U.S. Pat. No. 2,434,286 (1948).
10. F. G. Pany, Paper presented at Los Angeles Meeting, Electrochemical Society, Electronics Division Abstracts, No. 90, May 1962.

FUTURE MEETINGS OF
The Electrochemical Society

★ ★ ★

Washington, D. C., October 11, 12, 13, 14, and 15, 1964

Headquarters at the Sheraton-Park Hotel

Sessions probably will be scheduled on Batteries (including Round Table Discussion on Sealed Storage Batteries and, also, a Joint Symposium on Fuel Cells), Corrosion (including Symposia on Properties of Oxide Corrosion Products and, also, Metallurgical Factors Affecting the Corrosion Processes), Electrodeposition (including a Joint Symposium with Theoretical Electrochemistry Division on Mechanisms of Electrodeposition), Electronics (including Semiconductors), and Electrothermics and Metallurgy (including Symposium on Liquid Metal Corrosion and Phenomena jointly with the Corrosion Division and a symposium on Electron Microprobe)

★ ★ ★

San Francisco, Calif., May 9, 10, 11, 12, and 13, 1965

Headquarters at the Sheraton Palace, Sir Francis Drake, and St. Francis Hotels

Sessions probably will be scheduled on Electric Insulation, Electronics (including Luminescence and Semiconductors), Electrothermics and Metallurgy, Industrial Electrolytics, and Theoretical Electrochemistry

★ ★ ★

Buffalo, N. Y., October 10, 11, 12, 13, and 14, 1965

Headquarters at the Statler-Hilton Hotel

★ ★ ★

Cleveland, Ohio, May 1, 2, 3, 4, and 5, 1966

Headquarters at the Sheraton-Cleveland Hotel

★ ★ ★

Papers are now being solicited for the meeting to be held in San Francisco, Calif., May 9, 10, 11, 12, and 13, 1965. **Triplicate copies of the usual 75-word abstract, as well as of an extended abstract of 500-1000 words** (see notice on page 148C of this issue), are due at Society Headquarters, 30 East 42 St., New York, N. Y., 10017, *not later than December 15, 1964 in order to be included in the program. Please indicate on 75-word abstract for which Division's symposium the paper is to be scheduled, and underline the name of the author who will present the paper.* No paper will be placed on the program unless one of the authors, or a qualified person designated by the authors, has agreed to present it in person. Clearance for presentation of a paper at the meeting should be obtained before the abstract is submitted. An author who wishes his paper considered for publication in the JOURNAL or ELECTROCHEMICAL TECHNOLOGY should send triplicate copies of the manuscript to the Managing Editor of the appropriate publication, 30 East 42 St., New York, N. Y., 10017. Concerning papers to be published in the JOURNAL, see notice on per page charge on page 154C of this issue.

Presentation of a paper at a technical meeting of the Society does not guarantee publication in the JOURNAL or in ELECTROCHEMICAL TECHNOLOGY. However, all papers so presented become the property of The Electrochemical Society, and may not be published elsewhere, either in whole or in part, unless permission for release is requested of and granted by the Editor. Papers already published elsewhere, or submitted for publication elsewhere, are not acceptable for oral presentation except on invitation by a Divisional program Chairman.

Feature Section

Scientific Communication

Presidential Address[1]

Walter J. Hamer[2]

It is a great pleasure to address you here in this friendly city of Toronto. As we meet here it is interesting to recall that the name Toronto is of Indian origin and means "a meeting place." It was here that neighboring Indian tribes held rendezvous long before the coming of the white man to this hemisphere. As the capital of the province of Ontario, Toronto remains "a meeting place" for communication and exchange of ideas. The Electrochemical Society has met here on three previous occasions, the first meeting being in the fall of 1911.

It has been seventeen and a half years since The Electrochemical Society last met here. Since that time advances in science and technology have been many and significant. We have seen the harnessing of nuclear energy for peaceful purposes, the vast development in television, the commercial use of jet aircraft, flight by man into extraterrestial space, and advances in automation which are altering the course of life and the destiny of nations. Batteries using solar and nuclear energy have appeared. Transistors, lasers, masers, and hi-fi are realities. Transmutation of elements, the dream of the alchemist, has been further demonstrated. Eleven new transuranium elements, seven since World War II, have been produced by nuclear reactions and synthesis. Chlorophyll, insulin, and strychnine have been synthesized. Xenon and krypton have been found to be reactive, thus refuting the long held view that the rare gases are inert. Aside from these widely publicized developments, we now have a more fundamental understanding of natural and physical processes and a better insight into the structure of matter. We now know more about molten salts, nonstoichiometry, the atomic nucleus, the chemistry of the transmission of hereditary characters, the behavior of thin films, and the passivity of metals, to mention a few. One may ponder what the next seventeen and a half years will bring forth.

One might predict that the advances of the next decade will greatly surpass those of the immediate past. However, a problem of considerable concern to future developments has arisen. It is the one of scientific communication on which scientists and technologists have not, in general, taken issue. In some quarters the conviction prevails that if this problem is not adequately and rapidly solved science will become bogged down in its own products, and excess research costs, represented by duplication of research efforts, will mount to billions of dollars. Some even go so far as to predict a complete breakdown in the research effort. Then, of course, scientific accomplishments of the immediate future will pale in comparison with those of the immediate past.

[1] Delivered at the Toronto Meeting, May 5, 1964.

[2] Chief of Electrochemistry, National Bureau of Standards, Washington, D. C.

The Science Advisory Committee of the President of the United States appointed a Panel of Scientists to study this problem and its report of January 10, 1963, commonly called the "Weinberg Report," contained recommendations of importance to all scientific and technical societies. Basically, this Panel stated that all scientists and engineers must accept responsibility for the transfer of scientific information in the same degree and spirit in which they accept responsibility for research and development itself and must devote a larger share of their effort than heretofore to management of the ever-increasing scientific and technical record. They must take into consideration not only communication with those working in their own areas of science, but those in other scientific disciplines, and, in many cases, with the lay public. This Panel went further and said "We believe information is a part of research: that the links in the information transfer chain are welded together, and that in this age of information crisis, the creator of information must assume as much responsibility as possible for subsequent dissemination and retrieval of the information he creates. The page charge imposes on the technical author a financial responsibility that is consistent with this view of the information transfer chain. We therefore urge technical societies, regardless of their tradition, to turn to page-charge financing." The concern with which the matter of scientific communication is held is also shown by the fact that subcommittees of the United States Senate and House of Representatives are devoting time to ascertain possible ways to strengthen information, documentation, and communication programs in science and technology.

Now we may wonder how we reached this state of affairs on scientific communication. The basic answer to this question lies in the growth of science itself, for scientific communication is intertwined with all of science. Derek de Solla Price in his book "Science Since Babylon," published in 1961 by the Yale University Press, says of the phenomenal growth of science, ". . . the growth of science is something very much more active, much vaster in its problems, than any other sort of growth happening in the world today. For one thing, it has been going on for a longer time and more steadily than most other things. More important, it is growing much more rapidly than anything else. All other things in population, economics, nonscientific culture, are growing so as to double in roughly every human generation of say thirty to fifty years. Science in America is growing so as to double in only ten years ——it multiplies by eight in each successive doubling of all nonscientific things in our civilization, . . . the density of science in our culture is quadrupling during each generation. Alternatively, one can say that science has been growing so rapidly that all else, by comparison, has been almost stationary."

Measures of the expanding state of science are the vast increase in the number of scientists, the proliferation of scientific societies, the exponential growth in the number of scientific journals, and the fabulous sums of money that are being spent in support of scientific activity. During the past 35 years there has been roughly a tenfold increase in the number of scientists and engineers. In North America alone the number has increased from about 60,000 in 1930 to over 600,000 today, and it is estimated that the number will exceed two million by 1970. There is some evidence, however, that we are approaching the saturation point. Some believe the consequence of science saturation will be severe, others that we can tolerate saturation if the quality of scientists and engineers is improved. In any case, science will fare differently in an age of saturation than in one of expansion.

The last edition of "Scientific and Technical Societies of The United States and Canada" lists 1836 scientific societies. Also the recent edition of "International Scientific Organizations" lists 449 international organizations that maintain scientific communication services, such as documentation, information, or library services, and over 200 additional bodies that are engaged in scientific activities but do not provide communication services. In addition many government agencies and private groups now hold technical meetings on a scale comparable to those of societies. This proliferation of scientific and technical societies has placed a strain on societies to keep within their defined mission and to avoid overlapping of programs and overcrowding of the scientific calendar. Overlapping is most evident in committee activities. It may surprise you to know that at least five organizations are presently working on definitions in electrochemistry and six or seven are concerned with scientific units and symbols. One may argue that the perspectives of these groups differ, but when it is considered that they are invariably staffed by the same personnel the argument breaks down.

Our Society two years ago set up a Technical Committee to review the programs of the Society's nine Technical Divisions and to examine these programs in relation to those of other societies. There is now considerable pressure for intersociety programs. The Electrochemical Society, cognizant of its interdisciplinary nature, has participated in programs with other societies, dating from 1904 when it cosponsored technical sessions with the Fifth International Electrical Congress. Our Society in its history has cosponsored programs with nearly a dozen other national societies. Most societies must be facing the problem of intersociety activities, and it is hoped that mutual cooperation among societies will continue and thrive.

Since the first scientific journal appeared in the middle of the 17th century the number has grown exponentially until we have about 100,000 today. If this established pattern were to continue we would have approximately one million scientific and technical journals by the year 2000. Of course, these journals differ widely in substance and quality, but even so, the lesser ones cannot be passed over as inconsequential for here one may find, on occasion, a gem of truth. The rapid increase in publication led, as early as 1830, to the abstract journal which provides resumés of published articles. However, we have now reached the critical stage where we need an abstract periodical of the abstract journal, *i.e.*, we need to abstract the abstract. Also, we have the "annual reviews," the "modern advances," the "extended abstracts," and the "symposium monographs," etc., which give digests of recent advances.

In regard to financial support of science and technology, the United States Government, for example, in 1940 invested about 100 million dollars in scientific research and development; in 1963 this expenditure amounted to 12 billion dollars, and it is estimated it may reach 15 billion dollars this year. These expenditures represent a hundredfold increase in a little over two decades. All industrial nations show similar rates of increase in funds allotted to science and technology. In fact, those nations that started late show even higher rates of scientific growth and increase in scientific expenditures. With this kind of effort rests great responsibility. With this kind of effort has come the birth of the scientific advisor in government and the scientific advisory groups for many laboratories. With this kind of effort has come the realization of the need for broadened and improved scientific communication in all of its forms.

Scientific communication lies at the core of the vitality and integrity of science and serves to enhance mutual understandings between people and nations. Tracking stations located in various countries to monitor orbital flights unite scientists of various backgrounds in a common cause. Telstar and Relay have made possible global communications. In the year 1957 (July 1957 through December 1958), known as the International Geophysical Year, scientists of 66 nations collaborated on a grand scale to understand more fully the physical nature of the surface of the globe in relation to the ionosphere and the atmospheric envelope that surrounds the earth. The results of this endeavor were so fruitful that the work will continue under such successor programs as the World Magnetic Survey, the International Year of the Quiet Sun which started this year, and the International Upper Mantle Project in which the United States and Canada will have cooperative projects. Scientists also communicate internationally through their National Research Councils or through various international organizations such as the international standardizing bodies, the Unions, Federations, Associations, or Commissions. Our Electrochemical Society has two international programs at this meeting, the one on *Electron and Ion Beam Science and Technology* being cosponsored with the Metallurgical Society of AIME and the other on *Electrolytic Solutions.*

Along with the great increase in the number of scientific and technical journals has been the massive increase in the number of governmental and contractual reports. Some of these receive limited distribution to what is sometimes called the "invisible college," *i.e.*, to an "elite" or a select group of scientists who are especially trained in, or have a vested interest in, the subject, and who participate in "closed" symposia. This practice, if it were to expand, could mark the death knell of the research journal, in fact, of scientific societies. On the other hand, many of these reports receive wide distribution, so wide in fact, that it is questionable if subsequent publication in accredited journals can continue as accepted practice, if serious attempts are to be made to prevent overcrowding of the literature. A variation in the operation of the "invisible college" is the use by scientists of nontechnical media for release of discoveries. One society recently threatened to reject papers for its journals if the contents had been so released. This view was not well received, and was advanced, I believe, mainly because of the huge backlog in unpublished scientific articles, by limitations in available journal space, and

by the great increase in the cost of publication. In any case, it points out the seriousness of the "publication explosion."

It is painfully obvious that scientists cannot possibly keep up with the published scientific material. For example, if each of the 100,000 scientific and technical journals published only 100 articles a year the total number of articles facing the scientists, per year, would be 10 million. It is estimated that a backlog of 2,000,000 papers containing unevaluated data now exists. The literature has become so extensive that chemists and physicists, for example, stake out a small domain in their own fields and become authorities within this small domain. By such action they are then compelled to accept as authoritative the word of those in other domains and the scientist becomes authoritarian, a philosophy contrary to his inherent nature. A new approach to scientific communication is needed to reverse the ever-increasing trend, or the necessity, toward overspecialization which has been going on for a long time.

Man's progress has depended on his ability to accumulate and retrieve information. Today there is a threat to this program. Dr. William Grey Walter, the British neurologist, eloquently described this threat when he wrote "During the last two generations the rate of accumulation of knowledge has been so colossally accelerated that not even the most noble and most tranquil brain can now store and consider even a thousand part of it. . . . The root of this evil is that facts accumulate at a far higher rate than does the understanding of them. Rational thought depends literally on ratio, on proportions and relations between things. As facts are collected, the number of possible relations between them increases at an enormous rate."

There are those who believe that the "information problem" will be solved by mechanization or automation. They believe that some process of electronic sorting will solve the assembly of and the dissemination of scientific "know-how." Already we have seen systems based on punched cards and slot devices, those utilizing magnetic tape or magnetic spots, the digital and analog computers, the "learning machines," the "mechanized dictionaries," and the "language translators," or so many, in fact, that the Washington Academy of Sciences recently asked "Are we being computerized into automata?" Of course, information retrievals or processings cannot stand alone; they must go hand in hand with assimilation which is an essential ingredient in scientific response. Awareness of the assimilation problem has led to the establishment of various science centers, where aid is obtainable in specialized areas of science. These centers offer reviews, interpretations, compilations, evaluations, etc., and, therefore, are important chains in scientific communication. There are now about 400 such centers in the United States. When its assignment is completed the center is dissolved. One of the earliest centers compiled The International Critical Tables. It was closed when the "Tables" were published.

Many authorities believe that the answer to improve scientific communication and the overcrowding of the scientific literature lies in the mechanization or the automation of the publication processes. Perhaps papers will need to be published in code or some type of notation so that the information the papers contain can be readily stored in the memory of a computer for future retrieval and machine processing or microfilming. Perhaps a new language, a computer language, will be coined and used by all nations so that the scientists will have an international medium of expression, really a classified one, all of their own. In either approach scientists would need to familiarize themselves with a new method of composition that would lend itself to processing, storage, and retrieval. To date these proposals are nebulous, but societies must keep constantly alert to their possibilities.

Another remedy for the overcrowding of the scientific literature is the use of central depositories which several government agencies in the United States have found to be quite practical. By using central depositories scientists can refrain from unnecessary publication and yet make available their new material and thereby avoid being "scooped." In this approach authors deposit manuscripts in a central depository, which, in turn, announces the paper, with or without an abstract, in a bulletin, and then distributes the paper on request, in some cases on microfilm. Later, when the scientist has accumulated sufficient data he publishes the total in one comprehensive paper in an accredited journal; he thus avoids a series of papers with basically the same format but with each paper containing relatively little that is new. I have mentioned this in detail since the "Weinberg Report" called upon technical societies to consider serving as central depositories, stating "The Panel (on Scientific Information), although recognizing the difficulties of replacing the traditional techniques of communication *via* conventional journals, nevertheless urges technical societies to experiment with central depositories, or some variant thereof . . . , for at least some of their literature."

Two societies in the United States are following this recommendation in part. However, the general response has not been enthusiastic. Scientists are reluctant to relinquish the prestige that goes with publication in an accredited journal; also societies, except the very large ones, do not have the financial means to operate a depository; and the allotment of categories among the societies is not a matter on which agreement is easily attained. The Panel was careful to say "experiment with" rather than "adopt," and I believe it would be well for The Electrochemical Society to look at the matter through its Publication and Technical Committees.

Finally, the question arises as to the future of scientific societies in an age of automation, data processing, information retrieval, science centers, and central depositories. We know that many small enterprises in certain areas, banking, for example, have merged in order to obtain computer and related services; actually, it is a question if they could have survived otherwise. Will scientific societies need to tread the same path? I think not. Actually, the traditional role of the scientific society where personal contacts prevail and new ideas flourish, I am convinced, is becoming ever more important in an age of mechanization and automation. The role of the scientific society is of increasing importance in order to provide leadership in solving the problem of scientific communication: by serving as a forum for new ideas, new developments, and stimulating thought; by being at the frontiers of science; by maintaining the highest standards in publication and other means of communication; and by giving consideration to new methods that may be proposed for making available scientific information and discoveries. In these lights I am very optimistic for The Electrochemical Society. The Electrochemical Society was conceived as an interdisciplinary organization, has served well in this role, and is well equipped, through its members and background, to adapt to the changes of the future.

Extended Abstract Book Publication Program for the Society's 1965 Spring Meeting in San Francisco, Calif.

The Board of Directors has provided that the National Office shall assist Divisions with the mechanics of publishing Extended Abstracts for sessions involving 15 or more papers at our National Meetings.

The Divisions will handle the technical editing of the abstracts following which the Society Office will arrange for the printing and distribution of the books, thus relieving Division representatives of this responsibility. Each Division program will be the subject of a separate Extended Abstract Book.

This means that each author who submits a paper for presentation at our meeting should do three things:

1—Submit *three* copies of the usual 75-word abstract of the paper for publication in the printed program of the meeting;

2—Simultaneously submit *three* copies of an extended abstract of the paper of 500-1000 words; and

3—Send the 75-word abstract and the 500-1000-word extended abstract to Society Headquarters, 30 East 42 St., New York, N. Y., 10017, *not later than December 15, 1964.*

The Extended Abstract Books will be published by photo-offset reproduction *from typewritten copy submitted by the author.* Special care should therefore be given to the following typing instructions so as to establish uniformity in printing:

1—Abstracts are to be 500-1000 words in length.

2—Use white bond paper, size 8½ x 11 inches.

3—Abstracts should be typed SINGLE space.

4—Use 1¼ inch margins at the top and bottom and at the sides of each page.

5—All copy, including figures, symbols, and corrections, should be in black ink.

6—Figures should be pasted in within the typing dimensions indicated. Captions should be typed not wider than figure dimensions and pasted in proper place in the abstract. Figure captions should appear at bottom of figure. Table titles should appear at top of tables.

7—Wherever possible, avoid use of halftones.

8—Title of paper should be in capital letters. Author(s) name and affiliation should be typed immediately below. It is not necessary in the heading or body to designate paper as "Extended Abstract," or quote the Divisional Symposium involved.

9—Mail to Society Headquarters *unfolded.*

Members and JOURNAL subscribers will receive notice of Extended Abstracts Books to be scheduled for publication. The notices will be accompanied by order blanks for the copies desired. Orders should be submitted with remittance. The advance orders will be necessary for estimating numbers of books to be printed and will be mailed to purchasers prior to the Toronto meeting. Some extra copies will be available at the meeting but the advance-paid order is the only way to be assured of getting copies.

Annual Report of the Board of Directors, April 1, 1963-March 31, 1964

(Presented at Society Business Meeting, Toronto, May 5, 1964)

As you all know Robert K. Shannon who served this Society well as Executive Secretary from 1955 to 1964 passed away on January 9, 1964. Mr. Shannon contributed much to the arrangement and success of the Technical Program of this Toronto Meeting. Working with the Technical Committees in setting up the Technical Program for this meeting was his last official act. We have lost a good and kind friend. In respect to his memory, will you please stand and with me observe a minute of silence.

This is the 125th Annual Meeting of The Electrochemical Society and the fourth time we have met here in Toronto. A meeting in Canada is always an enjoyable occasion and each one serves to remind us of the great part Canada has played in developing the electrochemical industry in this continent.

I wish to extend a special welcome to the Metallurgical Society of AIME which is cosponsoring with us the international symposium on Electron and Ion Beam Science and Technology. I also wish to welcome those from countries outside this hemisphere.

Your Board of Directors has the following matters of importance and special interest to bring to the attention of members of the Society at this time.

Executive Secretary

The Board of Directors has appointed Ernest G. Enck as Executive Secretary of the Society for a two-year term starting on Thursday, May 7, 1964. As you will recall, Mr. Enck was appointed Acting Executive Secretary at the Board Meeting of January 10, 1964, to fill the position at the time of the death of Robert K. Shannon. Mr. Enck is extremely well qualified to be Executive Secretary having served the Society in many capacities. He served as Treasurer for a three-year term from 1961 to 1964, was re-elected for a second three-year term which he is now relinquishing, was General Convention Chairman of the National Meetings held in Philadelphia in 1949 and 1959, and served the Philadelphia Section as Treasurer, Vice-Chairman, and later as Chairman. The Electrochemical Society is most fortunate that Mr. Enck is willing to serve as its Executive Secretary for the next two years.

Treasurer

The Board of Directors has appointed Dr. Ralph A. Schaefer as Treasurer of the Society for a two-year term starting on Thursday, May 7, 1964, to fill the vacancy which was created when Ernest G. Enck resigned as the Society's Treasurer to accept the position of Executive Secretary. Dr. Schaefer is thoroughly familiar with the operations of the Society having served as its President, its Vice-President, and on its Board of Directors as Chairman of the Electrodeposition Division. The Society is most fortunate that Dr. Schaefer is willing to serve as Treasurer for the next two years.

Assistant Executive Secretary and Administrative Assistant to the Executive Secretary

The Board of Directors at its meeting on January 10, 1964, created two new staff positions, namely, Assistant Executive Secretary and Administrative Assistant to the Executive Secretary to facilitate operations in the National Office. Mr. Robert A. Kolbe was appointed Assistant Executive Secretary and Miss Rena Garlick Administrative Assistant to the Executive Secretary.

The India Section

On January 1, 1964, the India Section of the Society dissolved as a Local Section of The Electrochemical Society in order to organize as The Electrochemical Society of India. The India Section became the 12th Local Section of The Electrochemical Society in 1950 and during the 14 years of its affiliation was active in its support of the Society. The India Section issued a Bulletin known as the "Bulletin of The India Section of The Electrochemical Society" and from 1952 to 1963, inclusive, published 12 volumes which will remain as a permanent record in the scientific literature. The Electrochemical Society extends its best wishes to the Indian electrochemists in their new venture.

Page Charges

The Board of Directors at its Meeting in New York on September 29, 1963, on the recommendation of the Publication and Finance Committees, established a charge of $35.00 per printed page for articles published in the JOURNAL OF THE ELECTROCHEMICAL SOCIETY. This action became effective on February 1, 1964, and, therefore, is now in operation. The Board of Directors also voted to grant a 10% reduction in page for papers authored by one or more members of The Electrochemical Society and/or by one or more designated representatives of Patron or Sustaining Members of the Society. The Board of Directors also stressed in their action that papers will be accepted, as in the past, on the basis of merit by established practices of review, and that the payment of page charges will be waived by The Electrochemical Society when funds are not available.

Amendments to Bylaws

The Board of Directors approved of three amendments to the Bylaws of the Society for the purpose of:

1—clarifying an ambiguity in the section pertaining to appeals by a Division from a decision of the Technical Committee;

2—authorizing the Technical Committee to deal with questions of participation in inter-society affairs not only by the Society itself but also by one or more of its Divisions or Local Sections;

3—requesting Division inviting a foreigner to participate in a National Meeting to appoint an

official representative to serve as host for such visitors.

Society Representatives

During the year The Electrochemical Society had official representatives at the Centennial Celebration of the National Academy of Sciences in Washington, D. C., at the 29th Exposition of Chemical Industries in New York, at the presentation of the Society of Chemical Industry's Gold Medal to Dr. Max Tishler in Houston, at the presentation of the Perkin Medal Award to Dr. William J. Sparks in New York, at the Centenary Charter Convocation of Manhattan College of New York, at the seventy-fifth anniversary of Georgia Institute of Technology, and at the inauguration of William Louis Whitson as President of Clarkson College of Technology, Potsdam, N. Y.

Palladium Medal Award

The Board of Directors approved the Revised Rules for the Palladium Medal Award prepared by the Palladium Medal Committee.

Local Section Visits

This is the second year in which visits to the Local Sections were shared by the President and the three Vice-Presidents of the Society. I can report that these visits have been most enjoyable and have given these officers of the Society the opportunity to become better acquainted with the activities and problems of the Local Sections.

Lawrence Addicks

We wish to record with sorrow the passing on January 16, 1964, of Lawrence Addicks, the thirteenth President of our Society.

National Office

I can report that matters in the National Office are well in hand. Some reorganizations in addition to those I have already mentioned have been made. A new position of Manager of Publications has been created and Mr. Robert A. Kolbe has been appointed as the first Manager of Publications. In addition Mr. Kolbe will continue to serve as Assistant Executive Secretary. Finally, on behalf of the Board of Directors, I wish to express appreciation to Mr. Ernest G. Enck, who has given graciously of his time during the past four months in the capacity of Acting Executive Secretary.

Walter J. Hamer, *President*

Annual Report of the Secretary, April 1, 1963–March 31, 1964

(Presented at Society Business Meeting, Toronto, May 5, 1964)

It is a pleasure to review the progress which has been made by the Society during the past fiscal year.

Membership

The membership of the Society is at an all-time high of 3776 members. This compares with the previous year's total of 3606 and represents a net increase of 170 members.

Patron and Sustaining Memberships

Corporate support in the form of Sustaining Memberships showed an increase of 1 and now total 136. Patron Memberships remain at 6.

Publications

During the past year the number of papers submitted for publication in the JOURNAL continued to increase, and the budget for the JOURNAL was increased to permit the publication of additional papers.

Journal

A continuing study is being made to determine ways of providing funds for the publication of the larger volume of papers that can be anticipated in future years.

Electrochemical Technology

1963 was the first full year of publication of ELECTROCHEMICAL TECHNOLOGY. The response to this new publication has been most encouraging, and ELECTROCHEMICAL TECHNOLOGY is now self-supporting.

Extended Abstracts

During 1963 the responsibility for the Extended Abstract publication was delegated to the National Office. The Extended Abstract program has been enthusiastically received and supported by those in attendance at the National Meetings.

Monographs and Special Publications

The following monographs were approved for publication during the year 1963:

- Electrolytic Solutions
- Electrochemical Control of Corrosion
- Light Metal Corrosion
- Aqueous Corrosion and its Inhibition
- Plasma Technology
- Electron and Ion Beam Science and Technology

Program Issue

The complete program of the papers being presented at the Society's 1964 Fall Meeting in Washington, D. C., will appear in the August issue of the JOURNAL.

Becket Memorial Award

The F. M. Becket Memorial Award for 1964 was awarded to J. Keith Johnstone who will study this summer at Imperial College, University of London. Mr. Johnstone is the second recipient of this Award which was established by Union Carbide Corp.

Colin Fink Fellowship

The Colin Garfield Fink Fellowship was awarded to William G. Lemmermann of Columbia University, New York City.

Edward Weston Summer Fellowship

The Edward Weston Summer Fellowship was presented to Henry O. Daley, Jr. of Boston College, Chestnut Hill, Mass.

ECS Summer Fellowship

The Electrochemical Society Summer Fellowship was awarded to C. C. Liu, California Institute of Technology.

Young Author Prizes

The presentation of the Society's Young Author Prize and the Francis Mills Turner Award of the Reinhold Publishing Co. for the best papers appearing in the JOURNAL by young authors for 1963 will be made by President Hamer at our Banquet this evening.

Financial Statement of The Electrochemical Society, Inc.
Fiscal Year—April 1, 1963-March 31, 1964

Balance Sheet at March 31, 1964

Statement of Assets

Bank Balances & Cash

Chemical Bank New York Trust Company		
Corrosion Division	1,480.60	
Electric Insulation	211.18	
Electronics Division	1,894.51	
Electrodeposition Division	2,303.19	
Electrothermics and Metallurgy Division	1,818.98	
Theoretical Division	2,907.11	
Electro-Organic	56.19	
New Capital Equipment Fund	297.13	
Colin Garfield Fink Fellowship Fund	652.55	
Consolidated Fellowship Fund	1,429.96	
Weston Fellowship Fund	207.60	
Society Reserve Fund	4,866.50	
General Operating Fund	$ 54,745.41	$ 72,870.91
Petty Cash	80.41	
Excelsior Savings Bank — General Fund	10,433.60	
Greenwich Savings Bank — General Fund	10,070.19	
Chase Manhattan Savings Account — General Fund	10,414.39	
First National City Savings Account — General Fund	10,806.34	
Bowery Savings Bank — General Fund	10,524.40	
Chemical Bank Savings Account — Acheson Fund	3,332.44	
Chemical Bank Savings Account — Becket Fund	1,409.83	
Central Savings Bank — Richards Memorial Fund	936.17	$ 58,007.77
		$130,878.68

Custodian Fund

Electronics Division		$ 2,047.09

Consolidated Portfolio of Investments (Value 3/31/64)

Edward Goodrich Acheson Fund		$ 45,734.99	
F. M. Becket Memorial Fund		22,586.10	
Consolidated Fellowship Fund		44,944.60	
Colin Garfield Fink Fellowship Fund		9,885.82	
Edward Weston Fellowship Fund		18,165.78	
Society Reserve Fund		157,699.27	
Monograph Funds:			
Corrosion Division	$16,604.40		
Electrodeposition Division	1,000.00		
Electrothermics & Metallurgy Div.	4,000.00	21,604.40	320,620.96

Other Assets

Accounts Receivable		4,428.18	
Furniture and Fixtures	16,480.27		
Less Reserve For Depreciation	1,346.40	15,133.87	
Inventory		5,561.86	
Prepaid Postage		898.33	
Convention Advance		500.00	26,522.24
			$480,068.97

Statement of Liabilities and Special Funds

Liabilities

Accounts Payable	$ 5,190.60

Deferred Income

Journal Bound Volume	$ 1,147.54	
Electrochemical Technology Bound Volume	367.85	
Patron and Sustaining Membership Dues	17,115.00	
Membership Dues	43,355.53	
Life Memberships	2,222.58	
Journal Subscriptions	38,423.40	
Electrochemical Technology Subscriptions	12,942.34	
Abstracts	3,392.81	118,967.05

Special Funds

Awards and Fellowships:			
Edward Goodrich Acheson Fund		49,067.43	
F. M. Becket Memorial Award Fund		23,995.93	
Consolidated Fellowship Fund		46,374.56	
Colin Garfield Fink Fellowship Fund		10,538.37	
Richards Memorial Fund		936.17	
Edward Weston Fellowship Fund		18,373.38	149,285.84
Monographs Funds:			
Corrosion Division		$ 18,085.00	
Electronics Division		686.94	
Electrodeposition Division		3,180.84	
Electrothermics & Metallurgy	5,753.20		
Less Iron Ores Advance	$249.37		
Less Electron Beam Expenses	315.26	564.63	5,188.57
Theoretical Division			2,507.90	29,649.25
Extended Abstract Book Funds:				
Electrothermics & Metallurgy			65.78	
Electronics Division			1,207.57	
Electric Insulation Division			211.18	
Electrodeposition Division			122.35	
Theoretical Division			399.21	
Electro-Organic Division			56.19	2,062.28
Custodian Fund				
Electronics Division				2,047.09
Society Reserve Fund				162,565.77
General Fund		3,431.19		
New Capital Equipment		297.13	3,728.32	
Less Advances				
Electro-Organic Chemistry		500.00		
Technology of Columbium		439.45		
Vacuum-Metallurgy		(9.06)		
High Temperature Technology		232.25		
Modern Electroplating		530.87	1,693.51	
			2,034.81	
				10,301.09
				$480,068.97

Statement of Income and Expenses
The Electrochemical Society, Inc.
March 31, 1964

Income

Membership Dues	$ 63,940.18
Patron and Sustaining Memberships	23,386.25
Subscriptions:	
Electrochemical Technology	18,739.18
Journal of ECS	54,598.40
Reprints: (Net):	
Journal	5,889.88
Electrochemical Technology	756.01
Bound Volumes:	
Journal	1,526.58
Electrochemical Technology	383.13
Advertising:	
Journal	6,822.54
Electrochemical Technology	2,860.75
Conventions:	22,041.80
Extended Abstracts	4,247.73
Interest Earned on General Funds	1,652.31
Ten Year Index of Journal	995.00
Monograph Royalties	3,037.47
Income From Investments	6,225.23
Office Sale of Publications	2,142.20
	$219,244.64

Expenses

Print and Mail Journal	66,269.95
Print and Mail Electrochemical Technology	12,098.58
Salaries	86,434.47
Office Rental	14,900.04
Postage, Supplies and Miscellaneous	14,511.78
Bound Volumes:	
Journal	3,990.96
Electrochemical Technology	174.04
Local Sections and Divisions	1,751.00
New York Office Travel	1,788.52
Presidential Office Fund	2,310.28
Conventions	6,181.56
Membership Directory	467.18
Young Authors Prize	100.00
	$210,978.36
Excess Income Over Expenses	8,266.28
	$219,244.64

Certificate of Audit

I have examined the balance sheet and statement of income and expense of The Electrochemical Society, Incorporated, for the period April 1, 1963 to March 31, 1964. My examination was made in accordance with generally accepted auditing standards and, accordingly, included such tests of the accounting records as were considered necessary.

In my opinion, the balance sheet and statement of income and expenses present fairly the financial position of The Electrochemical Society, Incorporated, at March 31, 1964, in conformity with generally accepted accounting principles consistent with the prior years.

June 10, 1964

(Signed) N. W. Marinelli, *Auditor*

Electrochemical Society Awards

James A. Cunningham

E. J. Cairns

Martin Weinstein

Young Author's Prize 1963

At the Annual Banquet held on Tuesday, May 5, during the Toronto Meeting of The Electrochemical Society, James A. Cunningham, a senior engineer at Texas Instruments Inc., Dallas, Texas, was announced as the winner of the 1963 Young Author's Prize of $100. His prize-winning paper, written in cooperation with G. A. Watts entitled "Mechanism of Electrodeposition from Aqueous Solutions of Square Planar Complexes," appeared in the July 1963 issue of the JOURNAL.

Dr. Cunningham presently holds the position of senior engineer and head of the Small Signal Fabrication Technology Section at Texas Instruments Inc. Current research interests include semiconductor surfaces and electrical contacts, corrosion, inorganic synthesis, and electrodeposition. He has recently published a paper entitled "The Formation of Organic-Silicon Surfaces" in ELECTROCHEMICAL TECHNOLOGY.

He holds B.A., M.A., and Ph.D. degrees from the University of Texas. His doctorate, granted in 1961, is in Inorganic Chemistry.

He is a member of The Electrochemical Society, Phi Lambda Upsilon, and Sigma Xi.

Turner Memorial Award for 1963

E. J. Cairns of General Electric Co., Schenectady, N. Y., and Martin Weinstein of Tyco Laboratories, Inc., Waltham, Mass., are co-winners of the Francis Mills Turner Memorial Award, sponsored by the Reinhold Publishing Corp., in recognition of their papers which appeared in the JOURNAL during 1963: E. J. Cairns for the paper "Thermodynamics of Hydrocarbon Fuel Cells" written in cooperation with A. D. Tevebaugh and G. J. Holm, published in the October 1963 issue; Martin Weinstein for the paper "Thermodynamic Properties of the Manganese-Lead-Bismuth System" written with J. F. Elliott, published in the July 1963 issue.

The award, consisting of $100 worth of scientific and technical publications to each winner, was made to Dr. Cairns and Dr. Weinstein at the Society's Annual Banquet on May 5 in Toronto.

Dr. Cairns has been with General Electric Research Labs., as a member of the Physical Chemistry Section since 1959. While at G.E., he has been working in the fields of electrochemistry, fuel cells, and thermodynamics.

He received his B.S. degree in chemistry from the Michigan College of Mining and Technology in 1955; and a B.S. degree in chemical engineering in the same year. He was awarded a Ph.D. degree from the University of California (Berkeley) in kinetics and mixing phenomena. While at the University of California he held fellowships from the Dow Chemical Co., the University of California, and the National Science Foundation.

He is a member of the ACS, AIChE, AAAS, N. Y. Academy of Sciences, Phi Kappa Phi, Sigma Xi, Tau Beta Pi, Phi Lambda Upsilon, Phi Eta Sigma, and The Electrochemical Society. He is past representative on the Council of Local Sections, and is presently Secretary-Treasurer of the Mohawk-Hudson Section.

Dr. Martin Weinstein received a B. Met. E. degree from Rennsselaer Polytechnic Institute, Troy, N. Y., 1957, a M.Sc. and Sc.D. degree in Metallurgy from Massachusetts Institute of Technology, Cambridge, Mass., in 1959 and 1961, respectively.

His research at M.I.T. was concerned with the thermodynamics of liquid metallic solutions with emphasis on the correlation of electronic and chemical properties of binary and ternary systems. He joined Tyco Laboratories, Inc., Waltham, Mass., in 1961, where he is a senior scientist in Physical Metallurgy. His major research interest is in device materials science with particular emphasis on crystal growth, imperfections in solids, and new device configurations in compound semiconductors.

Dr. Weinstein is a member of The Electrochemical Society Sigma Xi, the American Institute of Metallurgical Engineers, and the American Society of Metals.

Notice to Members and Subscribers

(Re Changes of Address)

To insure receipt of each issue of the JOURNAL, please be sure to give us your old address, as well as your new one, when you move. Our records are filed by states and cities, not by individual names. The Post Office does not forward magazines.

We should have this information *by the 16th of the month* to avoid delays in receipt of the next issue.

Abstracts of "Recent News" Papers

Presented at Electronics Division Semiconductor Sessions, Toronto Meeting, May 3-7, 1964

Silicon Phosphide Precipitates in Diffused Silicon

P. F. Schmidt and R. Stickler, Westinghouse Research and Development Center, Pittsburgh 35, Pa.

The presence of a silicon phosphide phase in the surface layers of heavily-phosphorus-diffused silicon was suggested by the results of tracer experiments. Investigation of suitably thinned silicon specimens then led to the direct observation of the precipitate by transmission electron microscopy and to its crystallographic identification by means of electron diffraction.

Transmission Electron Microscope Investigations on Diffused Silicon Wafers with Relation to Electrical Properties of Semiconductor Devices

A. Knopp and R. Stickler, Westinghouse Electric Corp., Pittsburgh, Pa.

Uncontrollable variations of electrical properties of semiconductor devices are considered to be caused by relatively small concentrations of undesired impurities in the semiconductor material. Transmission electron microscope investigations on diffusion zones of silicon wafers showed that a correlation between electrical properties of devices and microheterogeneities in various diffusion zones exists. Due to mass spectrometric analysis, it seems very reasonable to correlate these microheterogeneities with the desired diffusion product and with heavy metals, especially copper and iron.

Surface Concentrations of Ga-Diffused Silicon as Functions of Ga-Temperature and Diffusion Systems

A. N. Knopp, Westinghouse Electric Corp., Youngwood, Pa.

Surface concentration of gallium diffused n-type silicon in a closed quartz ampoule system can be controlled by the partial vapor pressure of a metallic gallium source or by one of its oxides. The results of this investigation show that the surface concentration can be controlled by the "source" temperature and various parameters of the diffusion system, *e.g.*, by total pressure of our inert atmosphere and partial pressure of water vapor.

Five Probe Technique For Measuring Silicon Properties

D. I. Pomerantz, Lab. for Physical Science, P. R. Mallory & Co., Inc., Northwestern Industrial Park, Burlington, Mass.

A five probe technique described for measuring properties of diffused and epitaxial layers near a silicon junction. In addition to four conventional resistivity probes, a fifth contact is made to the substrate to bias the junction between substrate and layer. Sheet conductivity of the layer and capacitance of the junction are measured as a function of this bias, allowing a determination of carrier concentration and mobility as a function of distance from the junction.

Electron Microscopy of Diffusions in Semiconductors

R. J. Jaccodine, Bell Telephone Labs., Inc., Allentown, Pa.

An electron microscopic study of high concentration phosphorous diffusion ($>10^{19}/cm^3$) with silicon of (111) and (100) orientation has been undertaken. Samples were taken from both chemically polished and mechanically prepared material. Examples of observations of dislocation networks induced by diffusion are illustrated. Burger's vector determination, line orientation, and density are discussed. Similar observations made with high concentration boron is presented.

A New Dielectric Isolation Technique for High Quality Silicon Integrated Circuits

D. Mc Williams, C. Fa, G. Larchian, and O. Maxwell, Jr., Autonetics Div. of North American Aviation, Inc., 3370 East Anaheim Rd., Anaheim, Calif.

A new technique for improving integrated circuits has been developed by Autonetics' Solid State Devices Lab. Basically, it consists of growing a specific, but controlled, polycrystalline silicon layer over silicon dioxide. This yields isolated islands of single crystal silicon embedded in a polycrystalline substrate. A patent has been applied for under the title, "Electrically Isolated Semiconductor Devices on Common Crystalline Substrate." Devices fabricated by this "poly" technique show major advantages over the conventional monolithic structure as follows: the active regions are formed in high grade starting material (silicon); the parasitic capacitance is reduced by a factor of ten to one in comparison to conventional devices of identical areas; the isolation is excellent with a dielectric blocking voltage greater than 350v and resistance greater than 2×10^8 ohms (1 μa at 200v). The decreased parasitic capacitance of the poly process has extended the high frequency applications while the increased isolation makes possible integrated circuits with higher voltage ratings.

Detection of Low Concentrations of Metallic Impurities in Si

M. C. Duffy, W. J. Armstrong, and M. S. Hess, Components Div., International Business Machines Corp., Poughkeepsie, N. Y.

It has previously been shown that metallic impurities in silicon can cause "soft" reverse bias junction characteristics, and that P_2O_5 gettering can be used to "clean up" the soft junctions. This paper deals with a method of detecting extremely small quantities of these impurities in silicon. It was used to determine the processing step in which the impurities were introduced. This technique consists of forming high-purity P_2O_5 on silicon substrates by the *in situ* oxidation of PH_3 gas, passing the substrates through a thermal gettering cycle, and then analyzing the P_2O_5 by a standard spectrographic technique. Due to the concentrating effect of this method, it was possible to detect Fe, Ni, Cu, and Zn to the level of 10^{14} at./cm^3. It was determined that these elements are initially present in silicon and that significant amounts are removed by P_2O_5 gettering.

A Single Crystal Metal Base Transistor

J. Lindmayer, J. J. Casey, and R. R. Garnache, Research Center, Sprague Electric Co., North Adams, Mass.

Previous attempts to develop hot electron transistors have relied heavily on evaporative methods which result in two successive poly-

crystalline layers deposited usually on a single crystal substrate. This paper describes a metal base transistor, of single crystal structure throughout, in which the metal layer and the second semiconductor layer are deposited on a single crystal substrate by epitaxial techniques. The particular devices to be described have been made from the single crystal structure Si-$MoSi_2$-Si, in which $MoSi_2$ is the metallic layer. These new majority carrier devices have been characterized for voltage, current, and power gain, frequency response, and other electrical parameters, which are discussed in detail. The important aspects of similarity and dissimilarity between the metal base transistor and conventional transistors are pointed out, and theoretical justifications for these are given. Comparisons of low-temperature and high-temperature operation of metal base transistors and conventional transistors have been made. As expected, the alpha of the hot electron device improves with decreasing temperature, while that of the conventional transistors behave oppositely. The devices have been tested for radiation resistance at an integrated flux of 3×10^{14} NVT and have been found to have radiation resistance properties markedly superior to those of conventional transistors. Detailed results of these experiments are presented.

The Effect of Growth Parameters and Solute on the Radial Resistivity Uniformity of Czochralski Grown Silicon Crystals

K. E. Benson, Bell Telephone Labs., Inc., Allentown, Pa.

The effects of growth rate, seed rotation, crucible rotation, crystal diameter, solute, and solute concentration on the radial resistivity uniformity of Czochralski grown silicon crystals have been determined. A pronounced maximum in radial resistivity variation which increases with growth rate was found to exist at seed rotation rates of 10 rpm or crucible rotation rates of 25 rpm. When both seed and crucible rotations were used counter to each other, these maximums were still present indicating that seed rotation acts independently of crucible rotation in controlling the radial resistivity profile under the growth conditions investigated. The effect of crystal diameter and the solutes B, Ga, In, Al, P, As, and Sb were investigated for a seed rotation of 50 rpm and a growth rate of 11.2 cm/hr.

Crystal Defects in P-type Epitaxial Silicon

G. H. Schwuttke (Present address: International Business Machines Corp.) General Telephone & Electronics Labs., Bayside, N. Y., and V. Sils, Sylvania Electric Inc., Woburn, Mass.

P-type epitaxial Si films of 10 ohm-cm resistivity were grown by $SiCl_4$ vapor decomposition on the (111) face of boron-doped single-crystal silicon, ranging in resistivity from 10 to 0.001 ohm-cm resistivity. The influence of interfacial misfit introduced by the impurity concentration gradient between substrate and epitaxial films on epitaxial layer perfection was studied through x-ray diffraction microscopy. Large-area topographs revealed characteristic line defects in <110> directions. The x-ray measurements indicate that the faults are extended dislocations of the Lomer-Cottrell type. [Research supported by the U.S. Air Force Cambridge Research Lab. under contract AF(604)7313.]

A Slide Rule for Computing Dopant Profiles in Epitaxial Semiconductor Films

I. Amron, Bell Telephone Labs., Inc., Murray Hill, N. J.

A slide rule has been developed for the rapid calculation of the dopant concentration profiles of epitaxial semiconductor films from differential capacitance measurements. The slide rule uses the raw data directly and eliminates the need for the prior normalization of the data to unit area.

Etch Studies on Epitaxial and Bulk Silicon Using the Sirtl Etch

T. G. R. Rawlins, Research and Development Labs., Northern Electric Co., Ottawa, Ont., Canada

Studies have been undertaken to determine suitable etch times and procedures to give etch figures of crystallographic imperfections on epitaxial and bulk silicon having different conductivities and varying impurity concentration. These times range from 1-2 min and up for dislocations, and ½ min up for stacking faults, and vary with the density of imperfections. During the course of the work, etch figures, that are probably due to regions of high impurity concentration (or clustering) have occurred in low resistivity material. The rate of etching has been determined.

Distribution of Impurity Atoms in Epitaxial Silicon

B. A. Lombos and P. RaiChoudhury, Research and Development Labs., Northern Electric Co., Ottawa, Ont., Canada

The influence of the impurity content of the substrate material on the distribution of impurities in the epitaxial layer has been studied, and can be related to three main variables: (i) substrate impurity level, (ii) preheat and growth times, and (iii) preheat and growth temperatures. Different growth conditions have been used in an attempt to examine separately the simultaneously existing contributions. The evaluation of these experimental results gives some of the controlling parameters which are needed for

Page Charge Adopted for the JOURNAL

Increased costs of publication have made it necessary for The Electrochemical Society to institute a per page charge for publication in the JOURNAL.

At the Meeting of the Board of Directors held in New York on September 29, 1963 a charge of $35.00 per printed page was established by the Board of Directors, on recommendation of the Publication and Finance Committees, for papers published in the JOURNAL. This action becomes effective for papers received after February 1, 1964.

A 10% reduction in the page charge will apply to papers authored by one or more members of The Electrochemical Society and/or by one or more employees of Patron or Sustaining Members of the Society.

Papers are accepted for publication on the basis of merit by established practices of review. Acceptance of future papers for publication will not be dependent on payment of this invoice. Where funds are not available for payment of this charge it will be waived by The Electrochemical Society.

the understanding of the doping mechanism and for the possible adjustment of the impurity distribution and concentration in the epitaxial layer.

Optical Inhomogeneities in Gallium Arsenide

M. E. Drougard and J. B. Gunn, IBM Watson Research Center, Yorktown Heights, N. Y.

Local inhomogeneities and other defects have been observed by optical methods in pulled and epitaxially deposited crystals of gallium arsenide. The samples were lapped and polished and examined in transmitted light with an infrared image converter. A reasonably parallel illumination is sufficient to exhibit all the defects which have been seen up to now, but more detailed information can be obtained by Schlieren or phase contrast techniques. The physical mechanisms which make the defects visible are discussed.

Segregation of Dopant in GaAs Crystals Pulled from the Melt

T. S. Plaskett and S. E. Blum, IBM Watson Research Center, Yorktown Heights, N. Y.

Doped GaAs crystals, grown from the melt by the sealed Czochralski technique, were examined for chemical segregation by infrared transmission microscopy. The solute was observed to segregate in a striated (or banded) structure perpendicular to the growth axis and in some crystals segregated radially. Attempts were made to relate the segregation patterns to growth parameters.

X-Ray Diffraction Topographies of Imperfections in Gallium Arsenide by the Anomalous Transmission of X-rays

E. D. Jungbluth, General Telephone & Electronics Labs., Inc., Bayside 60, N. Y.

The Borrmann effect was utilized to form x-ray diffraction topographs of gallium arsenide single crystals grown by the Czochralski and the horizontal gradient freeze techniques. The dislocation densities in the Czochralski-type crystals are relatively high, and vary between 10^3 and 10^4 per cm^2 across the diameter and along the length of the ingot. The dislocation densities in the gradient freeze type crystals may be as low as 100 per cm^2, and little variation in the dislocation density was observed. Observations of dislocation contrast were made with respect to different reflections. The reflection dependency of segregation phenomena in solution-doped gallium arsenide were observed.

Interface-Alloy Epitaxial Heterojunctions

R. H. Rediker, S. Stopek, and J. H. R. Ward, Lincoln Lab., Massachusetts Institute of Technology, Lexington 73, Mass.

Epitaxial heterojunctions between GaAs and Ge and between GaAs and GaSb have been produced by melting only the interface between the two semiconductors. Kossel-line techniques and electron-beam microprobe analysis were used to investigate the nature of the heterojunction. In the interface alloying the wafers rotate and/or tilt with respect to each other as required for single crystal regrowth, which appears to be the lowest energy method for regrowing. Electrical properties of the junctions are discussed. (Operated with support from the U. S. Air Force.)

Preparation and Properties of AlAs-GaAs Mixed Crystals

J. F. Black and S. M. Ku, General Telephone & Electronics Labs., Inc., Bayside, N. Y.

AlAs-GaAs mixed crystals of graded energy gap were grown epitaxially onto GaAs substrates by a "closed-tube" iodide vapor transport process at a temperature of 700°C. Layers as thick as 10 mils with areas of several square centimeters were grown with composition varying from pure GaAs at the substrate-layer interface to 55 mole % AlAs at the surface. Electron-beam-probe microanalysis was used to determine lateral and transverse composition variation within the mixed crystal layer. By incremental grinding and x-ray fluorescence analysis, electrical and optical measurements were correlated with the AlAs-GaAs composition.

Injection Electroluminescence in AlAs-GaAs Diodes

S. M. Ku and J. F. Black, General Telephone & Electronics Labs., Inc., Bayside, N. Y.

P-n junction AlAs-GaAs diodes were made by diffusion of zinc at 800°C into epitaxial films with a graded energy gap. By control of junction depth, the emission wavelength could be varied according to the exact AlAs-GaAs composition at the p-n junction. The forward injection emission peaks were measured as a function of current at room and at liquid nitrogen temperature. Energy gap values obtained from the band-to-band emission peaks were correlated with composition at the p-n junction and compared to optical measurements of the energy gap in the epitaxial layer.

The Cleanness of Oxide Layers Produced on Silicon by Abrasion and by Etching

R. Stickler and J. W. Faust, Jr., Westinghouse Electric Corp., Pittsburgh, Pa.

Many steps in device fabrication take place through an oxide layer. In addition, oxide layers are used for surface stabilization. The perfection and cleanness of oxide layers on silicon were studied by transmission electron microscopy. Oxide layers formed by abrasion and also by mixed acid etchants were found to contain abrasive particles and other "dirt" while those from hydroxide etchants were found to be much cleaner.

Small Particles in Si

G. R. Booker and R. Stickler, Westinghouse Electric Corp., Pittsburgh, Pa.

Si grown by Czochralski or float zone techniques occasionally gives

December 1964 Discussion Section

A Discussion Section, covering papers published in the January-June, 1964 JOURNALS, is scheduled for publication in the December 1964 issue. Any discussion which did not reach the Editor in time for the June 1964 Discussion Section will be included in the December 1964 issue.

Those who plan to contribute remarks for this Discussion Section should submit their comments or questions in triplicate to the Managing Editor of the JOURNAL, 30 East 42 St., Rm. 1806, New York, N. Y., 10017, *not later than September 1, 1964.* All discussions will be forwarded to the author(s) for reply before being printed in the JOURNAL.

anomalously low yields of p-n junction devices, even though the resistivity, minority carrier lifetime, and dislocation density are within the normally acceptable ranges. When thinned areas of such Si specimens were examined in transmission in the electron microscope, large numbers of small particles embedded in the Si matrix were observed. The origin and identity of such particles and their effects on the electrical and mechanical properties of the Si are discussed.

Presented at the Silicon Diffusion and Device Technology Session, New York Meeting, Sept. 29, 30, Oct. 1, 2, and 3, 1963

The Role of Oxygen during Diffusion into Silicon from a Diborane Source

K. M. Busen, C. G. Pochop, and W. A. FitzGibbons, Research Center, Sprague Electric Co., North Adams, Mass.

The use of a mixture of phosphine (or diborane) and nitrogen as a source for the diffusion of phosphorus or boron into silicon has been described by Donovan and Smith. In their diffusion equipment oxygen is added to the mixture to prevent erosion of the silicon surface. The authors of this paper investigated a diffusion process where diborane was the impurity source, diluted by a mixture of oxygen and nitrogen. It was found that the oxygen concentration besides being influential for the surface conditions of the silicon after diffusion is an important factor for the magnitude of the surface concentration, C_o.

In three sets of experiments the amount of oxygen was varied while the diborane concentration was kept constant at 165, 100, or 45 ppm by volume, respectively. The resulting C_o, which was derived from V/I measurements depended linearly on the oxygen concentration as long as the latter was above 120, 100, or 80 ppm, respectively (range I). Below these values C_o first increased rapidly with decreasing oxygen content by nearly a factor of ten and then dropped back (range II). At the same time surface erosion of the silicon could be observed. The control of C_o within range II was very poor probably because of the deep pits due to the erosion. The behavior of the silicon seems to follow Wagner's theory which postulates that "at low oxygen content no layer of solid silica is expected to occur and the rate of attack due to the formation of volatile SiO is supposed to be proportional to the oxygen pressure in the bulk gas. Above a critical oxygen partial pressure, solid silica may be formed. . . ." In another set of experiments, where the oxygen concentration was kept constant (145 ppm), the surface concentration varied linearly with the diborane concentration.

ESC Officers for 1965-66

The Report of the Nominating Committee was approved by the Board of Directors at the Toronto Meeting.

The slate to be voted on this Fall is as follows:

President—Ernest Yeager; **Vice-President**—Ivor E. Campbell, Paul Delahay, and Charles W. Tobias; **Secretary**—Richard F. Bechtold.

Photographs and biographies of each candidate will appear in the October 1964 issue of the JOURNAL.

Personals

Frank L. LaQue, Vice-President of The International Nickel Co., Inc., received the honorary degree of Doctor of Laws from Queen's University, Kingston, Ont., at a convocation held on Saturday, May 16, in Kingston. Dr. LaQue, an alumnus of the University, was cited for the significant contributions he has made in research and development in the metals industry.

Dr. LaQue has been Vice-President of Inco since 1954, serving as manager of the Development and Research Div., from that time until 1962. He is, at present, engaged in rendering executive support to various activities of the company.

He joined Inco that same year and has since specialized in the field of corrosion and corrosion-resisting materials. It was under his leadership that Inco's well-known corrosion laboratory was established at Harbor Island (Kure Beach), N. C.

Dr. LaQue is chairman of the Advisory Panel for the Division of Metallurgy of the National Bureau of Standards, and is associated with the National Research Council of the National Academy of Sciences as chairman of the Subcommittee on Corrosion. He also serves as an advisor to the Metallurgical Dept. of Case Institute of Technology. He was

1965 Palladium Medal Award, ECS

The seventh Palladium Medal of The Electrochemical Society will be awarded at the Fall Meeting of the Society to be held in Buffalo, N. Y., October 10-14, 1965. The medal was established in 1951 by the Corrosion Division.

The candidate shall be distinguished for his original contributions to theoretical electrochemistry or to fundamental scientific knowledge of corrosion processes. He need not be a member of the Society. There shall be no restrictions or reservations made regarding his citizenship, age, or sex.

To be eligible, the candidate shall agree to receive the award in person at the designated national convention of the Society. He shall also agree to present a general lecture before the Society, at the above designated national convention, to be called the Palladium Medal Address. This address will in general describe some area of the candidate's researches, and will be presented at a time and place during the Convention to be specified in each instance by the Board of Directors.

Previous medalists have been: Carl Wagner, Max Planck Institut für Physikalische Chemie; N. H. Furman, Princeton University; U. R. Evans, Cambridge University; K. F. Bonhoeffer, Max Planck Institut für Physikalische Chemie (posthumous award); A. N. Frumkin, Electrochemical Institute of the USSR; and H. H. Uhlig, Massachusetts Institute of Technology.

Sections, Divisions, and members of the Society are invited to send suggestions for candidates, accompanied by supporting information, to Mr. Ernest G. Enck, Executive Secretary, The Electrochemical Society, Inc., 30 East 42 Street, New York, N. Y., 10017, for forwarding to the Committee Chairman. *Deadline for submission of suggestions is December 31, 1964.*

President of The Electrochemical Society during 1962-1963.

Paul Rüetschi has been appointed Technical Director of Leclanche, S.A., Yverdon, Switzerland, a well-known manufacturer of capacitors and batteries. During the past nine years Dr. Rüetschi was associated with The Electric Storage Battery Company, where he last held the position of manager, Electrochemistry Division, Carl F. Norberg Research Center, Yardley, Pa.

As a Past Chairman of the Theoretical Division of The Electrochemical Society, he has organized International Symposia at National ECS Meetings. He has served on several Award Committees of The Electrochemical Society.

Dr. Rüetschi is author of over 40 technical papers in the field of theoretical electrochemistry, reaction kinetics, surface chemistry, electrochemical energy conversion, and battery technology. He received the Young Author Award of The Electrochemical Society in 1957.

Victor Sils joined Transitron Electronics Corp. as manager of Epitaxial Materials, Integrated Circuit, and Transistor Div. Mr. Sils had previously served for three years as engineering specialist on epitaxial process development for General Telephone & Electronics, Sylvania Semiconductor Div.

Henry F. H. Wigton has joined Molectro Corp. of Santa Clara as head of Materials Research, it was announced recently. Dr. Wigton will establish an epitaxial facility for Molectro's integrated microcircuit manufacturing program. He joins Molectro after more than three years as a technical staff member of Fairchild Semiconductor Research and Development Labs. in Calif. He was previously associated with Minneapolis Honeywell, as senior scientist, and with E. I. DuPont, as a research chemist working on the oxidation and reduction of silicon, titanium, and niobium.

News Items

Electrochemical Symposium

The Industrial Electrolytic Division of the Society is planning a symposium on "Electrolytic Diaphragms and Separators" for the 1965 Spring Meeting of the Society in San Francisco, Calif.

Communications and inquiries regarding this symposium should be addressed to: Dr. Robert E. Meredith, Department of Chemical Engineering, Oregon State University, Corvallis, Oregon.

Corrosion Research Council

The 1964 annual meeting of the Corrosion Research Council will be held in Washington during the Fall

Meeting of the Society. The meeting is scheduled for 10:00 A.M. on Thursday, October 15, at the Sheraton-Park Hotel. In addition to the business meeting, members will review progress during the past year of research supported by the Council at university laboratories, and will also consider new proposals from qualified investigators.

The Corrosion Research Council was established in 1954 under the sponsorship of the Engineering Foundation, 345 East 47th Street, New York City. Currently, Dr. Earl A. Gulbransen of Westinghouse Electric Corp. is Chairman, and Frank T. Sisco is Executive Secretary. The object of the Council is to stimulate fundamental research in corrosion and to encourage training of students in this area. In this way, the several billion-dollar loss each year to the American economy through corrosion of metal structures can be abated making it possible for the overall product of American industry to reach a higher level. The research funds distributed by the Council are made available by various companies and industry associations in the United States and Canada.

Conference on Electrical Insulation

The Conference on Electrical Insulation of the National Academy of Sciences-National Research Council, will be held at the Union Carbide Corp., Parma Research Center, Cleveland, Ohio, on October 12, 13, and 14, 1964. For further information write to Mr. D. W. Thornhill, Staff Executive, Conference on Electrical Insulation, National Academy of Sciences, 2101 Constitution Ave., N. W., Washington, D. C., 20418.

Chemical Engineering Professorship Established

The New Jersey Zinc Co., New York, N. Y., has established the R. L. McCann Endowed Professorship in Chemical Engineering at Lehigh University with a gift of $100,000 to the University's Centennial Development Fund. The announcement of the endowed professorial post was made recently by Dr. Harvey A. Neville, president of Lehigh.

The gift was presented to the University by New Jersey Zinc to honor the long and distinguished career of its president, Mr. McCann, to both his company and his alma mater, Lehigh.

IEEE/PTGNS 1964 Nuclear Radiation Effects Conference

A nuclear radiation effects conference will be held in Seattle on the University of Washington campus July 20-24, 1964. The program includes sessions on dosimetry and nuclear measurements, fundamental topics, dielectrics, semiconductors, materials and components, analysis and design of circuits. Additional information may be obtained from: Mr. John C. Mitchell, Unit 2-53010, LTV-Vought Aeronautics Div., Ling-Temco-Vought, Inc., P. O. Box 5907, Dallas, Texas, 75222

Advertiser's Index

General Motors Corp., Research Labs. 158C

Great Lakes Carbon Corp., Graphite Products Div. ..... Cover 2

Keithley Instruments, Inc. 156C

Stackpole Carbon Co. 141C

Unitron, Inc. 157C

The Electrochemical Society

INSTRUCTIONS TO AUTHORS OF PAPERS

(Revised as of 4/1/64)

Address all correspondence to the Editor, JOURNAL OF THE ELECTROCHEMICAL SOCIETY, 30 East 42 St., New York, N. Y., 10017

GENERAL

Manuscripts must be submitted in triplicate to expedite review. They should be typewritten, double-spaced, with 2½-4 cm margins.

Title should be brief, followed by the author's name and professional connection. Authors should be as brief as is consistent with clarity and should omit introductory or explanatory material which may be regarded as familiar to specialists in the particular field. Proprietary and trade names should be avoided if possible; if used, they should be capitalized to protect the owners' rights.

Authors may suggest qualified reviewers for their papers, but the JOURNAL reserves the right of final choice.

TYPES OF ARTICLES

Technical Articles must describe original research of basic nature and must have adequate scientific depth. Articles of wide diversity of interest are appropriate, but subjects primarily covered in other specialized journals (*e.g.*, analytical or nuclear chemistry) are not considered appropriate. An ***Abstract*** of about 100 words should state the scope of the paper and summarize its results. Suitable headings and subheadings should be included, but sections should not be numbered. Articles in recent issues of the JOURNAL should be consulted for current style.

Technical Notes are used for reporting briefer research, developmental work, process technology; new or improved devices, materials, techniques, or processes which do not involve more extensive basic scientific study. No abstract is required.

Brief Communications are used only to report new information of scientific or technological importance which warrants rapid dissemination.

ILLUSTRATIONS

Drawings and ***Graphs*** ordinarily will be reduced to column width, 8.3 cm, and after such reduction should have lettering no less than 0.15 cm high. Lettering must be of letter-guide quality. India ink on tracing cloth or paper is preferred, but India ink on coordinate paper with blue ruling is acceptable. The sample graph shown on the reverse page conforms to suggestions of the American Standards Association (ASA Report Y15.1-1959).

Photographs should be used sparingly, must be glossy prints, and should be mailed with protection against folding. ***Micrographs*** should have a labeled length unit drawn or pasted on the picture.

Captions for figures (including photographs) must be included on a separate sheet. Captions and figure numbers must *not* appear in the body of the figure; they will be removed if they do.

Numerical Data should not be duplicated in tables and figures.

EQUATIONS

Mathematical Equations should be written on a single line if possible, and parentheses, brackets, the solidus (/), negative exponents, etc., may be used freely for this purpose. Authors are urged to consult Chapter VI of the "Style Manual" of the American Institute of Physics (available for $1.00 at American Institute of Physics, 57 East 55 St., New York, N. Y., 10022) and to follow the patterns described there.

SYMBOLS

If more than a few ***Symbols*** are used, they should be defined in a list at the end of the paper, with units given. For example:

$a, b \ldots$ = empirical constants of Brown equation

f_i° = fugacity of pure ith component, atm

D_v = volume diffusion coefficient, cm²/sec

ABBREVIATIONS UNITS

The AIP "Style Manual" referred to here gives a suitable list of common ***Abbreviations.*** Units usually will be abbreviated without periods throughout the text, as sec, min, hr, cm, mm, etc. **Metric Units** should be used throughout, unless English units are clearly more appropriate in the area of discussion.

POTENTIAL SIGNS

Electrode Potentials: Authors are urged to state and make use of the polarity of test electrodes with respect to the reference electrode used, *i.e.*, Zn is normally negative, Cu normally positive with respect to the standard hydrogen electrode. The sign for the emf of a cell should conform to the free energy change of the chemical reaction as written or implied, in accordance with the definition $\Delta G = -nFE$. These suggestions agree with the IUPAC conventions adopted in 1953. If any other convention is used, it should be stated clearly and used consistently throughout the manuscript.

REFERENCES

Literature References should be listed on a separate sheet at the end of the paper in the order in which they are cited in the text. Authors' initials must be given, and the style and abbreviations adopted by *Chemical Abstracts* should be used. Any recent issue of the JOURNAL may be consulted.

PUBLICATION CHARGE

A charge of $35 per printed page is made for publication of technical material in THIS JOURNAL. A 10% reduction is allowed if at least one author of an article is an ECS member or an employee of a Patron or Sustaining Member firm. However, acceptance of a manuscript is in no way dependent on such payment, and the charge may be waived in individual cases.

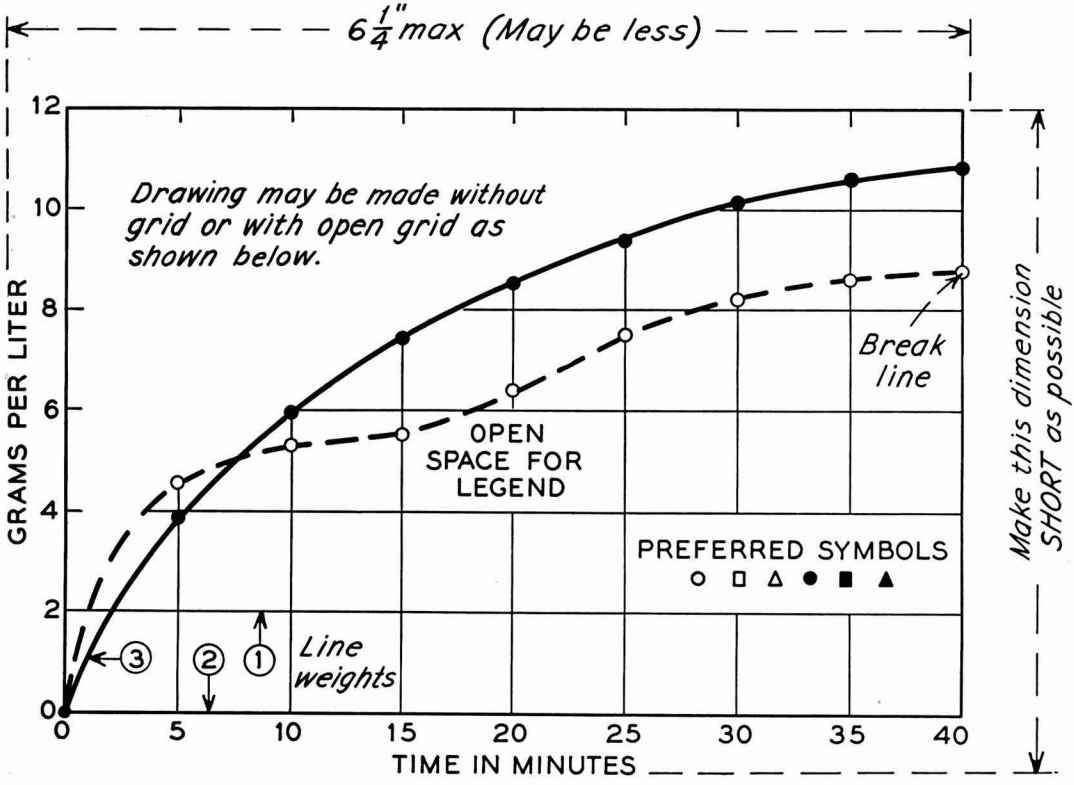

Remarks: Line weight 2 is used for borders and zero lines. When several curves are shown, each may be numbered and described in the caption. Lettering shown is approximately ⅛ in. In plotting current or potential as ordinate, increasing negative values should go down.

SAMPLE CURVE DRAWING FOR REDUCTION TO $\frac{1}{2}$ SIZE

The Electrochemical Society

Patron Members

Aluminum Co. of Canada, Ltd.,
Montreal, Que., Canada
International Nickel Co., Inc.,
New York, N. Y.
General Electric Co.
Capacitor Dept., Hudson Falls, N. Y.
Chemical Laboratory, Knolls Atomic Power Laboratory, Schenectady, N. Y.
Chemical and Materials Engineering Laboratory, Advanced Technology Laboratories, Schenectady, N. Y.
Chemistry Research Dept., Schenectady, N. Y.
Direct Energy Conversion Operation, West Lynn, Mass.
Lamp Division, Cleveland, Ohio
Materials & Processes Laboratory, Large Steam Turbine-Generator Dept., Schenectady, N. Y.
Metallurgy and Ceramics Research Dept., Schenectady, N. Y.
Olin Mathieson Chemical Corp.,
Chemicals Div., Research Dept., New Haven, Conn.
Union Carbide Corp.
Divisions:
Carbon Products Div., New York, N. Y.
Consumer Products Div., New York, N. Y.
Westinghouse Electric Corp., Pittsburgh, Pa.

Sustaining Members

Air Reduction Co., Inc., New York, N. Y.
Allen-Bradley Co., Milwaukee, Wis.
Allied Chemical Corp.
General Chemical Div., Morristown, N. J.
Alloy Steel Products Co., Inc., Linden, N. J.
Aluminum Co. of America,
New Kensington, Pa.
American Metal Climax, Inc.,
New York, N. Y.
American Potash & Chemical Corp.,
Los Angeles, Calif.
American Smelting and Refining Co.,
South Plainfield, N. J.
American Zinc Co. of Illinois,
East St. Louis, Ill.
American Zinc, Lead & Smelting Co.,
St. Louis, Mo.
M. Ames Chemical Works, Inc.,
Glens Falls, N. Y.
Ampex Corp., Redwood City, Calif.
Armco Steel Corp., Middletown, Ohio
Basic Inc., Maple Grove, Ohio
Bell Telephone Laboratories, Inc.,
New York, N. Y. (2 memberships)
Bethlehem Steel Co., Bethlehem, Pa.
(2 memberships)
Boeing Co., Seattle, Wash.
Burgess Battery Co., Freeport, Ill.
(2 memberships)
Burndy Corp., Norwalk, Conn.
Canadian Industries Ltd., Montreal,
Que., Canada
Carborundum Co., Niagara Falls, N. Y.
Chrysler Corp., Detroit, Mich.
Consolidated Mining & Smelting Co. of
Canada, Ltd., Trail, B. C., Canada
(2 memberships)
Continental Can Co., Inc., Chicago, Ill.
Cooper Metallurgical Associates, Cleveland,
Ohio
Corning Glass Works, Corning, N. Y.
Diamond Alkali Co., Painesville, Ohio
Dow Chemical Co., Midland, Mich.
Wilbur B. Driver Co., Newark, N. J.
(2 memberships)
E. I. du Pont de Nemours & Co., Inc.,
Wilmington, Del.
Eagle-Picher Co., Chemical and Metals Div.,
Joplin, Mo.
Eastman Kodak Co., Rochester, N. Y.
Thomas A. Edison Research Laboratory, Div.
of McGraw-Edison Co., West Orange, N. J.
Eltra Corp.,
Prestolite Div., Toledo, Ohio
C&D Batteries, Conshohocken, Pa.
Electric Storage Battery Co., Yardley, Pa.
Engelhard Industries, Inc., Newark, N. J.
(2 memberships)
The Eppley Laboratory, Inc., Newport, R. I.
(2 memberships)
Exmet Corp., Bridgeport, Conn.
Fairchild Semiconductor Corp., Palo Alto,
Calif.
FMC Corp.
Inorganic Chemical Div., Buffalo, N. Y.
Chlor-Alkali Div., South Charleston, W. Va.
Foote Mineral Co., Exton, Pa.
Ford Motor Co., Dearborn, Mich.
General Motors Corp.
Allison Div., Indianapolis, Ind.
Delco-Remy Div., Anderson, Ind.
Research Laboratories Div., Warren, Mich.
General Telephone & Electronics
Laboratories Inc., Bayside, N. Y.
(2 memberships)
Globe-Union, Inc., Milwaukee, Wis.
B. F. Goodrich Chemical Co.,
Cleveland, Ohio
Gould-National Batteries, Inc.,
Minneapolis, Minn.
Great Lakes Carbon Corp., New York, N. Y.

(Sustaining Members cont'd)

Hanson-Van Winkle-Munning Co., Matawan, N. J. (2 memberships)
Harshaw Chemical Co., Cleveland, Ohio (2 memberships)
Hercules Powder Co., Wilmington, Del.
Hill Cross Co., Inc., West New York, N. J.
Hoffman Electronics Corp., Semiconductor Div., El Monte, Calif.
Hooker Chemical Corp., Niagara Falls, N. Y. (3 memberships)
HP Associates, Palo Alto, Calif.
Hughes Research Laboratories, Div. of Hughes Aircraft Co., Malibu, Calif.
International Business Machines Corp., New York, N. Y.
International Minerals & Chemical Corp., Skokie, Ill.
International Resistance Co., Philadelphia, Pa.
ITT Federal Laboratories, Div. of International Telephone & Telegraph Corp., Nutley, N. J.
Jones & Laughlin Steel Corp., Pittsburgh, Pa.
K. W. Battery Co., Skokie, Ill.
Kaiser Aluminum & Chemical Corp.
Div. of Chemical Research, Permanente, Calif.
Div. of Metallurgical Research, Spokane, Wash.
Kawecki Chemical Co., Boyertown, Pa.
Kennecott Copper Corp., New York, N. Y.
Leesona Moos Laboratories, Div. of Leesona Corp., Jamaica, N. Y.
Arthur D. Little, Inc., Cambridge, Mass.
Lockheed Aircraft Corp., Missiles & Space Div., Sunnyvale, Calif.
Mallinckrodt Chemical Works, St. Louis, Mo.
P. R. Mallory & Co., Indianapolis, Ind.
Melpar, Inc., Falls Church, Va.
Miles Chemical Co., Div. of Miles Laboratories, Inc., Elkhart, Ind.
Minneapolis-Honeywell Regulator Co., Minneapolis, Minn.
Monsanto Chemical Co., St. Louis, Mo.
M&T Chemicals Inc., Detroit, Mich.
National Cash Register Co., Dayton, Ohio
National Lead Co., New York, N. Y.
National Research Corp., Cambridge, Mass.
National Steel Corp., Weirton, W. Va.
North American Aviation, Inc., El Segundo, Calif.
Northern Electric Co., Montreal, Que., Canada
Norton Co., Worcester, Mass.
Owens-Illinois Glass Co., Toledo, Ohio
Pennsalt Chemicals Corp., Philadelphia, Pa.
Phelps Dodge Refining Corp., Maspeth, N. Y.
Philco Corp., Research Div., Blue Bell, Pa.
Philips Laboratories, Inc., Irvington-on-Hudson, N. Y.
Pittsburgh Plate Glass Co., Chemical Div., Pittsburgh, Pa.
Potash Co. of America, Carlsbad, N. Mex.
Radio Corp. of America
Electronic Components and Devices, Lancaster, Pa.
Tube Div., Harrison, N. J.
RCA Victor Record Div., Indianapolis, Ind.
Ray-O-Vac Co., Madison, Wis.
Raytheon Co., Waltham, Mass.
Reynolds Metals Co., Richmond, Va.
Shawinigan Chemicals Ltd., Montreal, Que., Canada
Socony Mobil Oil Co., Inc., Dallas, Texas
Speer Carbon Co.
International Graphite & Electrode Div., St. Marys, Pa.
Sprague Electric Co., North Adams, Mass.
Stackpole Carbon Co., St. Marys, Pa.
Stauffer Chemical Co., New York, N. Y.
Texas Instruments, Inc., Dallas, Texas
Metals and Controls Corp., Attleboro, Mass.
3M Company, St. Paul, Minn.
Titanium Metals Corp. of America, Henderson, Nev.
Udylite Corp., Detroit, Mich. (4 memberships)
United States Borax & Chemical Corp., Los Angeles, Calif.
United States Steel Corp., Pittsburgh, Pa.
Univac, Div. of Sperry Rand Corp., New York, N. Y.
Universal-Cyclops Steel Corp., Bridgeville, Pa.
Upjohn Co., Kalamazoo, Mich.
Western Electric Co., Inc., Chicago, Ill.
Wyandotte Chemicals Corp., Wyandotte, Mich.
Yardney Electric Corp., New York, N. Y.